

https://dspace.org/

A bio-inspired 3D printed device for burn wounds

Giliomee, Johnel

2020
https://hdl.handle.net/10539/30412

Downloaded from a DSpace repository. https://dspace.org/

A Bio-Inspired 3D Printed Device for Burn Wounds

Johnel Giliomee



UNIVERSITY OF THE
WITWATERSRAND,
JOHANNESBURG

A thesis submitted to the Faculty of Health Sciences, University of the Witwatersrand, in fulfilment of the requirements for the degree of Doctor of Philosophy

Supervisor: Prof Viness Pillay

Department of Pharmacy and Pharmacology, Faculty of Health Sciences, University of the Witwatersrand, South Africa

Co-supervisors: Prof Yahya Choonara

Department of Pharmacy and Pharmacology, Faculty of Health Sciences, University of the Witwatersrand, South Africa

and

Prof Bert Klumperman

Department of Chemistry and Polymer Science, Faculty of Science

University of Stellenbosch, South Africa

June 2020

DECLARATION

I declare that this thesis is my own, unaided work. It is being submitted for the Degree of Doctor of Philosophy at the University of the Witwatersrand, Johannesburg. It has not been submitted before for any degree or examination at any other University.

……..

Johnel Giliomee

Signed at …….. on this ……day of June 2020.

Copyright © 2020 University of the Witwatersrand

All rights reserved

ABSTRACT

This study focused on the design, development and evaluation of 3D printed polypeptide-based hydrogel scaffolds as potential healing devices for burn wounds. The versatility of the hydrogels in terms of their physicochemical and biofunctional properties was explored to contribute to the development of biomaterial inks, suitable for 3D printing. 3D printed acellular scaffolds with customised physicochemical properties were further investigated to contribute to the limited knowledge on structure-function relationships of 3D printed scaffolds in terms of their *in vitro* and *in vivo* wound healing performance.

Controlled ring-opening polymerisation (ROP) and optimised hydrogel compositions were used to tailor the inherent physicochemical and biofunctional properties of a new library of hydrogels composed of poly(L-lysine-*ran*-L-alanine) and 4-arm poly(ethylene glycol) (P(KA)/4-PEG). This allowed the identification of P(KA)/4-PEG hydrogel compositions that displayed suitable combinations of properties for potential wound healing applications. One of the most promising hydrogels was the 4 wt% 1:1 functional molar ratio hydrogel with P(KA) concentrations as low as 0.65 wt%, which demonstrated low cytotoxicity and desirable cell adhesion towards fibroblasts.

P(KA)/4-PEG hydrogels were further processed into composite microgel pastes as new 3D biomaterial inks. The inks displayed good 3D printability, while the biofunctionality of the P(KA)/4-PEG hydrogels was retained. The physical properties of chitosan-P(KA)/4-PEG was further controlled using different 3D printing patterns. The mechanical properties of these scaffolds were relatively low with compressive and tensile moduli between ~45 and 147 Pa. Nonetheless, the scaffolds demonstrated adequate adhesion and spreading of fibroblasts seeded onto the scaffold surfaces for 4 days.

The *in vivo* performance of two chitosan-P(KA)/4-PEG scaffolds with porous and non-porous 3D printed architectures were then investigated using a full-thickness burn wound model of Sprague Dawley rats. These 3D printed scaffolds led to faster wound contraction in the first 5 days of the treatment, compared to the control groups. Interestingly, the porous 3D printed scaffold facilitated much reduced scar formation after 20 days. This was ascribed to the tailored physical properties of the porous 3D printed scaffold. However, histological evaluations could not provide definitive evidence to account for the improved scar appearance caused by the porous 3D printed scaffold.

To my dear husband, Jacques,

without whom this would not be possible

ACKNOWLEDGEMENTS

First, I want to thank my supervisors, Prof Viness Pillay, Prof Yahya Choonara and Prof Bert Klumperman, for their continued support and encouragement throughout my studies. To Prof Pillay and Prof Choonara I am truly grateful for the opportunity to be part of the Wits Advance Drug Delivery Platform (WADDP) research group. I also want to extend my gratitude to Prof Klumperman for the leap of faith he took in assisting me in my journey to the University of the Witwatersrand.

I am appreciative of the mentorship I received from Prof Pradeep Kumar and Dr Thashree Marimuthu. Your positive attitude and willingness to provide consultation has been a light in times of darkness. I am also very grateful for the technical assistance I received for various aspects of my research. I thank Dr Izak Kotze and Dr Hendrik Henning (Department of Chemistry) for NMR operation, Dr Helen Pfukwa and Dr Ingrid Heyns (Department of Chemistry and Polymer Science, Stellenbosch University) for SEC operation, Petra Dinham (Department of Mining Engineering) for SEM operation, Stephanie Malan and Dr Lisa Du Plessis (IDEXX) for histological analysis, and all the staff at the Central Animal Services (CAS) unit at the University of the Witwatersrand for their assistance and support during the *in vivo* animal studies. Furthermore, I thank the National Research Fund (NRF) for the funding towards my studies and travel grant.

To Sello Ramarumo, Bafana, Kleinbooi and Pride I am immensely grateful for the technical support they provided on a daily basis at WADDP. For being willing to go the extra mile, the encouragement and the friendships, I will forever be thankful. I am also indebted to my fellow students, Hillary Mndlovu, Funanani Takalani, Thope Moqejwa, Jacqueline Lekoloane and Kara de la Harpe who have eagerly assisted me during the *in vivo* animal studies. To all my friends in the WADDP group, Lara, Hillary, Kate, Gillian, Pakama, Lusanda, Lerato, Azraa, Anwary, Zainul, and Onyinye, I want to extend my heartfelt gratitude. I will always treasure the shared moments, the motivational speeches, and the inside jokes.

On a personal level, I am truly grateful to my parents for the opportunities they have granted me. To my late father, DC for instilling curiosity in me and for always encouraging me to do better, and to my mother, Marina for always believing in me and sometimes giving necessary hard words, *thank you and I love you, always*. Lastly, to my husband, Jacques, I cannot say thank you enough. *Without you, this endeavour would not have been possible. You have been my pillar of strength; you have kept me motivated in times I felt like giving up; you wiped my tears and put a smile on my face; you fed me world class food and looked after me; but most of all you still loved me throughout all of this. Dankie, my Bok. Ek is baie lief vir jou.*

CONTENTS

Declaration I

Abstract II

Acknowledgements IV

Contents V

List of Figures IX

List of Schemes XIV

List of Tables XV

Chapter 1: Prologue 1

1.1 Introduction 1

1.2 Aim and Objectives 2

1.3 Layout of the thesis 3

1.4 References 4

Chapter 2: Extrusion-based 3D Printing in Tissue Engineering, a general introduction 6

2.1 Introduction 6

2.2 Considerations for the 3D Biomaterial Ink 7

2.2.1 Thermoplastics 7

2.2.2 Pastes 10

2.2.3 Hydrogels and Reactive Resins 11

2.2.4 Bioinks 16

2.3 Considerations of the Scaffold Design 18

2.3.1 Surface Properties and Scaffold Chemistry 18

2.3.2 Porosity 21

2.3.3 Mechanical Properties 23

2.4 3D Printing in Wound Healing and Skin Regenerative Applications 25

2.5 Concluding Remarks 27

2.6 References 28

Chapter 3: Effect of Composition on the Physicochemical and Biological Properties of Polypeptide-Based Hydrogels for potential Application in Wound Healing 40

3.1 Introduction 40

3.2 Materials and Methods 42

3.2.1 Materials and general methods 42

3.2.2 Synthetic Procedures 42

3.2.3 Preparation of polypeptide-based hydrogels 44

3.2.4 Hydrogel Characterisation 44

3.2.5 *In vitro* cell studies 46

3.2.6 Antibacterial analysis 47

3.2.7 Statistical Evaluation 48

3.3 Results And Discussion 48

3.3.1 Preparation of Controlled Polypeptides 48

3.3.2 Preparation of a Library of Hydrogels 51

3.3.3 Assessment of the Rheological Nature of Selected P(KA)/4-PEG Hydrogels 53

3.3.4 Chemical Analysis of the Hydrogel Compositions 55

3.3.5 The Effect of Crosslinking and Concentration on the Hydrogel Network 57

3.3.6 The Biocompatibility Assessment of the Hydrogels 60

3.3.7 Evaluation of the Antibacterial Activity of the P(KA)/4-PEG Hydrogels 64

3.4 Conclusion 65

3.5 References 66

Chapter 4: Exploring the 3D Printability of poly(Lys_{60}-*ran*-Ala_{40})/4-arm PEG Hydrogels 71

4.1 Introduction 71

4.2 Materials and Methods 73

4.2.1 Materials and General Methods 73

4.2.2 Synthetic Procedures 73

4.2.3 Preparation and Characterisation of Hydrogel-Inks 74

4.2.4 3D Printability of the Biomaterial Inks 75

4.2.5 Scaffold Characterization 78
4.2.6 Statistical Evaluation 81
4.3 Results and Discussion 81
4.3.1 Preparation of Biomaterial Inks 81
4.3.2 Evaluation of the 3D Printability of the Biomaterial Inks 82
4.3.3 Evaluation of the Physical Properties of the Composite Microgel Scaffolds with "non-porous" 3D Printing Patterns 93
4.3.4 Effect of 3D Printing Pattern on the Physical Properties of CS-P(KA)/4-PEG Scaffolds 94
4.3.5 Effect of P(KA)/4-PEG Microparticles on the Biocompatibility of the Composite Microgels 96
4.4 Conclusion 97
4.5 References 99
Chapter 5: *In Vivo* Evaluation of a 3D Printed Scaffold as a Wound Healing Device on a Burn Wound Model of Sprague Dawley Rats 103
5.1 Introduction 103
5.2 Materials and Methods 104
5.2.1 Preparation of the Wound Healing Device 104
5.2.2 Study Design 105
5.2.3 Burn Wound Injury 106
5.2.4 Bandage Changes and Tissue Sampling 107
5.2.5 Wound Contraction Rate 107
5.2.6 Histological Assessment 107
5.2.7 Statistical Evaluation 108
5.3 Results and Discussion 108
5.3.1 Validation of the Burn Wound Model 108
5.3.2 Preparation and Application of the Wound Healing Device 110
5.3.3 Macroscopic Evaluation of the Wound Area 111
5.3.4 Histological Evaluation of the Wound Area 114

5.4 Conclusion 120

5.5 References 122

Chapter 6: Epilogue 125

6.1 General Conclusions 125

6.2 Recommendations for Future Work 127

6.3 References 129

Appendix A i

Appendix B ii

Appendix C iii

LIST OF FIGURES

Figure 2.1 SEM micrograph displaying a PEOT/PBT scaffold with hollow strands (A) (Moroni et al., 2006) and micro-computed tomography (μ-CT) image shows SPCL scaffold formed into tubular structure (B) (Silva et al., 2010)..... 9

Figure 2.2. SEM micrographs of PLLA scaffolds before NaCl leaching (A), and after NaCL leaching at 100× magnification (B) and 300× magnification (C) 11

Figure 2.3. A schematic representation of the different methods of crosslinking precursor hydrogels through ionic crosslinking: directly extruded into the crosslinking medium (A), extruded onto the printing platform fumed with crosslinking solution (B), coaxially extruded with a specially developed coaxial needle..... 14

Figure 2.4. Images of alginate/hyaluronic acid 3D printed into plotting medium without PVA and PEI clump (A) and with 0.95 % PVA and 0.1 % PEI (B)(Rajaram, Schreyer and Chen, 2014) 15

Figure 2.5. SEM micrographs show the strategies to improve the surface roughness of 3D printed scaffolds: PEOT/PBT scaffolds with solid round strands (A) and corrugated strands produced by using silicone needle inserts (B) (Bettahalli et al., 2013), PCL scaffolds fabricated without vibration (C) and with vibration at 50 Hz (Son and Kim, 2009), and PCL scaffolds without surface modification (E) and with surface modification by exposure to a chemical blowing procedure(Yoon, Kim and Koh, 2015) (F) 19

Figure 2.6. Images of a 3D printed scaffold of PLLA (a) coated with a combination of collagen and hyaluronic acid, stained with Trypan blue for better visualisation (b)(Ji, Jakus and Shah, 2013)..... 20

Figure 2.7. Schematic representation of the cross-hatch printing pattern (A), indicating strand diameter (d_1), strand spacing (d_2) and layer height (d_3), μCT scan of the 3D printed scaffold material network (B) and the scaffold pore network (C) (Billiet et al., 2014), and microscopy images of 3D printed scaffolds with 90° (D) and 45° (E) strand orientation (Moroni, de Wijn and van Blitterswijk, 2006) 23

Figure 3.1. ^{1}H NMR spectra of $K_{46}A_{33}$ before (top) and after (bottom) deprotection of the lysine residues. Asterisk (*) indicates residual solvent peaks from d^6-DMSO (d^5-DMSO and HDO, respectively), double asterisk (**) indicates residual solvent peak from D_2O (HOD), and triple asterisk (***) indicates trace impurities from diethyl ether (Gottlieb, Kotlyar and Nudelman, 1997). 51

Figure 3.2. A phase plot of the library of hydrogels 52

Figure 3.3. Time sweeps of the P(KA)/4-PEG hydrogels with 4 wt% (1:1 and 4:1 molar ratio) and 8 wt% (1:1 molar ratio)..... 54

Figure 3.4. Strain sweeps of the P(KA)/4-PEG hydrogels with 4 wt% (1:1 and 4:1 molar ratio) and 8 wt% (1:1 molar ratio) 55

Figure 3.5. Frequency sweeps of the P(KA)/4-PEG hydrogels with 4 wt% (1:1 and 4:1 molar ratio) and 8 wt% (1:1 molar ratio) 55

Figure 3.6. FTIR spectra of A) starting materials and B) hydrogels of 8 wt% with varying molar ratios 56

Figure 3.7. Column graph shows the concentration of free amines in the hydrogels compared to the calculated theoretical concentration. 57

Figure 3.8. Equilibrium swelling of "as is" and freeze-dried hydrogels as a function of NH_2: NHS ester molar ratio 59

Figure 3.9. SEM images of the internal morphology of freeze-dried hydrogels 59

Figure 3.10. The effect of hydrolytic degradation on the hydrogel mass for A) 1:1 B) 2:1 and C) 4:1 molar ratio P(KA)/4-PEG hydrogels, and D) the effect of molar ratio on the final degradation time of the P(KA)/4-PEG hydrogels is shown. Statistical significance for the 4 wt% hydrogels ($p < 0.05$) is indicated by the asterisk(*). The effect of concentration on the final degradation time was not statistically significant. 61

Figure 3.11. The effects of molar ratio of the 4 wt% P(KA)/4-PEG hydrogels on the cell viability of NIH 3T3 cells are shown. The statistical significance is indicated by an asterisk (*) for $p < 0.05$ and double asterisk (**) for $p < 0.01$. The difference between the positive control group (+) and the 1:1 molar ratio group was not significant. 63

Figure 3.12. Images of T3T NIH cell adhesion on A) well-plate B) well-plate with DMSO C) P(KA)/4-PEG hydrogel (4 wt%; 1:1 molar ratio) and D) P(KA)/4-PEG hydrogel (4 wt%; 8:1 molar ratio) on light microscope (scale bar = 200 μm) 63

Figure 3.13. Antibacterial activity against *S. aureus* bacterial species 64

Figure 4.1 The schematic illustrates the slicing of the CAD model of the 3D box-shaped design with dimensions of 10 × 10× 2 mm (l × w × h) into 2D layers using different layer heights of 0.32 mm and 0.16 mm, respectively, while the printing patterns are represented as 3D CAD models. The strand diameter was determined from the needle ID, while the strand spacing was selected through the built-in algorithms of Visual Machines (EnvisionTEC GmbH, Germany) used to fill-in the 2D layers. 76

Figure 4.2. A schematic representation of the direction of the force (indicated by green arrows) applied to the samples and the corresponding parameters, A and d, used during the respective compressive- and tensile tests 78

Figure 4.3 FTIR spectra of P(KA) before (black) and after (red) conjugation with 4-azidobenzoic acid 81

Figure 4.4 Fluorescence micrograph of micro-particles of P(KA)/4-PEG labelled with FITC in A) a dilute solution and B) a concentrated paste 82

Figure 4.5 Images of the extruded strands of (A) P(KA)-Az/4-(PEG) and (B) CS-P(KA)/4-PEG 83

Figure 4.6 The development of storage modulus of the P(KA)-Az/4-PEG with varying degrees of conjugation, indicating the primary crosslinking between 0 and 6000 s, and the secondary crosslinking from UV irradiation at ~7500 s and ~15000 s 83

Figure 4.7 The viscosity behaviour of the "composite microgel" inks showing shear thinning as the shear rate is increased (A), and the shear-thinning region fit to the power law regression (B) 84

Figure 4.8 Images of the extruded strands of (A) 4-PEG-P(KA)/4-PEG at 0.5 bar, (B) CS-P(KA)/4-PEG at 1.5 bar and (C) PVA-P(KA)/4-PEG at 1.1 bar after 1 s, indicating the extrusion velocities (yellow) calculated from the length of the strands 85

Figure 4.9 Images of the printed strands of 4-PEG-P(KA)/4-PEG at different printing pressures and different printing speeds 86

Figure 4.10 The effect of the 3D printing parameters on the strand width was investigated by varying the printing speed at constant pressures for the respective biomaterial inks (A) and varying the printing pressure at a constant speed of 20 mm/s 86

Figure 4.11 Image of the second layer of P(KA)-Az/4-PEG ink 3D printed with a 0.4 mm needle ID and 1 mm strand spacing 87

Figure 4.12 Images documenting the first four layers of the 3D printing process of (A) 4-PEG-P(KA)/4-PEG, (B) CS-P(KA)/4-PEG, and (C) PVA-P(KA)/4-PEG 3Dprinted with 0.4 mm needle ID and 1 mm strand spacing 88

Figure 4.13 Close-up images of the layer morphology of the fourth 3D printed layers of (A) PEG-P(KA)/4-PEG, (B) CS-P(KA)/4-PEG, and (C) PVA-P(KA)/4-PEG 3D printed with 0.4 mm needle ID and 1 mm strand spacing 88

Figure 4.14 3D printing of CS-P(KA)/4-PEG ink with (A) 0.4 mm needle ID and 1.0 mm strand spacing and (B) 0.2 mm needle ID and 0.5 mm strand spacing 89

Figure 4.15 Images of the "non-porous" 3D printed scaffolds, 4-PEG-Ac-P(KA)/4-PEG (A & D), CS-P(KA)/4-PEG (B & E), and PVA-P(KA)/4-PEG (C & F) 91

Figure 4.16 Images of the "porous" 3D printed CS-P(KA)/4-PEG 0.2 mm (A, LEFT) and 0.4 mm (A, RIGHT) scaffolds, and microscope images of the 0.2 mm (B &D) and 0.4 mm (C&E) scaffolds (top

& side view). Scaffolds in A, D, and E were freeze-dried for better visualisation. Scaffolds in B and C were hydrated. 92

Figure 4.17 SEM micrographs of the cross-sections of freeze-dried composite hydrogels, 4-PEG-P(KA)/4-PEG (A), CS-P(KA)/4-PEG (B), and PVA-P(KA)/4-PEG (C) 94

Figure 4.18 SEM micrographs of the "porous" 3D printed scaffolds of CS-P(KA)/4-PEG, 0.2 mm scaffold (A & B) and 0.4 mm scaffold (C & D) 96

Figure 4.19 Micrographs of CFDA-SE stained 3T3 fibroblasts cultured for 72 h on 4-PEG-Ac hydrogel (A), CS hydrogel (B), PVA hydrogel (C), 4-PEG-Ac-P(KA)/4-PEG (D), CS-P(KA)/4-PEG (E), and PVA-P(KA)/4-PEG (F) 97

Figure 4.20 Micrographs of CFDA-SE stained 3T3 fibroblasts cultured for 96 h on 0.2 mm scaffolds (A), and 0.4 mm scaffolds (B) 97

Figure 5.1 Images of the partial-thickness burn wound site 48 h after the burn wound creation (A), and the full-thickness wound after excision of the epidermis and the dermis (B) 109

Figure 5.2 Micrograph of the H & E stained skin tissue section of the partial-thickness burn wound at 4 × magnification (A), and 10 × magnification (B) 48 h after the burn wound creation. The epidermis and dermis are indicated by "E" and "D" respectively, while examples of infiltrating adipocytes are indicated by the arrows. 110

Figure 5.3 Images of the cylindrical scaffolds of CS-P(KA)4-PEG 3D printed with 0.2 mm needle ID and 0.5 mm strand spacing (A), and 0.4 mm needle ID and 1 mm strand spacing (B) 111

Figure 5.4 Images of the "porous" 3D printed scaffolds, top view (A), side view (B), and applied to the wound area (C) 111

Figure 5.5 A column graph of the wound contractions of the four treatment groups at days 5, 10, 15, and 20 indicates the statistically significant difference between the groups treated with porous 3D printed scaffolds and the control groups, treated with Jelonet or Bactigras after 5 days treatment. No significant difference (n.s) was observed between the non-porous and porous experimental groups after 5 days treatment. At days 10, 15 and 20, no significant difference was observed between the experimental and control groups. $p < 0.05$ is indicated with an asterisk (*) 114

Figure 5.6 Representative images of the wound morphology of the different treatment groups at days 5, 10, and 15 are showed, along with the images from three replicate experiments for the wound healing at day 20. 113

Figure 5.7 Histological images of tissue sections after 5 days of treatment of the "Jelonet"-group (A), "Bactigras"-group (B), "Non-porous"-group (C) and "Porous"-group (D), stained with H&E. GT: granulation tissue, S: subcutis, E: epidermis, D: dermis, Sc: scaffold fragments 115

Figure 5.8 Histological images of tissue sections after 10 days of treatment of the “Jelonet”-group (A), “Bactigras”-group (B), “Non-porous”-group (C) and “Porous”-group (D), stained with H&E. GT: granulation tissue, S: subcutis, E: epidermis, Sc: scaffold fragments 115

Figure 5.9 Histological images of tissue sections after 15 days of treatment of the “Jelonet”-group (A), “Bactigras”-group (B), “Non-porous”-group (C) and “Porous”-group (D), stained with H&E. GT: granulation tissue, S: subcutis, E: epidermis, Sc: scaffold fragments 116

Figure 5.10 Histological images of tissue sections after 20 days of treatment of the “Jelonet”-group (A), “Bactigras”-group (B), “Non-porous”-group (C) and “Porous”-group (D), stained with H&E., E: epidermis, D: dermis, Sc: scaffold fragments 116

LIST OF SCHEMES

Scheme 3.1 Synthesis of NCA amino acids and copolymerization via ROP 49

Scheme 3.2. The intermolecular crosslinking reaction between P(KA) and 4-PEG-SG will form the infinite covalent hydrogel network, P(KA)/4-PEG..... 53

Scheme 3.3 Schematic representation of the crosslinked P(KA)/4-PEG with the hydrolytically unstable ester indicated 60

Scheme 4.1 A general scheme for the photoactivation of arylazides and their reaction with amines (Hermanson, 2013) 72

LIST OF TABLES

Table 3.1. A summary of the polymer concentrations of the P(KA) and 4-PEG-SG used in the preparation of the library of hydrogel solutions to achieve the total polymer concentrations of 1 wt%, 2 wt%, 4 wt%, 6 wt%, and 8 wt%.....44

Table 3.2 Polypeptide synthesized by ROP of NCA amino acids.....49

Table 3.3: Average pore sizes of the P(KA)/4-PEG hydrogels with varying molar ratio and total polymer concentration.....60

Table 4.1 A summary of the preparation of the three composite microgel pastes.....74

Table 4.2 Summary of the 3D printing patterns.....77

Table 4.3 Summary of the 3D printing parameters.....77

Table 4.4 A summary of the model input and output parameters and the schematic representations of the CAD models.....80

Table 4.5 The shear-thinning viscosity coefficients, K and n of the "composite microgel" inks.....85

Table 4.6 The percentage deviation in scaffold dimensions compared to CAD dimensions.....91

Table 4.7 The percentage deviation of strand diameter and inter-strand spacing of hydrated scaffolds compared to intended printing pattern parameters.....92

Table 4.8 A summary of the physical properties of the composite hydrogels, 4-PEG-P(KA)/4-PEG, CS-P(KA)/4-PEG, and PVA-P(KA)/4-PEG.....94

Table 4.9 Effect of 3D Printing on the Physical Properties of CS-P(KA)/4-PEG Scaffolds.....95

Table 5.1 A summary of the 3D printing pattern of the "non-porous" and "porous" scaffold.....105

Table 5.2 Scoring system for semi-quantitative grading of histological features.....108

Table 5.3 Semi-quantitative histological grading of oedema in the wounds treated over 20 days **Error! Bookmark not defined.**

Table 5.4 Semi-quantitative histological grading of leukocytes present in the wounds treated over 20 days.....118

Table 5.5 Semi-quantitative histological grading of macrophages present in the wounds treated over 20 days.....118

Table 5.6 Semi-quantitative histological grading of the granulation tissue present in the wounds treated over 20 days.....119

Table 5.7 Semi-quantitative histological grading of the fibroblasts present in the wounds treated over 20 days 119

Table 5.8 Semi-quantitative histological grading of the epithelialisation present in the wounds treated over 20 days 120

Table 5.9 Semi-quantitative histological grading of the collagen present in the wounds treated over 20 days 120

CHAPTER 1: PROLOGUE

1.1 INTRODUCTION

The natural wound healing process involves an intricate cascade of events. Understanding the interactive processes involved in each of these events has been essential to the development of new wound therapies. The three overlapping phases of wound healing, namely inflammation, proliferation and remodelling have been extensively reviewed in numerous publications (Schilling, 1976; Singer and Clark, 1999; Broughton, Janis and Attinger, 2006; Barrientos et al., 2008; Sorg et al., 2017). Due to the complexity of the wound healing process, a plethora of new wound healing strategies is constantly being investigated. The ideal therapy should provide a combination of rapid wound closure; control over infections; prompt pain relief; minimal inconvenience to the patient; and minimal scarring, while maintaining low treatment costs and risks (Selig et al., 2012). The large number of people affected by wounds, and in particular burn wounds, motivates the need for improved wound therapies. Burns are considered as a leading cause of morbidity in low- and middle-income countries. According to a report by the World Health Organization (WHO) (2004), almost 11 million worldwide cases of burns requiring medical attention were reported in 2004. The resulting scars can affect victims on a physical, aesthetic, physiological, and social level and ultimately affect their quality of life (Leventhal, Furr and Reiter, 2006).

Currently available wound healing therapies, such as modern dressings and skin substitutes, have evolved far beyond the traditional dressings where a dry wound environment is maintained (Zarrintaj et al., 2017; Haddad et al., 2018; Stone et al., 2018; Watt and Pleat, 2018; Koehler, Brandl and Goepferich, 2018; Chouhan et al., 2019). It is now widely recognized that a warm moist wound environment is favourable to the wound healing process (Dreifke, Jayasuriya and Jayasuriya, 2015). Furthermore, certain therapies have been developed to play an active role in the wound healing. Biological dressings are typically composed of natural materials, such as collagen, elastin, hyaluronic acid and chitosan, which are known for their therapeutic role in wound healing (Boateng et al., 2008). Active compounds such as antimicrobials, growth factors and supplements, such as vitamins and minerals have also been incorporated into dressings to be delivered to the wound site (Demidova-Rice, Hamblin and Herman, 2012; Koehler, Brandl and Goepferich, 2018). Skin substitutes on the other hand, provide temporary or permanent replacement of the respective skin layers. Dermal substitutes are typically used along with epidermal substitutes, such as autografts or allografts in the case of partial- and full-thickness wounds, where extensive loss of the dermis occurred (Shahrokhi, Arno and Jeschke, 2014). The function of dermal substitutes is to mimic the basic properties of the ECM and promote faster epithelialisation and granulation. A variety of acellular and cell-containing dermal substitutes composed of biological and/or synthetic materials are currently available

(Shahrokhi, Arno and Jeschke, 2014). Some bilayered and multilayered modern dressings and skin substitutes have also been developed. Integra® is a popular example of a bilayered dermal substitute, specifically indicated for burn wounds (Shahrokhi, Arno and Jeschke, 2014). Another example includes the recently reported hybrid wound dressing where one layer acts as a drug depot for antibiotics and a second layer acts as a "sponge" for absorbing wound exudate (Zilberman et al., 2015). These types of therapies offer the advantage of combining different functions and material properties in one construct.

Recent advancements in 3D printing now allow fabrication of scaffolds composed of biological polymers such as proteins and hydrogel solutions (Ahangar et al., 2019). 3D printing techniques offer the advantage of accurately fabricating precisely designed micro- to macro-architectures (1-1000 μm) according to computer aided designs (CAD) (Pfister et al., 2004). Its precision and automation in fabricating micro-architectures can be superior to conventional techniques, such as micromolding, gas foaming, porogen leaching, phase separation and electrospinning, typically used to fabricate the porous architectures of modern wound dressings and skin substitutes. 3D printing is therefore regarded as a promising alternative for fabricating precisely controlled wound dressings and skin substitutes (Singh, Singh and Han, 2016; Matai et al., 2020; Singh et al., 2020).

1.2 AIM AND OBJECTIVES

The aim of this study was to design and develop a 3D printed wound healing device based on a new 3D biomaterial ink, that will exhibit superior wound healing properties. It will make use of the inherent physical and biological properties of a polypeptide-based hydrogel, precisely achievable through controlled ring-opening polymerisation (ROP) and optimised hydrogel compositions; along with the varied micro-architectures of the scaffold as a result of its accurately controlled fabrication, specifically achievable by 3D printing.

The objectives of this study can be summarized as follows:

1. To synthesize the selected NCA-aminoacid monomers and polypeptide random co-polymers via controlled ROP.
2. To prepare a library of polypeptide-based hydrogels and determine the effect of the hydrogel composition on their physical and biological properties.
3. To determine the 3D printability of a variety of proposed 3D biomaterial inks based on the polypeptide-based hydrogels.
4. To optimize the 3D printing conditions of selected 3D biomaterial inks and to fabricate a range of scaffolds with varying micro-architectures.
5. To determine the effect of 3D printed architectures on the physical and biological properties of the hydrogels.

6. To conduct *in vivo* studies on a burn wound model of Sprague Dawley rats to determine the wound healing efficacy and rate of wound closure

1.3 LAYOUT OF THE THESIS

In Chapter 2, an introduction to 3D printing in tissue engineering is provided as a background to the work presented in this thesis. Specific focus was placed on biomaterial ink processing, scaffold design considerations, and recent advances in 3D printed wound healing and skin regenerative therapies.

Chapter 3 presents the synthesis and characterisation of a library of polypeptide-based hydrogels. An evaluation of the effect of hydrogel composition on its physical and biological properties is provided.

In Chapter 4, the 3D printability of various polypeptide-based hydrogels is addressed. Composite microgel pastes are presented as new 3D biomaterial inks. In addition, the effect of 3D printing on the physical and biological properties of the 3D scaffolds is presented.

Chapter 5 addresses the performance of the 3D printed scaffolds as a wound healing device. An *in vivo* burn wound model of Sprague Dawley rats is validated in this chapter and used to evaluate the wound healing on a macroscopic level, in terms of wound closure and scarring, and on a microscopic level using histological evaluation.

Finally, in Chapter 6 a summary of the findings described in this thesis is given. The chapter is concluded with recommendations for future work.

1.4 REFERENCES

AHANGAR, P. et al. (2019) Current Biomedical Applications of 3D Printing and Additive Manufacturing. *Applied Sciences*, 9(1713), pp. 1–23.

BARRIENTOS, S. et al. (2008) Growth factors and cytokines in wound healing. *Wound repair and regeneration*, 16, pp. 585–601.

BOATENG, J.S. et al. (2008) Wound Healing Dressings and Drug Delivery Systems : A Review. *Journal of Pharmaceutical Sciences*, 97(8), pp. 2892–2923.

BROUGHTON, G., JANIS, J.E. and ATTINGER, C.E. (2006) The basic science of wound healing. *Plastic and reconstructive surgery*, 117(7S), pp. 12S-34S.

CHOUHAN, D. et al. (2019) Emerging and innovative approaches for wound healing and skin regeneration: Current status and advances. *Biomaterials*, 216, p. 119267.

DEMIDOVA-RICE, T.N., HAMBLIN, M.R. and HERMAN, I.M. (2012) Acute and Impaired Wound Healing : Pathophysiology and Current Methods for Drug Delivery , Part 2 : Role of Growth Factors in Normal and Pathological Wound Healing : Therapeutic Potential and Methods of Delivery. *Advances in skin & wound care*, 25(8), pp. 349–370.

DREIFKE, M.B., JAYASURIYA, A.A. and JAYASURIYA, A.C. (2015) Current wound healing procedures and potential care. *Materials Science & Engineering C*, 48, pp. 651–662.

HADDAD, A.G. et al. (2018) Skin Substitutes and Bioscaffolds:Temporary and Permanent Coverage. *Clinics in Plastic Surgery*, 44(3), pp. 627–634.

KOEHLER, J., BRANDL, F.P. and GOEPFERICH, A.M. (2018) Hydrogel wound dressings for bioactive treatment of acute and chronic wounds. *European Polymer Journal*, 100, pp. 1–11.

LEVENTHAL, D., FURR, M. and REITER, D. (2006) Treatment of keloids and hypertrophic scars: A meta-analysis and review of the literature. *Archives of Facial Plastic Surgery*, 8(6), pp. 362–368.

MATAI, I. et al. (2020) Progress in 3D bioprinting technology for tissue/organ regenerative engineering. *Biomaterials*, 226, p. 119536.

PFISTER, A. et al. (2004) Biofunctional Rapid Prototyping for Tissue-Engineering Applications : 3D Bioplotting versus 3D Printing. *Journal of Polymer Science Part A: Polymer Chemistry*, 42, pp. 624–638.

SCHILLING, J.A. (1976) Wound healing. *Surgical Clinics of North America*, 56(4), pp. 859–874.

SELIG, H.F. et al. (2012) The properties of an “ideal” burn wound dressing – What do we need in daily clinical practice? Results of a worldwide online survey among burn care specialists. *Burns*, 38(7), pp. 960–966.

SHAHROKHI, S., ARNO, A. and JESCHKE, M.G. (2014) The use of dermal substitutes in burn surgery: acute phase. *Wound repair and regeneration*, 22(1), pp. 14–22.

SINGER, A.J. and CLARK, R.A.F. (1999) Cutaneous Wound healing. *The New England Journal of Medicine*, 341, pp. 738–746.

SINGH, DEEPTI, SINGH, DOLLY and HAN, S.S. (2016) 3D Printing of Scaffold for Cells Delivery: Advances in Skin Tissue Engineering. *Polymers*, 8(19), pp. 1–17.

SINGH, S. et al. (2020) In situ bioprinting – Bioprinting from benchside to bedside? *Acta Biomaterialia*, 101, pp. 14–25.

SORG, H. et al. (2017) Skin Wound Healing : An Update on the Current Knowledge and Concepts. *European Surgical Research*, 58, pp. 81–94.

STONE, R.I. et al. (2018) Advancements in Regenerative Strategies Through the Continuum of Burn Care. *Frontiers in Pharmacology*, 9, p. 672.

WATT, S.M. and PLEAT, J.M. (2018) Stem cells, niches and scaffolds: Applications to burns and wound care. *Advanced Drug Delivery Reviews*, 123, pp. 82–106.

WHO (2004) *The Global Burden of Disease 2004*. [Online] http://www.who.int/healthinfo/global_burden_disease/2004_report_update/en/.

ZARRINTAJ, P. et al. (2017) Can regenerative medicine and nanotechnology combine to heal wounds? The search for the ideal wound dressing. *Nanomedicine*, 12(19), pp. 2403–2422.

ZILBERMAN, M. et al. (2015) Hybrid wound dressings with controlled release of antibiotics: Structure-release profile effects and in vivo study in a guinea pig burn model. *Acta Biomaterialia*, 22, pp. 155–163.

CHAPTER 2: EXTRUSION-BASED 3D PRINTING IN TISSUE ENGINEERING, A GENERAL INTRODUCTION

2.1 INTRODUCTION

Additive manufacturing (AM) or 3D printing, as it is most recently referred to, has been motivated for use in tissue engineering applications since the early 2000s (Yang et al., 2002; Hutmacher, Sittinger and Risbud, 2004). It was realised that the precise control over micro-scale architectures achievable by 3D printing can produce 3D tissue engineered scaffolds with controlled architectures (Yang et al., 2002; Jamróz et al., 2018; Ahangar et al., 2019). Micro-architectures such as internal porosity play have played an important role in the properties of 3D scaffolds, including mechanical strength and cell-scaffold interactions, which is essential to promote and support the ingrowth of tissue on a 3D scale (Loh and Choong, 2013; Kelly et al., 2018). Conventional and 3D printed scaffolds have traditionally been acellular and subsequently seeded with cells, while bioprinting allows the incorporation of living cells during the fabrication process to achieve better control over their spatial distribution. On the macro-scale, 3D printing could be used to produce patient-specific scaffold architectures for individualised tissue engineering interventions, by converting 3D data from x-ray computed tomography (CT) scans or magnetic resonance imaging (MRI) into computer-aided designs (CAD) (Ho, Ng and Yoon, 2015). 3D image data is then sliced into 2D sections for layer-by-layer addition of material to fabricate 3D constructs with precise outer and inner architecture. A wide variety of 3D printing technologies have been used to fabricate tissue engineering constructs including laser-based technology, such as stereolithography (SLA) and selective laser sintering (SLS); inkjet technology, such as 3D printing (3DP) – not to be confused with the collective term “3D printing” used synonymously with AM; and extrusion-based technology (Shirazi et al., 2015; Mota, Puppi, et al., 2015).

The first concept of extrusion-based 3D printing, named fused deposition modelling (FDM) was introduced to tissue engineering by the group of Hutmacher in the early 2000s (Zein et al., 2002). FDM uses a filament-type dispensing method, where filaments of thermoplastic material are melted as it enters the printing head and subsequently extruded through a thin needle-like nozzle. The material is then dispensed in 2D layers of continuous strands or dots to construct the 3D object. FDM is however limited to materials that could be processed into mechanically stable filaments. Extrusion-based technologies that followed FDM, such as syringe-type methods first described by Mulhaupt’s group (Landers and Mülhaupt, 2000), circumvented the material limitations of FDM, by making use of sample containers that feed the material to the nozzle in a form readily processable. Extrusion-based 3D printing was thereby expanded to processing a wide range of materials, including thermoplastics, pastes, reactive resins, hydrogels, and theoretically any viscous material with adequate

solidification mechanisms. It is also one of the 3D printing techniques that could incorporate bioprinting, where cells are added during printing process (Ozbolat and Hospodiuk, 2016).

To date, a significant number of non-commercial and commercial extrusion-based 3D printers had been used for tissue engineering studies (Fedorovich et al., 2011; Hockaday et al., 2012; Luo et al., 2013; Pati et al., 2014; Bertassoni et al., 2014; Deliormanlı, Liu and Rahaman, 2014; Song et al., 2015). The most notable is the 3D-Bioplotter® from EnvisionTEC, which makes use of a pneumatic-based system to drive the dispensing of material from a syringe barrel through a connected printing nozzle (Anon, 2017). Another popular example is the Fab@Home, which was the first open-source 3D printer (Hockaday et al., 2012; Anon, 2016). Contrary to the 3D Bioplotter™, the Fab@Home makes use of a mechanical dispensing system. While there are small differences in the dispensing mechanisms and sample containers of such extrusion-based 3D printers, terms such as 3D plotting (Yoon, Kim and Koh, 2015), 3D dispensing (Wagner et al., 2007), 3D fibre deposition (Song et al., 2015), 3D microplotting (Angarano et al., 2013), robotic dispensing (Rutz et al., 2015), robocasting (Yuan et al., 2015), and dispense plotting (Detsch et al., 2009) have all been used to refer to the same or fundamentally similar extrusion process.

Extrusion-based 3D printing has been considered as a very versatile technique, with promising applications in hard and soft tissue engineering as well as regenerative medicine (Mota, Danti, et al., 2015; Song et al., 2015; Li et al., 2015; Zhao et al., 2015; Kim et al., 2015; Martínez-Vázquez et al., 2015). In this chapter, the technical aspects associated with the fabrication of extrusion-based 3D printed scaffolds are discussed. This includes specific considerations and strategies with regards to material processing and scaffold design. Furthermore, the latest advances in 3D printing for wound healing and skin regenerative applications are evaluated. The chapter concludes with a brief discussion on the rationale and motivation for the research presented in this thesis.

2.2 CONSIDERATIONS FOR THE 3D BIOMATERIAL INK

The biomaterials selected for tissue engineering scaffolds should ideally have desirable mechanical stability and suitable degradation profiles. This includes numerous synthetic and natural polymers, ceramics, and composite materials. The list of biomaterials processable by extrusion-based 3D printing is mainly limited by their extrudability through the printer nozzle and subsequent solidification of the extruded material to maintain the structural integrity of the 3D object.

2.2.1 Thermoplastics

Thermoplastics are typically high molecular weight polymers, with amorphous or semi-crystalline characteristics. Above the glass transition temperature (T_g), amorphous polymers become viscous liquids and can be processed by techniques such as injection moulding and extrusion-based printing. Semi-crystalline polymers, on the other hand, need to be processed above their melting temperature (T_m). This transition from solid to viscous liquid is completely reversible; therefore solidification

upon cooling can easily afford the desired object architecture. In 3D printing of thermoplastics, cooling of the thin extruded strands below the processing temperature can be easily achieved. The viscosity of the molten material and the rate of solidification should, however, be considered in a close relationship. For example, lower viscosity solutions need to solidify faster in order for extruded strands to support their own weight. The rate of solidification is dependent on the difference in temperature drop between the molten material and the surroundings. Extrusion of thermoplastics at room temperature is generally sufficient for adequate solidification (Yoon, Kim and Koh, 2015).

Thermoplastics such as biodegradable polyesters and their copolymers are commonly processed by extrusion-based 3D printing for a variety of tissue engineering applications. This includes poly(L-lactic acid) (PLLA) (Xiong et al., 2001; Ji, Jakus and Shah, 2013), poly(L-lactide-*co*-glycolide) (PLGA) (Rücker et al., 2006; Al-Ahmad et al., 2011); poly(ε-caprolactone) (PCL) (Yoon, Kim and Koh, 2015; Kim et al., 2015; Cengiz et al., 2016), poly(ethylene oxide-terephthalate)/poly(butylene terephthalate) (PEOT/PBT) (Hendriks et al., 2013), poly(L-lactide-co-caprolactone) (Sun et al., 2012), and various copolymers of PCL and poly(ethylene glycol) (PEG) (Huang et al., 2004). These scaffolds have either been investigated "as is" or after post-printing modifications to the scaffolds. Such post-printing modifications are typically directed to improving the biocompatibility of the scaffold. A number of thermoplastic scaffolds with unusual architectural features have also been fabricated. This includes using coaxial polymer melts to produce hollow tubular extruded strands (Figure 2.1A) (Moroni et al., 2006; Bettahalli et al., 2011). Coaxial melting of PEOT/PBT and PCL or P(BMA/MMA), where PEOT/PBT formed the outer shell of the strand and PCL or P(BMA/MMA) formed the sacrificial inner core, afforded the hollow strands with potential drug delivery applications. Extrusion-based 3D printing has also been combined with thermally assisted forming to bend printed scaffold sheets into tubular forms (Figure 2.1B). PCL (Johnson et al., 2016) and blends of PCL and starch (SPCL) (Silva et al., 2010; Silva et al., 2011; Silva et al., 2013) have been used to fabricate tubular scaffolds for applications in tracheal tissue engineering and spinal cord injuries.

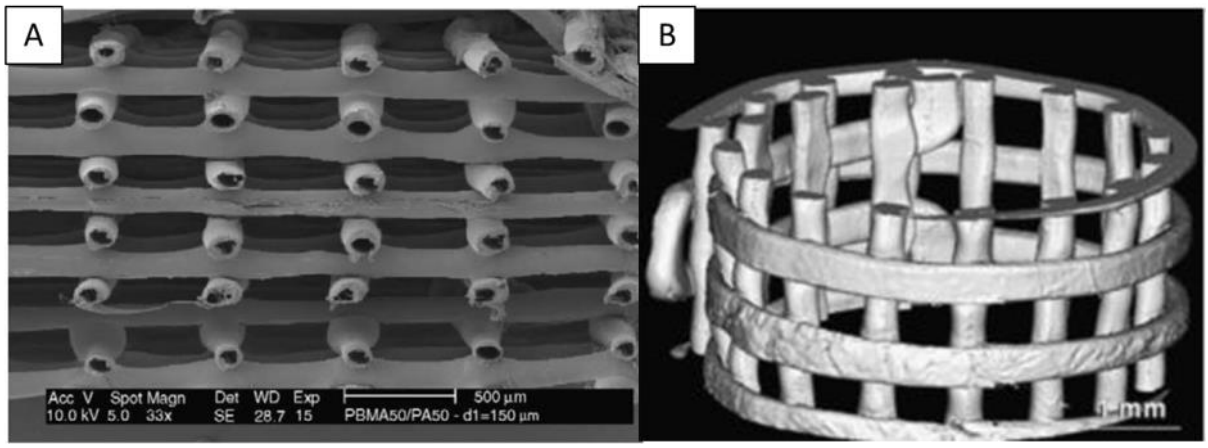


Figure 2.1 SEM micrograph displaying a PEOT/PBT scaffold with hollow strands (A) (Moroni et al., 2006) and micro-computed tomography (µ-CT) image shows SPCL scaffold formed into tubular structure (B) (Silva et al., 2010)

Thermoplastic composites incorporated with bioceramics or nanoparticles are also processable with extrusion-based 3D printing. Such scaffolds typically have improved mechanical properties and/or biocompatibility. Extrusion-based 3D printed scaffolds incorporated with bioceramics such as hydroxyapatite (HA) (Lee et al., 2010; Amorosaa et al., 2013; Nandakumar et al., 2013) and tricalcium phosphate (TCP) (Al-Ahmad et al., 2011) have primarily been studied for bone tissue engineering applications. Iron oxide-doped nanoparticles incorporated into PCL have also been 3D printed to produce magnetic scaffolds (Santis et al., 2011; Russo et al., 2013). Other 3D printed composite scaffolds of PCL included organic-inorganic hybrid particles of PCL/TiO_2 or PCL/ZrO_2 (De Santis et al., 2013). Such composites have been prepared either by co-melting the components (Amorosaa et al., 2013) or by mixing solutions of the polymer with the dry particles under stirring and subsequently forming dry pellets (Russo et al., 2013; De Santis et al., 2013). The formation of the composite evidently increases the viscosity of the thermoplastic and the pressure required for extrusion needs to be increased. Therefore the ratio of the components must be carefully considered, as it is limited by the pressure limitations of the specific 3D printer. Typically for extrusion-based 3D printing, the weight percentage (wt %) of the thermoplastic component remains between 70-90 wt % (Banobre-Lopez et al., 2011; Russo et al., 2013; Nandakumar et al., 2013).

A concern regarding extrusion-based 3D printing of thermoplastics is thermal degradation. To some degree, thermal degradation is experienced by all thermoplastics processed at high temperatures. The degree of thermal degradation is dependent on the thermal stability of the material as well as the exposure time to the high temperatures. For filament type dispensing methods, the material is only subjected to high temperatures for the short period it passes through the needle tip. However, for syringe type dispensing, the entire sample is heated and maintained at high temperatures for the duration of the printing process. Therefore thermal degradation is seen more prominently with syringe-type dispensing methods (Lee et al., 2016). Thermal degradation primarily reduces the

molecular weight of the polymers, which leads to changes in the material properties, including physical and mechanical properties (Lee et al., 2016). In tissue engineering, these properties are closely related to the regenerative properties of scaffolds and changes to these properties could potentially impair the overall performance of the scaffold.

2.2.2 Pastes

3D printed pastes comprise of powder dispersed within a polymeric solution to form thick slurries. The powders that typically range from bioceramics to bioactive glass have been selected based on their specific bioactivity. One of the roles of the polymeric component has been to form the dispersion with adequate viscosity for extrusion-based 3D printing. The addition of solvents into the pastes, compared to thermoplastic composites, have allowed the incorporation of a higher percentage of powders into the pastes. A wide range of ratios of powder: polymer, ranging from 0: 100 to 80: 20 have been used to prepare pastes for extrusion-based 3D printing (Ping et al., 2007; Coutu et al., 2011; Feito et al., 2011; Zhang, Zhao, Y. Zhu, et al., 2014; Zhang, Zhao, M. Zhu, et al., 2014). The rheological properties of the pastes should be fine-tuned to achieve the desired consistency, firstly for adequate extrusion within the viscosity constraints of the 3D printer; and secondly to obtain strands able to support their own weight. The desired consistency have generally been determined based on trial-and-error, where the composite ratios and amount of solvent was varied to change the viscosity of the pastes (Ping et al., 2006; Coutu et al., 2011; Salinas and Vallet-regí, 2016). When using organic solvents to prepare the pastes, an excess solvent have typically been used to assist with mixing of the composite, followed by evaporation of the solvent until an adequately viscous paste formed (Min, Kun, et al., 2015; Salinas and Vallet-regí, 2016). In addition to the trial-and-error approach, pastes have also been prepared according to a specific viscosity measured by rheometry (Jakus et al., 2015). An important consideration for the extrusion of inorganic composites is the size-range of the particles with respect to the nozzle diameter. At nozzle inner diameters (ID) of 580 μm or higher, no mention of particle sizes have been made (Calvo-guirado et al., 2012; Shruti et al., 2013; Li et al., 2015). However, at smaller ID between 410 μm and 150 μm, particles were generally sieved to obtain homogeneous size distributions below 50 μm (El-ayoubi et al., 2011; Liu et al., 2013; Zhang, Zhao, Y. Zhu, et al., 2014; Zhang, Zhao, M. Zhu, et al., 2014; Jakus et al., 2015). Furthermore, the homogeneity of the pastes should be ensured to prevent clogging of the nozzle, especially when using nozzle sizes < 250 μm. One of the strategies employed to reduce clogging, included forcing the paste through a fine mesh or sieve (Al-Ahmad et al., 2008; Chien et al., 2013). The solidification process of the extruded strands involved evaporation of the solvent system, either by air drying at room temperature (Sánchez-Salcedo et al., 2013), oven drying (Salinas and Vallet-regí, 2016) or lyophilisation (Chien, Makridakis and Shah, 2013). Depending on the solvent, solidification was often slow or only commenced post-printing; therefore, it is important that "wet-strands" maintain the structural integrity of the 3D scaffold prior to drying. After the drying process, some scaffolds have

been further subjected to calcining. This removed the polymeric component and densified the remaining bioceramic or bioactive glass to increase the mechanical properties of the scaffold (Haberstroh et al., 2010; Liu et al., 2013; Deliormanlı, Liu and Rahaman, 2014).



Figure 2.2. SEM micrographs of PLLA scaffolds before NaCl leaching (A), and after NaCL leaching at 100× magnification (B) and 300× magnification (C)

The polymeric component is however not always removed. Therefore careful consideration of the polymer properties (biocompatibility, mechanical strength, and degradation) with regards to the specific tissue engineering application needs to be taken. Examples of polymers used in the 3D printed pastes include PLGA (Coutu et al., 2011; Jakus and Shah, 2017), PCL (Calvo-guirado et al., 2012; Sánchez-Salcedo et al., 2013; Pei et al., 2016; Gómez-Cerezo et al., 2016) and poly(vinyl alcohol (PVA) (Rücker et al., 2008; Haberstroh et al., 2010; García-Alvarez, Izquierdo-Barba and Vallet-Regí, 2017), while bioceramic powders of hydroxyapatite (Coutu et al., 2011; Calvo-guirado et al., 2012; Sánchez-Salcedo et al., 2013) and TCP (Rücker et al., 2008; Haberstroh et al., 2010) have been incorporated in such pastes. Furthermore, a wide variety of pastes incorporated with bioactive glass (Liu et al., 2013; Deliormanlı, Liu and Rahaman, 2014; Li et al., 2015; Min, Kun, et al., 2015; Min, Shichang, et al., 2015; Gómez-Cerezo et al., 2016) have been processed with extrusion-based 3D printers. Apart from the osteoconductive and osteoinductive properties of bioactive glass, scaffolds incorporated with mesoporous bioactive glass (MBG) have also demonstrated excellent drug delivery properties. Such scaffolds have been loaded with anti-tuberculosis drugs for the potential treatment of osteoarticular tuberculosis (TB) (Li et al., 2015; Min, Kun, et al., 2015) and antibiotics (García-Alvarez, Izquierdo-Barba and Vallet-Regí, 2017). Other interesting pastes containing graphene nanoflakes have also been processed using extrusion-based 3D printing (Jakus and Shah, 2017). Graphene have typically been incorporated into biomaterials due to its osteogenic properties as a result of electrical conductivity. Scaffolds with improved surface properties have also been fabricated by using sodium chloride (NaCl) to act as a porogen (El-ayoubi et al., 2008; El-ayoubi et al., 2011). Subsequently, extruded scaffolds were washed with water to leach out the NaCl to form micropores on the strand surfaces along with the 3D printed macropores (Figure 2.2).

2.2.3 Hydrogels and Reactive Resins

Hydrogels provide 3D structural support similar to the extracellular matrix (ECM). Therefore, hydrogels have often been used as scaffolds in tissue engineering. Hydrogels are particularly suited for soft tissue engineering applications as they display similar mechanical properties to soft tissue.

Additional crosslinking or reinforcements have however been used to increase mechanical properties of hydrogels for potential hard tissue engineering applications. Hydrogels have typically been 3D printed in their precursor form. Their gelation, during or after the 3D printing process, was then used as the solidification mechanism to produce the final hydrogel structure. In order to obtain desirable 3D print fidelity, hydrogel inks require adequate viscosity to maintain their structural integrity prior to crosslinking (Kyle et al., 2017). Strategies to increase the viscosity of the ink included using high polymer concentrations (Schuurman et al., 2013), adding reinforcing materials (Wang et al., 2014; Martínez-Vázquez et al., 2015; Narayanan et al., 2016), and using near gel-phase or gel-phase inks (Lee et al., 2013; Rutz et al., 2015; Lewis, Green and Shah, 2018; Kim et al., 2018). The building blocks or polymers forming the hydrogels are often referred to as macromers. These can be classified according to their origin (natural or synthetic), chemical composition, electrostatic nature (neutral, ionic, amphotheric) and mechanism of gel formation (physical or chemical). For extrusion-based 3D printing, the mechanism of formation of the hydrogel is critical to the success of the fabrication procedure. Generally, the rapid formation of a stiff hydrogel from a viscous macromer solution have been required during the extrusion process. Alternatively, a highly viscous precursor solution, able to support its own structure, could be printed and post-print treated to fully solidify the extruded structure. Plotting media have also been used to improve the extrusion process. The plotting media could prevent the collapse of extruded strands, by means of buoyancy forces (Landers and Mülhaupt, 2000). Therefore the density of the plotting medium should match the density of the printing material. Furthermore, plotting media have been incorporated with crosslinking solutions to achieve controlled gelation during the printing process. The rate of gelation should be carefully controlled, as it should be fast enough to prevent flowing of the extruded gel precursor, while still allowing adequate adhesion between subsequent layers. Good adhesion is essential to the accuracy of the printing process as well as the final integrity of the scaffold. Swelling of the printing material in the medium or post-printing is another important factor that should be taken into account, as it could cause deviation from the intended 3D structure and should, therefore, be minimal (Landers, Hübner, et al., 2002). Many biodegradable hydrogels suitable for tissue engineering applications have been investigated. However, only hydrogels that displayed adequate rheology and controlled gelation mechanisms have been suitable for extrusion-based 3D printing (Kirchmajer, Gorkin III and in het Panhuis, 2015). Examples of these will be discussed in the following sections.

2.2.3.1 Thermal Gelation

Physical hydrogels that form naturally as a result of molecular entanglement or weak forces such as hydrogen bonding between the macromers typically have a gel transition temperature. The reversible transition between gel and solution can be utilised similar to the melting and setting of thermoplastics. For example, solutions of gelatin and agarose gel below their transition temperatures and have been heated to higher temperatures to extrude the viscous solutions through the printer needle (Landers,

Hübner, et al., 2002; Maher et al., 2009). Fast gelation has been achieved by extruding the solutions at temperatures near their gel phase onto a cooled platform or into a cold plotting medium. In the case of agarose, a good plotting medium was found to be aqueous gelatin solutions (Maher et al., 2009). Parameters that could affect the outcome of the printing process include the thermal behaviour of the printing material and the corresponding viscosity (Maher et al., 2009). The temperature of the material with respect to the plotting medium also needs to be optimized. Faster gelation could be achieved if the difference in the two temperatures is small, however at the cost of a viscosity increase of the precursor solution. Physical hydrogels, such as gelatin and agarose are however known for their weak mechanical properties and require additional reinforcements through polymer blending or secondary crosslinking, for use in tissue engineering applications.

2.2.3.2 Ionic- and Covalent-Based Gelation

Electrostatic interactions are strong and typically rapid, making it well suited for extrusion-based 3D printing. Viscous solutions of polyelectrolytes could be directly extruded into crosslinking solutions containing divalent or multivalent counterions. One example widely investigated is alginate extruded into plotting medium containing calcium ions. However, this type of crosslinking have been too rapid, as it prevented good adhesion between the subsequent layers (Landers, Pfister, et al., 2002). Therefore, extremely rapid crosslinking of alginate in $CaCl_2$ solutions has been limited by the addition of a retardant, such as EDTA, to the plotting medium (Landers, Pfister, et al., 2002). Furthermore, the viscosity of the printing solution could be increased to reduce the flowing of the extruded strands and thereby reduced crosslinking rates could be tolerated. For example, the viscosity of alginate has been increased by the addition of small amounts of $CaCl_2$ to form partially crosslinked alginate gel prior to the printing process (Ahn et al., 2012; Lee et al., 2013). Alginate has also been blended with other polymer solutions, such as gelatin (Wang et al., 2014; Neufurth et al., 2014) and hyaluronic acid (Wang et al., 2013; Rajaram, Schreyer and Chen, 2014; Rajaram, Schreyer and Chen, 2015), which resulted in increased viscosity of the printing material. Other methods of crosslinking alginate with $CaCl_2$ during the printing process included fuming alginate strands extruded in the air with $CaCl_2$ solutions (Lee et al., 2013; Rajaram, Schreyer and Chen, 2014); and coaxial printing of alginate and $CaCl_2$ solutions using custom coaxial dispensing needles (Costantini et al., 2016) (Figure 2.3). This method ensured that the surface of the strands was adequately cross-linked to maintain the intended strand architecture, while still allowing good adhesion between the layers. Successive post-print treatment with $CaCl_2$ solutions then allowed complete crosslinking and stiffening of the 3D scaffold. Reactive plotting media have also been investigated for other 3D printed materials. This includes the extrusion of viscous solutions of chitosan into solutions of NaOH, to precipitate the chitosan into stiff gel-like structures (Ang et al., 2002). Another example involved the extrusion of a fibrinogen solution into a plotting medium containing thrombin (England et al., 2017). The fast reaction between fibrinogen and thrombin afforded fibrin hydrogel scaffolds. It has often been seen that strands

extruded into plotting medium float and accumulate around the printing needle as a result of too much buoyancy of the strands (Maher et al., 2009) (Figure 2.4). The addition of thickening agents to the plotting medium, such as glycerol (Maher et al., 2009) or PVA (Rajaram, Schreyer and Chen, 2014; Rajaram, Schreyer and Chen, 2015; England et al., 2017), have adequately reduced the buoyancy of different extruded materials. Polyethylenimine (PEI), a polycation, has also been added to plotting media to improve the 3D printing of alginate (Rajaram, Schreyer and Chen, 2014).

Generally, chemical crosslinking through covalent bonding tends to be a slower process of gel formation and therefore could not be used as the primary crosslinking mechanism. Instead, self-supporting gels can be extruded and then covalently crosslinked post-printing. Not many examples of this type of extrusion-based 3D printing have been reported. One study by Rutz et al. (2015) showed how homobifunctional PEG-succinimidyl valerate (SVA), partially crosslinked with a variety of amine-containing polymers, could form self-supporting extrudable gels. By incorporating secondary crosslinking mechanisms into the building block of these gels, it was demonstrated that further post-print crosslinking reactions could afford stiff 3D structures suitable for use as potential tissue engineering scaffolds (Rutz et al., 2015).

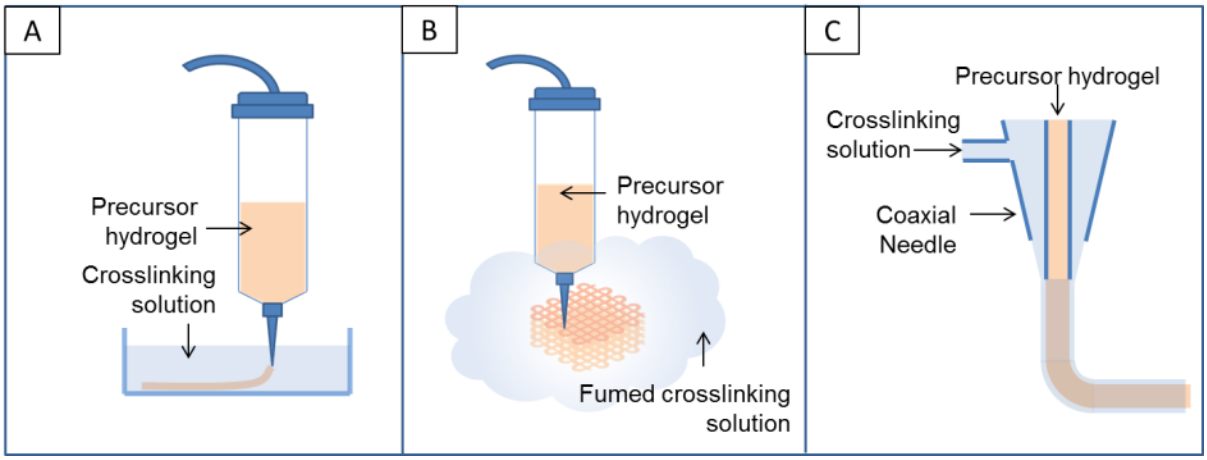


Figure 2.3. A schematic representation of the different methods of crosslinking precursor hydrogels through ionic crosslinking: directly extruded into the crosslinking medium (A), extruded onto the printing platform fumed with crosslinking solution (B), coaxially extruded with a specially developed coaxial needle

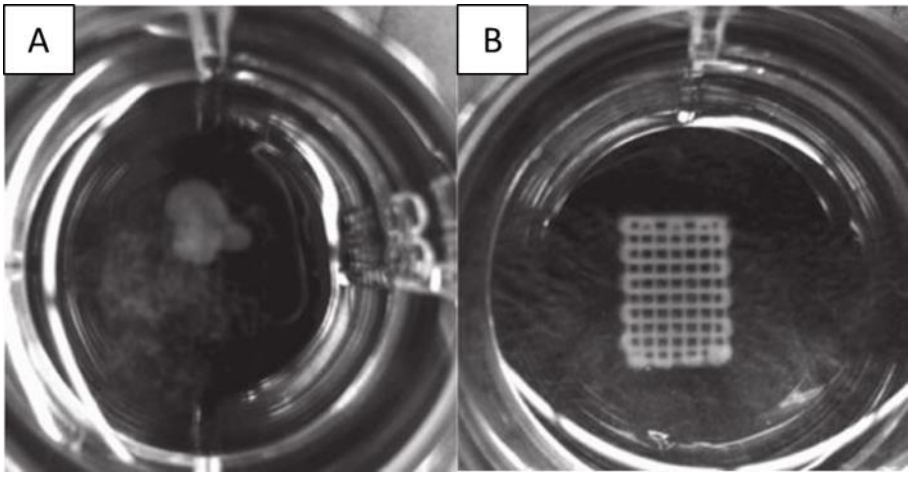


Figure 2.4. Images of alginate/hyaluronic acid 3D printed into plotting medium without PVA and PEI clump (A) and with 0.95 % PVA and 0.1 % PEI (B)(Rajaram, Schreyer and Chen, 2014)

2.2.3.3 Two-Step Gelation and ionic-covalent entanglement (ICE) hydrogels

Extrusion-based 3D printed scaffolds have also commonly been fabricated using two-step gelation mechanisms. Wüst et al. (2014) demonstrated that a composite gel of gelatin, alginate and hydroxyapatite can be 3D printed using a two-step gelation mechanism. First, the heated printing material (40 °C) was extruded onto the cooled platform (10 °C) to induce thermal gelation of the gelatin. Then post-printing, the alginate was ionically crosslinked with calcium ions by immersing the printed scaffold in a solution of $CaCl_2$. Subsequently, the gelatin which provided temporary support of the plotted structure could be leached out by heating the scaffold to 37 °C. Thermoreversible polymers have also been chemically modified with UV sensitive moieties to create UV curable polymers in the presence of photoinitiators. Billiet et al. (2014) investigated the 3D printing of a gelatin methacrylate solution, where post-print UV curing followed initial thermal gelation during the extrusion process. Poly(ethylene glycol)-*block*-poly(propylene glycol)-*block*-poly(ethylene glycol) (PEG-*b*-PPG-*b*-PEG), a thermoreversible gel with a lower critical solution temperature (LCST) close to physiological temperature was also functionalized with N-2,3-dimethylmaleimidoalanine, to obtain photosensitive PEG-*b*-PPG-*b*-PEG-AlaL, for 3D printing (Fedorovich et al., 2009). Photoinitiated crosslinking have also been known for its rapid reactions. Therefore it is suitable as the primary gelation mechanism for extrusion-based 3D printing of photosensitive material. For example, viscous PEG diacrylate (PEGDA) solutions containing photoinitiators have been extruded and exposed to UV radiation during the printing process (Maher et al., 2009; Hockaday et al., 2012). Kesti et al. (2015) also described a "tandem gelation", where hyaluronan grafted with poly (*N*-isopropyl acrylamide) (PNIPAAM) was blended with hyaluronan methacrylate or chondroitin sulfate methacrylate and a photoinitiator. The LCST behaviour of PNIPAAM was used to induce thermal gelation by extruding the material onto a heated substrate (35 -38 °C), while the photosensitive polymers was crosslinked by irradiating each layer for 10 s (365 nm, 6.09 $mW \cdot cm^{-2}$).

Furthermore, it was demonstrated that a number of ionic-covalent entanglement (ICE) hydrogels with a thermoreversible component could be successfully processed with extrusion-based 3D printing. These complex hydrogels containing multiple components, consisting of ionic as well as covalent crosslinking, have improved mechanical stability and allows the use of lower concentrations of polymers. Thermally reversible, ionically crosslinked κ-carrageenan/Ca^{2+}, blended with poly(oxyalkylene amine) and PEGDGE, have been extruded and solidified using thermal gelation (Bakarich et al., 2014). Slow covalent crosslinking via an exopy-amine addition of poly(oxyalkylene amine) and PEGDGE then commenced post-printing to form the ICE hydrogel scaffold.

2.2.4 Bioinks

Bioinks per the revised definition recently published by Groll et al. (2019) refer to *"a formulation of cells suitable for processing by an automated biofabrication technology that may also contain biologically active components and biomaterials"*. 3D bioprinting is a sub-category of biofabrication and requires that each step of the printing process maintain a physiologically suitable environment for the incorporation of cells.

The printing process begins with the formulation of the bioink. This could include single cells, cells aggregated in spheroids, cellular rods, cells organized in mini tissues or organoids, cells coated by a thin layer of material, cells seeded onto microcarriers, or encapsulated in tailored colloidal microenvironments (Groll et al., 2019). Bioinks may also contain bioactive molecules such as growth factors, DNA, miRNA, cytokines, exosomes, or biomaterials. Biomaterials have typically been added as a matrix material to bioinks to provide biochemical or mechanical function. Precursor hydrogels have been a popular choice as matrix materials for extrusion-based 3D bioprinting (Jose et al., 2016; Himene et al., 2016; Ozbolat and Hospodiuk, 2016). This included alginate (Fedorovich et al., 2011; Ahn et al., 2012), alginate / gelatin (Wang et al., 2014; Neufurth et al., 2014), gelatin methacrylamide (GelMa) (Billiet et al., 2014), alginate / hyaluronic acid (Rajaram, Schreyer and Chen, 2014; Rajaram, Schreyer and Chen, 2015), PNIPAAM grafted hyaluronic acid (HA-PNIPAAM) / methacrylated hyaluronic acid (HAMA) (Kesti et al., 2015), combinations of GelMA, HAMA and chondroitin sulfate amino ethyl methacrylate (CS-AEMA) (Costantini et al., 2016), PEG-SVA / gelatin or fibrinogen (Rutz et al., 2015), and Lutrol F127 (Fedorovich et al., 2008; Fedorovich et al., 2009). Cells have also been encapsulated in decellularised ECM (dECM) for extrusion-based 3D printing (Pati et al., 2014). One concern regarding hydrogels as the matrix material has been the weight percentage of the polymers. It has been found that cells in high concentration hydrogels have lower viability, due to limited diffusion (Kesti et al., 2015). On the other hand, higher polymer content is often required to obtain a higher viscosity, necessary to maintain the structural integrity of the extruded strands prior to gelation. A number of studies have therefore focused on developing robust hydrogels with low polymer content (<5 wt%) (Rajaram, Schreyer and Chen, 2015; Rutz et al., 2015). Kesti et al. (2015) intentionally leached out one of the polymers (i.e. HA-PNIPAAM) from the

hydrogel blend after the printing process. By using this leaching method, the cell viability increased from 34% to 91% at day 7.

The next step in the printing process is the extrusion of the bioink. During this step, the cells are inevitably subjected to the dispensing pressure in order to be extruded through the thin needle tip. Numerous studies have therefore investigated the effect of pressure and needle diameter on the cell viability (Chang, Nam and Sun, 2008; Ahn et al., 2012; Pati et al., 2014; Billiet et al., 2014). It has been seen that higher cell viability can be achieved with lower dispensing pressure and larger internal needle diameters (Chang, Nam and Sun, 2008; Derby, 2012; Billiet et al., 2014). Billiet et al. (2014) also found that the needle shape could have an effect on the cell viability. They showed that conical needles produced higher viability of HepG2 cells compared to cylindrical needles. On the other hand, some studies have shown that pressure from the printing process (Pati et al., 2014) and different needle ID (Ahn et al., 2012) have no significant effect on cell viability. Pati et al. (2014) suggested that myoblast cells encapsulated within decellularised ECM have been protected through cushioning from the matrix material. Subsequently, such 3D printed scaffolds showed cell viability as high as 95% after 24 hours, which correlated with non-printed scaffolds.

The printing process is concluded with the gelation of the bioink strands, which could be extruded either in plotting medium or in air. The gelation method should afford good scaffold architecture, while still maintaining high cell viability. However, the crosslinking method and components could have a significant effect on the cells. Billiet et al. (2014), demonstrated that UV-A irradiation doses increasing from 1350 to 5400 $mJ \cdot cm^{-2}$ have a detrimental effect on HepG2 cells encapsulated in gelatin methacrylamide scaffolds, with their viability decreasing from ~89 % to ~56 %. Furthermore, by exchanging the photoinitiator, 1-[4-(2-Hydroxyethoxy)-phenyl]-2-hydroxy-2-methyl-1-propane-1-one (Irgacure 2959) for the more cytocompatible 2,20-Azobis[2-methyl-N-(2-hydroxyethyl)propionamide] (VA-086), the cell viability was increased to ~98 % at UV-A irradiation doses of 1800 $mJ \cdot cm^{-2}$ (Billiet et al., 2014). At this radiation dosage, the strands showed minimal sagging and the scaffold porosity remained 100 % interconnected. Similarly, the components of the plotting medium for alginate/hyaluronic acid hydrogel have been selected to optimise cell viability as well as scaffold architecture (Rajaram, Schreyer and Chen, 2014). The addition of 0.95 % PVA to $CaCl_2$/HEPES crosslinking medium increased the RSC 96 cell viability from 64 % to 83% 5 minutes after printing, while 0.1% PEI improved the crosslinking of alginate, without affecting the cell viability. It was however seen that the cell viability drastically decreased upon increasing exposure time to the plotting medium (Rajaram, Schreyer and Chen, 2014). Extrusion of cell-laden hydrogels in air has resulted in different outcomes with regards to cell viability. Cell-laden alginate/hyaluronic acid hydrogels extruded in air and nebulized with the $CaCl_2$ crosslinking solution as described above, only afforded 61% cell viability after 5 min (Rajaram, Schreyer and Chen, 2014). On the other hand cell-laden dECM gels extruded at 15 °C and gelled at 37 °C under humidified conditions for 30 min

resulted in excellent cell viability of 95% (Pati et al., 2014). Also, PEG-SVA/gelatin and PEG-SVA/fibrinogen was extruded in air and the encapsulated human dermal fibroblasts (HDF) qualitatively showed successful viability (Rutz et al., 2015).

2.3 CONSIDERATIONS OF THE SCAFFOLD DESIGN

Three types of scaffolds, namely acellular-, cell-seeded- and cell-laden scaffolds have been fabricated using extrusion-based 3D printing. Acellular scaffolds and cell-seeded scaffolds rely on the infiltration and attachment of cells after the scaffolds have been fabricated. Cell-laden scaffolds, on the other hand, have been incorporated with cells during the fabrication process. Regardless of the type, all tissue engineering scaffolds need to comply with a number of basic requirements, in order to promote the ingrowth and survival of regenerating tissue as temporary support structures. Biocompatibility is often incorrectly assigned to all biomaterials, while the "Williams definition of biocompatibility" defines it as "*the ability of a material to perform with an appropriate host response within a specific application*" (Anon, 1999). This definition can also be conveyed to systems, such as scaffolds. Biocompatibility includes interactions between the host cells and the scaffold, which promotes desired outcomes such as cell attachment, proliferation, and differentiation. It is known that the physical and chemical properties of a scaffold play a role in these interactions. In extrusion-based 3D printing, a number of strategies have been developed in order to enhance the biocompatibility of the 3D printed scaffold.

2.3.1 Surface Properties and Scaffold Chemistry

Scaffolds fabricated by extrusion-based 3D printing have been known for their smooth strand surfaces, which tend to be associated with low cell attachment. A few strategies to change the morphology or roughness of the extruded strands have been reported (Figure 2.5). For example, Bettahali et al. (2013) used silicon inserts to produce corrugated strands of PEOT/PBT instead of the normal smooth strands. The change in surface morphology resulted in a higher surface area available for cell attachment. Son and Kim (2009) on the other hand used a piezoelectric transducer to vibrate the printing platform during the extrusion process, to produce PCL strands with a grooved surface. The grooved strands showed better cell attachment as a result of their increased surface roughness and hydrophilicity. Yoon, Kim and Koh (2015) also demonstrated that the surface roughness of extruded strands can be increased by using a chemical blowing agent post-printing. 3D printed PCL scaffolds were sprayed with the chemical blowing agent to produce nano- and micropores on the scaffold surface. Seeding the modified scaffold with chondrocytes initially showed better cell adhesion compared to normal scaffolds, however, after 4 weeks no significant difference between the two scaffolds was visible. Alternatively, extrusion-based 3D printing has been combined with porogen leaching to create micro-pores on scaffold surfaces. Pastes of PLLA or PLGA incorporated with NaCl as the porogen were extruded and post-print leached to produce the modified surface properties (El-

ayoubi et al., 2011; Daoud et al., 2012). As a result of the improved surface properties, the modified scaffolds afforded higher initial cell density and better cell adhesion when seeded with chondrocytes (El-ayoubi et al., 2011).

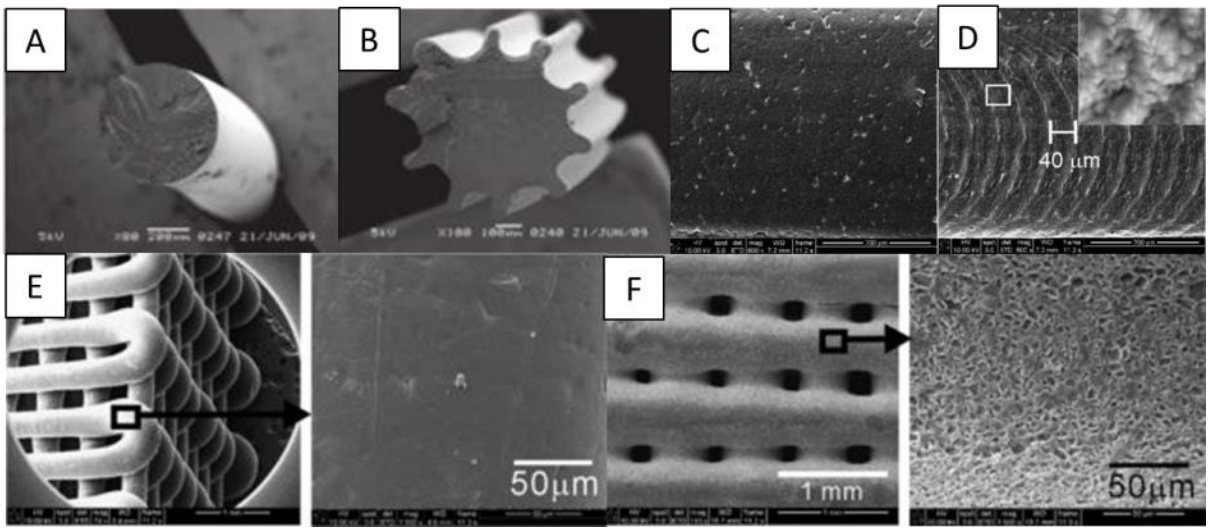


Figure 2.5. SEM micrographs show the strategies to improve the surface roughness of 3D printed scaffolds: PEOT/PBT scaffolds with solid round strands (A) and corrugated strands produced by using silicone needle inserts (B) (Bettahalli et al., 2013), PCL scaffolds fabricated without vibration (C) and with vibration at 50 Hz (Son and Kim, 2009), and PCL scaffolds without surface modification (E) and with surface modification by exposure to a chemical blowing procedure (Yoon, Kim and Koh, 2015) (F)

Scaffolds that have not been composed of inherently biocompatible or bioactive material could be blended or coated with additional components to achieve the desired host response. The incorporation of such components would depend on their sensitivity towards the printing conditions. For example, scaffolds composed of thermoplastics and pastes, where harsh processing conditions are typically necessary, could be coated with sensitive bioactive components post-printing. Hydrogel scaffolds on the other hand, which could be processed under milder conditions, allow direct incorporation of sensitive components prior to the printing process. A number of coating and direct incorporation strategies have been used in extrusion-based 3D printing to promote cell attachment. For example, collagen type I coated PLGA scaffolds compared to uncoated PLGA scaffolds showed increased cell attachment when seeded with osteoblast-like cells and bone marrow mesenchymal stem cells respectively (Schumann et al., 2009; Tavassol et al., 2010; Schumann et al., 2015). Similarly, PLLA has been coated with a combination of collagen and hyaluronic acid (Ji, Jakus and Shah, 2013) (Figure 2.6); and in another study with gelatin (El-ayoubi et al., 2008), to improve cell attachment. Poly-L-lysine has also been used for this purpose to coat SPCL scaffolds, prior to cell seeding (Silva et al., 2011). Blending cell-attaching polymers such as fibrinogen (Rutz et al., 2015), poly-L-lysine [88] or gelatin (Wang et al., 2014; Rutz et al., 2015) with other hydrogel solutions have also afforded scaffolds with superior cell attachment properties. Another strategy to enhance cell attachment have been to immobilise the Arg-Gly-Asp (RGD) tripeptide sequence onto the scaffold material (Gloria et al., 2012; Neufurth et al., 2015). The RGD sequence is a recognition motif present in ECM proteins,

which binds to integrins on the cell surface. A wide variety of chemical modifications could accommodate conjugation to RGD containing molecules. The conjugation reaction could then be performed either on the scaffold material prior to printing or on the scaffold surface post-printing. For example, PCL scaffolds have been aminolysed post-printing and then conjugated to the RGD containing peptide (GRGDY) via an epoxy crosslinker (Gloria et al., 2012). The bioactivated PCL scaffolds demonstrated enhanced cell adhesion and good spreading of cells when seeded with NIH 3T3 cells. In another example, elastin-like polymers functionalized with the RGD sequence along with hydroxyapatite binding sites have been used to coat hydroxyapatite scaffolds (Vila et al., 2016).

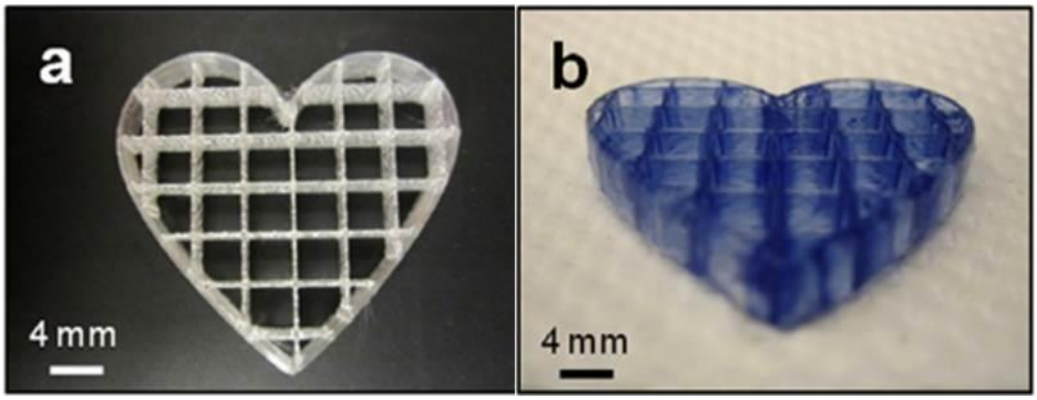


Figure 2.6. Images of a 3D printed scaffold of PLLA (a) coated with a combination of collagen and hyaluronic acid, stained with Trypan blue for better visualisation (b)(Ji, Jakus and Shah, 2013)

Apart from cell attachment, bioactive components could also promote other desired outcomes including cell growth, differentiation, and tissue-specific regenerative responses. Such bioactive components have ranged from biological components (growth factors, cytokines and cells) and polymers (Narayanan et al., 2016) to bioceramics and inorganic components (Zhu et al., 2016). Biological components, due to their sensitive nature have typically been encapsulated in coating materials such as collagen type I (Lindhorst et al., 2010; Kampmann et al., 2013), fibrin (Chang et al., 2014), Matrigel (Laschke et al., 2008) and alginate crosslinked with $CaCl_2$ (Yilgor et al., 2010; Huri et al., 2013). Lindhorst et al. (2010) reported increased neovascularization during *in vivo* studies of 3D printed scaffolds coated with collagen loaded with vascular endothelial growth factor (VEGF). In a similar study, scaffolds have been coated with VEGF as well as bone marrow-derived mesenchymal stem cells (bmMSC) (Kampmann et al., 2013). The addition of bmMSC to VEGF containing scaffolds further promoted micro-vascularization. The sequential release of two different bone morphogenetic proteins (BMP-2 and BMP-7) has also been achieved from 3D printed scaffolds and showed increased differentiation of mesenchymal stem cells compared to single and simultaneous releases (Yilgor et al., 2010). This study included coating 3D-printed scaffolds with BMP-loaded nanocapsules with different release profiles. *In vivo* investigation of this scaffold also demonstrated improved mineralized matrix formation and bone-implant union strength when applied to a critical-sized bone defect (Huri et al., 2013). In a recent study by Tarafder *et al*. (2016), it was however

demonstrated that sensitive biological molecules such as growth factors could be incorporated into thermoplastics prior to extrusion-based 3D printing. PCL was blended with PLGA microspheres loaded with growth factors and 3D printed at 120 °C. The growth factors were shielded from the high printing temperatures by the PLGA, as a result of the high melting temperature of PLGA (200 °C), along with its low heat conductivity.

2.3.2 Porosity

The porosity of the scaffold is here distinguished from the nano- and micropores that were discussed in the previous section as part of the surface properties of scaffolds. It is well known that the porosity and pore interconnectivity form an essential part of tissue engineering scaffolds. High porosity and good pore interconnectivity enable mass transport of nutrients, oxygen and cellular waste, which is essential to cell survival. Pore sizes larger than the average cell diameter (d> 10 μm) also allowed infiltration and migration of cells within the scaffold. It is however known that the pore sizes have an effect on the behaviour of the specific cell type or tissue that needs to be supported. The optimal pore sizes that have been reported do not always correlate between different studies, however they have still been used as guidelines in designing new tissue engineering scaffolds. Wang *et al*. (1999), for example, reported the optimal pore sizes as *"5 μm for neovascularization, 5–15 μm for fibroblast ingrowth, 20–125 μm for regeneration of adult mammalian skin, 100–400 μm for regeneration of bone, 40–100 μm for osteoid ingrowth and 20 μm for the ingrowth of hepatocytes"* (Whang et al., 1999).

In extrusion-based 3D printing, cross-hatch 3D printing patterns have typically been used to produce porous scaffolds, while a continuous strand of material is being extruded (Figure 2.7). It has been demonstrated that the percentage porosity could easily be varied by changing the printing pattern (Moroni, de Wijn and van Blitterswijk, 2006; Hamid et al., 2011; Hendriks et al., 2013). Moroni, de Wijn and van Blitterswijk (2006) produced a number of PEOT/PBT scaffolds with porosities ranging from 29% to 91% by changing the parameters of the printing pattern. The printing pattern is defined by the strand diameter, the strand spacing, the layer height, the orientation between layers, and staggered strand placements. The strand diameter is primarily determined by the ID of the printing needle, the printing speed, and pressure. Currently, available needles have limited the strand thickness to 100 μm (Rajaram, Schreyer and Chen, 2014), which consequently limited the printing resolution. The majority of extruded scaffolds, however, consist of strands with diameters ranging between 150 μm and 500 μm (Billiet et al., 2014; Müller et al., 2015; Song et al., 2015; Rutz et al., 2015; Martínez-Vázquez et al., 2015). Thinner strands have a higher surface to volume ratio, which could lead to an overall higher surface area and subsequently higher cell attachments (Hamid et al., 2011). Thicker strands, on the other hand, have often been easier to produce, since thicker needles are less prone to clogging and require less pressure for extrusion. The strand spacing, layer height, and orientation of the strands determine the pore sizes and shapes. It is, however, difficult to characterise the pores based

on their size and shape, due to the nature of the pores being intersecting horizontal and vertical channels as a result of the cross-hatch pattern (Figure 2.7). The strand spacing refers to the distance between the centres of two adjacent strands, while the inter-strand spacing between strands have typically been selected based on the reported optimal pore sizes for specific tissue engineering applications. For example, Lee *et al.* (2013) selected a spacing of 500 μm for scaffolds intended for bone tissue engineering, based on studies suggesting that 100 – 500 μm pore sizes are adequate for bone tissue. Similarly, a few studies investigating the vascularization of 3D plotted scaffolds selected pore sizes of 250 μm (Schumann et al., 2009; Lindhorst et al., 2010), which was previously supported by studies by Druecke *et al.* (2004). When selecting pore sizes, it should however be taken into account that large pore sizes encourage mass transport of essential nutrients, gases and metabolic waste removal, while smaller sizes favour intracellular signalling and cell attachment. Varying the pore sizes could also affect the overall porosity and surface area of the scaffold. Hamid et al. (2011) investigated the cell attachment and proliferation on three scaffolds with constant strand diameters (350 μm) and varying strand spacing (200 μm; 350 μm; 500 μm). The smallest strand spacing resulted in a higher surface area and thus higher cell attachment. The largest strand spacing, on the other hand, allowed the longest active proliferation, which was ascribed to "more empty space for cells to grow" (Hamid et al., 2011). Pore sizes were also related to the spreading of seeded cells, with smaller pores contributing to denser cell populations. This is in contrast with the findings of another study investigating two PCL scaffolds with different strand diameter and strand spacing. Denser cell populations grew on the scaffold with larger pores, as the hydrophobicity of PCL was less pronounced in larger pores compared to smaller pores, and thus allowed better penetration of cells into larger pores (Park et al., 2009). It should be noted that the size and shape of horizontal and vertical channels vary, since horizontal channels are dependent on the inter-strand spacing as well as the layer height; while vertical channels are a product of inter-strand spacing and the direction of strands in subsequent layers. For example, 90° rotations will result in square vertical channels, while 45° rotation will result in rhomboid channels (Figure 2.7). No significant difference between scaffolds with 0°/90° and 0°/45°/90°/135° strand orientations have been observed in terms of cell behaviours (Sun et al., 2012), however strand orientation have affected the mechanical properties as will be discussed later. "Shifting" the strands with a specified offset from previous layers forms a staggered pattern that alters or hinders the path of vertical channels. In a study by Yilgor et al. (2008), investigating printing patterns of PCL scaffolds, it was found that staggered patterns have higher initial cell adhesion and higher cell numbers when compared to non-staggered patterns. It was suggested that this type of strand positioning hinder the flow of cells during cell seeding and thereby provide higher available surface areas for cell attachment. Low cell seeding efficiencies on 0°/90° scaffold architectures without any offset have previously been ascribed to the easy flowing of cells through and out of the scaffold, as a result of the open vertical paths (Jukes et al., 2008). 3D plotted scaffolds with gradient pore sizes either increasing or decreasing from the outer layers inward also produced an offset

between strands in the x-y plane as the porosity is changed (Sobral et al., 2011). It was therefore seen that scaffolds with gradients have higher seeding efficiencies compared to scaffolds with homogenous pores, despite lower surface areas of the gradient scaffolds. Scaffolds with pore sizes decreasing from the outer layer to the middle also produce better cell distributions as a result of flow mechanics as described by Sobral et al. (2011).

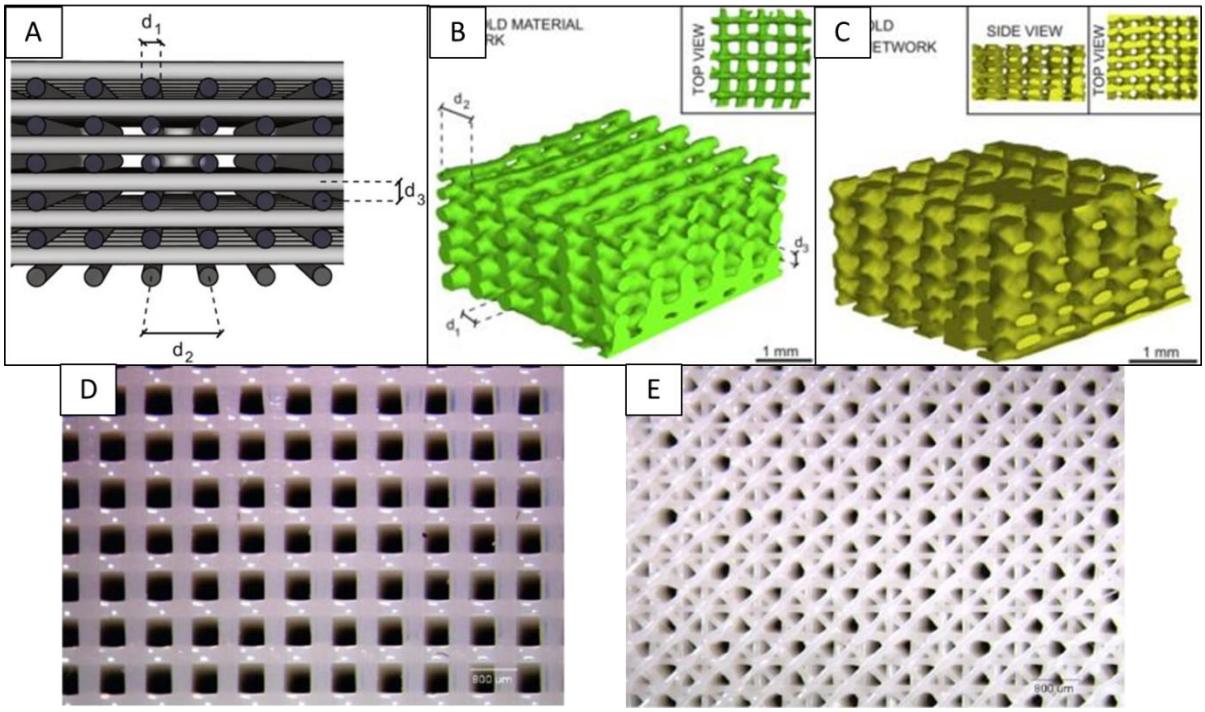


Figure 2.7. Schematic representation of the cross-hatch printing pattern (A), indicating strand diameter (d_1), strand spacing (d_2) and layer height (d_3), µCT scan of the 3D printed scaffold material network (B) and the scaffold pore network (C) (Billiet et al., 2014), and microscopy images of 3D printed scaffolds with 90° (D) and 45° (E) strand orientation (Moroni, de Wijn and van Blitterswijk, 2006)

2.3.3 Mechanical Properties

The mechanical properties of tissue engineering scaffolds should be correlated with the properties of the intended tissue type that is to be regenerated. While the properties of the scaffold material will play a role in the mechanical properties of the scaffold, the material processing and porosity of the scaffold will determine the final scaffold properties. The wide variety of materials that have been processable by extrusion-based 3D printing therefore allowed fabrication of scaffolds with very different mechanical properties suitable for hard and soft tissue engineering applications. 3D printing further allowed accurate alterations to the porosity and printing pattern which could be used to fine-tune the mechanical properties of the scaffold.

Bioactive glass scaffolds, produced from 3D plotted composite pastes and subsequent sintering have demonstrated superior mechanical properties. One specific study used silicate 13-93 to produce scaffolds with a compressive strength of 86 ± 9 MPa and elastic modulus of 13 ± 2 GPa which was comparable to the compressive strength (100 - 150 MPa) and elastic modulus (10 - 20 GPa) of cortical

bone (Liu et al., 2013). A number of 3D plotted scaffolds with mechanical properties similar to trabecular bone have also been investigated for bone tissue engineering. Such scaffolds typically have compressive strengths in the range of 2 MPa to 16 MPa (Zhang, Zhao, Y. Zhu, et al., 2014; Zhang, Zhao, M. Zhu, et al., 2014; Yoon, Kim and Koh, 2015; Zhao et al., 2015; Martínez-Vázquez et al., 2015). The incorporation of bioactive glass or calcium phosphate bioceramics such as hydroxyapatite and β-TCP evidently increased the mechanical properties of the scaffolds compared to non-composite scaffolds. In the case of hydrogel composites such as MBG/alginate (Luo et al., 2013) and hydroxyapatite/gelatine (Martínez-Vázquez et al., 2015), the hydrogel component provided a favourable environment for cell seeding or encapsulation, while the formation of a composite added the necessary mechanical properties, which largely lacks in hydrogels and limits their use in hard tissue engineering. Luo et al. (2013) reported a significant increase in compressive strength and modulus of alginate scaffolds incorporated with 30 - 50% mesoporous bioactive glass content compared to pure alginate scaffolds. The incorporation of bioceramic components have however often been limited by the processing pressure and consequently, its effect on the mechanical properties is limited. For example, Wüst et al. (2014) found that by varying the hydroxyapatite content from 0% to 8% in gelatine/alginate scaffolds, did not lead to large differences in their mechanical properties. Another approach to increase the mechanical properties of 3D printed hydrogel scaffolds was to alternate the hydrogel layers with other polymer layers. This has been demonstrated by printing hybrid alginate/PCL scaffolds, with its mechanical properties directly dependent on the volume fraction of the PCL (Lee et al., 2013; Izadifar et al., 2016). A large increase in the mechanical properties of 3D plotted N,O-carboxymethyl chitosan/alginate hydrogel scaffolds has also been reported, as a result of polyphosphate addition to the printing material (Müller et al., 2015). The reduced Young's modulus increased from 27 ± 3 kPa to 935 ±128 kPa. 3D printed scaffolds of pure and composite polymers with mechanical properties in the kPa range have particularly been explored for cartilage and soft tissue engineering applications (Hockaday et al., 2012; Bakarich et al., 2014; Neufurth et al., 2014; Kesti et al., 2015; Neufurth et al., 2015). Chemical crosslinking of 3D plotted hydrogels, as already discussed, could provide adequate mechanical properties to hydrogels for soft tissue engineering (Kesti et al., 2015; Rutz et al., 2015)

It is well-known that the mechanical properties of a structure or object are also dependent on its porosity. As discussed in the previous section, 3D printing allows accurate adjustment of % porosity over a wide range. Subsequently, 3D printed scaffolds with varying porosities have been used to demonstrate that the mechanical properties of the scaffolds can be fine-tuned. Particularly, dynamic mechanical analysis (DMA) of scaffolds composed of viscoelastic polymers showed an inverse relationship between dynamic stiffness and porosity (Moroni, de Wijn and van Blitterswijk, 2006; Sobral et al., 2011). Moroni, de Wijn and van Blitterswijk (2006) reported a significant increase in dynamic stiffness ranging from 0.186 ± 0.005 MPa to 13.7 ± 2.63 MPa with a decrease in porosity

from 91.2 % to 28.9 %. It has been demonstrated that apart from the porosity, the printing pattern also plays a role in the mechanical properties. For example, scaffolds with 0°/90° strand orientations display a greater compressive modulus compared to scaffolds with 0°/45°/90°/135° strand orientations (Moroni, de Wijn and van Blitterswijk, 2006; Sobral et al., 2011; Gloria et al., 2012; Cengiz et al., 2016). Also, scaffolds with no strand offset displayed a greater compressive modulus, compared to scaffolds with strand offsets (Yilgor et al., 2008). In both cases, the greater compressive modulus was most likely related to increased junction points between consecutive strands along the z-axis (Yilgor et al., 2008).

2.4 3D PRINTING IN WOUND HEALING AND SKIN REGENERATIVE APPLICATIONS

As new wound-healing strategies progress more towards tissue engineering, the need for control over scaffold properties becomes apparent. A number of studies have used extrusion-based 3D printing technology to fabricate scaffolds as potential wound dressings, skin substitutes, and skin equivalents. This includes 3D printed acellular scaffolds and cell-laden 3D bioprinted scaffolds.

For wound healing applications, acellular 3D printed scaffolds were typically investigated for their structure-function relationship. For example, Xu et al. (2018) 3D printed cellulose nanofibrils into $CaCl_2$ crosslinking solutions and further crosslinked the scaffolds with BDDE. They investigated the effect of 3D printing patterns on mechanical properties and fibroblast adhesion. Xu et al. (2019) further reported 3D printing of low concentrations of TEMPO-oxidised nanocellulose and GelMA. The crosslinked scaffolds demonstrated adequate physical and biological properties for potential wound healing applications. Shi et al. (2018) used gelatin/alginate composite material to 3D print scaffolds as potential dermal substitutes. The scaffolds were crosslinked with $CaCl_2$, EDC/NHS or combinations of $CaCl_2$ and EDC/NHS. The effect of crosslinking on the physical and biological properties of the scaffolds was investigated. Chen et al. (2018) investigated the wound healing potential of 3D printed scaffolds of gelatin and silk-sericin. They prepared the scaffolds with large pore sizes of ~300 to ~500 μm and achieved high transparency of the scaffolds for real-time monitoring of the wounds. Intini et al. (2018) fabricated chitosan-based 3D printed scaffolds with inter-strand distances of ~200 μm. The 3D printed scaffolds showed improved wound healing in an *in vivo* wound model of streptozotocin-induced diabetic rats, compared to a commercial product.

Other studies have further included drugs or growth factors into the 3D printed wound dressings. Xiong et al. (2017) reported 3D printed gelatin scaffolds coated with sulfonated silk fibroin to allow incorporation of FGF-2. While the 3D printed macropores were lost during the coating process, the scaffolds demonstrated enhanced skin regeneration properties. Long et al. (2019) 3D printed chitosan/pectin composite material incorporated with lidocaine as a potential pain-relieving wound dressing. Maver et al. (2018) also investigated the incorporation of lidocaine as well as diclofenac in

3D printed wound dressings of alginate and carboxymethyl cellulose. By combining 3D printing with electrospinning, a dual release profile of the drugs was achieved. The fast release of lidocaine from the electrospun layer could potentially provide immediate pain relief, while an extended release of diclofenac over 2 days from the 3D printed layer could potentially provide longer pain relief between dressing changes. Bilayered materials combining 3D printing with electrospinning are attractive as wound dressings since the 3D printed layer and electrospun layer can mimic the dermis and epidermis, respectively. Wang et al. (2019) produced a bilayer membrane (BLM) of 3D printed alginate and electrospun PLGA. The alginate layer was 3D printed as a solid layer with inherent microporosity, while the PLGA layer retained the moisture and acted as a bacterial barrier. In an *in vivo* wound model of rats, the BLM demonstrated accelerated wound healing compared to the untreated groups and groups treated with alginate and PLGA, respectively. Miguel et al. (2019) also reported a bilayered scaffold intended for wound healing, termed a "3D skin asymmetric construct". It was composed of electrospun PCL/silk sericin and 3D printed chitosan/sodium alginate.

3D bioprinted scaffolds for skin regeneration have recently been reviewed by Matai et al. (2020). These scaffolds have typically been bilayered or multi-layered, to mimic the dermal and epidermal components of native skin. Derr et al. (2019) reported the biofabrication of a 3D bioprinted skin equivalent (BPSE) in a multi-well plate format. The BPSE consisted of a 0.4 mm thick dermal layer extruded with a plunger dispenser, a thin basement membrane layer produced with a jetting dispenser, and an epidermal layer. Yoon et al. (2016) fabricated a cell-laden collagen scaffold composed of a keratinocyte layer representing the epidermis and a fibroblast layer representing the dermis. Although the scaffolds had a very low stiffness, it showed promising biocompatibility, with effective proliferation and migration of keratinocytes and fibroblasts. Admane et al. (2019) used silk fibroin/gelatin cell-laden bioink containing keratinocytes and fibroblasts, respectively for the fabrication of 3D bioprinted full-thickness skin equivalents. Won et al. (2019) further used skin decellularised extracellular matrix (dECM) to 3D bioprint cell-laden constructs of human dermal fibroblast as potential dermal substitutes.

In situ skin bioprinting has also been investigated for automated patient-specific treatment of skin wounds. This allowed bioprinted skin to follow the contour of the skin wounds while minimising scaffold preparation and treatment time (Singh et al., 2020). While *in situ* bioprinting has been proposed for other tissue regenerating applications, skin wounds are easily accessible and relatively simple compared to other tissue and organs (Singh et al., 2020). Albanna et al. (2019) reported *in situ* skin bioprinting of a fibrinogen/collagen solution containing fibroblasts for the dermal layer and keratinocytes for the epidermal layer, respectively. A real-time 3D laser scanner was used to determine the wound area for the *in situ* bioprinting process. In this proof of concept study, the *in situ* skin bioprinting was tested in *in vivo* murine and porcine wound models.

2.5 CONCLUDING REMARKS

The versatility in materials processable by extrusion-based 3D printing is unrivalled by other 3D printing techniques used for tissue engineering. The biomaterial inks, categorised in this chapter as thermoplastics, pastes, hydrogels and reactive resins, and bioinks have however been limited by their extrudability, the processing conditions specific to each type, and their solidification mechanisms. Covalently cross-linked hydrogels have generally not been considered as 3D printable, due to the irreversible nature of their crosslinking. Consequently, a large number of covalently cross-linked hydrogels with promising applications in tissue engineering have been excluded from 3D printing. 3D printable hydrogels used in tissue engineering studies are currently limited to a select few. For example, in wound healing applications as discussed in the previous section, the literature have been dominated by gelatin, alginate, chitosan, silk, and nanocellulose. Furthermore, studies on the structure-function relationship of 3D printed constructs for wound healing applications was primarily focussed on their *in vitro* performance. While few studies have reported on the *in vivo* application of 3D printed constructs, the widely claimed advantage of control over the structure-function relationship, as obtained through 3D printing, have rarely been demonstrated.

It is clear that new 3D biomaterial inks are underutilised, and the proposed advantages of 3D printing have been unexplored in wound healing applications. Therefore, we proposed the development of a 3D printed scaffold with bio-inspired properties as a potential wound healing device for burn wounds. By controlling the synthesis and composition of a synthetic polypeptide-based hydrogel, with previously reported biofunctionality, we envisioned a library of hydrogels with tuneable physical and biological properties. The ideal combination of these properties could be used to direct the potential application in wound healing and further processing into new 3D biomaterial inks. The newly proposed 3D biomaterial ink will potentially revolutionise the field by creating 3D printable covalently crosslinked hydrogels, while allowing precise control over the fabrication of micro-architectures through the 3D printing process. Finally, the control over the structure-function relationship of the 3D printed scaffolds will be evaluated in terms of their *in vitro* properties and *in vivo* performance in a wound healing model. While the specific study is focused on burn wounds, the concepts described in this thesis can be useful to a variety of applications including drug delivery and other soft tissue engineering applications.

2.6 REFERENCES

ADMANE, P. et al. (2019) Direct 3D bioprinted full-thickness skin constructs recapitulate regulatory signaling pathways and physiology of human skin. *Bioprinting*, 15, p. e00051.

AHANGAR, P. et al. (2019) Current Biomedical Applications of 3D Printing and Additive Manufacturing. *Applied Sciences*, 9(1713), pp. 1–23.

AHN, S. et al. (2012) Fabrication of cell-laden three-dimensional alginate-scaffolds with an aerosol - cross-linking process. *Journal of Materials Chemistry*, 22, pp. 18735–18740.

AL-AHMAD, A. et al. (2008) Bacterial and Candida albicans adhesion on rapid prototyping-produced 3D-scaffolds manufactured as bone replacement materials. *Journal of Biomedical Materials Research Part A*, 87A, pp. 933–943.

AL-AHMAD, A. et al. (2011) Comparison of bacterial adhesion and cellular proliferation on newly developed three-dimensional scaffolds manufactured by rapid prototyping technology. *Journal of Biomedical Materials Research Part A*, 98A(2), pp. 303–311.

ALBANNA, M. et al. (2019) In Situ Bioprinting of Autologous Skin Cells Accelerates Wound Healing of Extensive Excisional Full- Thickness Wounds. *Scientific Reports*, 9, p. 1856.

AMOROSAA, L.F. et al. (2013) Physiologic load-bearing characteristics of autografts, allografts, and polymer-based scaffolds in a critical sized segmental defect of long bone : an experimental study. *International Journal of Nanomedicine*, 8, pp. 1637–1643.

ANG, T.H. et al. (2002) Fabrication of 3D chitosan-hydroxyapatite scaffolds using a robotic dispensing system. *Materials Science and Engineering C*, 20(1–2), pp. 35–42.

ANGARANO, M. et al. (2013) Layered Gradient Nonwovens of In Situ Crosslinked Electrospun Collagenous Nanofi bers Used as Modular Scaffold Systems for Soft Tissue Regeneration. *Advanced Functional Materials*, 23, pp. 3277–3285.

BAKARICH, S.E. et al. (2014) Printed ionic-covalent entanglement hydrogels from carrageenan and an epoxy amine. *RSC Advances*, 4, pp. 38088–38092.

BANOBRE-LOPEZ, M. et al. (2011) Poly (caprolactone) based magnetic scaffolds for bone tissue engineering. *Journal of Applied Physics*, 109, pp. 1–3.

BERTASSONI, L.E. et al. (2014) Hydrogel bioprinted microchannel networks for vascularization of tissue engineering constructs. *Lab on a chip*, 14, pp. 2202–2211.

BETTAHALLI, N.M.S. et al. (2013) Corrugated round fibers to improve cell adhesion and proliferation in tissue engineering scaffolds. *Acta Biomaterialia*, 9(6), pp. 6928–6935.

BETTAHALLI, N.M.S. et al. (2011) Integration of hollow fiber membranes improves nutrient supply in

three-dimensional tissue constructs. *Acta Biomaterialia*, 7(9), pp. 3312–3324.

BILLIET, T. et al. (2014) The 3D printing of gelatin methacrylamide cell-laden tissue-engineered constructs with high cell viability. *Biomaterials*, 35(1), pp. 49–62.

CALVO-GUIRADO, L. et al. (2012) In-vivo behavior of Si-hydroxyapatite/polycaprolactone/DMB scaffolds fabricated by 3D printing. *Journal of Biomedical Materials Research Part A*, 101A, pp. 2038–2048.

CENGIZ, I.F. et al. (2016) Building the basis for patient-specific meniscal scaffolds: From human knee MRI to fabrication of 3D printed scaffolds. *Bioprinting*, 1–2, pp. 1–10.

CHANG, J.W. et al. (2014) Tissue-engineered tracheal reconstruction using three-dimensionally printed artificial tracheal graft: preliminary report. *Artificial organs*, 38(6), pp. E95–E105.

CHANG, R., NAM, J. and SUN, W. (2008) Effects of Dispensing Pressure and Nozzle Diameter on Cell Survival from Solid Freeform Fabrication–Based Direct Cell Writing. *Tissue Engineering Part A*, 14(1), pp. 41–48.

CHEN, C. et al. (2018) Three-Dimensionally Printed Silk-Sericin-Based Hydrogel Scaffold: A Promising Visualized Dressing Material for Real-Time Monitoring of Wounds. *ACS Applied Materials & Interfaces*, 10, pp. 33879–33890.

CHIEN, K.B. et al. (2013) In vivo acute and humoral response to three-dimensional porous soy protein scaffolds. *Acta Biomaterialia*, 9(11), pp. 8983–8990.

CHIEN, K.B., MAKRIDAKIS, E. and SHAH, R.N. (2013) Three-dimensional printing of soy protein scaffolds for tissue regeneration. *Tissue engineering. Part C, Methods*, 19(6), pp. 417–26.

COSTANTINI, M. et al. (2016) 3D bioprinting of BM-MSCs-loaded ECM biomimetic hydrogels for in vitro neocartilage formation. *Biofabrication*, 8(3), p. 35002.

COUTU, D.L. et al. (2011) Hierarchical scaffold design for mesenchymal stem cell-based gene therapy of hemophilia B. *Biomaterials*, 32, pp. 295–305.

DAOUD, J. et al. (2012) Dielectric spectroscopy for non-invasive monitoring of epithelial cell differentiation within three-dimensional scaffolds. *Physics in Medicine and Biology*, 57, pp. 5097–5112.

DELIORMANLI, A.M., LIU, X. and RAHAMAN, M.N. (2014) Evaluation of borate bioactive glass scaffolds with different pore sizes in a rat subcutaneous implantation model. *Journal of Biomaterials Applications*, 28(5), pp. 643–653.

DERBY, B. (2012) Printing and Prototyping of Tissues and Scaffolds. *Science*, 338(6109), pp. 921–926.

DERR, K. et al. (2019) Fully Three-Dimensional Bioprinted Skin Equivalent Constructs with Validated Morphology and Barrier Function. *Tissue Engineering - Part C: Methods*, 25(6), pp. 334–343.

DETSCH, R. et al. (2009) Biofunctionalization of dispense-plotted hydroxyapatite scaffolds with peptides : Quantification and cellular response. *Journal of Biomedical Materials Research Part A*, 92(2), pp. 493–503.

DRUECKE, D. et al. (2004) Neovascularization of poly(ether ester) block-copolymer scaffolds in vivo: Long-term investigations using intravital fluorescent microscopy. *Journal of Biomedical Materials Research Part A*, 68A(1), pp. 10–18.

EL-AYOUBI, R. et al. (2011) Design and Dynamic Culture of 3D-Scaffolds for Cartilage Tissue Engineering. *Journal of Biomaterials Applications*, 25, pp. 429–444.

EL-AYOUBI, R. et al. (2008) Design and Fabrication of 3D Porous Scaffolds to Facilitate Cell-based Gene Therapy. *Tissue Engineering - Part A*, 14, pp. 1037–1047.

ENGLAND, S. et al. (2017) Bioprinted fibrin-factor XIII-hyaluronate hydrogel scaffolds with encapsulated Schwann cells and their in vitro characterization for use in nerve regeneration. *Bioprinting*, 5, pp. 1–9.

Fab@Home Organization. (2016) [Online] Additive3D. Available from : https://additive3d.com/fabhome-organization/.

FEDOROVICH, N.E. et al. (2009) Evaluation of Photocrosslinked Lutrol Hydrogel for Tissue Printing Applications. *Biomacromolecules*, 10, pp. 1689–1696.

FEDOROVICH, N.E. et al. (2011) Scaffold Porosity and Oxygenation of Printed Hydrogel Constructs Affect Functionality of Embedded Osteogenic Progenitors. *Tissue Engineering - Part A*, 17, pp. 2473–2486.

FEDOROVICH, N.E. et al. (2008) Three-dimensional fiber deposition of cell-laden, viable, Patterned Constructs for Bone Tissue Printing. *Tissue Engineering - Part A*, 14(1), pp. 127–133.

FEITO, M.J. et al. (2011) Immobilization and bioactivity evaluation of FGF-1 and FGF-2 on powdered silicon-doped hydroxyapatite and their scaffolds for bone tissue engineering. *Journal of Materials Science: Materials in Medicine*, 22, pp. 405–416.

GARCÍA-ALVAREZ, R., IZQUIERDO-BARBA, I. and VALLET-REGÍ, M. (2017) 3D scaffold with effective multidrug sequential release against bacteria biofilm. *Acta Biomaterialia*, 49, pp. 113–126.

GLORIA, A. et al. (2012) Three-Dimensional Poly(ε-caprolactone) Bioactive Scaffolds with Controlled Structural and Surface Properties. *Biomacromolecules*, 13, pp. 3510–3521.

GÓMEZ-CEREZO, N. et al. (2016) In vitro colonization of stratified bioactive scaffolds by pre-osteoblast cells. *Acta Biomaterialia*, 44, pp. 73–84.

GROLL, J. et al. (2019) A definition of bioinks and their distinction from biomaterial inks. *Biofabrication*, 11, p. 13001.

HABERSTROH, K. et al. (2010) Bone repair by cell-seeded 3D-bioplotted composite scaffolds made of collagen treated tricalciumphosphate or tricalciumphosphate-chitosan- collagen hydrogel or PLGA in ovine critical-sized calvarial defects. *Journal of Biomedical Materials Research - Part B Applied Biomaterials*, 93B, pp. 520–530.

HAMID, Q. et al. (2011) Fabrication of three-dimensional scaffolds using precision extrusion deposition with an assisted cooling device. *Biofabrication*, 3, pp. 1–11.

HENDRIKS, J.A.A. et al. (2013) The effect of scaffold-cell entrapment capacity and physico-chemical properties on cartilage regeneration. *Biomaterials*, 34(17), pp. 4259–4265.

HIMENE, D.A.C. et al. (2016) Advanced Bioinks for 3D Printing : A Materials Science Perspective. 44(6), pp. 2090–2102.

HO, C.M.B., NG, S.H. and YOON, Y.-J. (2015) A review on 3D printed bioimplants. *International Journal of Precision Engineering and Manufacturing*, 16(5), pp. 1035–1046.

HOCKADAY, L.A. et al. (2012) Rapid 3D printing of anatomically accurate and mechanically heterogeneous aortic valve hydrogel scaffolds. *Biofabrication*, 4, pp. 1–12.

HUANG, M.-H. et al. (2004) Degradation and cell culture studies on block copolymers prepared by ring opening polymerization of ε-caprolactone in the presence of poly(ethylene glycol). *Journal of biomedical materials research. Part A*, 69(3), pp. 417–427.

HURI, P.Y. et al. (2013) A biomimetic growth factor delivery strategy for enhanced regeneration of iliac crest defects. *Biomedical Materials*, 8, pp. 1–8.

HUTMACHER, D.W., SITTINGER, M. and RISBUD, M. V (2004) Scaffold-based tissue engineering: rationale for computer-aided design and solid free-form fabrication systems. *Trends in Biotechnology*, 22(7), pp. 354–362.

INTINI, C. et al. (2018) 3D-printed chitosan-based scaffolds: An in vitro study of human skin cell growth and an in-vivo wound healing evaluation in experimental diabetes in rats. *Carbohydrate Polymers*, 199(July), pp. 593–602.

IZADIFAR, Z. et al. (2016) Analyzing Biological Performance of 3D-Printed, Cell-Impregnated Hybrid Constructs for Cartilage Tissue Engineering. *Tissue Engineering Part C: Methods*, 22(3), pp. 173–188.

JAKUS, A.E. et al. (2015) Three-Dimensional Printing of High-Content Graphene Scaffolds for

Electronic and Biomedical Applications. *ACS Nano*, 9, pp. 4636–4648.

JAKUS, A.E. and SHAH, R.N. (2017) Multi and mixed 3D-printing of graphene-hydroxyapatite hybrid materials for complex tissue engineering. *Journal of Biomedical Materials Research Part A*, 105(1), pp. 274–283.

JAMRÓZ, W. et al. (2018) 3D Printing in Pharmaceutical and Medical Applications – Recent Achievements and Challenges. *Pharmaceutical Research*, 35(35), pp. 1–22.

JI, E., JAKUS, A.E. and SHAH, R.N. (2013) In situ forming collagen–hyaluronic acid membrane structures: Mechanism of self-assembly and applications in regenerative medicine. *Acta Biomaterialia*, 9(2), pp. 5153–5161.

JOHNSON, C. et al. (2016) In vitro characterization of design and compressive properties of 3D-biofabricated/decellularized hybrid grafts for tracheal tissue engineering. *Journal of the Mechanical Behavior of Biomedical Materials*, 59, pp. 572–585.

JOSE, R.R. et al. (2016) Evolution of Bioinks and Additive Manufacturing Technologies for 3D Bioprinting. *ACS Biomaterials Science and Engineering*, 2, pp. 1662–1678.

JUKES, J.M. et al. (2008) Critical steps towards a tissue-engineered cartilage implant using embryonic stem cells. *Tissue Engineering - Part A*, 14, pp. 135–147.

KAMPMANN, A. et al. (2013) Additive effect of mesenchymal stem cells and VEGF to vascularization of PLGA scaffolds. *Microvascular Research*, 90, pp. 71–79.

KELLY, C.N. et al. (2018) Design and Structure–Function Characterization of 3D Printed Synthetic Porous Biomaterials for Tissue Engineering. *Advanced Healthcare Materials*, 7, p. 1701095.

KESTI, M. et al. (2015) A versatile bioink for three-dimensional printing of cellular scaffolds based on thermally and photo-triggered tandem gelation. *Acta Biomaterialia*, 11, pp. 162–172.

KIM, H. et al. (2018) Gelatin/PVA scaffolds fabricated using a 3D-printing process employed with a low-temperature plate for hard tissue regeneration : Fabrication and characterizations. *International Journal of Biological Macromolecules*, 120, pp. 119–127.

KIM, Y.S. et al. (2015) The Application of Three-Dimensional Printing in Animal Model of Augmentation Rhinoplasty. *Annals of biomedical engineering*, 43(9), pp. 2153–2162.

KIRCHMAJER, D.M., GORKIN III, R. and IN HET PANHUIS, M. (2015) An overview of the suitability of hydrogel-forming polymers for extrusion-based 3D-printing. *J. Mater. Chem. B*, 3(20), pp. 4105–4117.

KYLE, S. et al. (2017) ‘ Printability’ of Candidate Biomaterials for Extrusion Based 3D Printing: State-of-the-Art. *Advanced Healthcare Materials*, 6, p. 1700264.

LANDERS, R., PFISTER, A., et al. (2002) Fabrication of soft tissue engineering scaffolds by means of rapid prototyping techniques. *Journal of Materials Science*, 37, pp. 3107–3116.

LANDERS, R., HÜBNER, U., et al. (2002) Rapid prototyping of scaffolds derived from thermoreversible hydrogels and tailored for applications in tissue engineering. *Biomaterials*, 23, pp. 4437–4447.

LANDERS, R. and MÜLHAUPT, R. (2000) Desktop manufacturing of complex objects, prototypes and biomedical scaffolds by means of computer-assisted design combined with computer-guided 3D plotting of polymers and reactive oligomers. *Macromolecular Materials and Engineering*, 282, pp. 17–21.

LASCHKE, M.W. et al. (2008) Incorporation of growth factor containing Matrigel promotes vascularization of porous PLGA scaffolds. *Journal of Biomedical Materials Research Part A*, 85(2), pp. 397–407.

LEE, C.H. et al. (2010) Regeneration of the articular surface of the rabbit synovial joint by cell homing : a proof of concept study. *The Lancet*, 376(9739), pp. 440–448.

LEE, H. et al. (2013) Cell(MC3T3-E1)-Printed Poly(ε-caprolactone)/Alginate Hybrid Scaffolds for Tissue Regeneration. *Macromolecular Rapid Communications*, 34, pp. 142–149.

LEE, H. et al. (2016) Investigation of thermal degradation with extrusion-based dispensing modules for 3D bioprinting technology. *Biofabrication*, 8(1), p. 015011.

LEWIS, P.L., GREEN, R.M. and SHAH, R.N. (2018) 3D-printed gelatin scaffolds of differing pore geometry modulate hepatocyte function and gene expression. *Acta Biomaterialia*, 69, pp. 63–70.

LI, K. et al. (2015) Three-dimensionally plotted MBG / PHBHHx composite scaffold for antitubercular drug delivery and tissue regeneration. *Journal of Materials Science: Materials in Medicine*, 26, pp. 1–8.

LINDHORST, D. et al. (2010) Effects of VEGF loading on scaffold-confined vascularization. *Journal of Biomedical Materials Research Part A*, 95A, pp. 783–792.

LIU, X. et al. (2013) Mechanical properties of bioactive glass (13-93) scaffolds fabricated by robotic deposition for structural bone repair. *Acta Biomaterialia*, 9, pp. 7025–7034.

LOH, Q.L. and CHOONG, C. (2013) Three-Dimensional Scaffolds for Tissue Engineering Applications: Role of Porosity and Pore Size. *Tissue Engineering Part B: Reviews*, 19(6), pp. 485–502.

LONG, J. et al. (2019) A 3D printed chitosan-pectin hydrogel wound dressing for lidocaine hydrochloride delivery. *Materials Science & Engineering C*, 104, p. 109873.

LUO, Y. et al. (2013) Hierarchical mesoporous bioactive glass/alginate composite scaffolds fabricated

by three-dimensional plotting for bone tissue engineering. *Biofabrication*, 5, pp. 1–13.

MAHER, P.S. et al. (2009) Construction of 3D biological matrices using rapid prototyping technology. *Rapid Prototyping Journal*, 15, pp. 204–210.

MARTÍNEZ-VÁZQUEZ, F.J. et al. (2015) Fabrication of novel Si-doped hydroxyapatite/gelatine scaffolds by rapid prototyping for drug delivery and bone regeneration. *Acta biomaterialia*, 15, pp. 200–9.

MATAI, I. et al. (2020) Progress in 3D bioprinting technology for tissue/organ regenerative engineering. *Biomaterials*, 226, p. 119536.

MAVER, T. et al. (2018) Combining 3D printing and electrospinning for preparation of pain- relieving wound-dressing materials. *Journal of Sol-Gel Science and Technology*, 88, pp. 33–48.

MIGUEL, S.P. et al. (2019) Production and characterization of a novel asymmetric 3D printed construct aimed for skin tissue regeneration. *Colloids and Surfaces B: Biointerfaces*, 181(May), pp. 994–1003.

MIN, Z., SHICHANG, Z., et al. (2015) 3D-printed dimethyloxallyl glycine delivery scaffolds to improve angiogenesis and osteogenesis. *Biomaterials Science*, 3, pp. 1236–1244.

MIN, Z., KUN, L., et al. (2015) 3D-printed hierarchical scaffold for localized isoniazid/rifampin drug delivery and osteoarticular tuberculosis therapy. *Acta Biomaterialia*, 16, pp. 145–155.

MORONI, L. et al. (2006) Polymer hollow fiber three-dimensional matrices with controllable cavity and shell thickness. *Biomaterials*, 27, pp. 5918–5926.

MORONI, L., DE WIJN, J.R. and VAN BLITTERSWIJK, C.A. (2006) 3D fiber-deposited scaffolds for tissue engineering: Influence of pores geometry and architecture on dynamic mechanical properties. *Biomaterials*, 27, pp. 974–985.

MOTA, C., PUPPI, D., et al. (2015) Additive manufacturing techniques for the production of tissue engineering constructs. *Journal of Tissue Engineering and Regenerative Medicine*, 9(3), pp. 174–190.

MOTA, C., DANTI, S., et al. (2015) Multiscale fabrication of biomimetic scaffolds for tympanic membrane tissue engineering. *Biofabrication*, 7, pp. 1–21.

MÜLLER, W.E.G. et al. (2015) A new printable and durable N,O-carboxymethyl chitosan–Ca 2+ – polyphosphate complex with morphogenetic activity. *J. Mater. Chem. B*, 3(8), pp. 1722–1730.

NANDAKUMAR, A. et al. (2013) Monolithic and assembled polymer – ceramic composites for bone regeneration. *Acta Biomaterialia*, 9(3), pp. 5708–5717.

NARAYANAN, L.K. et al. (2016) 3D-Bioprinting of Polylactic Acid (PLA) Nanofiber−Alginate

Hydrogel Bioink Containing Human Adipose-Derived Stem Cells. *ACS Biomaterials Science and Engineering*, 2, pp. 1732–1742.

NEUFURTH, M. et al. (2014) Engineering a morphogenetically active hydrogel for bioprinting of bioartificial tissue derived from human osteoblast-like SaOS-2 cells. *Biomaterials*, 35(31), pp. 8810–9.

NEUFURTH, M. et al. (2015) Modular Small Diameter Vascular Grafts with Bioactive Functionalities. *PloS one*, pp. 1–24.

OZBOLAT, I.T. and HOSPODIUK, M. (2016) Current advances and future perspectives in extrusion-based bioprinting. *Biomaterials*, 76, pp. 321–343.

PARK, S. et al. (2009) 3D polycaprolactone scaffolds with controlled pore structure using a rapid prototyping system. *Journal of materials science. Materials in medicine*, 20, pp. 229–234.

PATI, F. et al. (2014) Printing three-dimensional tissue analogue with decellularized extracellular matrix bioink. *Nature Communications*, 5, pp. 1–11.

PEI, P. et al. (2016) Three-dimensional printing of tricalcium silicate/mesoporous bioactive glass cement scaffolds for bone regeneration. *Journal of Materials Chemistry B*, 4(46), pp. 7452–7463.

PING, J. et al. (2007) Bone ingrowth in porous titanium implants produced by 3D fiber deposition. *Biomaterials*, 28, pp. 2810–2820.

PING, J. et al. (2006) Porous Ti6Al4V scaffold directly fabricating by rapid prototyping: Preparation and in vitro experiment. *Biomaterials*, 27, pp. 1223–1235.

RAJARAM, A., SCHREYER, D. and CHEN, D. (2014) Bioplotting Alginate / Hyaluronic Acid Hydrogel Scaffolds with Structural Integrity and Preserved Schwann Cell Viability. *3D Printing*, 1, pp. 194–203.

RAJARAM, A., SCHREYER, D.J. and CHEN, D.X.B. (2015) Use of the polycation polyethyleneimine to improve the physical properties of alginate – hyaluronic acid hydrogel during fabrication of tissue repair scaffolds. *Journal of Biomaterials Science*, 26, pp. 433–445.

RÜCKER, M. et al. (2006) Angiogenic and inflammatory response to biodegradable scaffolds in dorsal skinfold chambers of mice. *Biomaterials*, 27, pp. 5027–5038.

RÜCKER, M. et al. (2008) Vascularization and biocompatibility of scaffolds consisting of different calcium phosphate compounds. *Journal of Biomedical Materials Research Part A*, 86(4), pp. 1002–1011.

RUSSO, T. et al. (2013) Systematic Analysis of Injectable Materials and 3D Rapid Prototyped Magnetic Scaffolds: From CNS Applications to Soft and Hard Tissue Repair/Regeneration.

Procedia Engineering, 59, pp. 233–239.

RUTZ, A.L. et al. (2015) A Multimaterial Bioink Method for 3D Printing Tunable, Cell-Compatible Hydrogels. *Advanced Materials*, 27, pp. 1607–1614.

SALINAS, A.J. and VALLET-REGÍ, M. (2016) Glasses in bone regeneration : A multiscale issue. *Journal of Non-Crystalline Solids*, 432, pp. 9–14.

SÁNCHEZ-SALCEDO, S. et al. (2013) Design and preparation of biocompatible zwitterionic hydroxyapatite. *Journal of Materials Chemistry B*, 1(11), p. 1595.

SANTIS, R. DE et al. (2011) A Basic Approach Toward the Development of Nanocomposite Magnetic Scaffolds for Advanced Bone Tissue Engineering. *Journal of Applied Polymer Science*, 122, pp. 3599–3605.

DE SANTIS, R. et al. (2013) Advanced Composites for Hard-Tissue Engineering Based on PCL/Organic–Inorganic Hybrid Fillers: From the Design of 2D Substrates to 3D Rapid Prototyped Scaffolds. *Polymer Composites*, 34(9), pp. 1417–1417.

SCHUMANN, P. et al. (2009) Consequences of seeded cell type on vascularization of tissue engineering constructs in vivo. *Microvascular Research*, 78(2), pp. 180–190.

SCHUMANN, P. et al. (2015) Decelerated vascularization in tissue-engineered constructs in association with diabetes mellitus in vivo. *Journal of Diabetes and Its Complications*, 29(7), pp. 855–864.

SCHUURMAN, W. et al. (2013) Gelatin-Methacrylamide Hydrogels as Potential Biomaterials for Fabrication of Tissue-Engineered Cartilage Constructs. *Macromolecular Bioscience*, 13(5), pp. 551–561.

SHI, L. et al. (2018) Three-Dimensional Printing Alginate / Gelatin Scaffolds as Dermal Substitutes for Skin Tissue Engineering. *Polymer Engineering and Science*, 10(58), pp. 1782–1790.

SHIRAZI, S.F.S. et al. (2015) A review on powder-based additive manufacturing for tissue engineering: selective laser sintering and inkjet 3D printing. *Science and Technology of Advanced Materials*, 16(3), p. 033502.

SHRUTI, S. et al. (2013) Mesoporous bioactive scaffolds prepared with cerium-, gallium- and zinc-containing glasses. *Acta biomaterialia*, 9(1), pp. 4836–44.

SILVA, N.A. et al. (2013) Benefits of Spine Stabilization with Biodegradable Scaffolds in Spinal Cord Injured Rats. *Tissue Engineering - Part C: Methods*, 19(2), pp. 101–108.

SILVA, N.A. et al. (2010) Development and Characterization of a Novel Hybrid Tissue Engineering – Based Scaffold for Spinal Cord Injury Repair. *Tissue Engineering - Part A*, 16(1), pp. 45–54.

SILVA, N.A. et al. (2011) Interactions between Schwann and olfactory ensheathing cells with a

starch/polycaprolactone scaffold aimed at spinal cord injury repair. *Journal of Biomedical Materials Research Part A*, 100A, pp. 470–476.

SINGH, S. et al. (2020) In situ bioprinting – Bioprinting from benchside to bedside? *Acta Biomaterialia*, 101, pp. 14–25.

SOBRAL, J.M. et al. (2011) Three-dimensional plotted scaffolds with controlled pore size gradients: Effect of scaffold geometry on mechanical performance and cell seeding efficiency. *Acta Biomaterialia*, 7, pp. 1009–1018.

SON, J. and KIM, G. (2009) Three-Dimensional Plotter Technology for Fabricating Polymeric Scaffolds with Micro- grooved Surfaces Three-Dimensional Plotter Technology for Fabricating Polymeric Scaffolds with Micro-grooved Surfaces. *Journal of Biomaterials Science*, 20, pp. 2089–2101.

SONG, B.R. et al. (2015) Three dimensional plotted extracellular matrix scaffolds using a rapid prototyping for tissue engineering application. *Tissue Engineering and Regenerative Medicine*, 12(3), pp. 172–180.

SUN, Y. et al. (2012) Degradable amorphous scaffolds with enhanced mechanical properties and homogeneous cell distribution produced by a three-dimensional fiber deposition method. *Journal of Biomedical Materials Research Part A*, 100A, pp. 2739–2749.

TARAFDER, S. et al. (2016) Micro-precise spatiotemporal delivery system embedded in 3D printing for complex tissue regeneration. *Biofabrication*, 8(2), p. 25003.

TAVASSOL, F. et al. (2010) Accelerated angiogenic host tissue response to poly (L-lactide-co-glycolide) scaffolds by vitalization with osteoblast-like cells. *Tissue Engineering - Part A*, 16(7), pp. 2265–2279.

The Williams Dictionary of Biomaterials:. (1999) Liverpool University Press.

There's Only One 3D-Bioplotter®. (2017) [Online] EnvisionTec. Available from : http://envisiontec.com/3d-printers/3d-bioplotter/.

VILA, M. et al. (2016) 3D silicon doped hydroxyapatite scaffolds decorated with Elastin-like Recombinamers for bone regenerative medicine. *Acta Biomaterialia*, 45, pp. 349–356.

WAGNER, M. et al. (2007) Comparative in vitro study of the cell proliferation of ovine and human osteoblast-like cells on conventionally and rapid prototyping produced scaffolds tailored for application as potential bone replacement material. *Journal of Biomedical Materials Research Part A*, pp. 1154–1164.

WANG, M.-D. et al. (2013) Novel crosslinked alginate/hyaluronic acid hydrogels for nerve tissue engineering. *Frontiers of Materials Science*, 7(3), pp. 269–284.

WANG, S. et al. (2019) Three Dimensional Printing Bilayer Membrane Scaffold Promotes Wound Healing. *Frontiers in Bioengineering and Biotechnology*, 7, pp. 1–11.

WANG, X. et al. (2014) Effect of bioglass on growth and biomineralization of SaOS-2 cells in hydrogel after 3D cell bioprinting. *PloS one*, 9(11), p. e112497.

WHANG, K. et al. (1999) Engineering Bone Regeneration with Bioabsorbable Scaffolds with Novel Microarchitecture. *Tissue Engineering*, 5(1), pp. 35–51.

WON, J. et al. (2019) A potential dermal substitute using decellularized dermis extracellular matrix derived bio-ink. *Artificial Cells, Nanomedicine, and Biotechnology*, 47(1), pp. 644–649.

WÜST, S. et al. (2014) Tunable hydrogel composite with two-step processing in combination with innovative hardware upgrade for cell-based three-dimensional bioprinting. *Acta Biomaterialia*, 10, pp. 630–640.

XIONG, S. et al. (2017) A Gelatin-sulfonated Silk Composite Scaffold based on 3D Printing Technology Enhances Skin Regeneration by Stimulating Epidermal Growth and Dermal Neovascularization. *Scientific Reports*, 7, p. 4288.

XIONG, Z. et al. (2001) Fabrication of porous poly(L-lactic acid) scaffolds for bone tissue engineering via precise extrusion. *Scripta Materialia*, 45, pp. 773–779.

XU, C. et al. (2018) 3D printing of nanocellulose hydrogel scaffolds with tunable mechanical strength towards wound healing application. *Journal of Materials Chemistry B*, 6, pp. 7066–7075.

XU, W. et al. (2019) On Low-Concentration Inks Formulated by Nanocellulose Assisted with Gelatin Methacrylate (GelMA) for 3D Printing toward Wound Healing Application. *ACS Applied Materials & Interfaces*, 11, pp. 8838–8848.

YANG, S. et al. (2002) The Design of Scaffolds for Use in Tissue Engineering. Part II. Rapid Prototyping Techniques. *Tissue Engineering*, 8(1), pp. 1–11.

YILGOR, P. et al. (2008) 3D Plotted PCL Scaffolds for Stem Cell Based Bone Tissue Engineering. *Macromolecular Symposia*, 269, pp. 92–99.

YILGOR, P. et al. (2010) Effect of scaffold architecture and BMP-2/BMP-7 delivery on in vitro bone regeneration. *Journal of materials science. Materials in medicine*, 21, pp. 2999–3008.

YOON, H. et al. (2016) Development of cell-laden 3D scaffolds for efficient engineered skin substitutes by collagen gelation. *RSC Advances*, 6, pp. 21439–21447.

YOON, H., KIM, G.H. and KOH, Y.H. (2015) A Micro-Scale Surface-Structured PCL Scaffold Fabricated by a 3D Plotter and a Chemical Blowing Agent. *Journal of Biomaterials Science*, 21, pp. 159–170.

YUAN, J. et al. (2015) The preliminary performance study of the 3D printing of a tricalcium phosphate scaffold for the loading of sustained release anti-tuberculosis drugs. *Journal of Materials Science*, 50, pp. 2138–2147.

ZEIN, I. et al. (2002) Fused deposition modeling of novel scaffold architectures for tissue engineering applications. *Biomaterials*, 23(4), pp. 1169–1185.

ZHANG, J., ZHAO, S., ZHU, M., et al. (2014) 3D-printed magnetic Fe3O4/MBG/PCL composite scaffolds with multifunctionality of bone regeneration, local anticancer drug delivery and hyperthermia. *J. Mater. Chem. B*, 2(43), pp. 7583–7595.

ZHANG, J., ZHAO, S., ZHU, Y., et al. (2014) Three-dimensional printing of strontium-containing mesoporous bioactive glass scaffolds for bone regeneration. *Acta Biomaterialia*, 10, pp. 2269–81.

ZHAO, S. et al. (2015) Three-dimensional printed strontium-containing mesoporous bioactive glass scaffolds for repairing rat critical-sized calvarial defects. *Acta biomaterialia*, 12, pp. 270–80.

ZHU, M. et al. (2016) Three-dimensional printing of cerium-incorporated mesoporous calcium-silicate scaffolds for bone repair. *Journal of Materials Science*, 51, pp. 836–844.

CHAPTER 3: EFFECT OF COMPOSITION ON THE PHYSICOCHEMICAL AND BIOLOGICAL PROPERTIES OF POLYPEPTIDE-BASED HYDROGELS FOR POTENTIAL APPLICATION IN WOUND HEALING

3.1 INTRODUCTION

The intricate process of wound healing is well-understood (Singer and Clark, 1999; Werner and Grose, 2003; Broughton, Janis and Attinger, 2006; Barrientos et al., 2008), and multiple strategies to treating wounds currently exist (Boateng et al., 2008; Shahrokhi, Arno and Jeschke, 2014; Stone et al., 2018). However, the search for the ideal treatment continues. The ideal treatment should provide a combination of rapid wound closure, control over infections, prompt pain relief, minimal inconvenience to the patient, and minimal scarring, while maintaining low treatment costs and risks (Selig et al., 2012). Advanced treatments, such as bioactive dressings and skin substitutes aim to achieve these criteria by mimicking the native skin and actively partaking in the wound healing process (Zarrintaj et al., 2017; Koehler, Brandl and Goepferich, 2018; Stone et al., 2018; Haddad et al., 2018). Hydrogel wound dressings are particularly interesting (Koehler, Brandl and Goepferich, 2018). Due to their ability to absorb 30 – 100% water (Jhon and Andrade, 1973), they can maintain a moist wound environment favourable to the wound healing process. The similarities between hydrogels and the macromolecular components of the extracellular matrix (ECM) have also long been recognised (Jhon and Andrade, 1973; Lee and Mooney, 2001). Their highly porous hydrated matrix gives them the ability to support the incorporation of cells as well as active components such as drugs and biological molecules (El-sherbiny and Yacoub, 2013; Koehler, Brandl and Goepferich, 2018).

Polypeptide-based hydrogels have gained particular interest in biomedical applications (Lu et al., 2014; Zhou and Li, 2018). This has mainly been ascribed to their inherent biological properties and widely tuneable physicochemical properties (Zhou and Li, 2018). Compared to naturally derived materials, which typically suffer from batch-to-batch variation and difficult extraction methods, polypeptides can be synthetically produced with controlled chemical and physical properties (Lee and Mooney, 2001). Controlled ring-opening polymerisation (ROP) is a widely reviewed technique used to produce polypeptides with controlled molecular weight and molecular weight distribution; and advanced architectures from *N*-carboxy anhydride (NCA) amino acids (González-Henríquez, Sarabia-Vallejos and Rodríguez-Hernández, 2017; Penczek, 2018). The use of natural- and synthetic amino acids allow the incorporation of biocompatibility, biodegradability, chemical functionality and specialised functionalities, like antimicrobial properties into polypeptides (Deng et al., 2014; Li et al., 2018). Polypeptides have been formed into functional hydrogels through a variety of physical or covalent crosslinking (Zhou and Li, 2018). The assembly of polypeptides into hierarchical and supramolecular structures drive the gelation of physical polypeptide-based hydrogels (Nowak et al.,

2002; Deming, 2005; Zhou and Li, 2018). The functional moieties on the side-chains of polypeptides also allow covalent crosslinking through a variety of chemical reactions (Zhou and Li, 2018).

Recently, a number of researchers have investigated the tissue engineering and wound healing potential of hydrogels composed of the well-known polypeptide, poly (L-lysine) (PLL) and its copolymers. PLL is commonly used as a coating due to its cell-adhesive properties. Contrary to PLL in its free polymer form, which is known to be cytotoxic to mammalian cells (Fischer et al., 2003; Kadlecova et al., 2012), PLL-based hydrogel networks have shown decreased cytotoxicity and even good biocompatibility (Pakstis et al., 2004). The free amines on the L-lysine side chains afford easy modification and chemical crosslinking into hydrogel networks. The biocompatibility of such hydrogels is dependent on several factors. Hynes et al. (2008) demonstrated the effect of the molecular weight of PLL and the amine content of the hydrogel on the proliferation and differentiation of neuronal stem cells. Pakstis et al. (2004) reported on the role of the morphology of the self-assembled polypeptide in the hydrogel compared to its free morphology in solution. Song, Rane and Christman (2012) also reported on the effect of the cationic to hydrophobic ratio of poly(Lys_x-*ran*-Ala_y) random copolymers crosslinked with multi-arm PEG into hydrogels. The hydrogels composed of poly(Lys_{60}-*ran*-Ala_{40}) showed good fibroblast cell adhesion and proliferation, as well as antibacterial activity. Fibroblast adhesion to scaffolds intended for wound regeneration is considered a desirable property, due to the role of fibroblasts in the natural wound healing process (Levinson, 2013; Darby et al., 2014). This includes their role in the secretion of cytokines, the production of extracellular matrix, and the contraction of the wound area (Broughton, Janis and Attinger, 2006). The physical properties of hydrogels such as porosity, swelling, mechanical properties, and biodegradability also play an important role in the potential tissue engineering applications (Lee and Mooney, 2001; Ambekar and Kandasubramanian, 2019). It is further known that there is a complicated interplay between the physicochemical and biofunctional properties of hydrogels and finding the ideal combination of these properties is desirable.

In this study, we investigated the effect of crosslinking and concentration on the properties of a new library of low concentration hydrogels composed of poly(Lys_{60}-*ran*-Ala_{40}) and multi-arm PEG. These covalently crosslinked hydrogels were produced through the reaction of primary amines from the polypeptide with *N*-hydroxysuccinimide (NHS) esters from functionalised multi-arm PEG. The reaction between primary amines and NHS esters is a well-known acylation reaction, where an amide is produced with the release of an NHS leaving group. In bioconjugation reactions, NHS esters are widely used to react with the α-amines at the *N*-terminus of proteins and peptides, and with the ε-amines of lysine side chains (Hermanson, 2013). The aim was to correlate the hydrogel composition with the desired physicochemical and biofunctional properties, to expand the assortment of PLL-based hydrogels suitable for wound healing. By controlling the synthesis of the polypeptide, using a facile method of controlled ROP, we were able to target the lysine to alanine ratio (K: A), molecular

weight, and a narrow molecular weight distribution. This allowed carefully controlling the degree of crosslinking using stoichiometric ratios of the functional groups of the polypeptide and the multi-arm PEG while maintaining low total polymer concentrations.

3.2 MATERIALS AND METHODS

3.2.1 Materials and general methods

All chemicals and solvents were purchased from commercial sources and used without further purification unless stated otherwise. Dry solvents were used as received and handled under dry inert gas. Fmoc-L-Lys(Boc)-OH, L-alanine, triphosgene, benzylamine, α-pinene, and trifluoroacetic acid (TFA) were purchased from Sigma Aldrich (St. Louise, MO, USA). 4-Arm PEG-succinimidyl glutarate (4-PEG-SG) (10 kDa) was procured from JenKem Technology (WA, US). SnakeSkin® Pleated dialysis tubing, (3500 MWCO) was purchased from Thermo Fischer Scientific. Moisture- and oxygen-sensitive reactions were carried out under an inert atmosphere using dry nitrogen (N_2) gas. All compounds were characterised by ^{1}H NMR spectroscopy using a Varian VXR-Unity (300 MHz or 400 MHz) spectrometer. Samples were dissolved in deuterated solvents. Chemical shifts are reported in parts per million (ppm), where tetramethylsilane (TMS) is used as internal reference. Splitting patterns were designated as s (singlet), d (doublet), t (triplet), q (quartet) and m (multiplet), whereas coupling constants (J) was reported in Hertz (Hz). Fourier transform infrared (FTIR) spectrometry was performed on a Spectrum 100 FT-IR Spectrometer (PerkinElmer, MA, US) fitted with a Universal ATR Sampling Accessory. Size exclusion chromatography (SEC) was measured on a system equipped with a Shimadzu LC-10AT isocratic pump, a Waters 717+ autosampler, a column system fitted with a PSS guard column (50 × 8 mm) in series with three PSS GRAM columns (300 × 8 mm, 10 µm, 2 × 3000 Å and 1 × 100Å) kept at 40 °C, a Waters 2487 dual wavelength UV detector, and a Waters 2414 differential refractive index (DRI) detector. *N*,*N*-Dimethylformamide (DMF) was used as the eluent, stabilized with 0.05% BHT (w/v) and 0.03 % LiCl (w/v), at a flow rate of 1 $mL \cdot min^{-1}$. Prior to analysis, polymer samples were filtered through 0.45 µm GHP filters. The molar masses of polymers were calculated against poly(methyl methacrylate) (PMMA) standards (Polymer Laboratories) ranging from 690 to 1.2×10^6 $g \cdot mol^{-1}$.

3.2.2 Synthetic Procedures

3.2.2.1 N_ε-tert-butyloxycarbonyl L-lysine (H-Lys(Boc)-OH)

H-Lys(Boc)-OH was prepared via the deprotection of Fmoc-Lys(Boc)-OH using a modification of a procedure described in literature (Höck et al., 2010). Fmoc-Lys(Boc)-OH (10.0 g, 21.3 mmol) was dissolved in DMSO (40 mL) and heated to 120 °C under reflux. The reaction mixture was stirred for 1 h, while a white precipitate formed. The product was isolated by precipitation in diethyl ether. Repeated washing with diethyl ether and vacuum drying afforded H-Lys(Boc)-OH as a white powder.

^{1}H NMR (300 MHz, DMSO) δ 6.75 (s, 1H), 3.07 (t, *J* = 6.10 Hz, 1H), 2.97-2.76 (q, 6.74, 2H), 1.75-1.44 (m, 2H), 1.44-1.15 (m, 13H)

3.2.2.2 Synthesis of N-carboxyanhydride (NCA) of N_ε-tert-butyloxycarbonyl L-lysine (NCA-Lys(Boc))

H-Lys(Boc)-OH (5.00 g, 20.3 mmol) and α-pinene (7.41 g, 54.4 mmol) were dissolved in dry THF (60 mL) in a 250 mL 3-neck round bottom flask. The solution was heated under inert reflux conditions. Triphosgene (2.76 g, 9.3 mmol) was dissolved in dry THF (24 mL) and added dropwise to the reaction mixture once reflux started. The solution became clear during the addition of triphosgene and then started forming a white precipitate byproduct. After 1 h, the reaction mixture was cooled and the precipitate removed by filtration. The mother liquor was reduced to a quarter of the volume. 20 mL *n*-heptane was added and the solution was heated to recrystallize. The pure product was obtained by repeated recrystallizations from *n*-heptane and THF (58 % yield). The product was then dried under vacuum and stored in a freezer under P_2O_5 and N_2 gas. ^{1}H NMR (500 MHz, DMSO-d_6) δ 9.08 (s, 1H), 6.78 (s, 1H), 4.43 (t, *J* = 6.0 Hz, 1H), 2.90 (q, *J* = 6.4 Hz, 2H), 1.92 – 1.56 (m, 2H), 1.47 -1.20 (m, 13H).

3.2.2.3 Synthesis of N-carboxyanhydride (NCA) of L-alanine (NCA-Ala)

L-Alanine (5.00 g, 56.1 mmol) and α-pinene (17.58 g, 129 mmol) were dissolved in dry THF (60 mL) in a 250 mL 3-neck round bottom flask. The solution was heated under inert reflux conditions. Triphosgene (11.16 g, 37.6 mmol) was dissolved in dry THF (24 mL) and added dropwise to the reaction mixture once reflux started. After 3 h, all solids disappeared and the solution was clear. The solution was reduced to a quarter of the volume and the same purification was followed as for NCA-Lys(Boc) (50 %). ^{1}H NMR (500 MHz, DMSO-d_6) δ 8.98 (s, 1H), 4.48 (q, *J* = 7.0 Hz, 1H), 1.33 (d, *J* = 7.1 Hz, 2H).

3.2.2.4 Random NCA Copolymerization

The targeted degree of polymerisation (DP) was 100, with a monomer ratio of NCA-Lys(Boc) to NCA-Ala of 0.6: 0.4. The polymerisation was performed as follows: NCA-Lys(Boc) (2.00 g, 7.34 mmol), NCA-Ala (0.56 g, 4.89 mmol) and dry DMF (15 mL) were added to a Schlenk tube. The monomer solution was then subjected to four repeated freeze-pump-thaw cycles. In a separate vial, benzylamine (0.013 g, 0.12 mmol) and dry DMF (2.5 mL) were sparged with N_2 gas. The benzylamine initiator solution was then added to the monomer solution under inert conditions. The final reaction mixture was cooled to 0 °C and placed under vacuum conditions. The reaction proceeded for 96 h at 0 °C. The protected polypeptide was isolated by precipitation from diethyl ether.

3.2.2.5 Deprotection of Polypeptides

Deprotection of the polypeptide was performed using TFA according to literature procedures. The protected polypeptide (1.00 g) was dissolved in TFA (5.00 g) and stirred for 2 hours. The polypeptide, poly(Lys_x-*ran*-Ala_y) was then precipitated in diethyl ether. Repeated washing with diethyl ether afforded a powdery white product. This was further purified via dialysis, using a 3.5 kDA MWCO Snakeskin, against distilled water changed twice daily for three days.

3.2.3 Preparation of polypeptide-based hydrogels

The polypeptide-based hydrogels were prepared with the synthesised polypeptide, **entry #2** in Table 3.2 (further referred to as P(KA) for simplicity), crosslinked with 4-PEG-SG. Different molar ratios of the free amines from P(KA) to the NHS esters from 4-PEG-SG (1:1, 2:1, 4:1, 8:1, and 16:1) and different polymer concentrations (1 wt%, 2 wt%, 4 wt%, 6 wt% and 8 wt%) were used. Solutions of P(KA) and 4-PEG-SG were prepared in phosphate buffers of pH 9 and pH 4, respectively. Equal volumes of each were then added together to make the precursor hydrogel solution with a pH of ~7. While the deprotonation of amines at higher pH will increase their reactivity, the hydrolysis of NHS esters also significantly increases at higher pH. Therefore, reactions between NHS esters and amines are typically performed under physiological conditions, where the hydrolysis rate of NHS esters and the reactivity of the amines are optimal. The precursor hydrogel solution was then allowed to gel over time.

Table 3.1. A summary of the polymer concentrations of the P(KA) and 4-PEG-SG used in the preparation of the library of hydrogel solutions to achieve the total polymer concentrations of 1 wt%, 2 wt%, 4 wt%, 6 wt%, and 8 wt%

Total Polymer Concentration	Molar Ratio									
	1:1		2:1		4:1		8:1		16:1	
	P(KA)	4-PEG	P(KA)	4-PEG	P(KA)	4-PEG	P(KA)	4-PEG	P(KA)	4-PEG
1 wt%	0.16	0.84	0.28	0.72	0.44	0.57	0.61	0.39	0.76	0.24
2 wt%	0.32	1.68	0.56	1.44	0.87	1.13	1.21	0.79	1.51	0.49
4 wt%	0.65	3.36	1.11	2.89	1.74	2.26	2.42	1.58	3.02	0.98
6 wt%	0.97	5.03	1.67	4.33	2.61	3.39	3.64	2.36	4.53	1.47
8 wt%	1.29	6.71	2.22	5.78	3.48	4.52	4.85	3.15	6.04	1.96

3.2.4 Hydrogel Characterisation

3.2.4.1 Gelation and Rheometry

The precursor hydrogel solutions (0.5 mL) were prepared in glass vials. After different time intervals, the vials were inverted to determine qualitatively if it was a solution or gel phase. Gels were also manipulated with a spatula and if it could be spread on the glass vial wall, the gel was designated "soft/gel-like". If the gel retained its shape, it was designated "hydrogel".

The gelation of selected hydrogel solutions was further investigated using a Thermo Scientific™ HAAKE™ MARS™ Rheometer, with a 35 mm cone plate with a 1 ° incline and a 0.052 mm gap distance fitted with a HAAKE™ Universal Temperature Controller. 0.2 mL of the precursor hydrogel solutions was added to the rheometer plate and allowed to gel. For time sweep experiments, the evolution of the storage modulus (G') and the loss modulus (G'') from t_0 was measured. A constant shear rate of 10 Pa at a frequency of 1 Hz was used to measure G' and G'' over a time of 1500 s.

For subsequent tests, gels were allowed to reach equilibrium. The time to equilibrium was determined from the time sweep and was implemented as a waiting time. Amplitude sweeps were performed to ensure that the moduli are recorded within the linear viscoelastic regime (LVE) (Zuidema et al., 2014). For amplitude sweeps, τ was increased from 0.01 Pa to 1000 Pa at a constant frequency of 1 Hz, while for frequency sweeps, the frequency was increased from 0.01 Hz to 100 Hz at a constant τ of 10 Pa.

3.2.4.2 Amine quantification

The amount of free amines present in the hydrogels were determined using a Kaiser assay against a standard concentration curve of H-Lys(Boc)-OH. This colourimetric assay is well-known for the quantification of amino acids, peptides and proteins (Friedman, 2004). It makes use of the formation of a purple dye complex, also known as Ruhemann's purple when ninhydrin reacts with primary amines. The formation of the Rhumann's purple complex allowed colourimetric quantification of the amines even though the hydrogels are insoluble (Kendall, 1963). However, longer incubation times were necessary to release the purple complex from the hydrogel to the surrounding solution. The amount of free amines was quantified from UV/vis spectroscopy using a standard curve of H-Lys(Boc)-OH. The concentration of free amines was calculated based on the weights of freeze-dried hydrogels. A ninhydrin solution containing equal volumes of each component in a Kaiser Kit (Sigma Aldrich, St. Louise, MO, USA), was freshly prepared and used immediately. Freeze-dried samples of hydrogels were suspended in 1 mL of the prepared ninhydrin solution in test tubes. The test tubes were closed with aluminium foil and parafilm and incubated for 30 min at 80 °C. The test tubes were then left to cool to room temperature and 4 mL ethanol was added. The solutions were then filtered through 0.45 μm PVDF syringe filters. The UV absorbance was then measured at 570 nm on a UV spectrophotometer using a quartz cuvette with 10 mm path length.

3.2.4.3 Pore morphology

The pore sizes were analysed using scanning electron microscopy (SEM). Hydrogel samples were washed and swollen in deionised water to remove residual phosphate buffer salts that were introduced during the hydrogel preparation. The swollen samples were frozen at -80 °C overnight, and lyophilised. Vertical cuts of the dried samples were made. The dried samples were mounted on stubs with the cross-section plane facing upwards. Samples were then coated with gold (Au) using an SPI™

Sputter Coater. SEM Micrographs of the pores were taken using a FEI™ Phenom™ Desktop SEM (Thermo Fisher Scientific, MA, USA). The images were analysed using FIJI (v. 1.51n, ImageJ, URL: https://imagej.net/Fiji) (Schindelin et al., 2012) and the size distributions calculated using 40 to 60 measurements from 3 or more images with size distributions approximating normal distributions

3.2.4.4 Swelling behaviour

The equilibrium swelling ratio (ESR) of the library of hydrogels was investigated in their "as is" and "freeze-dried" form, respectively. For the "as is" ESR, the hydrogel samples were prepared as described under section 3.2.4.1 "Gelation and Rheometry" and swollen in PBS. The swollen hydrogel was placed on filter paper to remove excess water and weighed. The weight was recorded over time until it remained constant. The final weight was then recorded as the wet weight, W_W. The swollen hydrogel was then washed with deionised water to remove the residual PBS buffer salts, frozen at -80 °C overnight, and lyophilised. The weight of the sample was then recorded as the dry weight, W_D. For the "freeze-dried" ESR, the hydrogel samples were washed in deionised water, frozen at -80 °C and lyophilised. The weight of the dry samples was recorded as W_D. The samples were then swollen in PBS until the weight remained constant and the final weight was recorded as W_W.

The ESR for the "as is" and "freeze-dried" samples calculated using the following equation:

$$ESR = \frac{(W_W - W_D)}{W_D} \quad \text{Eq. 3.1}$$

3.2.4.5 Degradation time

Hydrolytic degradation of the freeze-dried hydrogels was performed in PBS (pH 7.2) at 37 °C at constant agitation from an orbital shaker and daily PBS solvent changes. Over 28 days, the wet weight of the hydrogels was taken after drying the excess PBS on filter paper. If the hydrogel was visibly disintegrated, no weight was recorded and the time recorded as the degradation time in days.

3.2.5 *In vitro* cell studies

Cytotoxicity and cell adhesion was tested on NIH 3T3 mouse fibroblast cells, using 4 wt% P(KA)/4-PEG hydrogels with molar ratios of 1:1 to 16:1.

3.2.5.1 Cytotoxicity

Hydrogel discs were prepared by placing 20 µL of the precursor hydrogel solutions between a microscope slide and cover slip, along with a 1 mm spacer and allowed to gel for 1 hour. The hydrogels were prepared under sterile conditions, washed with PBS (pH 7.2), and swollen in fresh media overnight. Prior to the cytotoxicity study, 100 µL cells in fresh medium (7500 cells/well) were added to 96 well plates and incubated for 24 h with 5% CO_2 at 37 °C. The media covering the cells were then replaced with fresh media and the hydrogel disks that were swollen in media were added

onto the seeded cell layers. The control groups contained the cell layers with no hydrogel disks. In the positive control group, only fresh medium were added to the cells, while in the negative control group, the cells were treated with fresh medium and 50 μL DMSO. The cytotoxicity of the hydrogels was then determined using an MTT assay, after 24 h incubation with 5% CO_2 at 37 °C. Viable cells metabolize MTT into purple formazan crystals, which can be solubilized and the concentration quantitatively measured using UV spectroscopy. The cytotoxicity is therefore indirectly determined based on the number of metabolically active cells in reference to control groups. For the MTT assay, the hydrogel disks were carefully removed, without disturbing the cell layer and 20 μL of the MTT solution was added to each well and incubated for 4 hours. The media in each well was then aspirated, 100 μL DMSO was added to dissolve the formazan crystals, and the plate placed on an orbital shaker for 40 min. The supernatant from each well was then transferred to a clean plate and the absorbance measured at 570 nm (absorbance maximum of formazan) and 620 nm (reference absorbance) on a Victor™ X3 2030 Multilabel Reader (PerkinElmer, MA, US). The measurements were recorded from samples prepared in triplicate from two independent experiments. The percentage viable cells were calculated using the following formula:

$$\%\ viable\ cells = \frac{abs_{sample} - abs_{ref}}{abs_{control} - abs_{ref}} \times 100 \qquad \text{Eq. 3.2}$$

3.2.5.2 Cell adhesion

70 μL of the precursor hydrogel solutions were added to the 96 well plate and allowed to gel for 1 hour. Hydrogels were then washed with PBS (pH 7.2) and swollen in fresh media overnight. 100 μL NIH 3T3 cells in fresh medium (7500 cells/well) were added onto the surface of the prepared hydrogels. The control groups contained no hydrogels. In the positive control group, 100 μL cells were added to the 96 well plate, while the negative control group, contained 100 μL cells and 50 μL DMSO. The cell adhesion was then assessed after 48 h incubation at 37 °C with 5% CO_2. The cellular adhesion was qualitatively evaluated using a CKX53 light microscope (Olympus, Tokyo, Japan).

3.2.6 Antibacterial analysis

3.2.6.1 Agar Disk Diffusion Assay

The antibacterial properties of the 4 wt% P(KA)/4-PEG hydrogels with molar ratios of 1:1 to 8:1 were analysed against *S. aureus* (29523) and *P. aeruginosa* (27853) bacterial species using the agar disk diffusion method (Balouiri, Sadiki and Ibnsouda, 2016). The disk-diffusion method is based on the diffusion of the active component into the surrounding agar, which then causes a growth inhibitory zone around the disk containing the antibacterial agent.Hydrogel disks were prepared according to the procedure described under section "3.2.5.1 Cytotoxicity" and placed on agar plates spread with 100 μL of the respective bacterial cultures in trypsin soy broth (TSB) using McFarland standard dilutions.

Ciprofloxacin disks were used as a positive control for antibacterial properties. The plates were then incubated at 37 °C. After 24 h, inhibition zones surrounding the disks were inspected.

3.2.6.2 Broth Dilution Assay

100 µL of the precursor hydrogel solutions (4 wt%; 1:1, 2:1, 4:1, 8:1 and 16:1 molar ratios) were added to a 96 well plate and allowed to gel for 1 hour. Hydrogels were then sterilized by UV irradiation (256 nm wavelength) for 10 min and washed with PBS. 100 µL of the respective bacterial cultures in TSB using McFarland standard dilutions were added onto the hydrogels. For the positive control, 100 µL Ciprofloxacin (0.01 mM) solution was added to 100 µL of the bacterial cultures. For the negative control, 100 µL TSB was added to 100 µL bacterial cultures. The plates were then incubated at 37 °C for 24 h. For optical density (OD) readings, the supernatant was transferred to clean well plates and the OD measured at 690 nm using a Victor™ X3 2030 Multilabel Reader from PerkinElmer. Colony-forming units (CFU) were counted from spread plates of serial dilutions.

3.2.7 Statistical Evaluation

Results were reported as mean ± standard deviation and normal distribution was assumed. One-way analysis of variance (ANOVA) and student's *t*-test were used for comparison between groups. A value of $p < 0.05$ was considered statistically significant.

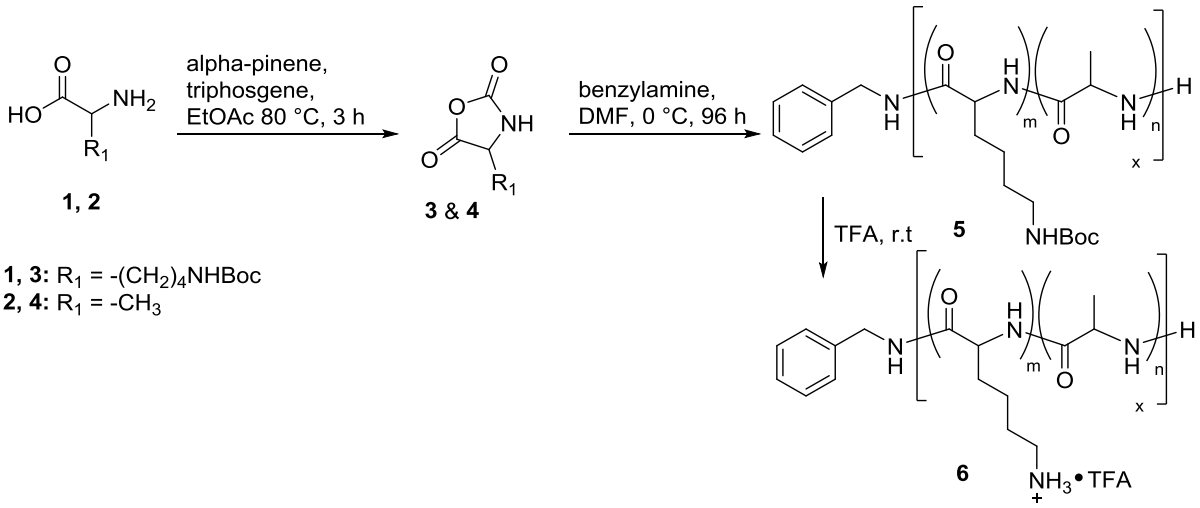
3.3 RESULTS AND DISCUSSION

3.3.1 Preparation of Controlled Polypeptides

The NCA monomers, NCA-Lys(Boc) and NCA-Ala was produced according to literature procedures where triphosgene is used with α-pinene as HCl scavenger (Scheme 1) (Habraken et al., 2010). Recrystallization produced the NCA monomers in high purity. Removal of impurities such as *N*-chloroformyl amino acid chlorides and α-isocyanato acid chlorides was carefully considered since they are known to influence the ability to control the subsequent ROP (Aliferis, Iatrou and Hadjichristidis, 2004; Penczek, 2018).

The synthesis of the polypeptide copolymer, poly(Lys_m-*ran*-Ala_n), was controlled using literature procedures, where benzylamine was used as initiator at 0 °C (Scheme 3.1) (Dmitrovic et al., 2012). Control over any living chain-growth polymerization, also just referred to as living polymerization, requires initiation primarily from the propagating chain, while transfer and termination reactions remain absent (Jenkins et al., 1996). NCA ROP is conventionally initiated via nucleophiles such as primary amines. These polymerizations are however highly susceptible to side reactions and termination reactions and are therefore difficult to control (González-Henríquez, Sarabia-Vallejos and Rodríguez-Hernández, 2017; Penczek, 2018). Strategies to control NCA ROP initiated with primary amines include the use of high purity chemicals and vacuum techniques (Aliferis, Iatrou and Hadjichristidis, 2004). It was also reported that low reaction temperatures could reduce the side

reactions and afford living polymers suitable for advanced copolymer synthesis (Vayaboury et al., 2004; Habraken et al., 2010; Habraken et al., 2011; Dmitrovic et al., 2012). This eliminates the need for specialised polymerisation techniques using transition metal catalysts, organocatalytic systems, ammonium halide initiators and silazane mediators (González-Henríquez, Sarabia-Vallejos and Rodríguez-Hernández, 2017).



Scheme 3.1 Synthesis of NCA amino acids and copolymerization via ROP

Table 3.2 Polypeptide synthesized by ROP of NCA amino acids

Entry	DP_{exp} [a]	K: A ratio[a]	$M_{n\ Target}$ (g·mol^{-1})	$M_{n\ NMR}$ (g·mol^{-1})	$M_{n\ SEC}$ (g·mol^{-1}) [b]	Đ [b]	Free Amine (µmol·mg^{-1})
#1	79	0.63 : 0.37	18342	14862	20928	1.33	2.55±0.14
#2	96	0.60 : 0.40	18342	17608	26933	1.18	2.02±0.11

[a] Degree of polymerization (DP) and K: A ratio determined from ^{1}H NMR spectroscopy
[b] Number average molecular weight (M_n) and dispersity ($Đ$) determined from SEC using PMMA as standard

Since no further chain-extension after the initial polymerization was required, it was adequate to assess the number average molar mass (M_n), and dispersity ($Đ$) as a measure of the control over the polymerization. The expected M_n determined from conversion was not possible from ^{1}H NMR spectroscopy due to overlapping between monomer and polymer signals. Instead, the targeted M_n was correlated against the experimental M_n determined from ^{1}H NMR spectroscopy and SEC (Table 3.2). From ^{1}H NMR spectroscopy, the experimental $M_{n,\ NMR}$ was calculated using Eq. 3.3,

$$M_{n,\ NMR} = DP_{NMR}(x_K M_K + x_A M_A) + M_I \qquad \text{(Eq. 3.3)}$$

where x_K and x_A is the respective molar fractions of H-Lys(Boc)-OH and L-alanine, and M_K, M_A and M_I is the molar masses of H-Lys(Boc)-OH, L-alanine and benzylamine respectively. Figure 3.1 gives the ^{1}H NMR spectrum of a typical poly(Lys(Boc)$_x$-*ran*-Ala$_y$) copolymer. The DP was determined from the ratio between the integrated benzyl chain end signal at **i**, and the integrated polypeptide

backbone signal at **a,b** on Figure 3.1. It should be noted that this calculation of DP is based on the assumption that all chains were initiated by benzylamine. The lower DP from **entry #1** compared to **entry #2** could be due to differences in the polymerization rate or loss of control over the polymerization. Based on the higher *Đ* obtained for **entry #1** compared to **entry #2**, it is evident that slightly less control over the polymerization of **entry #1** was obtained. Loss of control can be from initiation from moisture traces and from side reactions that can take place during the polymerization of NCA monomers (Habraken et al., 2010). The discrepancy between $M_{n,\ NMR}$ and $M_{n,\ SEC}$ was expected, since the SEC calibration was based on poly (methyl methacrylate) (PMMA) standards. Therefore M_n and *Đ* values are not the true values for poly(Lys_x-*ran*-Ala_y), but instead are relative to PMMA standards. The experimental ratios of K:A reported in Table 3.2. as 0.63 :0.37 and 0.6: 0.4, respectively, correlated well to the targeted ratio of 0.6: 0.4. These K:A ratios were also calculated from the ^{1}H NMR spectra of the protected poly($Lys(Boc)_x$-*ran*-Ala_y) copolymers. Signal **f** was attributed to the two CH_2 protons from K, while signals **a,b** was attributed to the CH backbone protons from both K and A.

The protected poly($Lys(Boc)_x$-*ran*-Ala_y) copolymers was deprotected using TFA and assessed using ^{1}H NMR spectroscopy. In Figure 3.1 it is seen that the large signal at ~1.3 ppm, corresponding to the 9 CH_3 protons from the Boc group, is absent after deprotection. The free amines in the form of TFA salts were further quantified using the Kaiser assay (Table 3.2). The higher free amine concentration from **entry #1** corresponds with the higher K:A ratio compared to **entry #2**. The amount of free amines was further used to calculate the molar ratios for the preparation of the hydrogels.

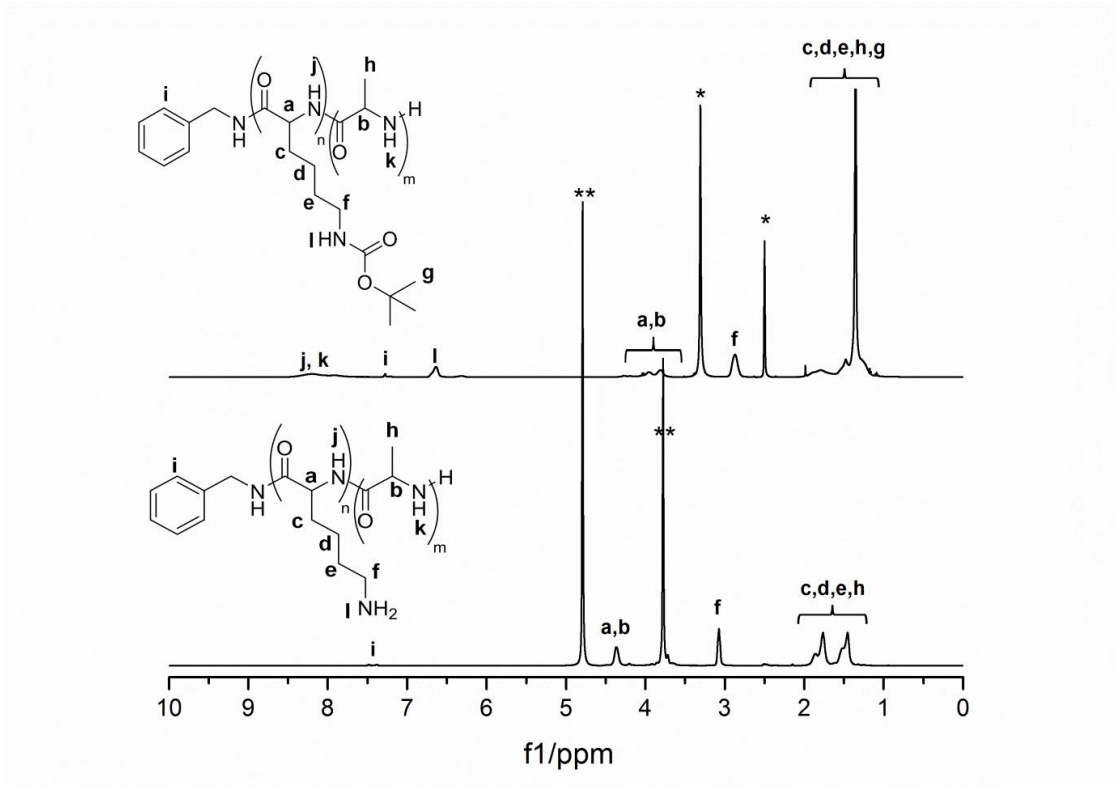


Figure 3.1. ^{1}H NMR spectra of $K_{46}A_{33}$ before (top) and after (bottom) deprotection of the lysine residues. Asterisk (*) indicates residual solvent peaks from d^6-DMSO (d^5-DMSO and HDO, respectively), double asterisk (**) indicates residual solvent peak from D_2O (HOD), and triple asterisk (***) indicates trace impurities from diethyl ether (Gottlieb, Kotlyar and Nudelman, 1997).

3.3.2 Preparation of a Library of Hydrogels

A library of hydrogel solutions were prepared by varying the functional molar ratio of amines from the polypeptide (further referred to as P(KA)) to succinimidyl esters from 4-PEG-SG, while the total polymer concentration was kept constant at 1 wt%, 2 wt%, 4 wt%, 6 wt% and 8 wt% (Section 3.2.3, Table 3.1). The vial inversion test was used to qualitatively identify the solutions as either liquid, gel-like or hydrogel (Raghavan and Cipriano, 2006). This allowed the construction of a phase plot, which provided a visual presentation of how the molar ratio and concentration controlled the sol-gel transition of P(KA)/4-PEG (Figure 3.2). P(KA) had ~60 amine functional groups, while the 4-PEG-SG had four NHS ester functional groups. When the average effective functionality is >2, crosslinking can occur. This crosslinking can lead to the formation of an infinite network of the polymers (Scheme 3.2). A higher polymer concentration and a functional molar ratio closer to 1:1 was expected to lead to a more densely formed polymer network, with the likelihood of forming a hydrogel increased (Pekcan and Kara, 2012). A clear phase transition was observed as the total polymer concentration increased from 1 wt% to 4 wt%. It is known that the polymer concentration affects the crosslinking, with higher concentrations favouring intermolecular crosslinking and lower concentrations favouring intramolecular crosslinking (Li and McCoy, 2004). In the reaction between P(KA) and 4-PEG-SG, complete intermolecular crosslinking will see each of the four arms of 4-PEG-SG reacted to a

different P(KA) polymer molecule. In intramolecular crosslinking, two or more of the 4-PEG-SG arms will react with the same P(KA) polymer molecule. Therefore, intermolecular crosslinking favours the formation of the infinite gel network (Scheme 3.2), while intramolecular crosslinking favours the solution phase. A change in phase from liquid to hydrogel was not necessarily observed over the range of selected molar ratios. This is likely due to the high effective functionality of the P(KA) and 4-PEG-SG, still favouring intermolecular crosslinking even as the functional molar ratio shifts from equimolar ratios. The materials designated as gel-like were noted as the sol-gel transition. These were found to be sticky and pliable with a spatula, contrary to the materials designated as hydrogels that maintained their 3D shape. It is likely that the number of intermolecular crosslinks, compared to intramolecular crosslinks was too little to form a stiff gel.

Critical gelation concentrations below 10 wt% are generally considered as low (Loh, Goh and Li, 2007; Xu et al., 2014). Low concentration hydrogels are attractive for tissue engineering applications as they constitute lower toxicity and higher porosity. In this study, the concentration of P(KA) was varied from as little as 0.65 wt% to 6.04 wt% for the hydrogels with total polymer concentrations of 4 wt%, 6 wt% and 8 wt%. Due to their robust nature, these hydrogels were selected for further investigation.

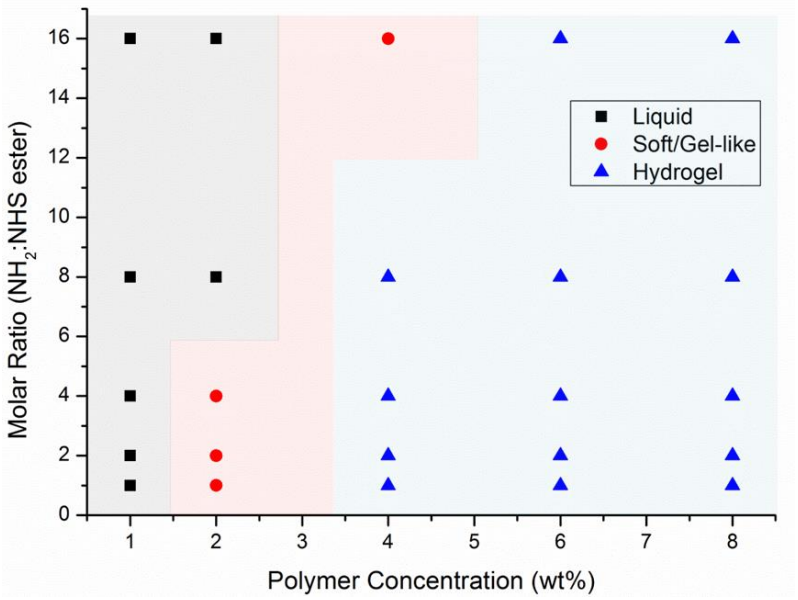
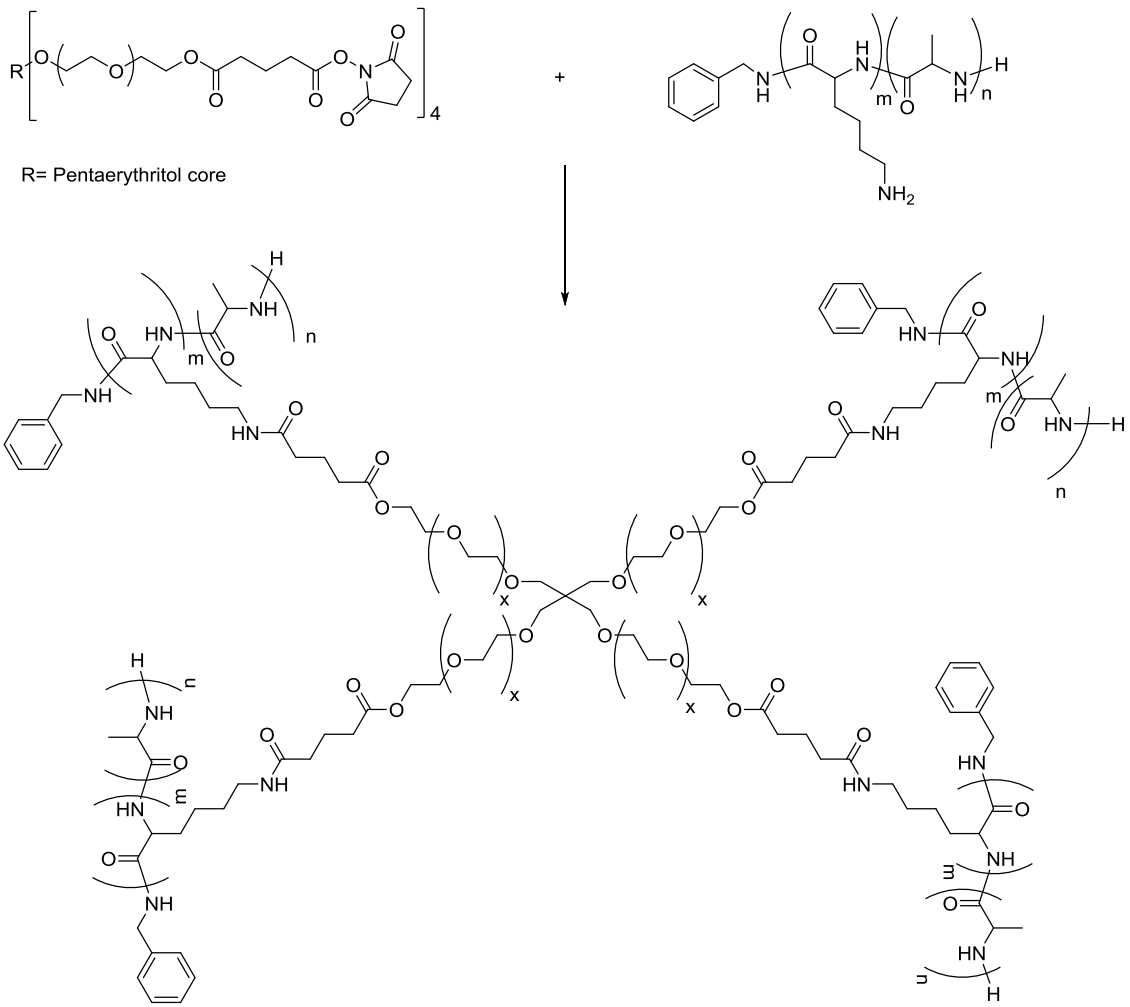


Figure 3.2. A phase plot of the library of hydrogels



Scheme 3.2. The intermolecular crosslinking reaction between P(KA) and 4-PEG-SG will form the infinite covalent hydrogel network, P(KA)/4-PEG.

3.3.3 Assessment of the Rheological Nature of Selected P(KA)/4-PEG Hydrogels

Small-amplitude oscillatory shear (SAOS) was used to characterise the gelation time and equilibrium modulus of selected P(KA)/4-PEG hydrogels. Time sweeps were performed immediately upon mixing the two hydrogel components and the evolution of the storage modulus (G') and loss modulus (G'') over time was recorded (Figure 3.3). The gelation of the 4 wt% hydrogel with 1:1 molar ratio reached stability at 8 min near 2400 Pa, while the 4:1 molar ratio hydrogel reached stability at 15 min near 4800 Pa. While the 4:1 molar ratio hydrogel is expected to have a lower degree of crosslinking, it also had a much higher P(KA) mass ratio (Table 3.1), compared to the 1:1 molar ratio hydrogel. A lower degree of crosslinking is expected to result in a less stiff hydrogel, due to a lower crosslinking density and a larger mesh size. However, the higher stiffness observed for the 4:1 molar ratio hydrogel compared to the 1:1 molar ratio hydrogel, is most likely due to the measurement being taken on the native, non-swollen hydrogels during their formation. In the 4:1 molar ratio hydrogel, the higher mass ratio of P(KA), which has a higher molar mass compared to 4-PEG, could explain the higher observed stiffness of the hydrogel in its native form compared to the 1:1 molar ratio hydrogel.

The gelation of the 8 wt% hydrogel with 1:1 molar ratio reached stability in 25 min near 10 000 Pa. This correlates with the expected trend that higher concentration polymers will lead to a stiffer hydrogel. For the three tested hydrogels, a strain of 10 Pa was within the LVE as determined from the amplitude sweeps (Figure 3.4). Within this region, the moduli are independent of the amplitude of the deformation. The equilibrium shear modulus (G_e) was ~3400 Pa for the 4 wt% 1:1 molar ratio hydrogel, ~5400 Pa for the 4 wt% 4:1 molar ratio hydrogel, and ~11 000 Pa for the 8 wt% 1:1 molar ratio hydrogel at 1 Hz (Figure 3.5). For gels, the G_e is typically recorded at lower frequencies, where tan δ (also G"/G') <1 (Zuidema et al., 2014). The G_e displayed by the P(KA)/4-PEG hydrogels correlate with the range of elastic moduli of 100 Pa to greater than 20 kPa for PLL/PEG hydrogels reported by Hynes et al. (2008). It is well known that the mechanical properties of hydrogels are closely related to cell behaviour such as adhesion, proliferation, and migration (Vedadghavami et al., 2017). Dermal fibroblasts have been shown to migrate on a 3D gradient-based collagen hydrogel from a nearly 1 MPa to 2 MPa elastic modulus regions, demonstrating preference for a stiffer environment (Hadjipanayi, Mudera and Brown, 2009). Nonetheless, natural biomaterials such as collagen, fibrin, elastin, gelatin and hyaluronic acid with generally low stiffness are widely used as skin dressings and skin substitutes (Sheikholeslam et al., 2018).

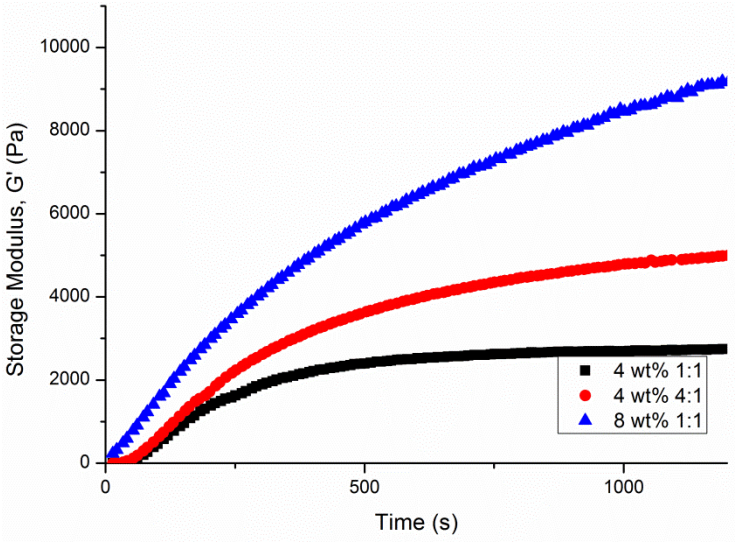


Figure 3.3. Time sweeps of the P(KA)/4-PEG hydrogels with 4 wt% (1:1 and 4:1 molar ratio) and 8 wt% (1:1 molar ratio)

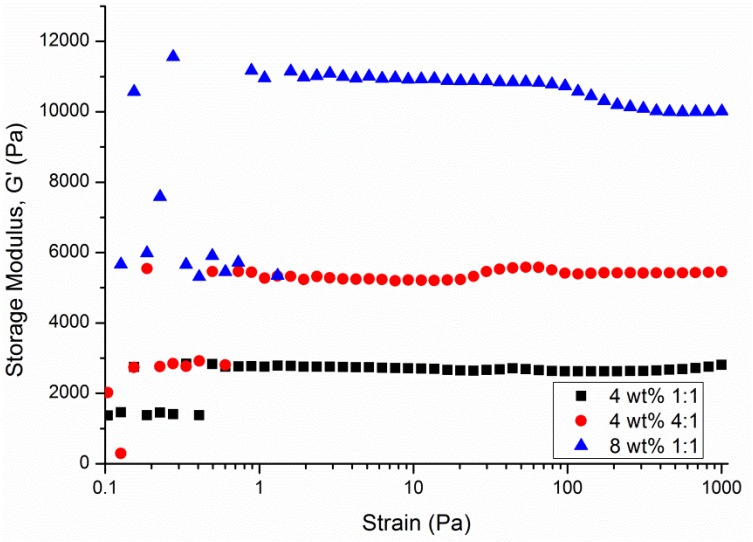


Figure 3.4. Strain sweeps of the P(KA)/4-PEG hydrogels with 4 wt% (1:1 and 4:1 molar ratio) and 8 wt% (1:1 molar ratio)

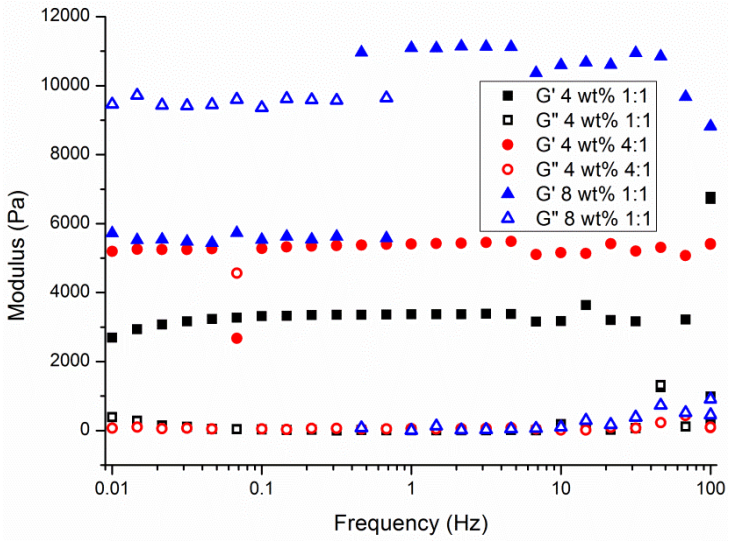


Figure 3.5. Frequency sweeps of the P(KA)/4-PEG hydrogels with 4 wt% (1:1 and 4:1 molar ratio) and 8 wt% (1:1 molar ratio)

3.3.4 Chemical Analysis of the Hydrogel Compositions

FTIR analysis was used to provide qualitative information on the chemical compositions of the library of P(KA)/4-PEG hydrogels. The most notable IR bands from P(KA) observed in Figure 3.6a was assigned according to the well-documented bands from PLL (Singh, 1999; Rozenberg and Shoham, 2007). This includes the ν_1 proton mode band of the peptide group at 3287 cm^{-1}, the ν_1 band of the side-chain NH_3^+ at 3056 cm^{-1}, the amide I CO group stretching band at 1654 cm^{-1}, and the amide II band from the in-plane deformational mode of the NH group at 1544 cm^{-1} (Rozenberg and Shoham, 2007). The position of the latter two bands is supportive of the mainly random coil conformation of P(KA). The ν_1 band of the side-chain NH_3^+ has been used by Rozenberg and Shoham (2007) to estimate the relative content of protonated side-chain NH_3^+ groups in samples isolated from different

pH solutions. The relative intensity of this band for P(KA) with respect to the ν_1 proton mode band of the peptide group is seen to decrease for P(KA)/4-PEG. Such a decrease in the relative content of NH_3^+ groups could be due to the crosslinking with NHS esters. The change in intensity of IR bands of P(KA) and 4-PEG from the P(KA)/4-PEG spectra correlate with the changing composition of the hydrogels as the molar ratio was increased from 1:1 to 16:1.

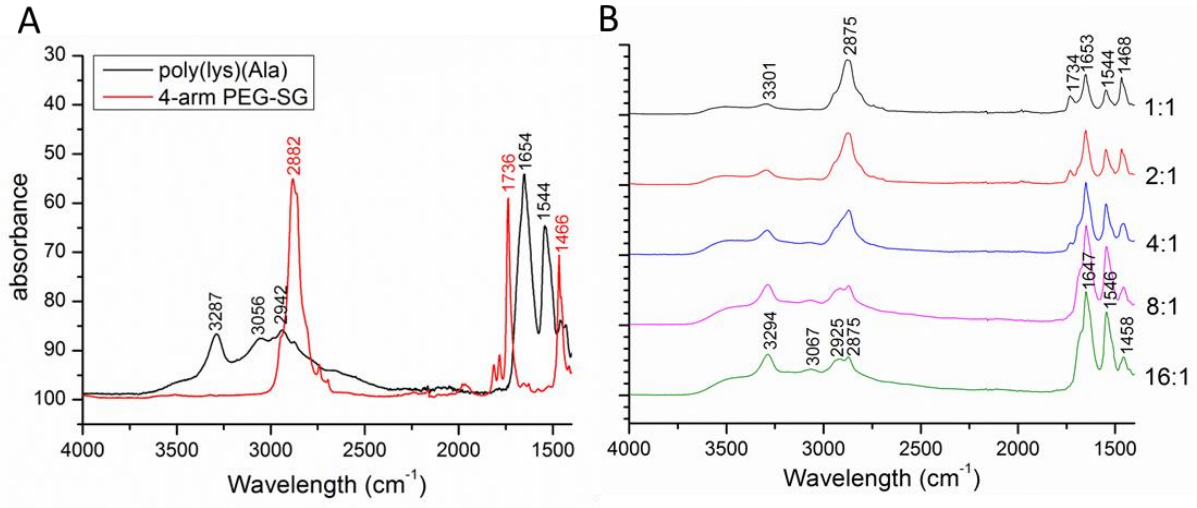


Figure 3.6. FTIR spectra of A) starting materials and B) hydrogels of 8 wt% with varying molar ratios

The concentration of free amines present in the hydrogel networks after crosslinking increased from ~0.2 μmol·mg^{-1} for the 1:1 molar ratio hydrogels to ~2.0 μmol·mg^{-1} for the 16:1 molar ratio hydrogels. This can be compared to the theoretical free amines present when assuming complete reaction between the amines and NHS esters. It is seen from Figure 3.7 that the amounts of free amines present after crosslinking follow the theoretical trend, indicating reasonable control over the preparation of the hydrogels. It is however seen that the experimental values are slightly higher compared to theoretical values. The theoretical values were calculated based on the assumption that each molecule of 4-PEG has 4 NHS ester end groups. However, NHS ester hydrolysis prior to the reaction was not taken into account. It is also expected that the hydrolysis of NHS esters will compete with the acylation reaction (Hermanson, 2013). Furthermore, experimental parameters like the time elapsed before mixing the 4-PEG solution with the P(KA) solution and their mixing rate will play a role in the crosslinking. A noticeable increase in the variance of the data of the 8:1 and 16:1 hydrogels may indicate higher sensitivity of the crosslinking reaction to the experimental parameters as the concentration of NHS esters becomes very low.

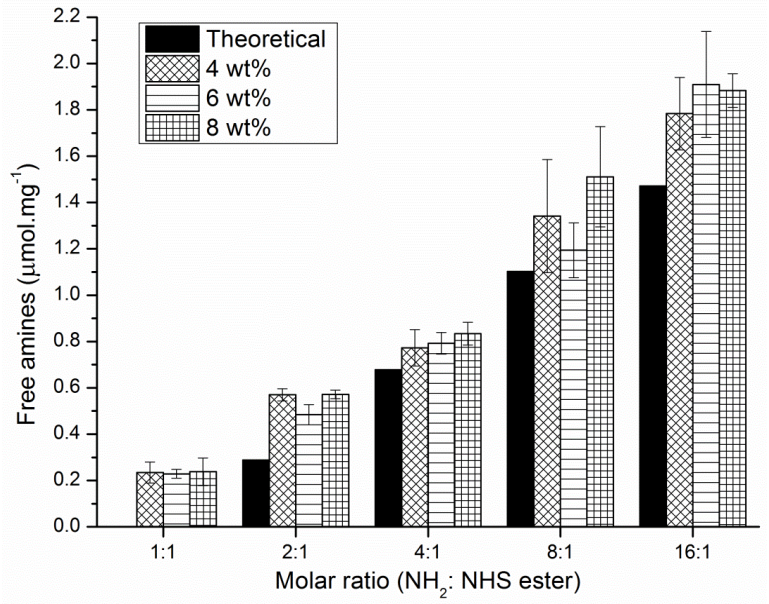


Figure 3.7. Column graph shows the concentration of free amines in the hydrogels compared to the calculated theoretical concentration.

3.3.5 The Effect of Crosslinking and Concentration on the Hydrogel Network

The equilibrium swelling theory of Flory and Rehner can be used to determine certain properties of the hydrogel network structure, including the average molar mass between crosslinks (M_c), crosslinking density (ρ_c), and mesh size (ξ) (Khan and Ranjha, 2014; Shet et al., 2015). The calculations for M_c, ρ_c and ξ as derived from the original theory by Flory and Rehner, require certain polymer parameters which are unknown for the P(KA)/4-PEG hydrogels. However, determining these parameters was deemed beyond the scope of this study. Nonetheless, according to the theory M_c is proportional to the equilibrium swelling ratio (ESR). Investigating the ESR and hydrogel morphology provided adequate insight into the effect of crosslinking and polymer concentration.

The ESR of the library of hydrogels was investigated in their "as is" and freeze-dried form in deionized water. Freeze-drying is widely used to induce the formation of micro-scale porous networks for tissue engineering applications (Annabi et al., 2010; Peng and Chen, 2011; Zhang et al., 2015; Sun et al., 2016; Reys et al., 2017). Such micro-scale porosity is essential to promote cell infiltration, and mass transfer of nutrients and cellular waste (Annabi et al., 2010). The freezing process causes the formation of ice crystals, and a subsequent phase separation of the water and the polymer network. As a result, the polymer network is condensed into membrane-like structures. This can affect the native structure of the hydrogel and lead to differences between the ESR of the "as is" and freeze-dried hydrogels. The effect of crosslinking and concentration on the ESR is seen in Figure 3.8. An increase in the molar ratio of P(KA)/4-PEG hydrogels caused an increase in ESR. As expected, the lower degrees of crosslinking will allow more expansion of the polymer network (Shet et al., 2015). In the "as-is" hydrogels, the ESR increased approximately 10 fold over the range of molar ratios, while for the freeze-dried hydrogels the ESR only increased five-fold. Furthermore, the effect of polymer

concentration played a significant role in the ESR of the "as is" hydrogels. The increase in polymer concentration caused a decrease in ESR. The higher polymer concentration presumably caused a denser polymer network less able to expand (Khan and Ranjha, 2014). This further correlates with a larger intermolecular versus intramolecular crosslinking. However, this effect was statistically insignificant in the freeze-dried hydrogels ($p>0.05$).

The morphology of the freeze-dried hydrogels was investigated using SEM. Uniform pores separated by membrane-like structures were seen on the inner-structure of the freeze-dried P(KA)/4-PEG hydrogels (Figure 3.9). However, it was observed that the pores were not fully interconnected. A surface skin at the scaffold-air interface is commonly formed in freeze-dried hydrogels as a result of interface tension (Ho et al., 2004). The higher molar ratios of 8:1 and 16:1 produced almost completely collapsed freeze-dried skins. Therefore viewing the morphology of their inner-structures was not possible. Their inner membranes were most likely too weak to support the 3D structure after freeze-drying, due to the low degree of crosslinking. Evidence of this can be seen in Figure 3.9, where the inner membranes become less rigid and slightly collapsed as the molar ratio is increased from 1:1 to 4:1. While it was difficult to determine the actual pore sizes from such deformed structures, pore sizes were measured as they appear on the images (Table 3.3). Nonetheless, the results correlated with the ESR findings. A significant increase in the average pore sizes was observed as the molar ratio from the 4 wt% and 6 wt% hydrogels was increased from 1:1 to 4:1 (p <0.001). The larger pore sizes correlate with a lower degree of crosslinking. This effect from molar ratio seems dependent on the total polymer concentration, as it becomes less significant on the 8 wt% hydrogels with molar ratios increasing from 1:1 to 4:1 (p = 0.001). Similarly, the effect of polymer concentration on the morphology of the hydrogels seemed closely related to the molar ratio. An increase in polymer concentration from 4 wt% to 8 wt% caused a statistically significant decrease in pore sizes for the 2:1 and 4:1 molar ratio hydrogels (p < 0.001), while it remained insignificant for the 1:1 molar ratio hydrogels (p = 0.119). The smaller pore sizes were related to the denser polymer network of the higher concentration hydrogels. The smaller size range of the 1:1 hydrogels correspond with the optimal pore size range of 20-125 μm reported for the regeneration of adult mammalian skin (Annabi et al., 2010).

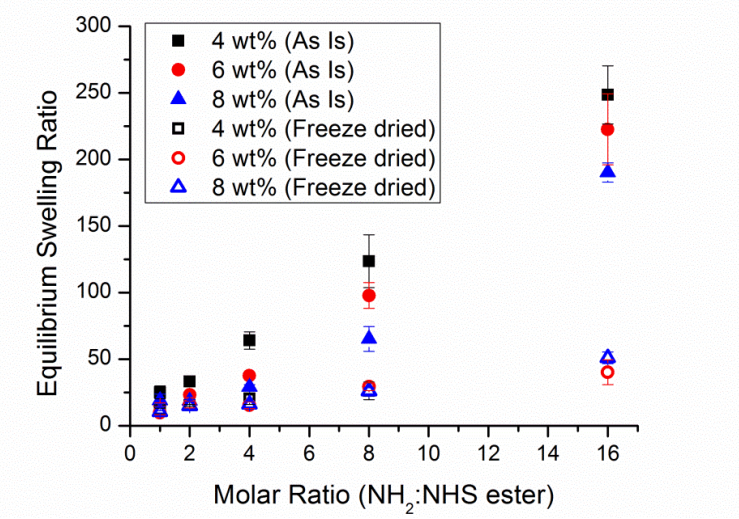


Figure 3.8. Equilibrium swelling of "as is" and freeze-dried hydrogels as a function of NH_2: NHS ester molar ratio

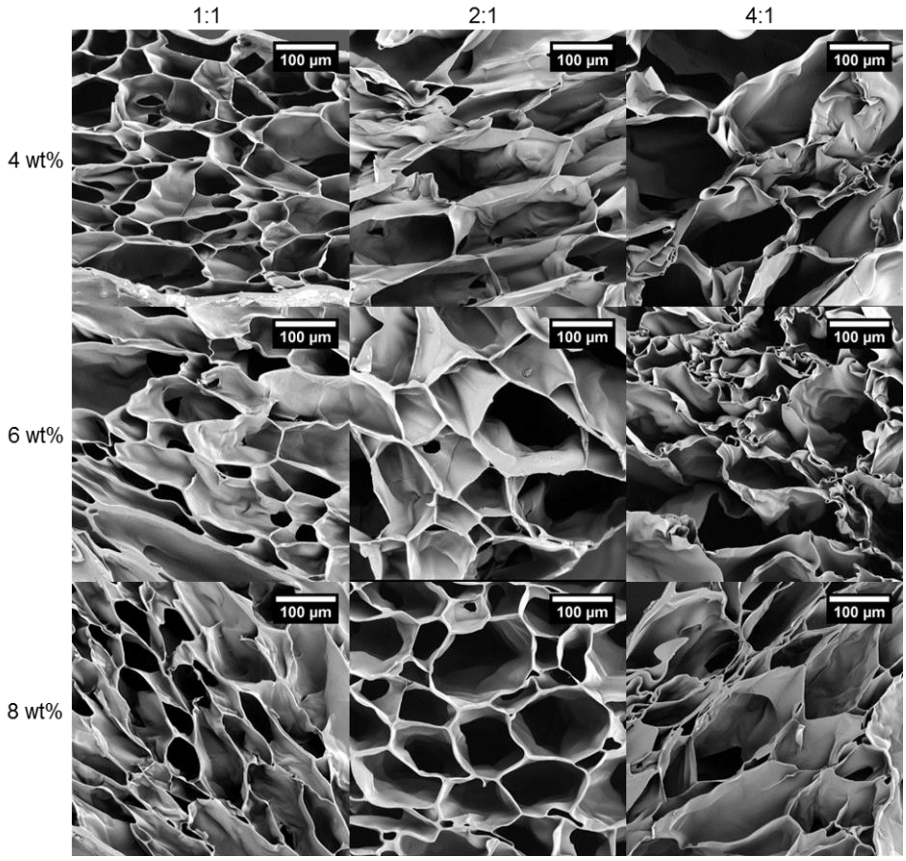


Figure 3.9. SEM images of the internal morphology of freeze-dried hydrogels

Table 3.3: Average pore sizes of the P(KA)/4-PEG hydrogels with varying molar ratio and total polymer concentration

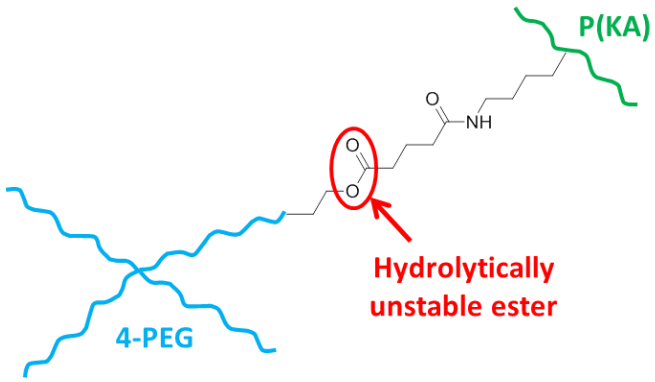
Hydrogel	Average Pore Size (µm)[a]		
	1:1	2:1	4:1
4 wt%	91 ± 39[b,c,k,l]	239 ± 68[b,d,n,o]	255 ± 51[c,d,q,r]
6 wt%	132 ± 58[e,f,k,m]	157 ± 48[e,g,n,p]	181 ± 64[f,g,q,s]
8 wt%	128 ± 55[h,i,l,m]	125 ± 45[h,j,o,p]	165 ± 67[i,j,r,s]

[a] Calculated from 40 to 60 measurements from 3 or more images with size distributions approximating normal distributions

[b-s] The statistical *p*-values were obtained from T-tests between the experimental data with corresponding annotations, e.g. "[cb]" indicates correlation between 4 wt% 1:1 and 4 wt% 2:1. *p*-Values indicated below:
[b] $p < 0.001$; [c] $p < 0.001$; [d] $p = 0.086$; [e] $p = 0.014$; [f] $p < 0.001$; [g] $p = 0.021$; [h] $p = 0.377$; [i] $p = 0.001$; [j] $p < 0.001$
[k] $p = 0.050$; [l] $p = 0.119$; [m] $p = 0.333$; [n] $p < 0.001$; [o] $p < 0.001$; [p] $p < 0.001$; [q] $p < 0.001$; [r] $p < 0.001$; [s] $p = 0.116$

3.3.6 The Biocompatibility Assessment of the Hydrogels

The *in vitro* biocompatibility of the hydrogels was assessed in terms of degradation, cytotoxicity, and cell adhesion. The hydrolytic degradation of the hydrogels was investigated in a PBS buffer (pH 7.2). The remaining ester bonds in the spacer between the crosslinked 4-PEG and P(KA) are known to be hydrolytically cleavable (Scheme 3.3) (Overby and Feldman, 2019). Cleavage of these bonds can lead to the eventual dissolution of the hydrogel as the polymer network becomes disintegrated. The change in hydrogel mass as a function of time is often investigated as a measure of the disintegration of the hydrogel (Wang et al., 2016). However, varying effects of crosslinking and concentration on the mass of the P(KA)/4-PEG hydrogels as they degraded provided little insight into the actual rate of degradation. For the 1:1 molar ratio hydrogels, a gradual decrease in hydrogel mass was observed, while for the higher molar ratio hydrogels a combination of mass increases and decreases was seen (Figure 3.10 A, B & C). It can be expected that as the crosslinks are cleaved, more flexibility in the polymer network can also lead to higher swelling degrees and therefore an increase in hydrogel mass.



Scheme 3.3 Schematic representation of the crosslinked P(KA)/4-PEG with the hydrolytically unstable ester indicated

In addition, the final degradation time of the P(KA)/4-PEG hydrogels was determined as the time when the hydrogel was visually disintegrated and unable to be weighed. In Figure 3.10 D the degradation time is seen to decrease from ±26 days to ±10 days with the molar ratios increasing from

1:1 to 16:1. This followed the expected trend that hydrogels with lower degrees of crosslinking will degrade faster. However, the effect of polymer concentration was statistically insignificant ($p>0.05$). The relatively short degradation times correspond well with the rate of normal wound healing. Regeneration of the dermal and epidermal layers typically takes place within 21 days (Shahrokhi, Arno and Jeschke, 2014). Therefore, the 1:1 and 2:1 molar ratio P(KA)/4-PEG hydrogels will be able to provide continued support to the healing wound while being gradually resorbed into the regenerated skin tissue.

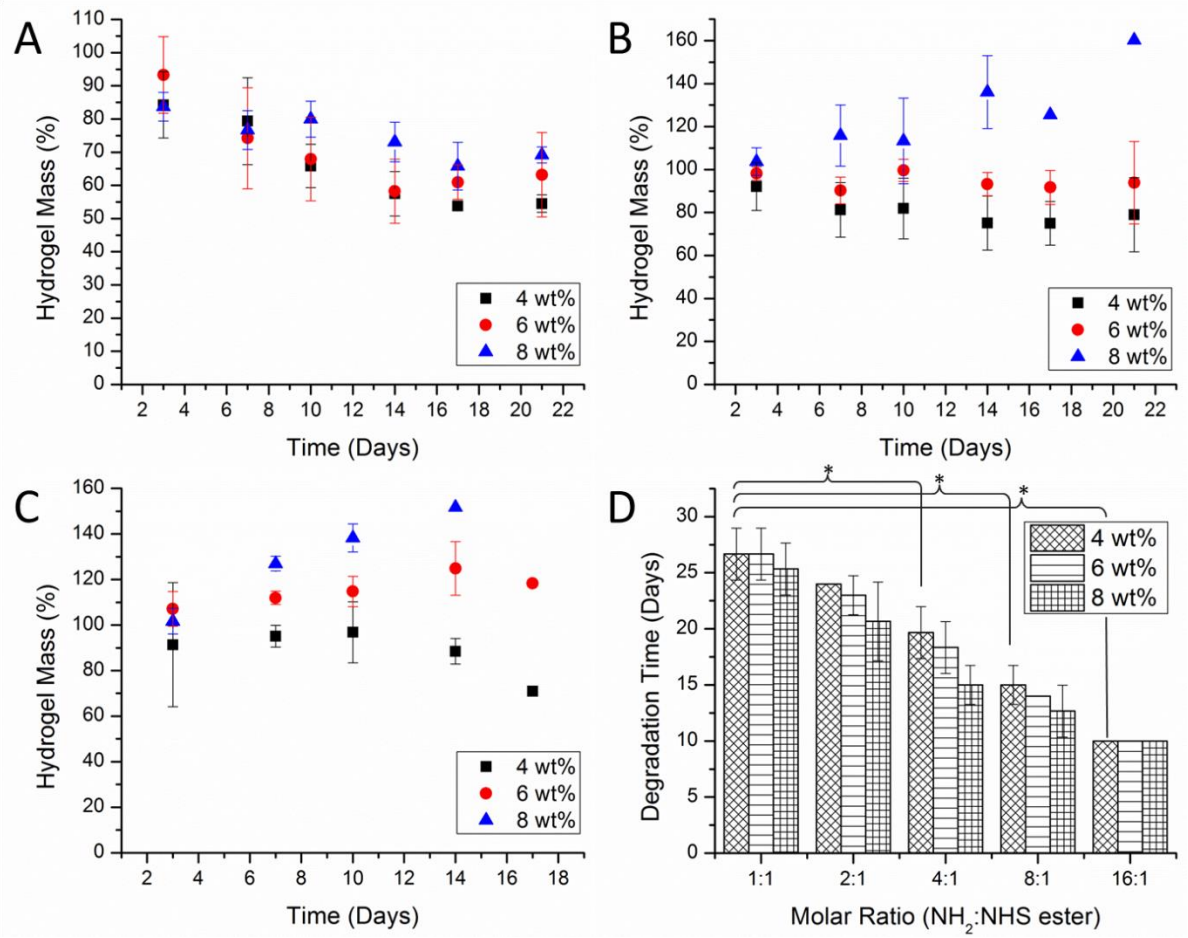


Figure 3.10. The effect of hydrolytic degradation on the hydrogel mass for A) 1:1 B) 2:1 and C) 4:1 molar ratio P(KA)/4-PEG hydrogels, and D) the effect of molar ratio on the final degradation time of the P(KA)/4-PEG hydrogels is shown. Statistical significance for the 4 wt% hydrogels ($p < 0.05$) is indicated by the asterisk (*). The effect of concentration on the final degradation time was not statistically significant.

The effect of molar ratio of P(KA)/4-PEG hydrogels with 4 wt % polymer concentration on the % cell viability of NIH 3T3 fibroblast cells was determined using the MTT assay. It can be seen from Figure 3.11 that hydrogels prepared with a higher molar ratio caused a statistically significant decrease in the % cell viability ($p < 0.05$). The difference in % cell viability between the positive control group and the 1:1 molar ratio hydrogels was insignificant. From these results it was reasoned that the

cytotoxicity of the 1:1 molar ratio hydrogels was adequately low for further tissue engineering applications.

In addition to the cytotoxicity study, the cellular adhesion to the surface of the P(KA)/4-PEG hydrogels with 4 wt % polymer concentration was assessed using light microscopy. Due to the transparent nature of the hydrogels, it was possible to view the morphology of the cells on the surface of the hydrogels. An elliptical, stretched cellular morphology is indicative of good cellular adhesion of fibroblasts, while poor adhesion is characterized by a spherical cellular morphology (Song, Rane and Christman, 2012). The morphology of the cells on the P(KA)/4-PEG hydrogel with a 1:1 molar ratio indicated good cellular adhesion, similar to the positive control (Figure 3.12). The P(KA)/4-PEG hydrogels with 2:1, 4:1 and 8:1 all showed poor cell adhesion. As an example, the cell morphology of the 8:1 hydrogel in comparison with the negative control (DMSO) is shown in Figure 3.12. An increase in cellular debris was also noted as the molar ratio was increased, indicating potential cell membrane disruption. This corresponds with the observed decrease in % cell viability as the molar ratio was increased.

The cytotoxicity of cationic polypeptides has been ascribed to the electrostatic interaction with anionic phospholipids in the cell membrane, causing membrane disruption and cell death (Wang et al., 2004). Fischer et al. (2003) investigated the cytotoxicity of different polycations, including PLL towards fibroblasts. They identified molecular weight and charge density as the main factors influencing the interaction of the polycations with the cell membrane. Hydrogels of PLL and its copolymers have lower cytotoxicity than the free polymers, most likely due to the decrease in charge density (Hynes et al., 2008; Wang et al., 2013). The charge density is reported as being dependent on the number of cations, as well as the three-dimensional structure and flexibility of the macromolecules. Hynes et al. (2008) identified PLL-based hydrogels with free amine concentrations higher than 3 μmol/mg as cytotoxic to NSC cells, while hydrogels with lower concentration amines maintained the cell viability. As discussed earlier, the concentration of free amines in the P(KA)/4-PEG hydrogels increased as the molar ratio increased. Therefore, the charge density of the P(KA) is expected to increase and the cytotoxicity towards the NIH 3T3 cells is seen to follow the anticipated trend. Strategies to lower the charge densities on the high molar ratio P(KA)/4-PEG hydrogels can include modifying the free amines through chemical conjugation (Hynes et al., 2008).

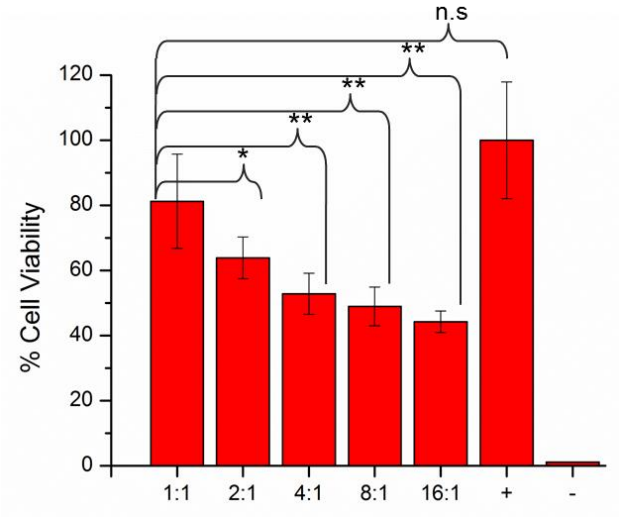


Figure 3.11. The effects of molar ratio of the 4 wt% P(KA)/4-PEG hydrogels on the cell viability of NIH 3T3 cells are shown. The statistical significance is indicated by an asterisk (*) for $p < 0.05$ and double asterisk (**) for $p < 0.01$. The difference between the positive control group (+) and the 1:1 molar ratio group was not significant.

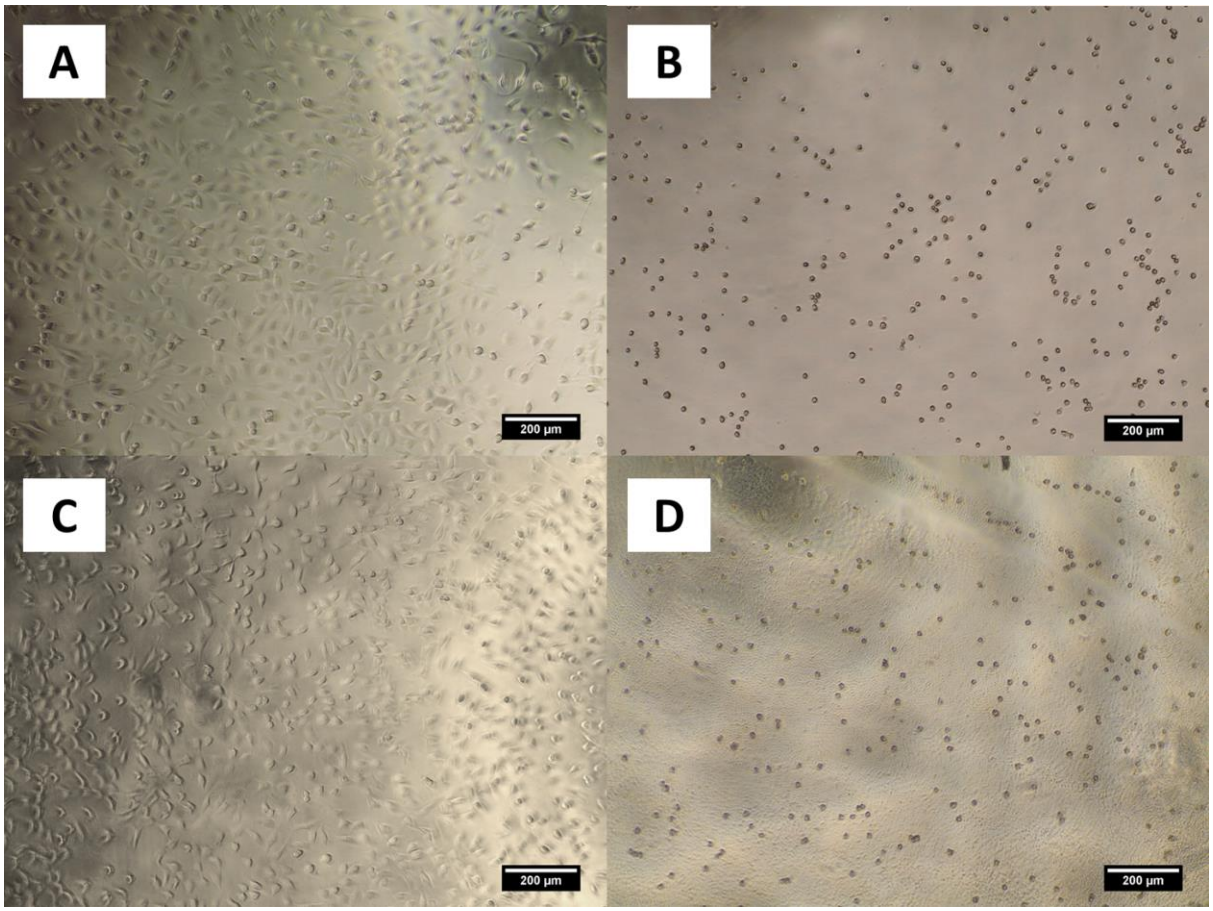


Figure 3.12. Images of T3T NIH cell adhesion on A) well-plate B) well-plate with DMSO C) P(KA)/4-PEG hydrogel (4 wt%; 1:1 molar ratio) and D) P(KA)/4-PEG hydrogel (4 wt%; 8:1 molar ratio) on light microscope (scale bar = 200 µm)

3.3.7 Evaluation of the Antibacterial Activity of the P(KA)/4-PEG Hydrogels

No inhibitory zones was observed for the P(KA)/4-PEG hydrogels, when testing their antibacterial activity with the agar disk diffusion method (results not shown). In the case of inherently antibacterial hydrogels, the active component forms part of the hydrogel network and no active component was expected to diffuse out of the hydrogels (Li et al., 2018). Therefore, a modified broth dilution method was used to investigate the antibacterial effect of the P(KA)/4-PEG hydrogels when in contact with bacterial solutions (Song, Rane and Christman, 2012; Balouiri, Sadiki and Ibnsouda, 2016). Furthermore, we tested the antibacterial activity of the free P(KA) polypeptides against ciprofloxacin. Based on OD readings and CFU counts, the P(KA)/4-PEG hydrogels with varying molar ratios correlated with the negative control containing no ciprofloxacin as antibiotic, while the free P(KA) showed some bacterial inhibition. Results for *S. aureus* bacterial species are shown in Figure 3.13.

The activity of the free P(KA) can be correlated with the antimicrobial co-peptides reported by Zhou et al.(2010). They synthesised random co-peptides containing lysine as hydrophilic amino acid and alanine, phenylalanine or leucine as hydrophobic amino acid (Zhou et al., 2010). These co-peptides with typically short chain lengths and different hydrophilic to hydrophobic amino acid ratios did not show any specific secondary structures. Nonetheless, their antimicrobial activity was ascribed to membrane disruption. It is interesting to note that despite the similarities between the P(KA)/4-PEG hydrogels reported here and the poly(Lys_{60}-*ran*-Ala_{40})-based hydrogels reported by Song, Rane and Christman (2012), their antibacterial activity does not correlate. They further reported that the poly(Lys_{60}-*ran*-Ala_{40})-based hydrogels showed good antibacterial activity, while its precursor polypeptide, poly(Lys_{60}-*ran*-Ala_{40}), did not inhibit bacterial growth. The parameters that influence the antibacterial activity of polypeptides when incorporated in hydrogels are not yet fully understood. In the current study, within the range of parameters tested, it was not possible to determine the effect of crosslinking on the antibacterial activity. Further investigation into the antibacterial properties of P(KA)-based hydrogels is required.

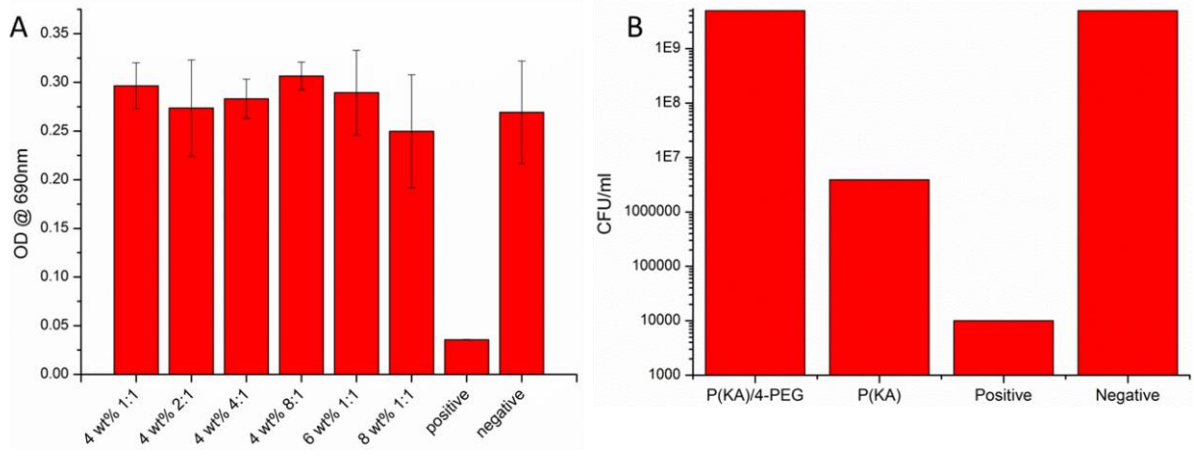


Figure 3.13. Antibacterial activity against *S. aureus* bacterial species

3.4 CONCLUSION

The facile synthesis of P(KA) using controlled ROP afforded well-controlled polypeptides with narrow molecular weight distributions. The development of a library of P(KA)/4-PEG hydrogels allowed investigation into the effects of reactant ratios and overall polymer concentration during gel formation on the physicochemical and biofunctional properties of these hydrogels. It was found that the properties of the hydrogels could be tuned significantly. This included the gelation time, mechanical properties, amine content, swelling behaviour, pore sizes, degradation time, and cell behaviour. The cell behaviour was found to be particularly sensitive to the molar ratio of the components in the hydrogels. The higher free amine concentration can be associated with a higher positive charge density and provided an explanation for the increase in cytotoxicity for hydrogels with increasing molar ratio. Contrary to the free P(KA), which displayed some bacterial inhibition, P(KA)/4-PEG hydrogels did not display any antibacterial activity. This is most likely related to the low polypeptide content in the hydrogel. Nonetheless, these hydrogels offer attractive tunability to meet certain criteria favourable to wound healing applications. The 4 wt% hydrogel with a molar ratio of 1:1 demonstrated adequate swelling behaviour and mechanical properties suitable for soft tissue engineering, while the pore sizes and degradation time correlated with the requirements for regenerating skin tissue. These hydrogels further demonstrated very low cytotoxicity and good cell adhesion.

3.5 REFERENCES

ALIFERIS, T., IATROU, H. and HADJICHRISTIDIS, N. (2004) Living Polypeptides. *Biomacromolecules*, 5(5), pp. 1653–1656.

AMBEKAR, R.S. and KANDASUBRAMANIAN, B. (2019) Progress in the Advancement of Porous Biopolymer Scaffold: Tissue Engineering Application. *Industrial & Engineering Chemistry Research*, 58, pp. 6163–6194.

ANNABI, N. et al. (2010) Controlling the Porosity and Microarchitecture of Hydrogels for Tissue Engineering. *Tissue Engineering Part B: Reviews*, 16(4), pp. 372–383.

BALOUIRI, M., SADIKI, M. and IBNSOUDA, S.K. (2016) Methods for in vitro evaluating antimicrobial activity : A review $. *Journal of Pharmaceutical Analysis*, 6(2), pp. 71–79.

BARRIENTOS, S. et al. (2008) Growth factors and cytokines in wound healing. *Wound repair and regeneration*, 16, pp. 585–601.

BOATENG, J.S. et al. (2008) Wound Healing Dressings and Drug Delivery Systems : A Review. *Journal of Pharmaceutical Sciences*, 97(8), pp. 2892–2923.

BROUGHTON, G., JANIS, J.E. and ATTINGER, C.E. (2006) The basic science of wound healing. *Plastic and reconstructive surgery*, 117(7S), pp. 12S-34S.

DEMING, T.J. (2005) Polypeptide hydrogels via a unique assembly mechanism. *Soft Matter*, 1, pp. 28–35.

DENG, C. et al. (2014) Functional polypeptide and hybrid materials : Precision synthesis via alpha-amino acid N-carboxyanhydride polymerization and emerging biomedical applications. *Progress in Polymer Science*, 39(2), pp. 330–364.

DMITROVIC, V. et al. (2012) Random Poly(Amino Acid)s Synthesized by Ring Opening Polymerization as Additives in the Biomimetic Mineralization of CaCO3. *Polymers*, 4, pp. 1195–1210.

EL-SHERBINY, I.M. and YACOUB, M.H. (2013) Hydrogel scaffolds for tissue engineering : Progress and challenges. *Global Cardiology Science & Practice*, 38, pp. 1–27.

FISCHER, D. et al. (2003) In vitro cytotoxicity testing of polycations: influence of polymer structure on cell viability and hemolysis. *Biomaterials*, 24, pp. 1121–1131.

FRIEDMAN, M. (2004) Applications of the Ninhydrin Reaction for Analysis of Amino Acids , Peptides , and Proteins to Agricultural and Biomedical. *Journal of Agricultural and Food Chemistry*, 52, pp. 385–406.

GONZÁLEZ-HENRÍQUEZ, C.M., SARABIA-VALLEJOS, M.A. and RODRÍGUEZ-HERNÁNDEZ, J. (2017)

Strategies to Fabricate Polypeptide-Based Structures via Ring-Opening Polymerization of N-Carboxyanhydrides. *Polymers*, 9(11), p. 551.

GOTTLIEB, H.E., KOTLYAR, V. and NUDELMAN, A. (1997) NMR Chemical Shifts of Common Laboratory Solvents as Trace Impurities. *Journal of Organic Chemistry*, 62, pp. 7512–7515.

HABRAKEN, G.J.M. et al. (2010) How controlled and versatile is N-carboxy anhydride (NCA) polymerization at 0 °C? Effect of temperature on homo- , block- and graft (co)polymerization. *Polymer Chemistry*, 1, pp. 514–524.

HABRAKEN, G.J.M. et al. (2011) Optimization of N-carboxyanhydride (NCA) polymerization by variation of reaction temperature and pressure. *Polymer Chemistry*, 2(6), pp. 1322–1330.

HADDAD, A.G. et al. (2018) Skin Substitutes and Bioscaffolds:Temporary and Permanent Coverage. *Clinics in Plastic Surgery*, 44(3), pp. 627–634.

HADJIPANAYI, E., MUDERA, V. and BROWN, R.A. (2009) Guiding cell migration in 3D: a collagen matrix with graded directional stiffness. *Cell Motil. Cytoskelet.*, 66(3), pp. 121–128.

HERMANSON, G.T. (2013) *Bioconjugate Techniques*. Third edit. AUDET, J. and PREAP, M. (eds.). London: Elsevier Inc.

HO, M. et al. (2004) Preparation of porous scaffolds by using freeze-extraction and freeze-gelation methods. *Biomaterials*, 25, pp. 129–138.

HÖCK, S. et al. (2010) Thermal Cleavage of the Fmoc Protection Group. *Chimia*, 64(3), pp. 200–202.

HYNES, S.R. et al. (2008) A library of tunable poly(ethylene glycol)/poly (L-lysine) hydrogels to investigate the material cues that influence neural stem cell differentiation. *Journal of Biomedical Materials Research Part A*, 89, pp. 499–509.

JENKINS, A.D. et al. (1996) Glossary of Basic Terms in Polymer Science. *Pure and Applied Chemistry*, 68(12), pp. 2287–2311.

JHON, M.S. and ANDRADE, J.D. (1973) Water and hydrogels. *Journal of Biomedical Materials Research*, 7(6), pp. 509–522.

KADLECOVA, Z. et al. (2012) Comparative study on the in vitro cytotoxicity of linear, dendritic, and hyperbranched polylysine analogues. *Biomacromolecules*, 13(10), pp. 3127–37.

KENDALL, P.A. (1963) Use of the Ninhydrin Reaction for Quantitative Estimation of Amino Groups in Insoluble Specimens. *Nature*, 197(4874), pp. 1305–1306.

KHAN, S. and RANJHA, N.M. (2014) Effect of degree of cross-linking on swelling and on drug release of low viscous chitosan/poly(vinyl alcohol) hydrogels. *Polymer Bulletin*, 71, pp. 2133–2158.

KOEHLER, J., BRANDL, F.P. and GOEPFERICH, A.M. (2018) Hydrogel wound dressings for bioactive

treatment of acute and chronic wounds. *European Polymer Journal*, 100, pp. 1–11.

LEE, K.Y. and MOONEY, D.J. (2001) Hydrogels for Tissue Engineering. *Chemical Reviews*, 101(7), pp. 203–225.

LI, R. and MCCOY, B.J. (2004) Inter- and Intramolecular Crosslinking Kinetics: Partitioning According to Number of Crosslinks. *Macromolecular R*, 25, pp. 1059–1063.

LI, S. et al. (2018) Antibacterial Hydrogels. *Advanced Science*, 5(5), p. 1700527.

LOH, X.J., GOH, S.H. and LI, J. (2007) New Biodegradable Thermogelling Copolymers Having Very Low Gelation Concentrations. *Biomacromolecules*, 8(2), pp. 585–593.

LU, H. et al. (2014) Recent advances in amino acid N-carboxyanhydrides and synthetic polypeptides: chemistry, self-assembly and biological applications. *Chemical Communications*, 50, pp. 139–155.

NOWAK, A.P. et al. (2002) Rapidly recovering hydrogel scaffolds from self-assembling diblock copolypeptide amphiphiles. 417(May), pp. 424–428.

OVERBY, R.J. and FELDMAN, D.S. (2019) Influence of Poly (Ethylene Glycol) End Groups on Poly (Ethylene Glycol)-Albumin System Properties as a Potential Degradable Tissue Scaffold. *Journal of Functional Biomaterials*, 10(1), pp. 1–12.

PAKSTIS, L.M. et al. (2004) Effect of Chemistry and Morphology on the Biofunctionality of Self-Assembling Diblock Copolypeptide Hydrogels. *Biomacromolecules*, 5, pp. 312–318.

PEKCAN, O. and KARA, S. (2012) Gelation Mechanisms. *Modern Physics Letters B*, 26(27), pp. 1230019–1.

PENCZEK, S. (2018) *Models of Biopolymers By Ring-Opening Polymerization*. CRC Press.

PENG, Z. and CHEN, F. (2011) Hydroxyethyl Cellulose-Based Hydrogels with Various Pore Sizes Prepared by Freeze-Drying. *Journal of Macromolecular Science, Part B*, 50, pp. 340–349.

RAGHAVAN, S.R. and CIPRIANO, B.H. (2006) Gel Formation: Phase diagrams using table top rheology and calorimetry. In: WEISS, R. and TERECH, P. (eds.) *Molecular Gels: Materials with Self-Assembled Fibrillar Networks*. Springer Netherlands, pp. 233–244.

REYS, L.L. et al. (2017) Influence of freezing temperature and deacetylation degree on the performance of freeze-dried chitosan scaffolds towards cartilage tissue engineering. *European Polymer Journal*, 95, pp. 232–240.

ROZENBERG, M. and SHOHAM, G. (2007) FTIR spectra of solid poly- L -lysine in the stretching NH mode range. *Biophysical Chemistry*, 125, pp. 166–171.

SCHINDELIN, J. et al. (2012) Fiji: an open-source platform for biological-image analysis, *Nature*

methods, 9(7), pp. 676-682.

SELIG, H.F. et al. (2012) The properties of an "ideal" burn wound dressing – What do we need in daily clinical practice? Results of a worldwide online survey among burn care specialists. *Burns*, 38(7), pp. 960–966.

SHAHROKHI, S., ARNO, A. and JESCHKE, M.G. (2014) The use of dermal substitutes in burn surgery: acute phase. *Wound repair and regeneration*, 22(1), pp. 14–22.

SHEIKHOLESLAM, M. et al. (2018) Biomaterials for Skin Substitutes. *Advanced Healthcare Materials*, 7, p. 1700897.

SHET, R. et al. (2015) Effect of Crosslinking Agent Concentration on the Properties of Unmedicated Hydrogels. *Pharmaceutics*, 7, pp. 305–319.

SINGER, A.J. and CLARK, R.A.F. (1999) Cutaneous Wound Healing. *The New England Journal of Medicine*, 341(10), p. 738.

SINGH, B.R. (1999) *Basic Aspects of the Technique and Applications of Infrared Spectroscopy of Peptides and Proteins*. ACS Sympos. Washington, DC: American Chemical Society.

SONG, A., RANE, A.A. and CHRISTMAN, K.L. (2012) Antibacterial and cell-adhesive polypeptide and poly (ethylene glycol) hydrogel as a potential scaffold for wound healing. *Acta Biomaterialia*, 8, pp. 41–50.

STONE, R.I. et al. (2018) Advancements in Regenerative Strategies Through the Continuum of Burn Care. *Frontiers in Pharmacology*, 9, p. 672.

SUN, K. et al. (2016) Comparison of three-dimensional printing and vacuum freeze-dried techniques for fabricating composite scaffolds. *Biochemical and Biophysical Research Communications*, 477(4), pp. 1085–1091.

VAYABOURY, W. et al. (2004) Living Polymerization of alpha-Amino Acid N-Carboxyanhydrides (NCA) upon Decreasing the Reaction Temperature. *Macromolecular Rapid Communications*, 25, pp. 1221–1224.

VEDADGHAVAMI, A. et al. (2017) Manufacturing of hydrogel biomaterials with controlled mechanical properties for tissue engineering applications. *Acta Biomaterialia*, 62, pp. 42–63.

WANG, R. et al. (2016) Antimicrobial and biocompatible ε-polylysine-γ-poly(glutamic acid)-based hydrogel system for wound healing. *Journal of Bioactive and Compatible Polymers*, 31(3), pp. 242–259.

WANG, S.S.S. et al. (2013) Genipin-cross-linked poly(l-lysine)-based hydrogels: Synthesis, characterization, and drug encapsulation. *Colloids and Surfaces B: Biointerfaces*, 111, pp. 423–431.

WANG, Y.X. et al. (2004) Effects of the chemical structure and the surface properties of polymeric biomaterials on their biocompatibility. *Pharm Res*, 21, pp. 1362–1373.

WERNER, S. and GROSE, R. (2003) Regulation of Wound Healing by Growth Factors and Cytokines. *Physiological Reviews*, 83, pp. 835–870.

XU, Y. et al. (2014) Synthesis, characterization, biodegradability and biocompatibility of a temperature-sensitive PBLA-PEG-PBLA hydrogel as protein delivery system with low critical gelation concentration. *Drug Development and Industrial Pharmacy*, 40(9), pp. 1264–1275.

ZARRINTAJ, P. et al. (2017) Can regenerative medicine and nanotechnology combine to heal wounds? The search for the ideal wound dressing. *Nanomedicine*, 12(19), pp. 2403–2422.

ZHANG, J. et al. (2015) Pore architecture and cell viability on freeze dried 3D recombinant human collagen-peptide (RHC)-chitosan scaffolds. *Materials Science & Engineering C*, 49, pp. 174–182.

ZHOU, C. et al. (2010) High Potency and Broad-Spectrum Antimicrobial Peptides Synthesized via Ring-Opening Polymerization of alpha-Aminoacid-N-carboxyanhydrides. *Biomacromolecules*, 11, pp. 60–67.

ZHOU, X. and LI, Z. (2018) Advances and Biomedical Applications of Polypeptide Hydrogels Derived from α-Amino Acid N-Carboxyanhydride (NCA) Polymerizations. *Advanced Healthcare Materials*, 7(15), p. 1800020.

ZUIDEMA, J.M. et al. (2014) A protocol for rheological characterization of hydrogels for tissue engineering strategies. *Journal of Biomedical Materials Research B: Applied Biomaterials*, 102B(5), pp. 1063–1073.

CHAPTER 4: EXPLORING THE 3D PRINTABILITY OF POLY(LYS_{60}-*RAN*-ALA_{40})/4-ARM PEG HYDROGELS

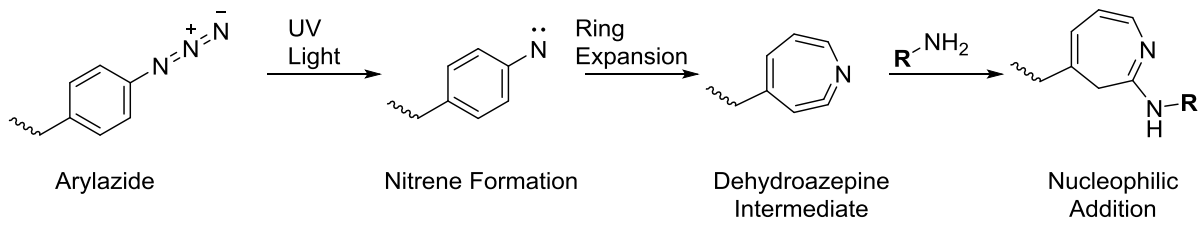
4.1 INTRODUCTION

Three-dimensional (3D) printing in the field of biomedical engineering has seen a rapid increase in popularity in the last few years. This includes applications in tissue engineering, regenerative medicine, therapeutic delivery systems, medical device fabrication, and disease modelling and diagnostics (Jamróz et al., 2018; Ngo et al., 2018; Ahangar et al., 2019). Using 3D printing to fabricate precisely designed 3D architectures according to computer-aided design (CAD) allows the fabrication of scaffolds with controlled properties such as porosity, permeability, and mechanical strength (Yang et al., 2002; Mota et al., 2015; Kelly et al., 2018). Controlling these properties are particularly important in tissue engineering, as it controls the ability to incorporate cells into the scaffolds through bioprinting or post-print cell seeding (Fan, Staufer and Accardo, 2019; Singh and Jonnalagadda, 2020). Hydrogels form a popular class of 3D printable biomaterials or biomaterial inks as they have recently been termed (Kirchmajer, Gorkin III and in het Panhuis, 2015; Groll et al., 2019). This is mainly due to their tissue-mimicking properties, making them suitable for tissue engineering applications. A number of hydrogels are also suitable for bioprinting due to their mild processing conditions (Panwar and Tan, 2016; Gopinathan and Noh, 2018).

Hydrogels are typically 3D printed as their precursor materials. Their gelation, during or after the 3D printing process, is then used as the solidification mechanism to produce the final hydrogel structure. In order to obtain ideal 3D printed structures, the hydrogel precursor materials require adequate viscosity to maintain their structural integrity prior to crosslinking (Kyle et al., 2017). Strategies to increase the viscosity of the hydrogel precursor material include using increased polymer concentrations (Schuurman et al., 2013), adding composite materials (Wang et al., 2014; Martínez-Vázquez et al., 2015; Narayanan et al., 2016), and using near gel-phase or gel-phase inks (Lee et al., 2013; Rutz et al., 2015; Lewis, Green and Shah, 2018; Kim et al., 2018). Near gel-phase inks include gelatin solutions that are 3D printed at temperatures near their sol-gel transition (Kim et al., 2018). Gel-phase inks include partially crosslinked gels such as alginate solutions mixed with low concentrations of calcium chloride (Lee et al., 2013). Rutz et al. (2015) also reported the 3D printing of covalently cross-linked gel phase inks. Through carefully controlled crosslinking, they demonstrated how partially crosslinked hydrogels can be 3D printed. Another example of gel phase inks include the jammed microgel ink recently reported by Highley et al. (2019). While the hydrogel microparticles are in their gel phase, the jammed microgel displayed elastic behaviour at low strains and shear thinning at high strain rates. Apart from these examples, covalently cross-linked hydrogels are typically not considered as 3D printable, due to the irreversible nature of their crosslinking.

Consequently, a large number of covalently cross-linked hydrogels with promising applications in tissue engineering are excluded from 3D printing.

The poly(Lys_{60}-*ran*-Ala_{40})/4-arm PEG (P(KA)/4-PEG) hydrogels explored in this study is an excellent example of a covalently crosslinked hydrogel, considered non-3D printable in conventional 3D printing terms. In this chapter, two approaches to developing P(KA)/4-PEG into 3D printable biomaterial inks were investigated. The first approach was based on the partial crosslinking of hydrogels to produce pliable materials as reported by Rutz et al. (2015). By incorporating primary and secondary crosslinking mechanisms into the hydrogel precursor components, the biomaterial ink can be synthesised via the primary crosslinking, while the secondary crosslinking is responsible for post-print solidification. The crosslinking between P(KA) and 4-PEG-SG was well-studied in Chapter 3 and the phase plot (Section 3.3.2) was used to identify soft pliable gels. The soft gel with a concentration of 2 wt% and a 4:1 molar ratio was selected as potential hydrogel precursor components for the biomaterial inks. The reaction between the free amines from P(KA) and the N-hydroxysuccinimidyl ester from 4-PEG-SG can be seen as the primary crosslinking. The secondary crosslinking mechanism will be introduced on the P(KA) through chemical conjugation with aryl azides. Rickett et al. (2011) reported the production of photoreactive chitosan with 4-azidobenzamide functionality, by reacting the amines in chitosan with 4-azidobenzoic acid through EDC coupling. Aryl azides are known for their rapid photo-crosslinking without the need for photoinitiators (Hermanson, 2013). The reaction involves the photolysis of aryl azides into reactive nitrene (Hermanson, 2013). The crosslinking with amines through nitrene chemistry then takes place as depicted in Scheme 4.1. The second approach uses hydrogel microparticles incorporated into a composite microgel paste. Composite pastes incorporating inorganic particles or polymer particles in a hydrogel precursor solution have been reported as biomaterial inks for 3D printing (Haberstroh et al., 2010; Wüst et al., 2014; Wang et al., 2014; Neufurth et al., 2014). Apart from the viscosity gain, the addition of such particles also adds biofunctionality to the material. The solidification of these composite inks is dependent on the gelation of the hydrogel in which the particles are suspended. To our knowledge, this is the first study investigating composite microgel pastes as biomaterial inks for 3D printing.



Scheme 4.1 A general scheme for the photoactivation of arylazides and their reaction with amines (Hermanson, 2013)

The 3D printability of the P(KA)/4-PEG inks developed through these two approaches was assessed in terms of extrudability, layer-stacking ability, 3D print fidelity, and solidification (Kyle et al., 2017; Paxton et al., 2017). The combination of these criteria is considered as the fundamental requirements for any extrusion-based 3D ink (Kyle et al., 2017; Paxton et al., 2017). In addition, the properties of the composite microgel materials and the effect of the 3D printing pattern on the physical properties were evaluated. It was proposed that the processing of P(KA)/4-PEG into 3D printed scaffolds will allow further tunability of the physical properties of P(KA)/4-PEG hydrogels, while enhancing the biofunctionality of the scaffolds.

4.2 MATERIALS AND METHODS

4.2.1 Materials and General Methods

All chemicals and solvents were purchased from commercial sources and used without further purification unless stated otherwise. Dry solvents were used as received and handled under dry inert gas. 4-Azidobenzoic acid (2 M in *tert*-butyl methyl ether), *N*-(3-dimethylaminopropyl)-*N*′-ethylcarbodiimide hydrochloride (EDC), *N*,*N*,*N*′,*N*′-tetramethylethylenediamine (TEMED), 2-hydroxy-4′-(2-hydroxyethoxy)-2-methylpropiophenone (Irgacure 2959), fluorescein-5-isothiocyanate (FITC), 5-carboxyfluorescein diacetate succinimidyl ester (CFDA-SE), chitosan (medium molecular weight; 75-85 % deacetylated) and poly(vinyl alcohol) (M_w = 89000 - 98000, 99% hydrolysed) were purchased from Sigma-Aldrich (St. Louise, MO, USA). 4-arm PEG succinimidyl glutarate (10 kDa) and 4-arm PEG-acrylate (10 kDa) were purchased from JenKem Technology (WA, US). All camera and microscope images were processed using ImageJ (version 1.51n) software. FTIR spectrometry was performed on a Spectrum 100 FT-IR Spectrometer (PerkinElmer, MA, US) fitted with a Universal ATR Sampling Accessory.

4.2.2 Synthetic Procedures

4.2.2.1 Functionalisation of poly(Lys_{60}-ran-Ala_{40}) with 4-azidobenzoic acid

Degrees of conjugation of 20% and 40% were targeted. For the 20% conjugation, the following procedure was used:

Poly(Lys_{60}-*ran*-Ala_{40}) (synthesised as described in Chapter 3) (200 mg) was dissolved in 15 mL distilled water. 4-Azidobenzoic acid solution (2 M, 1.0 mL, 0.24 mmol), EDC (70 mg, 0.45 mmol) and TEMED (150 μL) were added to the P(KA) solution. The pH was then adjusted to 4-6 and the flask covered with foil. The reaction was left to stir for 72 h, after which it was dialysed against distilled water for 5 days. P(KA)-Az was obtained via lyophilisation.

4.2.3 Preparation and Characterisation of Hydrogel-Inks

4.2.3.1 Approach 1: Partially-crosslinked hydrogels

Soft/gel-like materials of P(KA)-Az/4-PEG (as identified from Chapter 3) were prepared according to the procedure described in Chapter 3 for P(KA)/4-PEG hydrogels with a concentration of 2 wt% and a 4:1 molar ratio. For these inks, functionalised P(KA)-Az replaced the P(KA) used in Chapter 3.

4.2.3.2 Approach 2: Composite microgel pastes

P(KA)/4-PEG hydrogels with 8 wt% and 1:1 molar ratio were prepared according to the procedure described in Chapter 3. After the hydrogel equilibrated for 1 hour, it was ground in its wet state with a mortar and pestle into a fine paste of microparticles.

Three respective hydrogel precursor solutions were prepared as follows. A 4-PEG-Ac solution of 15 wt% was prepared in distilled water containing 0.5 wt% Irgacure 2959 and was degassed for 10 min under N_2 gas. A chitosan (CS) solution of 2 wt% was prepared in an acetic acid solution of 2 % (v/v). A poly(vinyl alcohol) (PVA) solution of 10 wt% in distilled water was prepared by autoclaving to dissolve the PVA.

The P(KA)/4-PEG hydrogel microparticles was then mixed with the hydrogel precursor solution of either 4-arm PEG-acrylate (4-PEG-Ac), CS, or PVA at a 50:50 weight ratio (Table 4.1). The final weight of the ink was then adjusted to the initial P(KA)/4-PEG weight.

Table 4.1 A summary of the preparation of the three composite microgel pastes

Biomaterial Ink	**P(KA)/4-PEG microparticles (50 wt%)**	**Hydrogel precursor solution (50 wt%)**
4-PEG-Ac-P(KA)/4-PEG	P(KA)/4-PEG (8 wt%; 1:1 molar ratio)	4-PEG-Ac (15 wt%) and Irgacure 2959 (0.5 wt%) in dist. H_2O
CS-P(KA)/4-PEG		CS (2 wt%) in acetic acid 2 % (v/v)
PVA-P(KA)/4-PEG		PVA (10 wt%) in dist. H_2O

4.2.3.3 Rheology

The primary and secondary crosslinking of P(KA)-Az/4-PEG was monitored on the ElastoSense™ Bio^2 until G' reached equilibrium. This non-destructive rheological technique allowed assessment of the 2-step crosslinking process.

For the primary crosslinking, a total volume of 3 mL of the P(KA)-Az and 4-PEG-SG precursor solutions were added to a calibrated sample holder. The measurements of G' and G" were started as soon as the P(KA)-Az and 4-PEG-SG components were mixed.

For the secondary crosslinking, the instrument measurements were paused for three cycles. For the first cycle, the sample was irradiated for 10 min with a UV light source (365 nm wavelength). For the

second cycle, the sample was not irradiated as a control to ensure no artificial effect on G' was caused as a result of the pausing. For the final cycle, the sample was irradiated for 20 min. This increased irradiation time served as a second experimental cycle to evaluate if further crosslinking occurred. The measurement after each cycle commenced until G' reached equilibrium.

4.2.3.4 Fluorescent Microscopy

Fluorescent microscopy was used to assess the morphology and particle size of the P(KA)/4-PEG microparticles. 20 mg of the P(KA)/4-PEG microparticles was diluted in 1 mL distilled water. 100 µL FITC (250 µM) in ethanol was diluted in 10 mL water. 100 µL of the FITC solution was added to the microparticles and allowed to react for 20 min. 20 µL of the microparticle solution was then placed between a microscope slide and a coverslip and viewed on a Leica MZ10F fluorescence microscope using a GFP3 filter with excitation wavelengths of 450-490 nm and barrier filter wavelengths of 500-550 nm. A Leica DFC365FX camera and LAP (v4.5, Leica) software were used to capture images with pseudo colour modifications matching the emission wavelength of FITC at 518 nm.

4.2.4 3D Printability of the Biomaterial Inks

4.2.4.1 Viscosity

The rotational shear viscosity was measured on a Thermo Scientific™ HAAKE™ MARS™ Rheometer (Thermo Fisher Scientific, MA, US), with a 35 mm cone plate with a 1 ° incline and a 0.052 mm gap distance fitted with a HAAKE™ Universal Temperature Controller (Thermo Fisher Scientific, MA, US). 0.2 mL of the composite microgel inks prepared as described above, were placed on the rheometer plate and the viscosity (η) measured as a function of shear rate ($\dot{\gamma}$) ranging from 0.0001 to 2000 s^{-1}. This allowed investigation into the shear thinning viscosity behaviour of the composite microgel inks.

4.2.4.2 Extrudability

The extrudability of the biomaterial inks through nozzle tips with 0.4 mm and 0.2 mm ID was investigated using the 3D Bioplotter® (EnvisionTEC GmbH, Germany).

For the "partially cross-linked" inks the precursor P(KA)-Az and 4-PEG solutions were added to the 30 mL syringe barrels (Nordson EFD) fitted with a plunger and a plastic tapered nozzle (Nordson EFD). The syringe barrel was then inserted into the printing head and left for 60 min to equilibrate at 25 °C.

The "composite microgel pastes" were added to syringe barrels fitted with a plunger and the tip closed with a stopper. The syringe barrel was then centrifuged at 4000 rpm for 5 min to remove any air bubbles.

The "composite microgel pastes" were then extruded for 1 s at set pressures and the morphology of the strands were visually analysed. The length (mm) of the extruded strands were analysed from digital images using FIJI (v. 1.51n, ImageJ, URL: https://imagej.net/Fiji) (Schindelin et al., 2012) to determine the extrusion velocity ($mm \cdot s^{-1}$).

4.2.4.3 Strand Optimization

Optimisation of the strands were performed using the "manual parameter tuning" function on Visual Machines (version 2.8.130r7, Envisiontec GmbH) software to extrude single strands of the "composite microgel paste" at varied speed or pressure intervals to optimise the strand width. The built-in camera was used to capture images of the strands and the images were calibrated using a 1 mm interval ruler.

4.2.4.4 3D printing

CAD models of 3D box-shaped geometries were prepared and converted into 2D layers using the BioplotterRP (version 3.0, Envisiontec GmbH) slicer software (Figure 4.1). The slicing file was transferred to the Visual Machines algorithm for the layer-by-layer fabrication using the 3D Bioplotter® (EnvisionTEC GmbH, Germany). The built-in algorithms were used to produce cross-hatch printing patterns by varying the strand diameter, the strand spacing, and the layer slicing height, while the orientation between the layers were set at 90° angles (Table 4.2).

"Composite microgel pastes" were prepared and loaded into the syringe barrel as described under section "4.2.4.2 Extrudability". 3D constructs were 3D printed using the parameters summarised in Table 4.3.

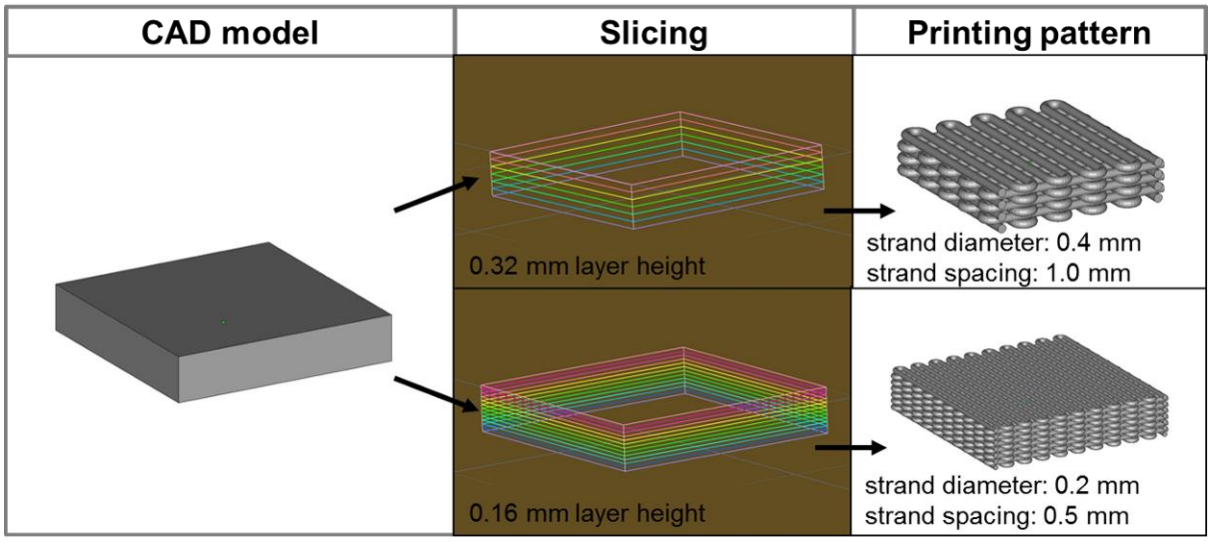


Figure 4.1 The schematic illustrates the slicing of the CAD model of the 3D box-shaped design with dimensions of 10 × 10× 2 mm (l × w × h) into 2D layers using different layer heights of 0.32 mm and 0.16 mm, respectively, while the printing patterns are represented as 3D CAD models. The strand diameter

was determined from the needle ID, while the strand spacing was selected through the built-in algorithms of Visual Machines (EnvisionTEC GmbH, Germany) used to fill-in the 2D layers.

Table 4.2 Summary of the 3D printing patterns

Cross-Hatch Pattern Parameters	3D Printed Pattern		
	"Non-Porous"	"Porous"	
Strand Diameter (mm)*	0.4	0.4	0.2
Strand Spacing (mm)	0.4	1.0	0.5
Inter-Strand Spacing (mm)**	0	0.6	0.3
Layer Slicing Height (mm)	0.32	0.32	0.16
Layer Orientation	90°	90°	90°

*Strand diameter based on the needle ID
**Inter-strand spacing is the distance between two adjacent strands

Table 4.3 Summary of the 3D printing parameters

Parameters	Biomaterial Inks			
	4-PEG-P(KA)/4-PEG	PVA-P(KA)/4-PEG	CS-P(KA)/4-PEG	
Needle ID (mm)	0.4	0.4	0.4	0.2
Pressure (Bar)	0.4	1.0	1.4	2.3
Speed ($mm \cdot s^{-1}$)	21	19	20	19
Pre-flow delay (s)	0	0	0.30	0.25
Post-flow delay (s)	0	0	-0.02	-0.05

4.2.4.5 Post-print solidification

Due to the varying chemical compositions of the different "composite microgel pastes" prepared in this study, each ink required a solidification mechanism specific to the components of the ink.

After printing, the 4-PEG-Ac-P(KA)/4-PEG constructs were placed in a UV box fitted with a 365 nm wavelength light source and irradiated for 10 min. The UV-crosslinked scaffolds were then frozen at -20 °C overnight and further cooled to - 60 °C before lyophilizing.

The CS-P(KA)/4-PEG constructs were frozen at -20 °C immediately after printing. After overnight freezing, the scaffolds were further cooled to - 60 °C before lyophilizing. The scaffolds were then washed in absolute ethanol (99.9%), followed by subsequent washes with ethanol in distilled water dilutions (90 %, 80 %, 70 %, 60 %, 50 %, 30 %, 10% and 0 % ethanol). Each washing cycle was allowed to equilibrate for 1 h in order to remove any traces of acetic acid. The scaffolds were then lyophilized.

For the PVA-P(KA)/4-PEG constructs, the solidification was achieved by freeze-thaw cycles. Six cycles of freezing at - 20 °C for 16 hours followed by 8 hours of thawing at room temperature were used to produce the physically cross-linked scaffolds. The scaffolds were then lyophilized.

4.2.4.6 3D print fidelity

The dimensions of the 3D printed scaffolds in their hydrated state were compared to the intended dimensions and the deviation used as a measure of the 3D print fidelity. For the "non-porous" 3D printed scaffolds, three measurements per geometrical side (width, length, and height) were measured with a digital calliper. The % deviations from the intended CAD dimensions were calculated from the average measured dimensions. For the "porous" scaffolds the strand diameter and inter-strand spacing were measured using an SZX7 stereomicroscope (Olympus, Tokyo, Japan). The average dimensions from three measurements were compared with the intended printing pattern in Table 4.2

4.2.5 Scaffold Characterization

4.2.5.1 Mechanical

The compressive- and tensile moduli were calculated as the gradient of the linear section of stress vs strain plots. Stresses and strains were calculated using the following equations,

$$\boldsymbol{stress} = \frac{\boldsymbol{F}}{\boldsymbol{A}} \qquad \text{(Eq. 4.1)}$$

$$\%\ \boldsymbol{strain} = \frac{\boldsymbol{\Delta d}}{\boldsymbol{d_i}} \times \mathbf{100} \qquad \text{(Eq. 4.2)}$$

where F is the force applied in Newton (N), A is the calculated area over which the force is applied, Δd is the change in sample dimension (parallel to the direction of the force applied) and d_i is the initial sample dimension (see Figure 4.2).

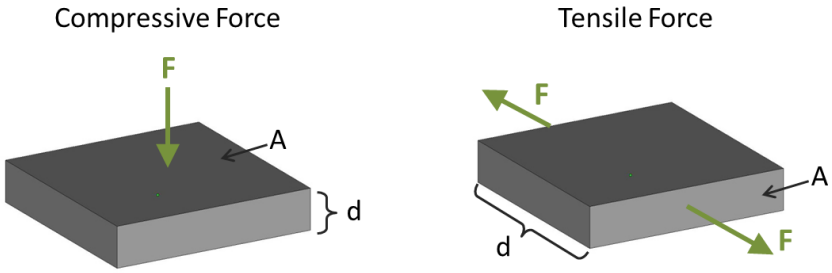


Figure 4.2. A schematic representation of the direction of the force (indicated by green arrows) applied to the samples and the corresponding parameters, A and d, used during the respective compressive- and tensile tests

All scaffold dimensions were determined from three measurements per geometrical side, measured with a digital calliper. The average of each side was then used to calculate d_i and A for the respective tests as indicated in Figure 4.2.

Compressive tests were performed on a TA.XT*plus* Texture Analyser (Stable Micro Systems™, Surrey, UK). 30 % strain was applied to the samples hydrated in distilled H_2O at a rate of 1%•s^{-1}.

Uniaxial tensile tests were performed using a BioTester™ (CellScale™, ON, Canada). The bio-rakes with tine diameter of 305 μm and tine spacing of 1.7 mm were used to mount the samples. A 30 % strain over a duration of 60 s was used.

4.2.5.2 Swelling

The equilibrium swelling ratio (ESR) of the scaffolds was determined from the following equation,

$$\boldsymbol{ESR} = \frac{(\boldsymbol{W_W} - \boldsymbol{W_D})}{\boldsymbol{W_D}} \quad \text{(Eq.4.3)}$$

W_W is the wet weight of the hydrogel after swelling in PBS and W_D is the dry weight of the hydrogel after freeze-drying.

4.2.5.3 Porosity

The pore sizes were analysed using a scanning electron microscopy (SEM). Sections of the freeze-dried scaffolds were mounted on metal stubs using carbon tape and coated twice with carbon and once with gold/palladium using a sputter coater. Micrographs of the face and cross-sections were taken using a SIGMA 03-39 field emission electron microscop (FE SEM) (ZEISS, Germany). The images were analysed using FIJI (v. 1.51n, ImageJ, URL: https://imagej.net/Fiji) (Schindelin et al., 2012) and the average pore sizes calculated using 40 to 60 measurements from 3 images with size distributions approximating normal distributions

The porosity of the scaffolds was determined by taking the weight of the dry scaffold, W_1 and then placing it in ethanol acting as inert solvent. When there were no more visible air bubbles within the scaffold, the scaffold was removed and excess ethanol was removed from the surface with filter paper. The weight of the scaffold filled with ethanol was then taken as W_2. This was then used to calculate the volume of the pores, V_p using the following equation,

$$\boldsymbol{V_p} = \frac{\boldsymbol{W_2} - \boldsymbol{W_1}}{\boldsymbol{\rho_{EtOH}}} \quad \text{(Eq. 4.4)}$$

where ρ_{EtOH} is the density of ethanol at 25 °C (0.785 g·cm^{-3}). The porosity was then calculated as a percentage of the bulk scaffold volume, V_s, using the following equation,

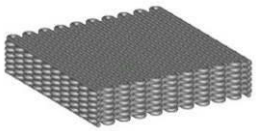
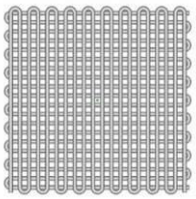
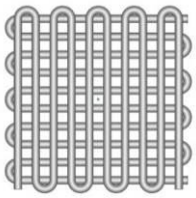
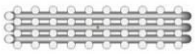
$$\%\,\boldsymbol{porosity} = \frac{\boldsymbol{V_p}}{\boldsymbol{V_s}} \times \mathbf{100} \quad \text{(Eq. 4.5)}$$

The architectures of the "porous" 3D printed scaffolds were further modelled with CAD using SketchUp (version 15.3.331, Trimble). From the CAD model, the scaffold volume and surface area were determined using Magics (version 18.03, Materialise, Belgium) (Table 4.4). The theoretical % porosity was calculated using the following equation,

$$\%\,\boldsymbol{porosity} = \frac{\boldsymbol{V_s} - \boldsymbol{V_m}}{\boldsymbol{V_s}} \times \mathbf{100} \quad \text{(Eq. 4.6)}$$

where V_s is the bulk scaffold volume and V_m is the modelled volume of the cross-hatch structure.

Table 4.4 A summary of the model input and output parameters and the schematic representations of the CAD models

Model	3D View	Top View	Cross-section
Strand diameter: 0.241 mm Volume: 119 mm^3 Surface area: 2009 mm^2			
Strand diameter: 0.457 mm Volume: 120 mm^3 Surface area: 1062 mm^2			

4.2.5.4 In vitro cell adhesion studies

NIH 3T3 mouse fibroblast cells were used for cell adhesion studies. For adhesion onto the "non-porous" scaffolds, small discs of the scaffolds were prepared by placing ~30 μL of the "composite microgel pastes" between a glass slide and coverslips with 1 mm spacers. The inks were then cross-linked using the solidification method described under "section 4.2.4.5 Post-print solidification". The scaffolds were then sterilised under UV light (265 nm) for 10 min and hydrated in fresh medium overnight. The scaffolds were then placed in 48 well plates and 200 μL cells in fresh medium (15 000 cells/well) were added onto the scaffolds. The cells were then cultured for 72 h at 37 °C with 5% CO_2.

For adhesion onto the "porous" 3D printed scaffolds, 10 × 10 × 2 mm scaffolds of CS-P(KA)/4-PEG were prepared as described above. The scaffolds were sterilised under UV light for 10 min and hydrated in fresh medium overnight. The scaffolds were then placed in 12 well plates and 2 mL cells in fresh medium (75 000 cells/mL) were added onto the scaffolds. The cells were then cultured for 96 h at 37 °C with 5% CO_2.

To visualise the cells adhered to the scaffolds, the cells were stained with CFDA-SE. After the specified incubation times, the medium was carefully removed and replaced with equal volumes of 5 μM CFDA-SE in PBS (pH 7.2). The plates were then incubated for 8 min at 37 °C with 5% CO_2. The staining solutions were then removed and replaced with equal volumes of fresh medium and incubated for 5 min. This washing step was repeated twice and the scaffolds then viewed on a Leica MZ10F fluorescent microscope using the same procedure described above for FITC stains.

4.2.6 Statistical Evaluation

Results were reported as mean ± standard deviation. One-way analysis of variance (ANOVA) and student's *t*-test were used for comparison between groups. A value of $p < 0.05$ was considered statistically significant.

4.3 RESULTS AND DISCUSSION

4.3.1 Preparation of Biomaterial Inks

4.3.1.1 "Partially cross-linked" inks

The characteristic azide peak at ~2120 cm^{-1} confirmed the conjugation using FTIR (Figure 4.3). The decrease in amines due to the conjugation was measured using the Kaiser assay. The degree of conjugation was then calculated using the difference in absorbance as a percentage of the initial absorbance of P(KA). The experimental degree of conjugation for the two targeted degrees of 20% and 40% was calculated as 32% and 58%, respectively. Since the primary crosslinking, as well as the secondary crosslinking required free amines on P(KA), only partial conjugation of P(KA), was targeted. P(KA)-Az was then crosslinked with 4-PEG to form the ink, P(KA)-Az/4-PEG.

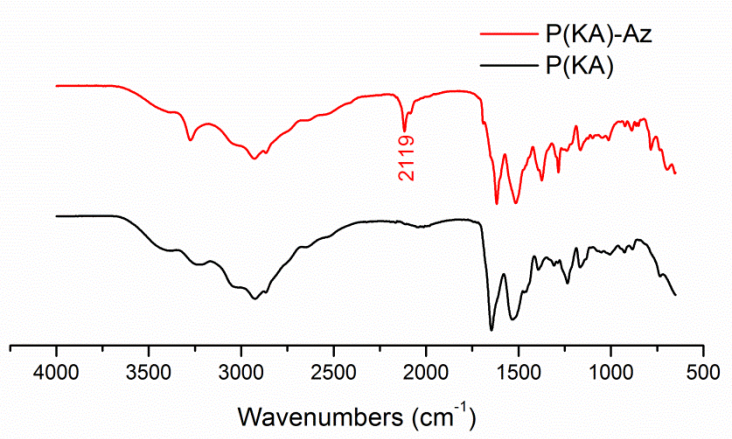


Figure 4.3 FTIR spectra of P(KA) before (black) and after (red) conjugation with 4-azidobenzoic acid

4.3.1.2 "Composite microgel" inks

The microparticles of P(KA)/4-PEG was observed as a combination of single and aggregated particles in dilute solutions using fluorescent microscopy (Figure 4.4A). The morphology of the particles was irregular, with a broad size distribution. Nonetheless, the preparation method was preferred due to its robust application in producing fine pastes able to pass through needle tips with 0.4 mm and 0.2 mm ID. In the concentrated paste, the particles were seen as closely packed together (Figure 4.4).

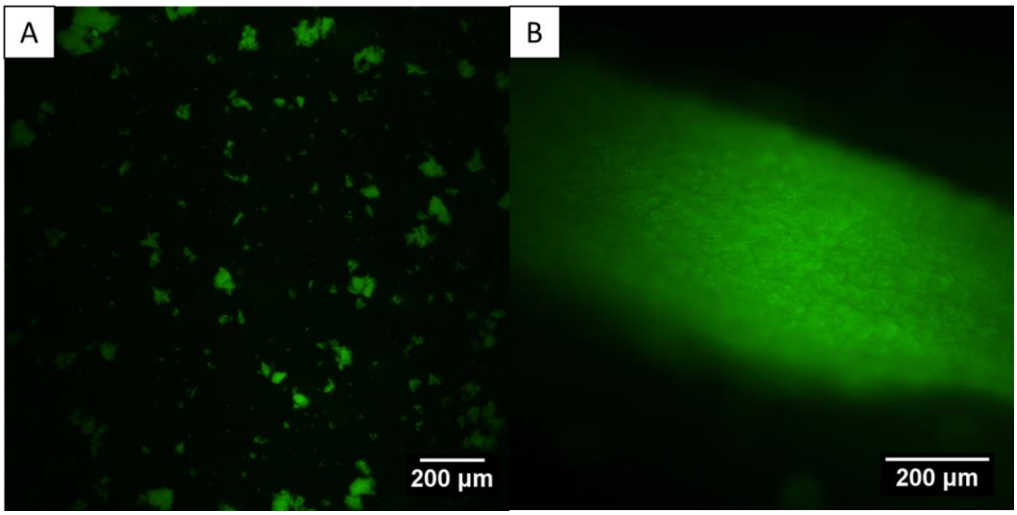


Figure 4.4 Fluorescence micrograph of micro-particles of P(KA)/4-PEG labelled with FITC in A) a dilute solution and B) a concentrated paste

4.3.2 Evaluation of the 3D Printability of the Biomaterial Inks

4.3.2.1 Extrudability and viscoelasticity

The morphology of the extruded "partially crosslinked" inks was seen as irregular discontinuous lumps of material (Figure 4.5A). The "composite microgel" inks, on the other hand, were extruded as smooth continuous strands (Figure 4.5B). The first criterion used for determining the 3D printability of prepared inks is their extrudability through the needle tip. It has been reported that the material needs to be extruded through the needle tip at a reasonable rate within the operating parameters of the 3D printer (Paxton et al., 2017). A reasonable rate will be fast enough to ensure a viable production time, while premature drying of extruded ink is prevented and slow enough to ensure optimal 3D print fidelity (Paxton et al., 2017). Furthermore, the morphology of the extruded material should be smooth and strand-like (Ouyang et al., 2016).

Ouyang et al. (2016) demonstrated how the over-gelation of bioinks containing gelatin and alginate led to the extrusion of irregular and fragmented strand morphologies. Rutz et al. (2015) further reported soft partially crosslinked gels with storage moduli (G') of 1-100 Pa as 3D printable, while stiff gels with G' higher than 150 Pa were not 3D printable. The gelation of P(KA)-Az/4-PEG with 32% and 58 % conjugated Az, equilibrated after ~ 50 min at a G' of ~ 220 Pa and ~200 Pa, respectively (Figure 4.6). The G' of these "partially crosslinked" inks fall within the stiff non-3D printable range reported by Rutz et al.(2015). However, preliminary studies on hydrogels with lower crosslinking degrees also led to the extrusion of fragmented, albeit softer gels. While Rutz et al. briefly reported certain gels as behaving similarly, no further explanation was provided.

As part of the rheological characterisation of the P(KA)-Az/4-PEG ink, a preliminary investigation into the secondary crosslinking was performed (Figure 4.6). After the inks were equilibrated for 6000 s, the rheological measurements were paused for 3 cycles. During the first cycle, the samples were

UV irradiated for 10 min. This was followed by a control cycle without UV irradiation, while in the final cycle the samples were UV irradiated for 20 min. However, the increase in G' after the two UV irradiation cycles was too small to have an effect on the solidification of the P(KA)-Az/4-PEG inks.

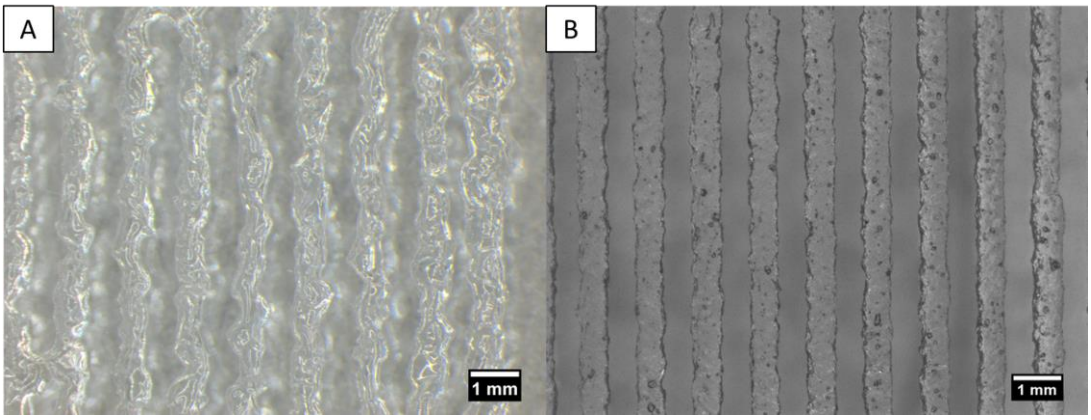


Figure 4.5 Images of the extruded strands of (A) P(KA)-Az/4-(PEG) and (B) CS-P(KA)/4-PEG

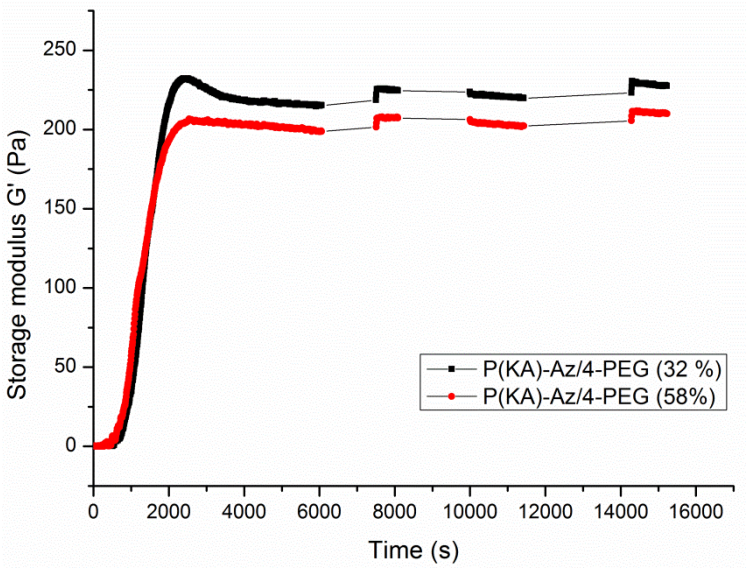


Figure 4.6 The development of storage modulus of the P(KA)-Az/4-PEG with varying degrees of conjugation, indicating the primary crosslinking between 0 and 6000 s, and the secondary crosslinking from UV irradiation at ~7500 s and ~15000 s

The "composite microgel" inks were expected to behave more like the jammed microgel inks as reported by Highley et al.(2019). At low strain, jammed microgels demonstrated an elastic response, while at increasing strain the microgels reached a yielding point, followed by a shear-thinning response (Highley et al., 2019). The viscosity behaviour of the "composite microgel" inks all showed Newtonian behaviour at low shear rates and non-Newtonian shear thinning between shear rates of 0.1 and 1000 s^{-1} (Figure 4.7). The shear-thinning regions of the plots were fitted to a power law regression using the following equation,

$$\eta = K\dot{\gamma}^{n-1} \quad \text{(Eq. 4.7)}$$

where η is the viscosity (Pa·s), $\dot{\gamma}$ is the shear rate (s^{-1}), and K and n are shear-thinning coefficients as summarised in Table 4.5. Paxton et al. used the viscosity coefficients to determine the average extrusion velocity, $\bar{v}$ of various materials using the following equation,

$$\bar{v} = \left(\frac{-\Delta P}{2LK}\right)\left(\frac{n}{3n+1}\right)R^{\frac{n+1}{n}} \quad \text{(Eq. 4.8)}$$

where ΔP is the pressure, L is the needle length and R is the needle diameter (Paxton et al., 2017). The calculated extrusion velocity at various printing parameters was then used to screen the materials according to a "3D printability window". It should be noted that the above calculation for $\bar{v}$ models the extrusion velocity based on a cylindrical needle, while a tapered needle was used in this study. Complex modelling of the flow dynamics inside tapered needles were beyond the scope of this study. Instead, we used the experimental extrusion velocity determined at specific extrusion pressures to evaluate the 3D printability of the "composite microgel" inks (Figure 4.8). The inks could be extruded through needle IDs of 0.4 mm and 0.2 mm at pressures within the instrumental limits (0.1 - 5.0 bar) of the 3D Bioplotter®. Furthermore, the extrusion velocities were within the 3D printability window of 0 - 40 mm·s^{-1} as identified by Paxton et al. (2017). Based on our experience with the 3D Bioplotter®, this range can be justified for its good shape printing fidelity. The 4-PEG-Ac-P(KA)/4-PEG ink required the least pressure and still extruded at a velocity of more than double the velocity of the other two inks. This correlates with the lower shear viscosities of 4-PEG-Ac-(PKA)/4-PEG measured at shear rates higher than ~2 s^{-1} (Figure 4.7). CS-P(KA)/4-PEG required a higher pressure to extrude at a velocity similar to PVA-P(KA)/4-PEG. This correlates with the trend in shear viscosities measured at shear rates higher than ~38 s^{-1}, where CS-P(KA)/4-PEG has a shear viscosity higher than PVA-P(KA)/4-PEG. It further highlights the complexity of correlating shear viscosity measurements with 3D printing conditions. Small differences in the viscosity behaviour of materials can have significant effects on their extrusion velocity and their shear rates within the 3D printing needle.

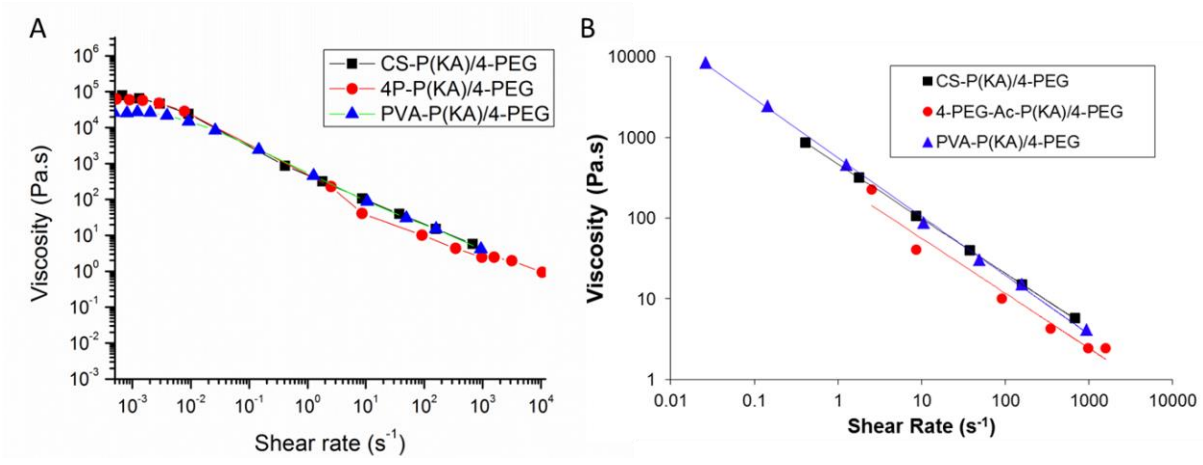


Figure 4.7 The viscosity behaviour of the "composite microgel" inks showing shear thinning as the shear rate is increased (A), and the shear-thinning region fit to the power law regression (B)

Table 4.5 The shear-thinning viscosity coefficients, K and n of the "composite microgel" inks

"Composite microgel" ink	K	n
4-PEG-P(KA)/4-PEG	301	0.276
CS-P(KA)/4-PEG	471	0.321
PVA-P(KA)/4-PEG	563	0.270

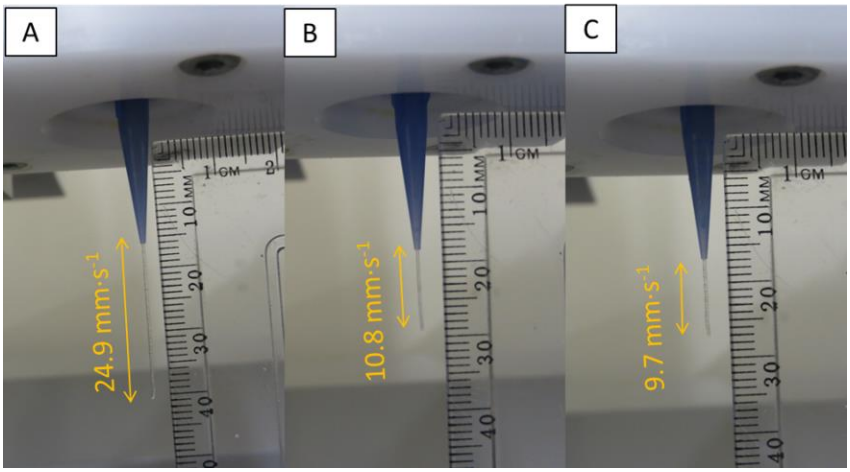


Figure 4.8 Images of the extruded strands of (A) 4-PEG-P(KA)/4-PEG at 0.5 bar, (B) CS-P(KA)/4-PEG at 1.5 bar and (C) PVA-P(KA)/4-PEG at 1.1 bar after 1 s, indicating the extrusion velocities (yellow) calculated from the length of the strands

4.3.2.2 Strand optimization and 3D layer stacking

The extrusion of the inks in the air is generally considered a good starting point for determining the printing parameters. However, further optimisation of the pressure and printing speed was required to obtain good 3D print fidelity. The effect of these parameters on the strand width is shown in Figure 4.9 and Figure 4.10. As expected, an increase in pressure at constant speed led to a higher material volume being dispensed per printing area and therefore a thicker strand width, while higher printing speed at constant pressure led to a lower material volume being dispensed per printing area, seen as a thinner strand width. Where the material volume was too low, it led to a discontinuous strand. This can be seen for the 4-PEG-Ac-P(KA)/4-PEG ink in Figure 4.9 at a constant printing speed of 20 mm/s and a pressure of 0.2 bar.

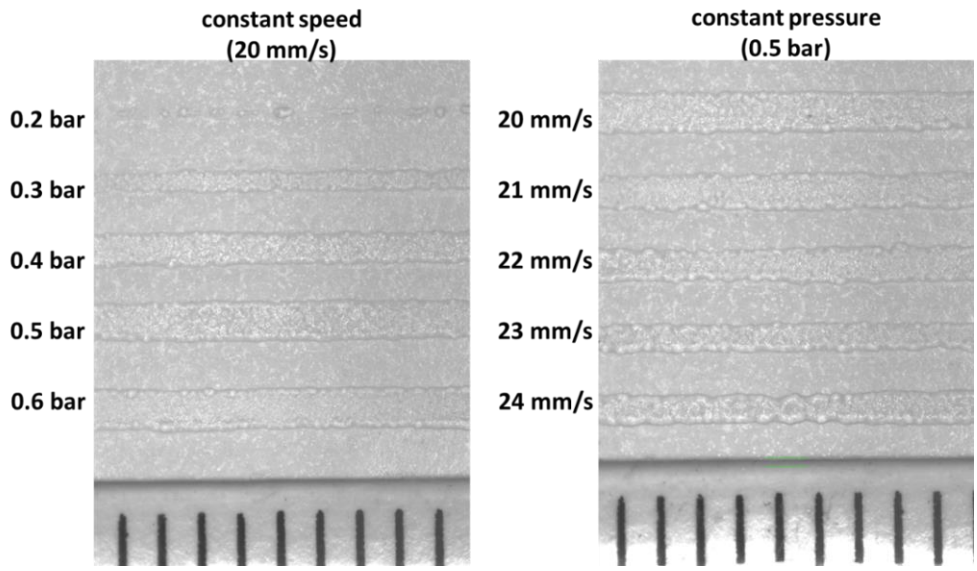


Figure 4.9 Images of the printed strands of 4-PEG-P(KA)/4-PEG at different printing pressures and different printing speeds

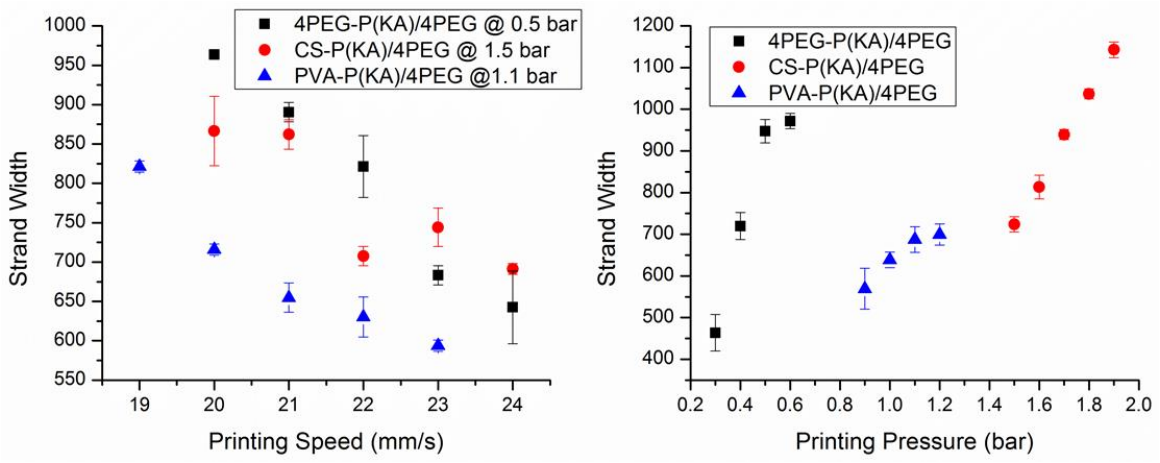


Figure 4.10 The effect of the 3D printing parameters on the strand width of the respective composite microgel pastes was investigated by varying the printing speed at constant pressures (A) and varying the printing pressure at a constant speed of 20 mm/s (B).

The layer slicing height was further taken into account when selecting the strand width. The layer slicing height is an arbitrary input parameter used in the slicing process to convert the 3D CAD design into 2D layers. It translates to the needle offset between two consecutive layers, to account for the height of the dispensed material. For this study, a slicing height of 80 % of the needle ID was selected. At strand widths matching the needle ID, this slicing height will allow adequate overlap between the layers and thereby good adhesion between the layers. Printing at larger strand widths will cause more overlap between the layers and essentially cause fusion of the layers and a loss 3D print fidelity. It is noted from Figure 4.10 that the majority of the strand widths are larger than the needle ID of 0.4 mm. From our 3D printing experience with the 3D Bioplotter®, good adhesion to the built plate is achieved by printing the first layer at a height of 80% of the needle diameter. However, this causes flattening of the strands, which corrects after the third layer of printing.

3D layer stacking of the "partially crosslinked" ink, P(KA)-Az/4-PEG, further confirmed the non-printability of these inks. Apart from the irregular morphology of the strands, the layers also fused together (Figure 4.11). 3D layer stacking of the "composite microgel" inks showed that all three inks could be 3D printed in layers (Figure 4.12). Closer inspection of the morphology of the layers, showed slight fusion of the layers of 4-PEG-Ac-P(KA)/4-PEG and PVA-P(KA)/4-PEG (Figure 4.13). The vertical pores formed by these inks can be seen as more rounded, due to sagging of the strands and fusion of the layers. The CS-P(KA)/4-PEG inks showed excellent layer stacking properties. The strands showed no evidence of sagging and the vertical pores had square morphologies. Subsequently, CS-P(KA)/4-PEG inks were selected for further optimisation of the 3D printing parameters to produce square scaffolds with 15 mm width and 2 mm height and different printing patterns (Table 4.2, Figure 4.14). The "porous" 3D printed scaffolds with these patterns were further referred to as the 0.4 mm scaffolds (0.4 mm needle ID; 1.0 mm strand spacing) and the 0.2 mm scaffolds (0.2 mm needle ID; 0.5 mm strand spacing).

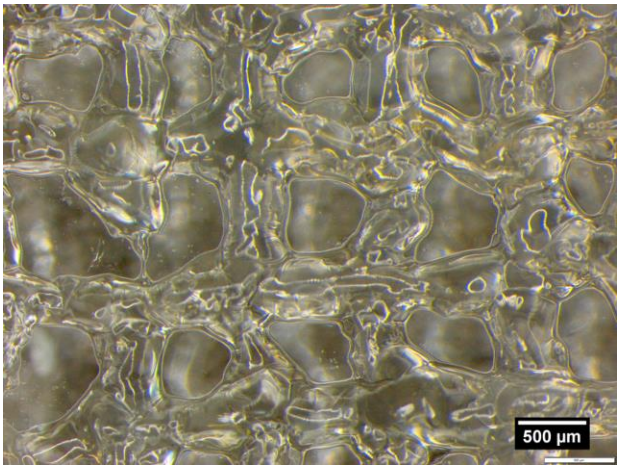


Figure 4.11 Image of the second layer of P(KA)-Az/4-PEG ink 3D printed with a 0.4 mm needle ID and 1 mm strand spacing

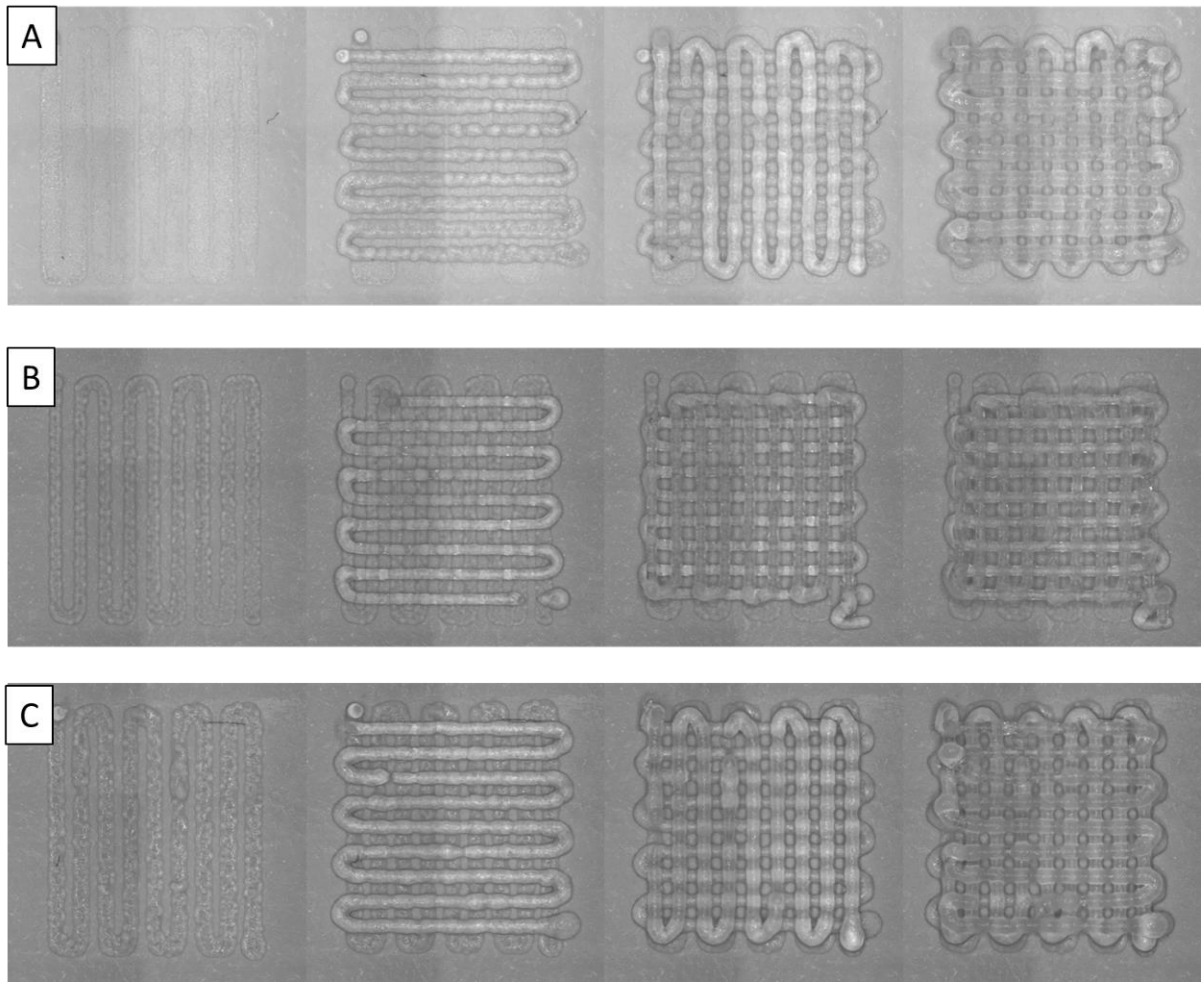


Figure 4.12 Images documenting the first four layers of the 3D printing process of (A) 4-PEG-P(KA)/4-PEG, (B) CS-P(KA)/4-PEG, and (C) PVA-P(KA)/4-PEG 3Dprinted with 0.4 mm needle ID and 1 mm strand spacing.

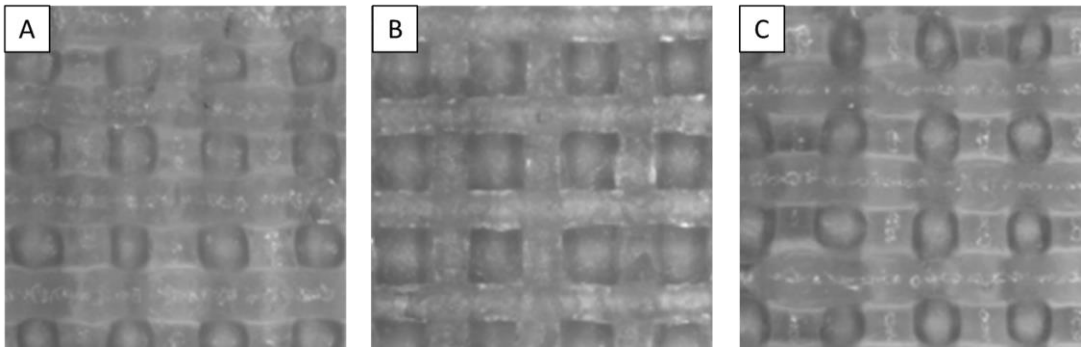


Figure 4.13 Close-up images of the layer morphology of the fourth 3D printed layers of (A) PEG-P(KA)/4-PEG, (B) CS-P(KA)/4-PEG, and (C) PVA-P(KA)/4-PEG 3D printed with 0.4 mm needle ID and 1 mm strand spacing

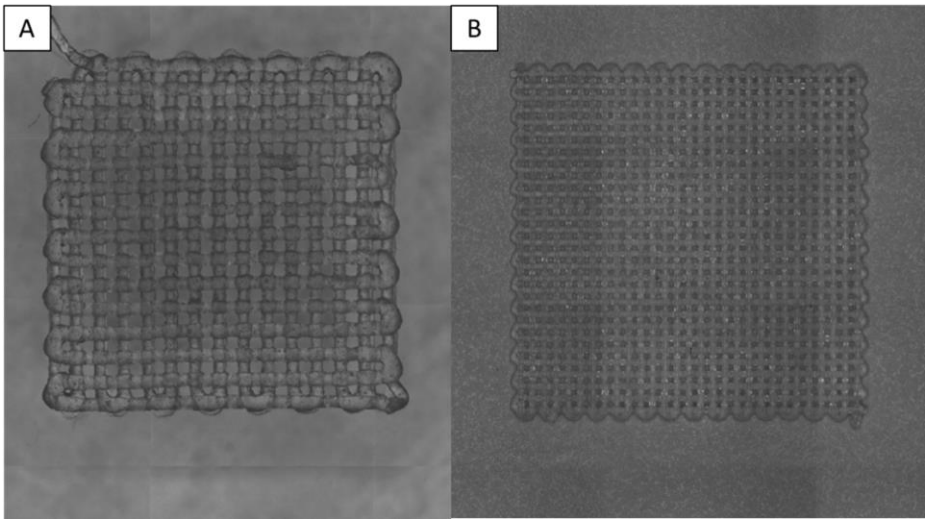


Figure 4.14 3D printing of CS-P(KA)/4-PEG ink with (A) 0.4 mm needle ID and 1.0 mm strand spacing and (B) 0.2 mm needle ID and 0.5 mm strand spacing

4.3.2.3 Post-print solidification and 3D print fidelity

The final step in determining the 3D printability of the "composite microgel" inks was to evaluate their solidification mechanism and 3D print fidelity. "Non-porous" 3D printing patterns of the "composite microgel" inks were investigated for this purpose. The solidification of the "composite microgel" inks was dependent on the gelation of the polymer solutions, 4-PEG-Ac, CS and PVA, acting as a matrix material for the P(KA)/4-PEG hydrogel microparticles. All three inks produced stiff scaffolds able to be lifted with a spatula after their respective solidification procedures (Figure 4.15), demonstrating successful incorporation of the hydrogel microparticles into a hydrogel matrix. However, the ease of the crosslinking and the post-print processing time for each ink is discussed below. Furthermore, the 3D print fidelity of the final scaffolds was quantified in terms of dimensional deviations from the CAD dimensions.

In this study, 4-PEG-Ac-P(KA)/4-PEG was photo-crosslinked for 10 min to achieve complete solidification of all layers. Photo-crosslinking is widely used in 3D printing due to its ease of use and its bioprinting applications (Pereira and Bártolo, 2015; Ozbolat and Hospodiuk, 2016). The gelation of 4-PEG-Ac was based on the photo-polymerisation of the acrylate moieties in the presence of a photoinitiator (Irgacure 2959). Shorter crosslinking times led to incomplete solidification of lower layers, while longer crosslinking times caused drying around the edge of the scaffolds. Post-print washing of 4-PEG-Ac-P(KA)/4-PEG scaffolds were further required to remove cytotoxic photoinitiators. The crosslinking time correlates well with the post-print photo-crosslinking time of 7.5 min reported for PEG-diacrylate (PEGDA) inks (Joas et al., 2018). In-situ photo-crosslinking of each layer can eliminate the need for post-print photo-crosslinking. Also, using photoinitiators with low cytotoxicity such as LAP can eliminate the need for post-print washing. 4-PEG-Ac-P(KA)/4-PEG

scaffolds showed significant swelling, which led to a 33.3 ± 1.5 % deviation from the CAD dimensions (Table 4.6).

The 3D printed CS-P(KA)/4-PEG scaffolds were produced by freeze-drying and subsequent washing with ethanol and distilled water to remove residual acetic acid. Unwashed scaffolds on the other hand, dissolved within less than two hours. CS hydrogel scaffolds for tissue engineering applications have been produced through a variety of covalent and ionic crosslinking reactions (Berger et al., 2004). The gelation of CS through neutralisation of the solution pH was also reported. Ang et al. (2002) 3D printed CS-based inks into a crosslinking solution containing sodium hydroxide (NaOH) to obtain fast neutralisation of the acetic acid solution used to dissolve CS. Bergonzi (2019) further investigated different neutralizing agents such as potassium hydroxide (KOH), sodium bicarbonate and ammonia vapours for the gelation of 3D printed CS. The solidification method used for the 3D printed CS-P(KA)/4-PEG scaffolds prepared in this study, required no optimisation of crosslinking solutions, which can be difficult and tedious. However, the washing steps can add to the post-print processing time. Nonetheless, this method proved highly successful in retaining the 3D printed structures. A16.4 ± 2.7 % deviation in the overall scaffold dimensions in relation to the CAD dimensions was found.

PVA-P(KA)/4-PEG scaffolds were prepared with 3-6 freeze-thaw cycles. While 3 cycles were adequate to provide solidification, the higher number of cycles led to a more robust construct. PVA is widely used in 3D printing as a supporting structure or a sacrificial material (Al-Ahmad et al., 2008; Walker, Lee and Wu, 2012). However, it rarely forms part of the final 3D printed scaffold. Kim et al. (2018) reported the 3D printing of gelatine/PVA blends for hard tissue engineering applications. A popular method of producing PVA hydrogel scaffolds is through freeze-thaw cycles. It is well known that a larger number of cycles will lead to a stiffer gel, due to an increase in the crystallinity of the polymer chains with every freezing step (Stauffer and Peppast, 1992). This method of post-print processing is very simple, however, it took the longest compared to the 4-PEG-Ac-P(KA)/4-PEG and CS-P(KA)/4-PEG scaffolds. Based on the overall scaffold dimensions, PVA-P(KA)/4-PEG scaffolds led to the smallest deviation from the CAD dimensions (Table 4.6). However, from Figure 4.15 it is seen that the PVA-P(KA)/4-PEG scaffold was tapered towards the top. Due to the number of repeat freeze-thaw cycles, it is likely that the scaffold dried slightly during the thawing process. Nonetheless, this effect can be minimised by maintaining the scaffold in a sealed environment during the thawing process.

In addition to the "non-porous" 3D printed scaffolds, the 3D print fidelity of the "porous" 3D printed scaffolds of CS-P(KA)/4-PEG was evaluated in terms of their printing patterns (Figure 4.16, Table 4.7). The intended vertical and horizontal channels as a result of the cross-hatch printing pattern can be seen from the top and side views of the scaffolds (Figure 4.16B, C, D & E). The deviations from the intended printing patterns correlate with the overall deviation from the CAD dimensions as a result of the material swelling (Table 4.6). It should be noted that the strand optimisation also played a

role in the deviation from the printing pattern. The strand optimisation used in this study was a crude process of balancing the strand diameter with the layer height. This was especially difficult with the smaller strand diameters of the 0.2 mm scaffold, as the layer height was prone to becoming too thin, which caused inadequate adhesion of extruded strands onto existing layers. Therefore, larger strand diameters were used for the 0.2 mm scaffold to ensure the layer height remains optimised for the total printing process.

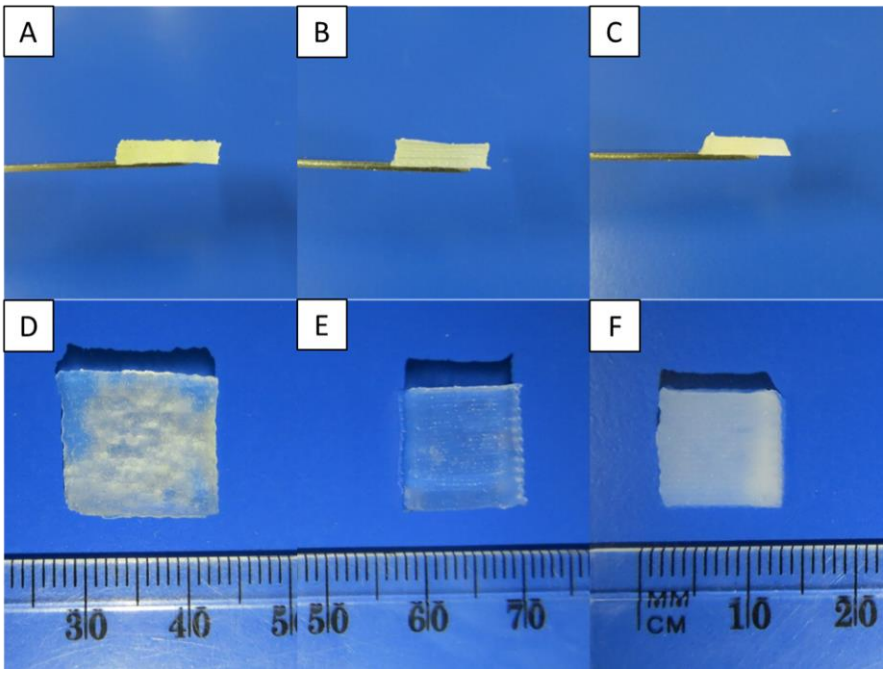


Figure 4.15 Images of the "non-porous" 3D printed scaffolds, 4-PEG-Ac-P(KA)/4-PEG (A & D), CS-P(KA)/4-PEG (B & E), and PVA-P(KA)/4-PEG (C & F)

Table 4.6 The percentage deviation in scaffold dimensions compared to CAD dimensions

Scaffold	% Deviation
4-PEG-Ac-P(KA)/4-PEG	33.3 ± 1.5
CS-P(KA)/4-PEG	16.4 ± 2.7
PVA-P(KA)/4-PEG	10.4 ± 2.1

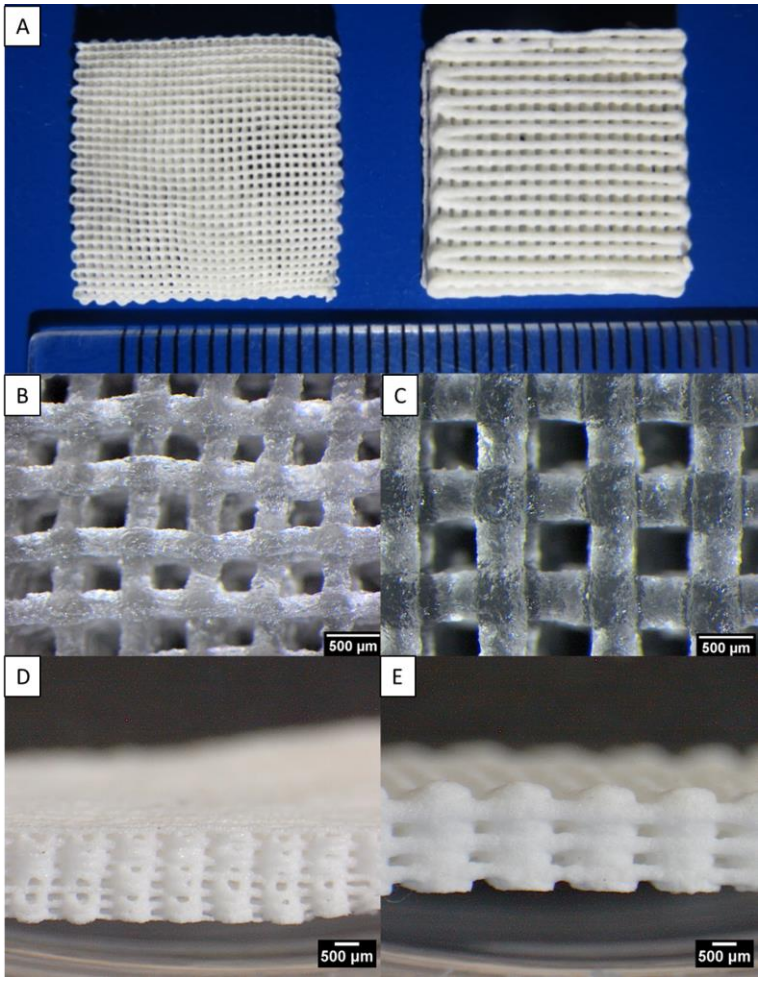


Figure 4.16 Images of the "porous" 3D printed CS-P(KA)/4-PEG 0.2 mm (A, LEFT) and 0.4 mm (A, RIGHT) scaffolds, and microscope images of the 0.2 mm (B &D) and 0.4 mm (C&E) scaffolds (top & side view). Scaffolds in A, D, and E were freeze-dried for better visualisation. Scaffolds in B and C were hydrated.

Table 4.7 The percentage deviation of strand diameter and inter-strand spacing of hydrated scaffolds compared to intended printing pattern parameters

Scaffold	Dimensions (µm)		Deviation (%)	
	Strand Diameter	Inter-strand Spacing	Strand Diameter	Inter-strand Spacing
0.2 mm Scaffold	241 ± 18	297 ± 37	20.7 ± 9.0	7.9 ± 6.0
0.4 mm Scaffold	457 ± 17	542 ± 28	14.2 ± 3.8	10.0 ± 4.0

4.3.3 Evaluation of the Physical Properties of the Composite Microgel Scaffolds with "non-porous" 3D Printing Patterns

The porosity of composite microgel scaffolds of 4-PEG-Ac-P(KA)/4-PEG, CS-P(KA)/4-PEG, and PVA-P(KA)/4-PEG was evaluated using SEM (Figure 4.17). These scaffolds all displayed an interconnected porous network. As summarised in Table 4.8, the average pore sizes of the scaffolds are within the ideal range of 20 to 125 μm reported for the regeneration of adult mammalian skin (Annabi et al., 2010). Further assessment of the percentage porosity of the scaffolds indicated that CS-P(KA)/4-PEG has the highest porosity at 82.6%, while PVA-P(KA)/4-PEG had the lowest porosity at 64.4%. It was seen that the scaffolds with larger pore sizes did not necessarily have a higher porosity. Instead, the scaffolds that appeared to have a higher interconnectivity and thinner membrane structures surrounding the pores had a higher % porosity. For tissue engineering applications, a higher pore interconnectivity provides better mass transfer of nutrients and cellular waste (Annabi et al., 2010).

As discussed in Chapter 3, the equilibrium swelling ratio (ESR) is closely related to the network structure of hydrogels. The ESR of the composite microgel scaffolds followed the same trend as the pore sizes. The larger pore sizes can indicate to a more flexible network structure and therefore allow more swelling of the scaffold, and vice versa.

Furthermore, the mechanical properties of the 4-PEG-Ac-P(KA)/4-PEG, CS-P(KA)/4-PEG, and PVA-P(KA)/4-PEG scaffolds were assessed under tensile and compressive stress. PVA-P(KA)/4-PEG scaffolds had the highest moduli under tensile and compressive stress. It is further seen that CS-P(KA)/4-PEG had the lowest moduli. It has been shown that porosity can play an important role in the mechanical properties of hydrogels (Lanasa, Hoffecker and Bryant, 2011). In this study, a higher porosity of the composite microgel scaffolds corresponded with lower mechanical properties. The materials reported here can be classified as microgel-filled hydrogels as defined by Richtering and Saunders (2014). Since no chemical or physical crosslinking between the microparticles and the hydrogel matrix was employed, the composite systems were not expected to have an increased modulus compared to the parent hydrogels (Richtering and Saunders, 2014).

Table 4.8 A summary of the physical properties of the composite hydrogels, 4-PEG-P(KA)/4-PEG, CS-P(KA)/4-PEG, and PVA-P(KA)/4-PEG

Scaffold	Average Pore Size (µm)	% Porosity	Equilibrium Swelling Ratio	Tensile Modulus (Pa)	Compressive Modulus (Pa)
4-PEG-P(KA)/4-PEG	102 ± 36	75.9 %	16.86 ± 1.97	203	235 ± 59
CS-P(KA)/4-PEG	72 ± 31	82.6 %	13.28 ± 0.80	132 ± 21	167 ± 41
PVA-P(KA)-4-PEG	33 ± 13	64.4 %	9.81 ± 1.03	711 ± 75	367 ± 3

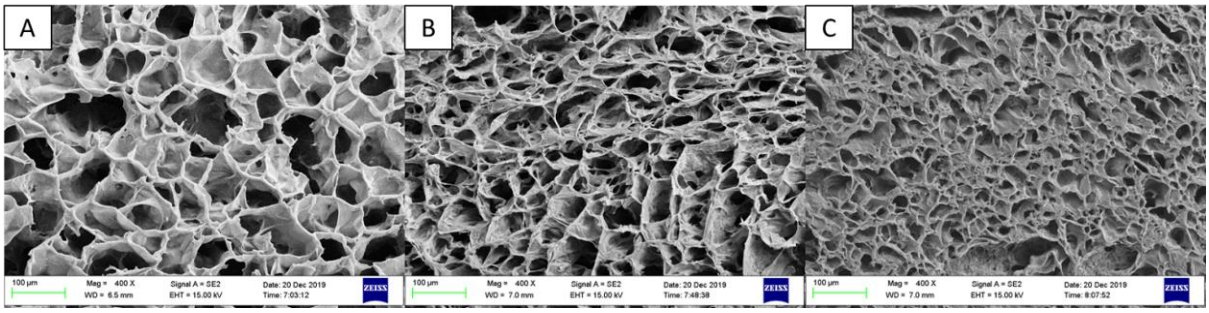


Figure 4.17 SEM micrographs of the cross-sections of freeze-dried composite hydrogels, 4-PEG-P(KA)/4-PEG (A), CS-P(KA)/4-PEG (B), and PVA-P(KA)/4-PEG (C)

4.3.4 Effect of 3D Printing Pattern on the Physical Properties of CS-P(KA)/4-PEG Scaffolds

Micro-pores spread over the surface of the strands of the scaffolds were visible with SEM (Figure 4.18). However, these were combined with non-porous areas, indicating the formation of a surface skin due to the freeze-drying process. Cross-sections of the scaffolds showed interconnected porous networks within the strands. The average sizes of these micro-pores (Table 4.9) were slightly smaller than the pores from the "non-porous" 3D printed scaffolds of CS-P(KA)/4-PEG. The formation of micro-pores was driven by the formation of ice crystals during the freeze-drying process. It is known that the rate of freezing affects the size of the crystals. Due to the larger surface area to volume ratio of the "porous" 3D printed scaffolds compared to the non-porous scaffolds, they are expected to freeze faster than the "non-porous" 3D printed scaffolds and could explain the decrease in pore sizes as a result of 3D printing. The differences in the micro-pore sizes between the 0.2 mm scaffolds and the 0.4 mm scaffolds were found to be insignificant ($p>0.05$).

The macro-porosity as a result of the 3D printing pattern shows the formation of square vertical channels running into the face of the scaffolds (Figure 4.18A & C). These channels are intersected by

horizontal channels running into the cross-section of the scaffolds, forming an interconnected network of channels (Figure 4.18B & D). The distance between strands were determined in the hydrated form as 297 ± 37μm and 542 ± 28 μm for the 0.2 mm and 0.4 mm scaffolds, respectively (Table 4.7). The theoretical macro-porosities of the 3D printed scaffolds were further calculated from CAD models, based on the experimental input parameters for strand diameter and strand spacing. As expected, the porosity of the 0.2 mm scaffolds was similar to the 0.4 mm scaffolds since the strand spacing, as well as the strand diameter, was changed with a factor of 2. On the other hand, the surface area to volume ratio (A : V ratio) of the 0.2 mm scaffold is almost 2 times larger than the 0.4 mm scaffold. The larger surface area is favourable to a higher cell infiltration.

The macro-porosity was further seen to affect the mechanical properties of CS-P(KA)/4-PEG scaffolds. Under tensile stress, the "porous" 3D printed scaffolds had lower moduli than the "non-porous" 3D printed CS-P(KA)/4-PEG scaffolds. However, the difference between the 0.2 mm scaffolds and the 0.4 mm scaffold was very small. Under compressive stress, the 0.4 mm scaffolds had a slightly lower modulus compared to the "non-porous" 3D printed scaffold, while the modulus of the 0.2 mm scaffold was more than three times smaller (Table 4.9). Schipani et al. (2020) correlated the change in printing pattern of PCL scaffolds with a change in scaffold porosity and used the latter to justify the differences in the compressive moduli of different scaffolds. For example, by increasing the strand spacing and thereby increasing the porosity, the compressive modulus was found to decrease. Also by decreasing the strand diameter, the porosity was increased and the compressive modulus decreased (Schipani et al., 2020). However, they did not model the effect of strand diameter at constant porosity on the mechanical properties.

Table 4.9 Effect of 3D Printing on the Physical Properties of CS-P(KA)/4-PEG Scaffolds

Scaffold	Average Pore Size (μm)	Porosity (%)	Theoretical Porosity (%)	A:V ratio	Tensile Modulus (Pa)	Compressive Modulus (Pa)
0.2 mm	54 ± 20	98 %	40.3 %	16.8	91	45 ± 8
0.4 mm	49 ± 18	98 %	39.6 %	8.8	82	147 ± 14

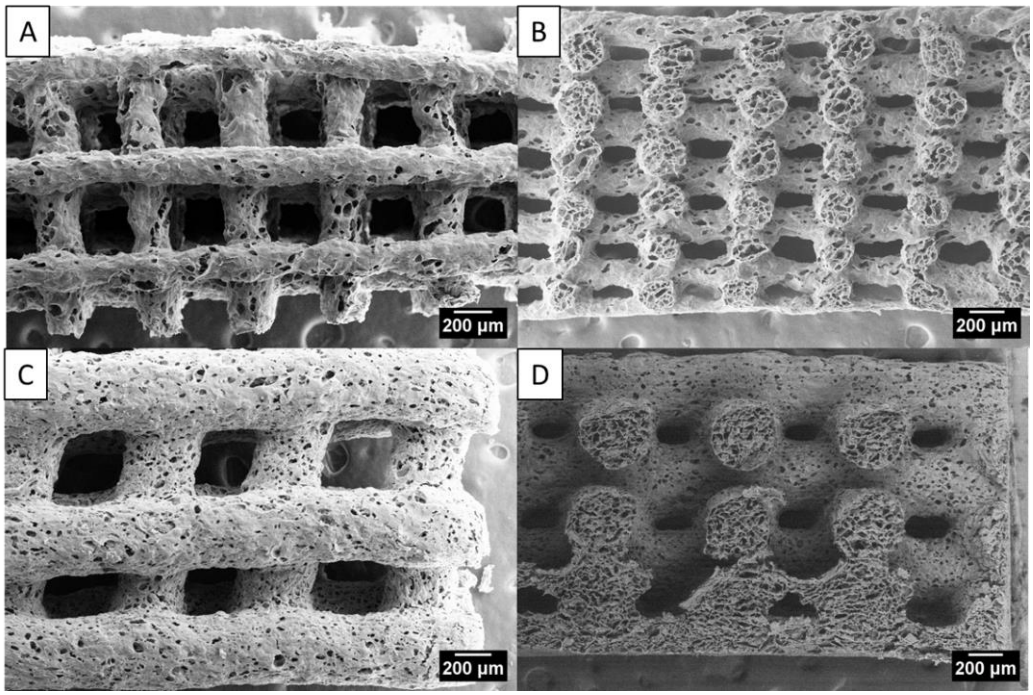


Figure 4.18 SEM micrographs of the "porous" 3D printed scaffolds of CS-P(KA)/4-PEG, 0.2 mm scaffold (A & B) and 0.4 mm scaffold (C & D)

4.3.5 Effect of P(KA)/4-PEG Microparticles on the Biocompatibility of the Composite Microgels

The adhesion and migration of NIH 3T3 fibroblasts on 4-PEG-Ac-P(KA)/4-PEG, CS-P(KA)/4-PEG, and PVA-P(KA)/4-PEG scaffolds was qualitatively assessed with fluorescence microscopy in comparison to 4-PEG-Ac, CS and PVA hydrogels. On the 4-PEG-Ac and the PVA hydrogels, no attached cells were observed on the hydrogel surface. PEG is widely used for its hydrogel properties (Zhu, 2010). However, due to its hydrophilicity and its low protein adsorptivity, PEG is also known for its low cell adhesion properties (Zhu, 2010). PVA is also known to have low cell adhesion properties. CS, on the other hand, showed large numbers of cells spread over the hydrogel surface. This was in agreement with the well-known cell adhesion properties of CS hydrogels (Ahmadi et al., 2015). On the composite microgels, clusters of cells are seen as spreading over the scaffold surfaces. Therefore, the addition of P(KA)/4-PEG microparticles to PEG and PVA greatly enhanced the biofunctionality of these hydrogels. Furthermore, the spreading of NIH 3T3 cells on the 3D printed CS-P(KA)/4-PEG scaffolds was also visualised. After 4 days of culturing, the cells were seen as migrating along the 3D printed strands.

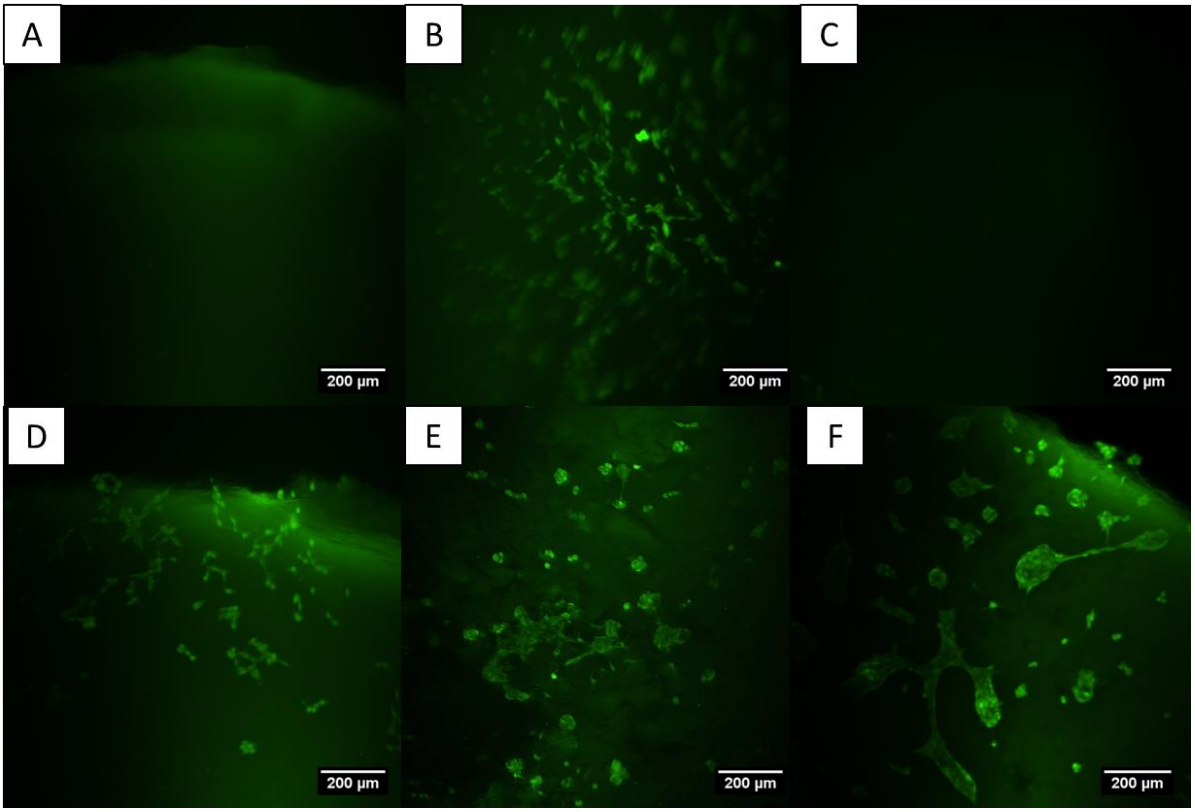


Figure 4.19 Micrographs of CFDA-SE stained NIH 3T3 fibroblasts cultured for 72 h on 4-PEG-Ac hydrogel (A), CS hydrogel (B), PVA hydrogel (C), 4-PEG-Ac-P(KA)/4-PEG (D), CS-P(KA)/4-PEG (E), and PVA-P(KA)/4-PEG (F)

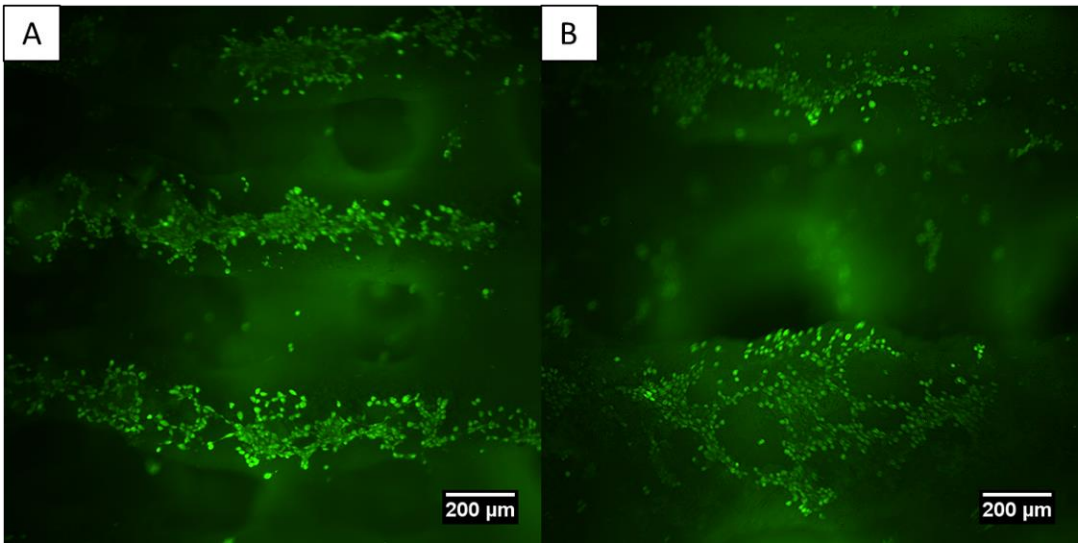


Figure 4.20 Micrographs of CFDA-SE stained NIH 3T3 fibroblasts cultured for 96 h on 0.2 mm scaffolds (A), and 0.4 mm scaffolds (B)

4.4 CONCLUSION

From the two approaches investigated to develop P(KA)/4-PEG hydrogels into biomaterial inks, only the "composite microgel" inks were 3D printable. These inks could be produced through the facile processing of P(KA)/4-PEG hydrogels into fine microparticles. The incorporation of these

microparticles into polymer matrices, afforded robust self-supporting inks, able to be 3D printed with high fidelity. Moreover, this approach demonstrated great versatility in terms of the hydrogel matrix components and the solidification mechanisms, with all three tested "composite microgel" inks showing good 3D printability. The physical properties of the 3D printed scaffolds could also be tuned based on the hydrogel matrix components. Based on the criteria used to assess the 3D printability, CS-P(KA)/4-PEG ink demonstrated the best properties. This ink proved highly successful in printing scaffolds with narrow strand diameter (~200 μm) and narrow strand spacing (~500 μm) while the integrity of the vertical and horizontal pores was maintained. By using different needle IDs and strand spacing, certain physical properties of the hydrogels could be tuned while the porosity was kept constant. This included the surface area to volume ratio, the macro-pore sizes, and the mechanical properties. Furthermore, this approach of incorporating P(KA)/4-PEG microparticles into the "composite microgel" inks proved successful in retaining the biocompatibility of P(KA)/4-PEG hydrogels and even enhanced the biofunctionality of the bioinert 4-PEG and PVA hydrogels.

4.5 REFERENCES

AHANGAR, P. et al. (2019) Current Biomedical Applications of 3D Printing and Additive Manufacturing. *Applied Sciences*, 9(1713), pp. 1–23.

AHMADI, F. et al. (2015) Chitosan based hydrogels : characteristics and pharmaceutical applications. *Research in Pharmaceutical Sciences*, 10(1), pp. 1–16.

AL-AHMAD, A. et al. (2008) Bacterial and Candida albicans adhesion on rapid prototyping-produced 3D-scaffolds manufactured as bone replacement materials. *Journal of Biomedical Materials Research Part A*, 87A, pp. 933–943.

ANG, T.H. et al. (2002) Fabrication of 3D chitosan-hydroxyapatite scaffolds using a robotic dispensing system. *Materials Science and Engineering C*, 20(1–2), pp. 35–42.

ANNABI, N. et al. (2010) Controlling the Porosity and Microarchitecture of Hydrogels for Tissue Engineering. *Tissue Engineering Part B: Reviews*, 16(4), pp. 372–383.

BERGER, J. et al. (2004) Structure and interactions in covalently and ionically crosslinked chitosan hydrogels for biomedical applications. *European Journal of Pharmaceutics and Biopharmaceutics*, 57, pp. 19–34.

BERGONZI, C. et al. (2019) Study of 3D-printed chitosan scaffold features after different post-printing gelation processes. *Scientific Reports*, 9(362), pp. 1–11.

FAN, D., STAUFER, U. and ACCARDO, A. (2019) Engineered 3D Polymer and Hydrogel Microenvironments for Cell Culture Applications. *Bioengineering*, 6(113), p. 6040113.

GOPINATHAN, J. and NOH, I. (2018) Recent trends in bioinks for 3D printing. *Biomaterials Research*, 22(11), pp. 1–15.

GROLL, J. et al. (2019) A definition of bioinks and their distinction from biomaterial inks. *Biofabrication*, 11, p. 13001.

HABERSTROH, K. et al. (2010) Bone repair by cell-seeded 3D-bioplotted composite scaffolds made of collagen treated tricalciumphosphate or tricalciumphosphate-chitosan- collagen hydrogel or PLGA in ovine critical-sized calvarial defects. *Journal of Biomedical Materials Research - Part B Applied Biomaterials*, 93B, pp. 520–530.

HERMANSON, G.T. (2013) *Bioconjugate Techniques*. Third edit. AUDET, J. and PREAP, M. (eds.). London: Elsevier Inc.

HIGHLEY, C.B. et al. (2019) Jammed Microgel Inks for 3D Printing Applications. *Advanced Science*, 6, p. 1801076.

JAMRÓZ, W. et al. (2018) 3D Printing in Pharmaceutical and Medical Applications – Recent

Achievements and Challenges. *Pharmaceutical Research*, 35(35), pp. 1–22.

JOAS, S. et al. (2018) Extrusion-Based 3D Printing of Poly(ethylene glycol) Diacrylate Hydrogels Containing Positively and Negatively Charged Groups. *Gels*, 4(69), pp. 1–17.

KELLY, C.N. et al. (2018) Design and Structure–Function Characterization of 3D Printed Synthetic Porous Biomaterials for Tissue Engineering. *Advanced Healthcare Materials*, 7, p. 1701095.

KIM, H. et al. (2018) Gelatin/PVA scaffolds fabricated using a 3D-printing process employed with a low-temperature plate for hard tissue regeneration : Fabrication and characterizations. *International Journal of Biological Macromolecules*, 120, pp. 119–127.

KIRCHMAJER, D.M., GORKIN III, R. and IN HET PANHUIS, M. (2015) An overview of the suitability of hydrogel-forming polymers for extrusion-based 3D-printing. *J. Mater. Chem. B*, 3(20), pp. 4105–4117.

KYLE, S. et al. (2017) ' Printability' of Candidate Biomaterials for Extrusion Based 3D Printing: State-of-the-Art. *Advanced Healthcare Materials*, 6, p. 1700264.

LANASA, S.M., HOFFECKER, I.T. and BRYANT, S.J. (2011) Presence of pores and hydrogel composition influence tensile properties of scaffolds fabricated from well-defined sphere templates. *Journal of Biomedical Materials Research Part B: Applied Biomaterials*, 96B(2), pp. 294–302.

LEE, H. et al. (2013) Cell(MC3T3-E1)-Printed Poly(ε-caprolactone)/Alginate Hybrid Scaffolds for Tissue Regeneration. *Macromolecular Rapid Communications*, 34, pp. 142–149.

LEWIS, P.L., GREEN, R.M. and SHAH, R.N. (2018) 3D-printed gelatin scaffolds of differing pore geometry modulate hepatocyte function and gene expression. *Acta Biomaterialia*, 69, pp. 63–70.

MARTÍNEZ-VÁZQUEZ, F.J. et al. (2015) Fabrication of novel Si-doped hydroxyapatite/gelatine scaffolds by rapid prototyping for drug delivery and bone regeneration. *Acta biomaterialia*, 15, pp. 200–9.

MOTA, C. et al. (2015) Additive manufacturing techniques for the production of tissue engineering constructs. *Journal of Tissue Engineering and Regenerative Medicine*, 9(3), pp. 174–190.

NARAYANAN, L.K. et al. (2016) 3D-Bioprinting of Polylactic Acid (PLA) Nanofiber−Alginate Hydrogel Bioink Containing Human Adipose-Derived Stem Cells. *ACS Biomaterials Science and Engineering*, 2, pp. 1732–1742.

NEUFURTH, M. et al. (2014) Engineering a morphogenetically active hydrogel for bioprinting of bioartificial tissue derived from human osteoblast-like SaOS-2 cells. *Biomaterials*, 35(31), pp. 8810–9.

NGO, T.D. et al. (2018) Additive manufacturing (3D printing): A review of materials, methods,

applications and challenges. *Composites Part B: Engineering*, 143, pp. 172–196.

OUYANG, L. et al. (2016) Effect of bioink properties on printability and cell viability for 3D bioplotting of embryonic stem cells. *Biofabrication*, 8(3), p. 35020.

OZBOLAT, I.T. and HOSPODIUK, M. (2016) Current advances and future perspectives in extrusion-based bioprinting. *Biomaterials*, 76, pp. 321–343.

PANWAR, A. and TAN, L.P. (2016) Current Status of Bioinks for Micro-Extrusion-Based 3D Bioprinting. *molecules*, 21(685), p. 21060685.

PAXTON, N. et al. (2017) Proposal to assess printability of bioinks for extrusion-based bioprinting and evaluation of rheological properties governing bioprintability. *Biofabrication*, 9, p. 044107.

PEREIRA, R.F. and BÁRTOLO, P.J. (2015) 3D Photo-Fabrication for Tissue Engineering and Drug Delivery. *Engineering*, 1(1), pp. 90–112.

RICHTERING, W. and SAUNDERS, B.R. (2014) Gel architectures and their complexity. *Soft Matter*, 10, pp. 3695–3702.

RICKETT, T.A. et al. (2011) Rapidly Photo-Cross-Linkable Chitosan Hydrogel for Peripheral Neurosurgeries. *Biomacromolecules*, 12, pp. 57–65.

RUTZ, A.L. et al. (2015) A Multimaterial Bioink Method for 3D Printing Tunable, Cell-Compatible Hydrogels. *Advanced Materials*, 27, pp. 1607–1614.

SCHINDELIN, J. et al. (2012) Fiji: an open-source platform for biological-image analysis, *Nature methods,* 9(7), pp. 676-682.

SCHIPANI, R. et al. (2020) Integrating finite element modelling and 3D printing to engineer biomimetic polymeric scaffolds for tissue engineering. *Connective Tissue Research*, 61(2), pp. 174–189.

SCHUURMAN, W. et al. (2013) Gelatin-Methacrylamide Hydrogels as Potential Biomaterials for Fabrication of Tissue-Engineered Cartilage Constructs. *Macromolecular Bioscience*, 13(5), pp. 551–561.

SINGH, M. and JONNALAGADDA, S. (2020) Advances in bioprinting using additive manufacturing. *European Journal of Pharmaceutical Sciences*, 143, p. 105167.

STAUFFER, S.R. and PEPPAST, N.A. (1992) Poly(vinyl alcohol) hydrogels prepared by freezing-thawing cyclic processing. *Polymer*, 33(18), pp. 3932–3936.

WALKER, J.M., LEE, M. and WU, B. (2012) Recent Advances in 3D Printing of Tissue Engineering Scaffolds. In: LIEBSCHNER, M.A.K. (ed.) *Computer-Aided Tissue Engineering SE - 15*. Methods in Molecular Biology. Humana Press, pp. 257–267.

WANG, X. et al. (2014) Effect of bioglass on growth and biomineralization of SaOS-2 cells in hydrogel after 3D cell bioprinting. *PloS one*, 9(11), p. e112497.

WÜST, S. et al. (2014) Tunable hydrogel composite with two-step processing in combination with innovative hardware upgrade for cell-based three-dimensional bioprinting. *Acta Biomaterialia*, 10, pp. 630–640.

YANG, S. et al. (2002) The Design of Scaffolds for Use in Tissue Engineering. Part II. Rapid Prototyping Techniques. *Tissue Engineering*, 8(1), pp. 1–11.

ZHU, J. (2010) Bioactive Modification of Poly(ethylene glycol) Hydrogels for Tissue Engineering. *Biomaterials*, 31(17), pp. 4639–4656.

CHAPTER 5: *IN VIVO* EVALUATION OF A 3D PRINTED SCAFFOLD AS A WOUND HEALING DEVICE ON A BURN WOUND MODEL OF SPRAGUE DAWLEY RATS

5.1 INTRODUCTION

Burn wounds typically lead to large areas of skin tissue loss. Full-thickness burn wounds involve damage to the epidermis, the dermis and deeper subcutaneous structures (Stone et al., 2018). Normal wound healing processes are typically inadequate to provide rapid wound closure to full-thickness wounds. Apart from the systemic inflammatory response, extensive healing times, and severe scarring, such wounds can be life-threatening due to their high infection risk (Stone et al., 2018). Dermal grafts and skin substitutes provide adequate wound closure and a temporary dermal matrix for full-thickness burn wounds. It has also been reported that such treatments can reduce the scarring effect of normal wound healing (Sharpe and Martin, 2013). The variety of currently available skin substitutes ranging from natural to synthetic materials have been thoroughly reviewed (Shahrokhi, Arno and Jeschke, 2014; Sheikholeslam et al., 2018; Stone et al., 2018; Haddad et al., 2018).

The latest advancements in skin substitutes and skin regeneration include the use of 3D printing and bioprinting (Vijayavenkataraman, Lu and Fuh, 2016; He et al., 2018; Haddad et al., 2018). In particular, bioprinting has been used to produce 3D printed skin equivalents with representative skin layers consisting of keratinocytes and fibroblasts, respectively (Cubo et al., 2016; Kim et al., 2018; Liu et al., 2019; Derr et al., 2019). Intini et al. (2018) also reported a 3D printed chitosan-based scaffold with *in vivo* wound healing potential. 3D printing is widely cited for its ability to produce tissue engineering scaffolds with high controllability in terms of internal architecture, which directly affects the physical and biological properties. Cross-hatch 3D printing patterns are typically used in tissue engineering studies. It allows easy variations in the architectures by changing the strand diameter, strand spacing, orientation between layers, and staggered strand placements. While a few studies have correlated the 3D printed architecture of scaffolds with their mechanical properties and their cell-seeding efficiency, Kelly et al. (2018) found that definitive studies on the structure-function relationship of 3D printed materials still largely lacks. Specifically, in *in vivo* wound healing studies, the structure-function relationship of 3D printing are underexplored.

In this phase of the study, the aim was to investigate the performance of the 3D printed system on an *in vivo* wound healing model. It was however recognised that a number of *in vitro* wound models have been developed as an alternative to *in vivo* animal models to study wound healing. This includes the wounding of 2D cell monolayers; 3D scaffolds populated with skin cells; tissue engineered human skin equivalents, and *ex vivo* human skin (Chen et al., 2014; Kilsdonk et al., 2013; Coolen et al,

2008). Since these models do not represent the whole wound healing milieu, they are primarily used to investigate cell migration and reepithelialisation. *In vivo* animal models, on the other hand, are typically used to study deep partial thickness and full thickness burn wounds (Qu and Nourbakhsh, 2017; Guo et al., 2017; Veen, 2010). The CS-P(KA)/4-PEG biomaterial prepared in Chapter 4, demonstrated desirable physical and biological properties. While chitosan was primarily used as a matrix for the P(KA)/4-PEG microparticles during the 3D printing process, it is also widely used in tissue engineering applications due to its biocompatibility, biodegradability, and inherent antimicrobial properties (Ahmadi et al., 2015). It has also been reported that chitosan accelerates the infiltration of inflammatory cells and the formation of granulation tissue in wound healing applications (Ueno, Mori and Fujinaga, 2001). Mekhail, Jahan and Tabrizian (2014) has also reported on hydrogel blends of chitosan and poly-L-lysine, with enhanced fibroblast adhesion and proliferation.

Furthermore, the CS-P(KA)/4-PEG material demonstrated superior 3D printable properties and facilitated investigation into the effect of 3D printing on the physical properties of the scaffolds. In this chapter, a full-thickness burn wound model of Sprague Dawley rats was used to investigate the *in vivo* wound healing performance of two CS-P(KA)/4-PEG 3D printed scaffolds with porous and non-porous architectures. It was proposed that the distinct physical properties of the two scaffolds achieved through 3D printing, would affect their *in vivo* performance. The wound healing was evaluated in terms of wound contraction, scar formation, and histological assessment.

5.2 MATERIALS AND METHODS

5.2.1 Preparation of the Wound Healing Device

3D printable inks of CS-P(KA)/4-PEG were prepared according to the procedures described in Chapter 4. A 3D Bioplotter® (EnvisionTEC GmbH, Germany) was used to prepare cylindrical scaffolds with 1.5 mm diameter and 1.3 mm height. The scaffolds were prepared with a needle tip having an ID of 0.2 mm. Two different scaffolds, one with a "non-porous" 3D printed architecture and a "porous" 3D printed architecture were prepared (Table 5.1). The scaffolds were frozen at -20 °C immediately after printing. After overnight freezing, the scaffolds were further cooled to -60 °C before lyophilizing. The scaffolds were then washed in absolute ethanol (99.9%), followed by subsequent washes with ethanol in distilled water dilutions (90%, 80%, 70%, 60%, 50%, 30%, 10% and 0% ethanol). Each washing cycle was allowed to equilibrate for 1 h in order to remove any traces of acetic acid. The scaffolds were then lyophilised. After lyophilisation, the scaffolds were sterilised under UV light (265 nm) for 10 min and then washed with 70% ethanol. Sterile PBS (pH 7.2) dilutions (40%, 50%, 70%, 90% and 100%) in ethanol was then used to wash the scaffolds.

Table 5.1 A summary of the 3D printing pattern of the "non-porous" and "porous" scaffold

Pattern Parameter	"Non-porous" Scaffold	"Porous" Scaffold
Strand diameter (mm)*	0.2	0.2
Strand spacing (mm)	0.2	0.5
Inter-strand spacing (mm)**	0.0	0.3
Layer height	0.16	0.16
Layer Orientation	90°	90°

*Strand diameter based on the needle ID
**Inter-strand spacing is the distance between two adjacent strands

5.2.2 Study Design

All animal studies were performed in compliance with the "Guidelines for the Use and Care of Animals" published by the Animal Ethics Screening Committee (AESC) and ethics clearance (2018/10/51C) was approved by the AESC of the University of the Witwatersrand.

Fifty-eight (58) male Sprague Dawley rats weighing 250 - 300 g were utilized in this study, with 10 rats allocated to a pilot study and 48 rats allocated to the experimental study. The rats were housed in single cages while they acclimatise to the laboratory conditions for 7-14 days. The rats were provided with water and food in accordance with a standard rat diet *ab libitum*. The temperature of the cages was controlled at ~ 25 °C and a 12 hour light/12 hour dark cycle was maintained.

The pilot study was used to evaluate the degree and reproducibility of the burn wound (Group A; n=5) and to ensure the efficacy of the pain management (Group B; n=5). The evaluation of the pain management during a pilot study was required by the AESC of the University of the Witwatersrand. The report from this study is included in the Appendices (see Appendix C) and its approval by the AESC warranted continuation of the full experimental study. For the experimental study, the treatment groups were divided into one control group (n =12), one comparative group (n = 12), and two experimental groups (n=12). After the burn wound was created, the animals were randomly divided into four groups and each group was assigned to the relevant treatment groups as described below.

Pilot study: (n = 10/group)

Group A: Evaluation of degree and reproducibility of the burn wound

Group B: Evaluation of pain management

Treatment groups: (n = 12/group)

"Jelonet" (Control group): Plain non-medicated paraffin gauze, Jelonet◊ (Smith & Nephew)

"Bactigras" (Comparative group): Paraffin gauze medicated with chlorhexidine acetate, Bactigras◊ (Smith and Nephew)

"Non-porous"(Experimental group): "Non-porous" 3D printed scaffold of CS-P(KA)/4-PEG

"Porous" (Experimental group): "Porous" 3D printed scaffold of CS-P(KA)/4-PEG

5.2.3 Burn Wound Injury

A severe burn wound model representing full-thickness tissue loss was created on the upper dorsal area of the rats, according to the procedures of a study previously carried out at the Central Animal Services (CAS) unit (Mayet, 2016). During the preparation and surgical procedure of the burn wound model, the blood pressure and body temperature of the rats was monitored using a BP monitor attached to the foot of the rats.

The burn wound injury can be divided into the following three steps:

Step 1: Wound Site Preparation

The animals were pre-treated with analgesics to reduce their shock reaction to the pain. This included jelly cubes medicated with tramadol (4 mg/kg) given to the rats 12 hours before the burn procedure. One hour before the procedure, the rats also received a dose of morphine (0.1 mL/100 g) as an analgesic. The rats were then anaesthetised in an isoflurane gas chamber and immobilized in the ventral position. The hair on the upper dorsal area of the rats was removed using an electric shaver and the area was disinfected with an alcohol swab. The position where the burn wound was to be made was indicated with a marker, 1 cm towards the right of the spinal cord and 1 cm from the shoulder blade towards the rat middle. L-block local anaesthesia was induced at the marked position, by injecting lignocaine.

Step 2: Burn Procedure

A metal probe with a diameter of 15 mm was preheated to 71 -75 °C in boiling water and applied to the shaved area for 10 s to create the burn wound. After the creation of the burn wound, the rats were given analgesics twice daily for the remainder of the study. This analgesic was in the form of jelly cubes medicated with Tramadol (4 mg/kg).

Step 3: Surgical Removal of the Scab

48 hours after the rats were burned; the scab from the burned area was surgically removed to create the full-thickness burn wound model. One hour before the procedure, the rats received a dose of morphine (0.1 mL/100 g) as an analgesic. They were then anaesthetised with isoflurane as an inhalation anaesthetic agent and immobilised in the lateral position. The damaged skin tissue including the epidermis and the dermis was then removed. The relevant treatments were applied according to the different treatment groups. These primary treatments were then covered with secondary bandages.

5.2.4 Bandage Changes and Tissue Sampling

Bandage changes were performed every 5 days, while the rats were anaesthetised with isoflurane gas.

After 5, 11, 15 and 20 days, three rats from each treatment group were euthanised by the direct intercardial administration of sodium pentobarbitone (200 mg/kg) to ensure fast and painless death to the rats [27]. Tissue samples of the wound areas and surrounding tissue were then taken.

5.2.5 Wound Contraction Rate

Photographs for visual inspection of the different treatment groups were taken at days 0, 5, 11, 15 and 20 days post-application. This provided a visual record of the healing process to be compared between the different treatment methods.

FIJI (v. 1.51n, ImageJ, URL: https://imagej.net/Fiji) (Schindelin et al., 2012) was used to determine the respective wound areas from the photographs. The wound contraction rate was determined by comparing the initial wound area (A_0) with the wound area on corresponding days after wounding (A_d), using the following equation,

$$\%\ wound\ contraction = \frac{A_0 - A_d}{A_0} \times 100$$

5.2.6 Histological Assessment

Tissue sections from the wounded area, the wound bed, and healthy tissue surrounding the burn area were excised for histological studies. The tissue sections were fixed in 10% phosphate-buffered formalin (pH 7) at room temperature. The samples were prepared by IDEXX laboratories (South Africa). The samples were cut and processed in an automated tissue processor into 5-6 μm sections that were mounted on slides to be stained in an automated Haematoxylin and Eosin tissue stainer. Histological evaluation and semi-quantitative grading was performed by pathologists from IDEXX laboratories provided with blind samples. A scoring system from Nussbaum, Mazzulli and Pritzker (2009) was used for the semi-quantitative grading of histological features (Table 5.2).

Table 5.2 The scoring system for semi-quantitative grading of histological features reported by Nussbaum, Mazzulli and Pritzker (2009) was used by pathologists from IDEXX laboratories (South Africa) during blind sampling.

Histological Feature	Grading	Description
Oedema	0	No evidence
	1	Focal presence at the wound margins
	2	Present in <50% of wound tissue examined
	3	Present in >50% of wound tissue examined
Leukocytes	0	No evidence
	1	Mild Presence
	2	Moderate number of cells
	3	Prominent feature
Macrophages	0	No evidence
	1	Mild presence
	2	Moderate number of cells
	3	Prominent feature
Granulation tissue	0	No evidence
	1	Present at wound margins
	2	Present in <50% of wound tissue examined
	3	Present in >50% of wound tissue examined
Fibroblasts	0	No evidence
	1	Present only in perivascular spaces
	2	Present in <50% of wound tissue examined
	3	Present in >50% of wound tissue examined
Collagen	0	No evidence
	1	Focal presence in fibroblasts around new capillaries
	2	Moderated amount in repair tissue
	3	Dominant feature
Epithelisation	0	No evidence
	1	Epidermal thickening and cell migration at wound margins
	2	>50% of wound epithelialised
	3	Epithelisation complete

5.2.7 Statistical Evaluation

Results were reported as mean ± standard deviation. One-way analysis of variance (ANOVA) and student's *t*-test were used for comparison between groups. A value of $p < 0.05$ was considered statistically significant. Due to the ordinal nature of the semi-quantitative histological grading, scores from three samples were reported as the mode.

5.3 RESULTS AND DISCUSSION

5.3.1 Validation of the Burn Wound Model

The creation of the burn wound was investigated during the pilot study to ensure a reproducible burn wound model was used for the *in vivo* study. It is known that temperature, contact time and contact pressure will determine the extent of the burn wound. Boiling water is often used to heat metal rods to create the burn wound (Cai et al., 2014; Mayet, 2016). By using a thermocouple, the contact

temperature of a metal rod heated in boiling water was determined. A maximum temperature range of 71 - 75 °C was reached after heating the rod for 30 - 60 min. To simulate the burn wound creation, the probe was removed from the boiling water and placed on a cool surface for 10 s. The maximum temperature range was then reached after 5 min of heating. Therefore, at least 30 min of initial heating time and 5 min heating time between burn procedures were allowed. The partial-thickness burn wound was created with a contact time of 10 s and slight pressure on the probe to ensure uniform, perpendicular contact with the skin.

It is known that burn wounds are dynamic, with necrosis developing over time. Therefore, the wounds were allowed to stabilize for 48 hours. The appearance of the burn wounds was pale at the contact area of the metal rod and slightly red around the perimeter of the wound (Figure 5.1A). The pale colouration can be associated with deep-partial thickness wounds (Guo et al., 2017). The histological assessment allowed further evaluation of the tissue damage at the wound site. The epidermis appeared thin and multifocally lost in the middle of the lesions, while coagulative necrosis of the deep dermis was evident. Adipose infiltration ranging from mild to severe was visible in the deep dermis of the lesion (Figure 5.2). In addition, the infundibular portions of hair follicles showed some damage. However, the follicular isthmus and hair bulbs were still intact. Nonetheless, the lesions were compatible with partial-thickness burn wounds. Consequently, to create the full-thickness wound and to mimic the clinical treatment of full-thickness burn wounds (Lan et al., 2014), the burn wound was excised before the application of treatments (Figure 5.1B).The method to create the burn wounds closely resembled the method reported by Guo et al.(2017). They created partial-thickness burns in Sprague Dawley rats using an in-house created device heated to 70 °C and placed on the rat skin for 10 s at a pressure equal to the weight of the device (Guo et al., 2017).

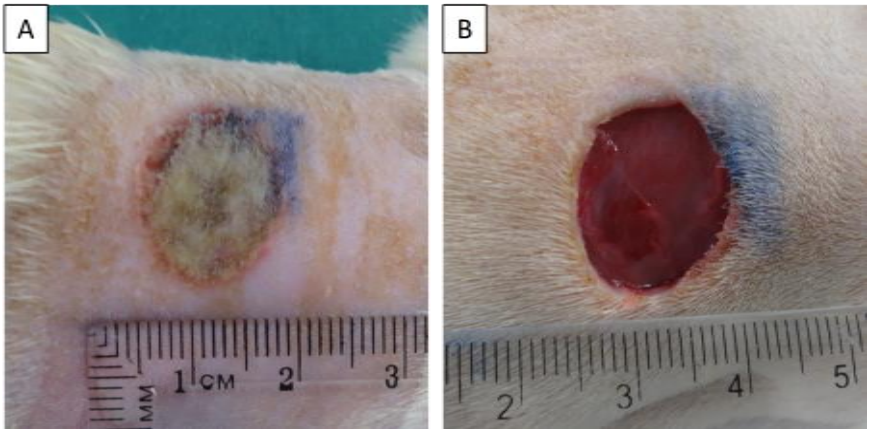


Figure 5.1 Images of the partial-thickness burn wound site 48 h after the burn wound creation (A), and the full-thickness wound after excision of the epidermis and the dermis (B)

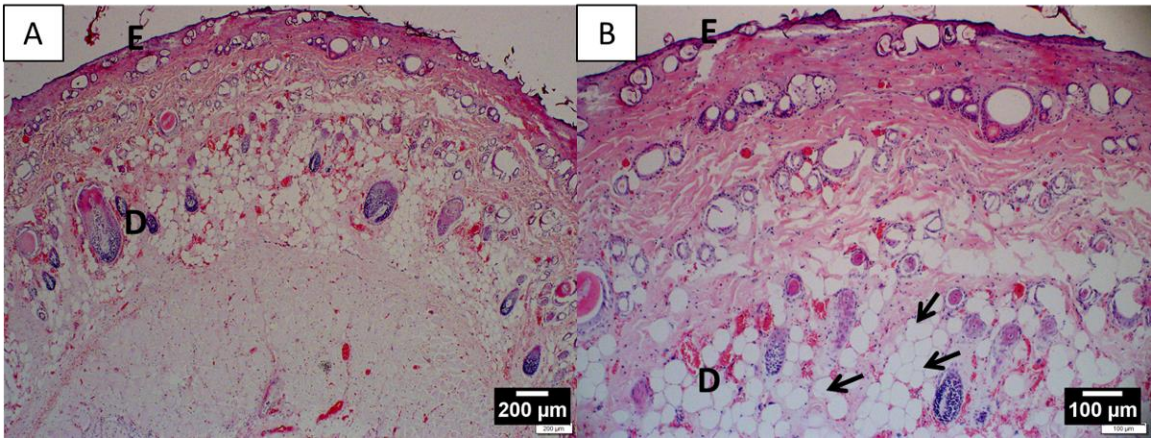


Figure 5.2 Micrograph of the H & E stained skin tissue section of the partial-thickness burn wound at 4 × magnification (A), and 10 × magnification (B) 48 h after the burn wound creation. The epidermis and dermis are indicated by "E" and "D" respectively, while examples of infiltrating adipocytes are indicated by the arrows.

5.3.2 Preparation and Application of the Wound Healing Device

Cylindrical scaffolds of CS-P(KA)/4-PEG were prepared as "non-porous" and "porous" 3D printed scaffolds. The physical properties of the scaffolds were well-controlled by their 3D printed architectures as characterised in Chapter 4. In particular, the "porous" 3D printed scaffolds consisted of micro-pores from the inherent material properties and macro-pores from the cross-hatch printing pattern, while the "non-porous" 3D printed scaffolds only consisted of micro-pores. The macro-pores increased the total porosity and the surface area to volume ration of the "porous" 3D printed scaffolds. Also, the tensile modulus and compressive modulus of the "porous" scaffolds with 0.2 mm needle diameter and 0.5 mm strand spacing were significantly lower compared to the "non-porous" scaffolds. It is known that the porosity and mechanical properties of wound treatments can play a great role in the wound healing and scar-forming process (Levinson, 2013). A 0.2 mm needle ID was further selected for the 3D printing due to the increased resolution of the resulting constructs compared to the 0.4 mm needle ID (Figure 5.3). To match the size of the burn wound site, the scaffolds were designed with a diameter of 15 mm. The excised full-thickness wound was slightly larger than the burn wound. However, due to the swelling of the scaffold, the scaffolds fit adequately into the wound area (Figure 5.4). The height of 1.3 mm was selected according to the height of commercial skin substitutes (Haddad et al., 2018).

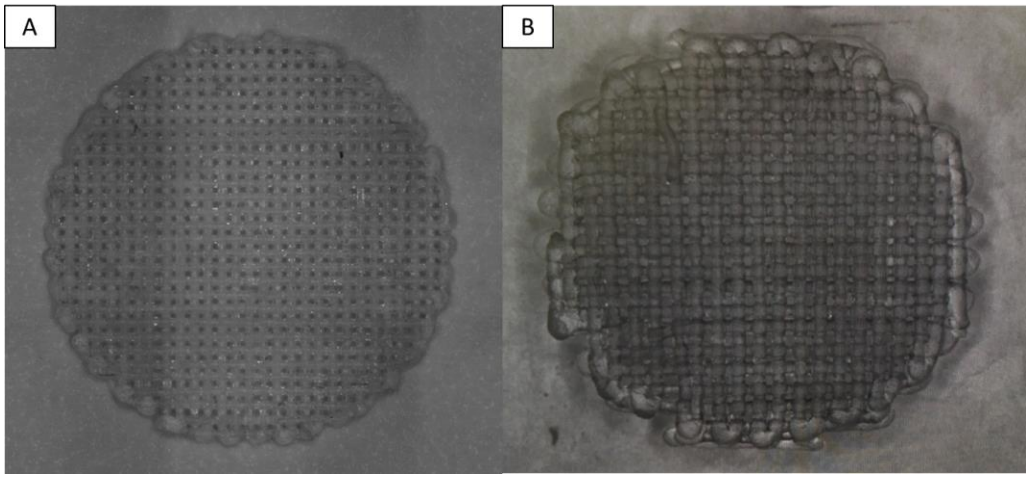


Figure 5.3 Images of the cylindrical scaffolds of CS-P(KA)4-PEG 3D printed with 0.2 mm needle ID and 0.5 mm strand spacing (A), and 0.4 mm needle ID and 1 mm strand spacing (B)

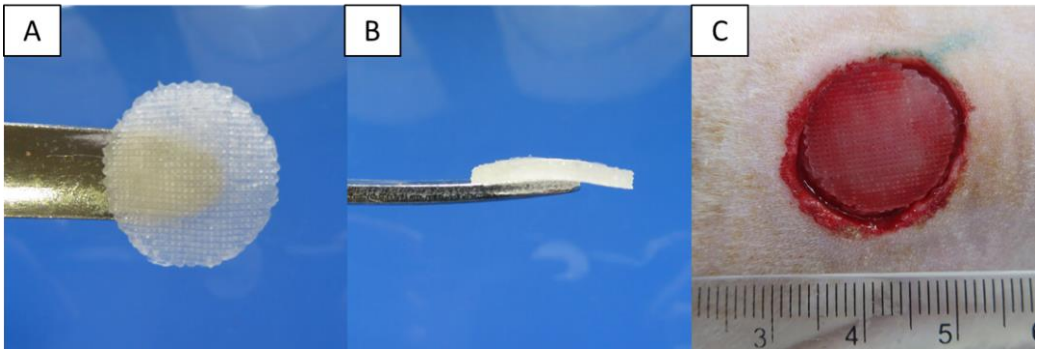


Figure 5.4 Images of the "porous" 3D printed scaffolds, top view (A), side view (B), and applied to the wound area (C)

5.3.3 Macroscopic Evaluation of the Wound Area

Digital images of the wound areas were used to track the wound closure based on the initial wound area on day 0 (Figure 5.5). In Figure 5.6, it can be seen that the wound contraction in the "non-porous"-group and the "porous"-group were significantly higher ($p < 0.05$) compared to the "Jelonet"- and "Bactigras"-groups after five days of treatment. In this first five days of treatment, the wound areas from the "non-porous"-group and the "porous"-group decreased by more than 50 %. However, no significant difference between the "non-porous"-group and the "porous"-group was observed ($p > 0.05$). From days 10 to 20, the rate in wound contraction of all the groups decreased and reached a plateau at day 20. While some difference in the contraction between the groups were observed, none were found to be statistically significant ($p > 0.05$). In rodents and other loose skin animals, wound contraction is the primary mechanism during which wound healing takes place (Dorsett-martin, 2004; Veen et al., 2010; Sami, Heiba and Abdellatif, 2019). In human skin, epithelialisation is the primary mechanism of wound healing, even though wound contraction does occur to a lesser extent (Veen et al., 2010). Nonetheless, the wound contraction rate is commonly used to assess the wound healing process during *in vivo* studies (Mittal and Kumar, 2014; Muhammad et al., 2016; Guo et al., 2017).

While a fast contraction rate is favourable to faster wound closure, excessive contraction has also been associated with scar formation (Levinson, 2013).

The appearance of the wounds was further investigated to assess the scar formation from the different treatments (Figure 5.5). All the groups showed visible scars after 20 days, with varying morphology, colour, and topography. The morphology of the scars was linear, compared to the initial cylindrical wound. The colour of the scars from all treatment groups appeared red compared to the surrounding skin. The red colour can be associated with erythema from high vascularity of the newly formed tissue (Lee et al., 2016). Objective analysis of the colouration of scars has been reviewed by Lee et al. (2016). A simple method that does not require specialised equipment, involves taking digital images of the wound area and then assessing the Red, Green and Blue (RGB) colour intensities using software such as ImageJ (Smith et al., 2015). This method relies on a constant distance and lighting when taking each image. In this study, a large variation between the RGB intensities of the unwounded areas as controls made it difficult to correlate with the colour from the wounded areas. Nonetheless, it can be seen that the colour of the scars of the "Jelonet"-, "Bactigras"- and "non-porous"-groups were distinctly different from the unwounded areas with a definitive wound margin. The colour of the scar from the "porous" group did not show a definite margin, but rather faded into the unwounded areas. The distinctive wound margins were also related to the topography of the wound. Sunken or raised scars had margins that were more distinct. This was observed with the scars from the "Jelonet"-, "Bactigras"-, and "non-porous"-groups, that all appear slightly sunken. The scars from the "porous" group appeared flush with the unwounded areas. From these evaluations, it can be concluded that the "porous"-groups had the least scarring effect, with a near scarless appearance after only 20 days.

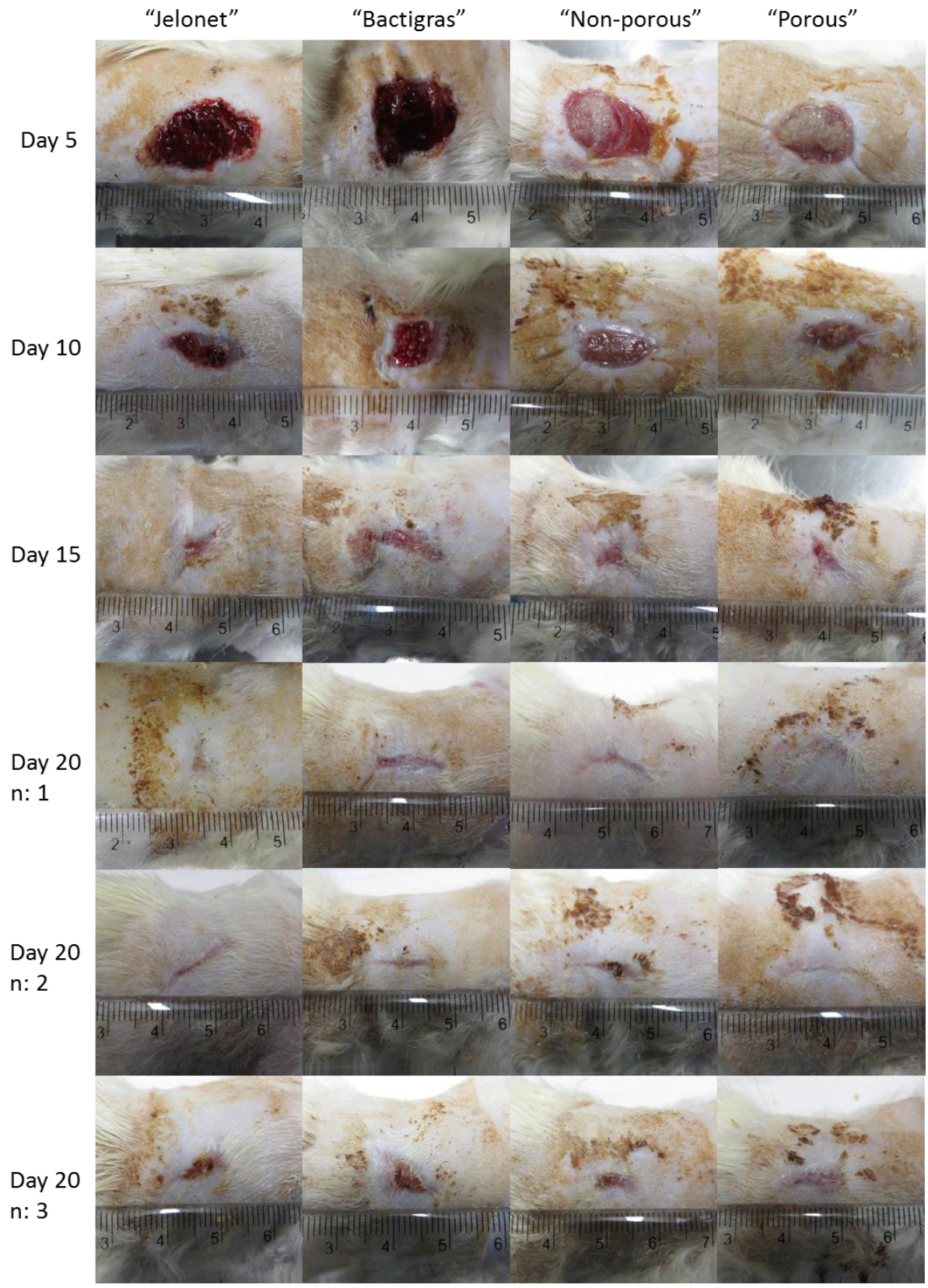


Figure 5.5 Representative images of the wound morphology of the different treatment groups at days 5, 10, and 15 are showed, along with the images from three replicate experiments for the wound healing at day 20.

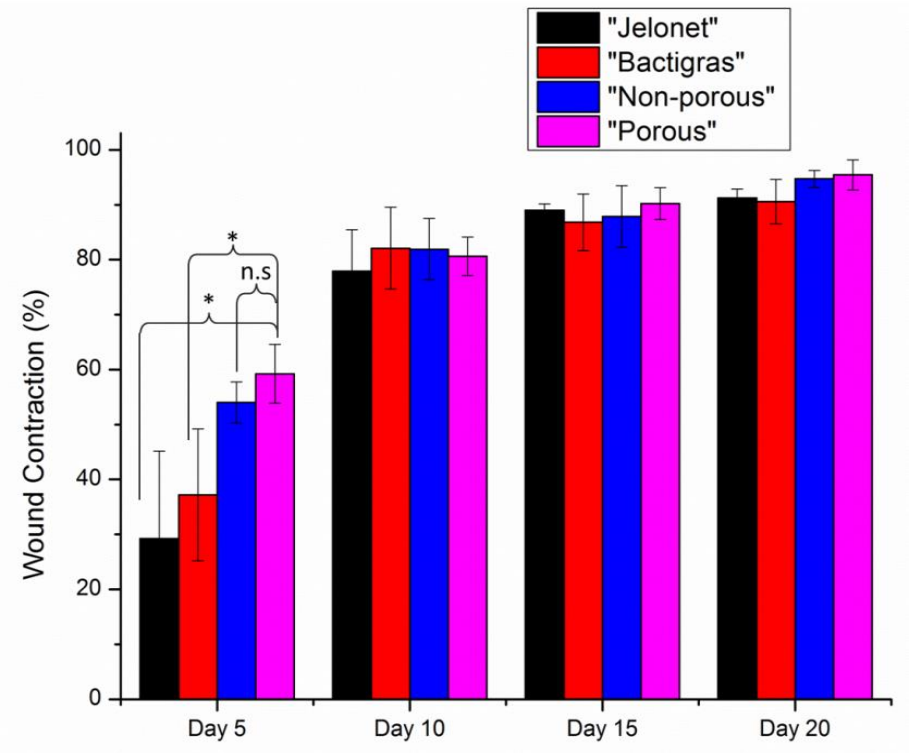


Figure 5.6 A column graph of the wound contractions of the four treatment groups at days 5, 10, 15, and 20 indicates the statistically significant difference between the groups treated with porous 3D printed scaffolds and the control groups, treated with Jelonet or Bactigras after 5 days treatment. No significant difference (n.s) was observed between the non-porous and porous experimental groups after 5 days treatment. At days 10, 15 and 20, no significant difference was observed between the experimental and control groups. $p < 0.05$ is indicated with an asterisk (*).

5.3.4 Histological Evaluation of the Wound Area

The histological assessment provided further information on the microscopic scale of the wound healing process. Prominent tissue features visible with H&E staining (Figure 5.7, Figure 5.8, Figure 5.9, and Figure 5.10) were graded according to Table 5.2 as reported by Nussbaum, Mazzulli and Pritzker (2009). The grading and specific histological observations will be discussed below.

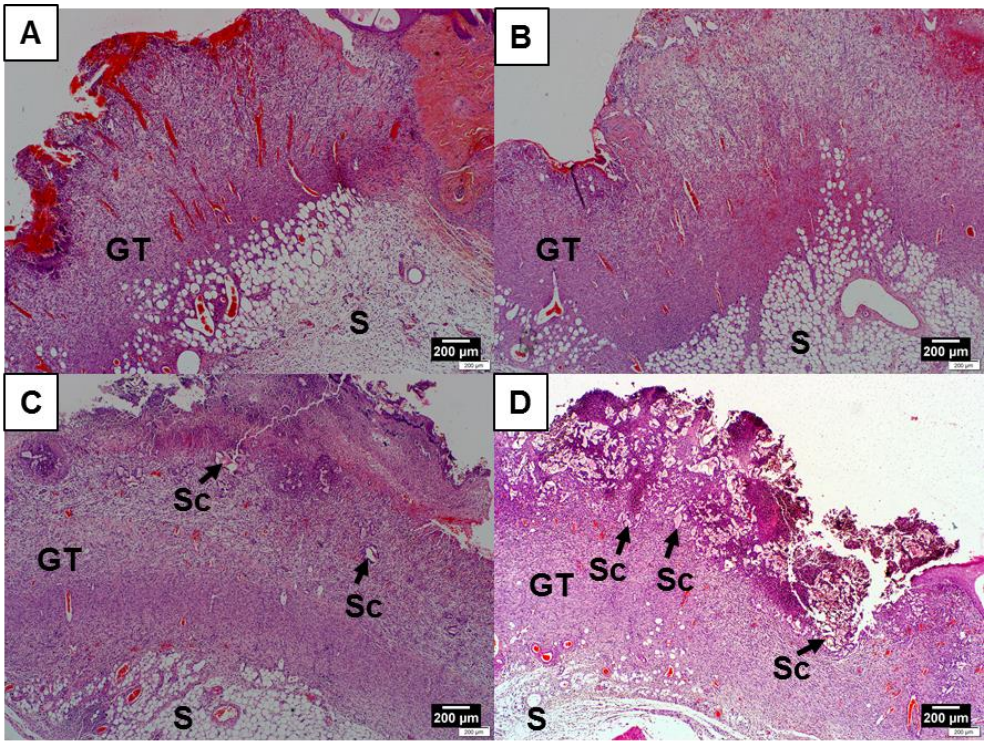


Figure 5.7 Histological images of tissue sections after 5 days of treatment of the "Jelonet"-group (A), "Bactigras"-group (B), "Non-porous"-group (C) and "Porous"-group (D), stained with H&E. GT: granulation tissue, S: subcutis, E: epidermis, D: dermis, Sc: scaffold fragments

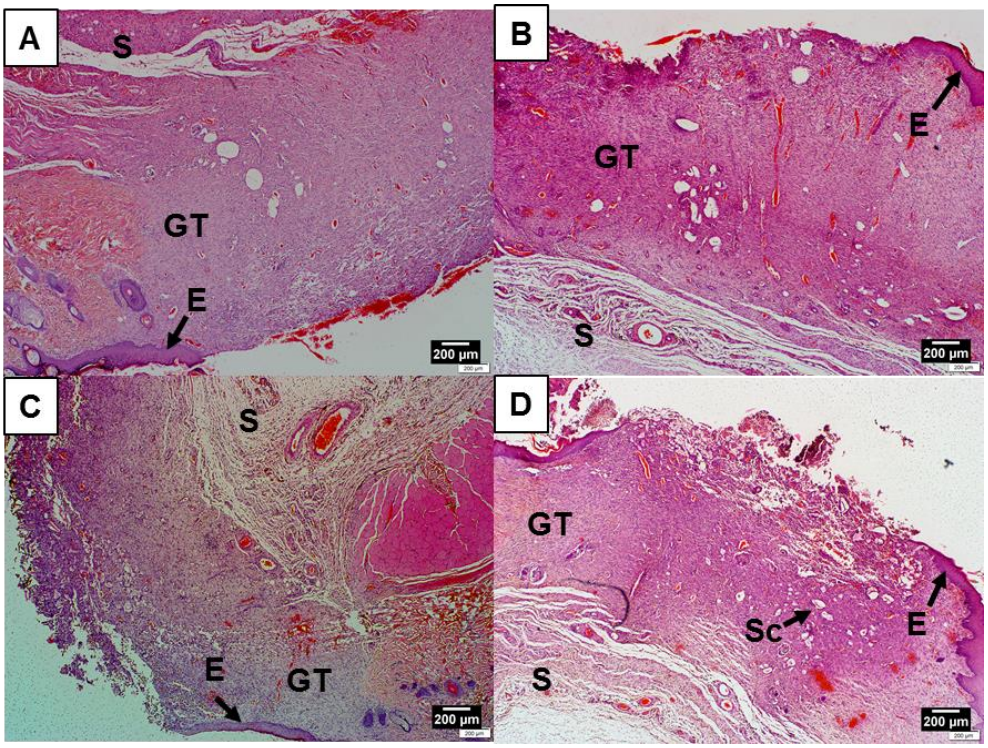


Figure 5.8 Histological images of tissue sections after 10 days of treatment of the "Jelonet"-group (A), "Bactigras"-group (B), "Non-porous"-group (C) and "Porous"-group (D), stained with H&E. GT: granulation tissue, S: subcutis, E: epidermis, Sc: scaffold fragments

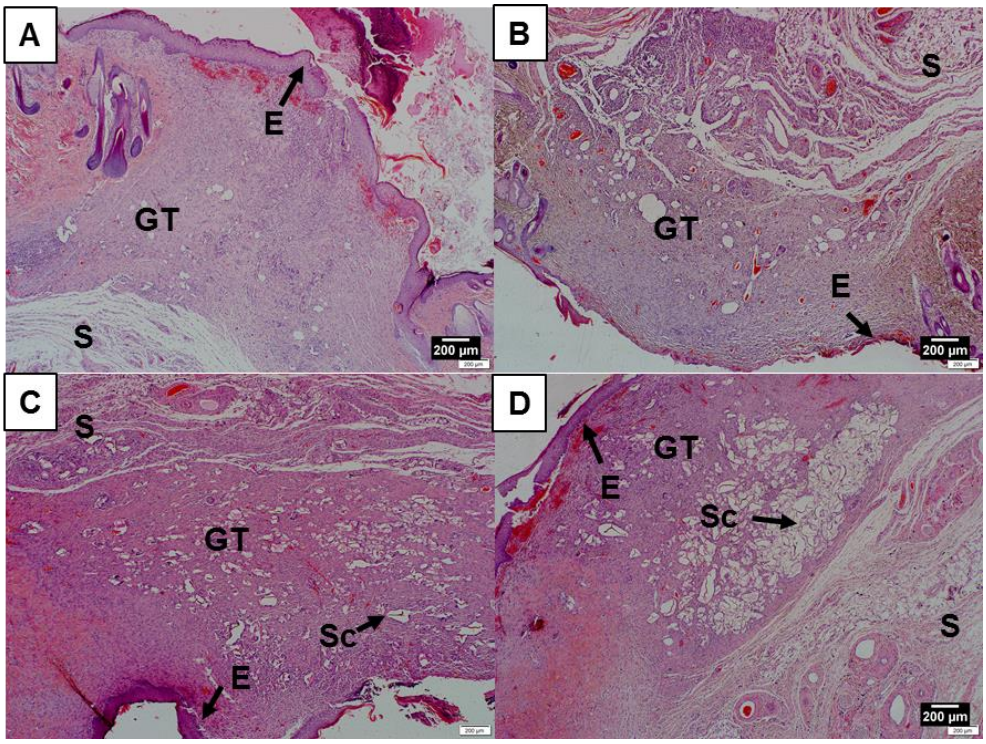


Figure 5.9 Histological images of tissue sections after 15 days of treatment of the "Jelonet"-group (A), "Bactigras"-group (B), "Non-porous"-group (C) and "Porous"-group (D), stained with H&E. GT: granulation tissue, S: subcutis, E: epidermis, Sc: scaffold fragments

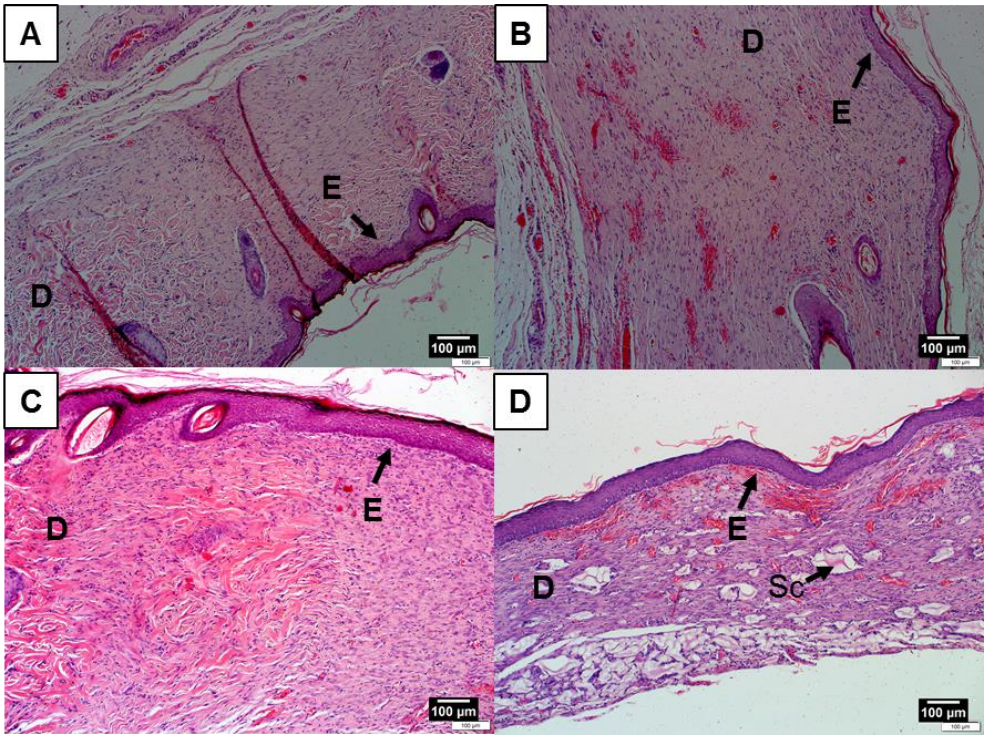


Figure 5.10 Histological images of tissue sections after 20 days of treatment of the "Jelonet"-group (A), "Bactigras"-group (B), "Non-porous"-group (C) and "Porous"-group (D), stained with H&E., E: epidermis, D: dermis, Sc: scaffold fragments

5.3.4.1 Assessment of oedema and inflammatory cell infiltration

Oedema is primarily expected in the first few days after wounding. After 5 days, no oedema was visible in the lesions of any of the treatment groups and remained absent until day 20. Leukocytic infiltrates were identified as lymphoplasmacytic and neutrophilic. On day 5, lymphocytic inflammation was mostly associated with the interstitium of the granulation tissue reaction and the perivascular regions in the subcutis of the lesions. Neutrophils were also prominent in the lesions within the ulcerated surface areas, including the crusts, and in the immediately underlying stromal reaction. Macrophages were most prominent in the granulomas in the deep dermis and subcutis of the lesions. They were also associated with the inflammation within the granulation tissue. In areas where macrophages surrounded loose hair shafts in response to follicular rupture and furunculosis, they indicate an endogenous foreign body type reaction. In the "non-porous"-group and the "porous"-group, macrophages were also associated with fibrillar strands of eosinophilic material that are mildly polarising. This is most likely due to an exogenous foreign body type reaction as a result of the wound healing scaffolds.

The leukocyte gradings of the "Jelonet"-, "non-porous"- and "porous"-groups indicated a decrease in the presence of leukocytes between day 5 and day 20 (Table 5.3). This correlates with the stages in normal wound healing, where inflammation is prominent during the first stage of wound healing and dissipates as the wound healing progresses. The leukocytes present in the "porous"-groups remained moderate over a longer period, compared to the "Jelonet"- and "non-porous"-group, while the "Bactigras"-group remained moderate over the 20 day period. The presence of the macrophages in the "Jelonet"- and "non-porous"-groups remained mild over the 20 day period; the "Bactigras"-group showed a late-stage increase from mild to severe; while the "porous"-group showed a late-stage decrease from moderate to mild (Table 5.4). It was expected that the chitosan in the "non-porous"- and "porous"-group will cause an early inflammatory response (Ueno, Mori and Fujinaga, 2001). The difference in the gradings between the "porous"- and "non-porous"-groups is likely caused by the difference in porosity and surface area of the two scaffolds. The higher porosity and higher surface area of the porous scaffold likely caused an elevated and prolonged inflammatory response in the "porous"-group. The inflammatory cells are known to play a key role in the wound healing cascade of events (Broughton, Janis and Attinger, 2006). Macrophages are particularly important in the transitioning from the inflammatory phase to the proliferative phase. However, reduced inflammation has also been associated with scarless foetal wound healing (Adzick and Lorenz, 1994; Martin, 1997).

Table 5.3 Semi-quantitative histological grading of leukocytes present in the wounds treated over 20 days

Day	Leukocytes Grading			
	"Jelonet"	**"Bactigras"**	**"Non-porous"**	**"Porous"**
5	2	2	2*	3
10	1	2	1	2
15	1	2	1	1
20	1	2	1	1

*Mode was not applicable due to high variability in group and grading reported as the median

Table 5.4 Semi-quantitative histological grading of macrophages present in the wounds treated over 20 days

	Macrophages Grading			
Day	**"Jelonet"**	**"Bactigras"**	**"Non-porous"**	**"Porous"**
5	1	1	1	2
10	1	1	1	2
15	1	3	1	2
20	1	2	1	1

5.3.4.2 Assessment of fibroblast infiltration and granulation tissue formation

In full-thickness wounds, where tissue loss extends from the epidermis to the dermis and deeper tissue, the wound healing takes place via second intention healing (Sorg et al., 2017). This requires the formation of granulation tissue before re-epithelialisation can occur. In this study, the granulation tissue formation was most prominent in the lesions where complete epithelial covering was not yet present. The granulation tissue contained fibroblastic infiltration and vertical capillaries as would be expected. On day 5, the lesions in all the groups showed granulation tissue formation in the dermis and subcutis. However, in the "Jelonet"- and "Bactigras"-groups, the granulation tissue was still in a developing form, while in the "non-porous"- and "porous"-groups, the granulation tissue was characterised as mature. In the "non-porous"- and "porous"-groups, the granulation tissue formation was also associated with the inflammatory response to the eosinophilic material as described under the previous section. The arrangement of the fibroblasts was more haphazardly in the developing granulation tissue. In mature granulation tissue, the fibroblasts were arranged horizontally and parallel to the ulcerated surface.

As the wound healing progressed, the lesions became more contracted and smaller with overlying complete re-epithelialisation. On day 20, these lesions yielded prominent dermal fibrosis indicative of repair, while granulation tissue was not as prominent or absent. In Table 5.5, a decrease in the grading of the granulation tissue was noted for all treatment groups between day 15 and day 20. The grading of fibroblast infiltration coincided with the granulation tissue formation. In Table 5.6, the grading of

the fibroblasts changed from severe to moderate in the "Jelonet", "non-porous"- and "porous"-groups, while it remained severe in the "Bactigras"- group. Pure fibroblastic bundles in the absence of granulation tissue were more prominent in these later stages of wound healing. It was also more prominent peripherally to areas of granulation tissue.

The role of fibroblasts in normal and scarless wound healing have been widely investigated (Levinson, 2013; Darby et al., 2014). In normal wound healing, activated fibroblasts and fibroblasts differentiated into myofibroblasts secrete cytokines, produce extracellular matrix, and contract the wound area (Broughton, Janis and Attinger, 2006). While the contractile function promote faster wound closer, it has also been associated with greater scarring (Levinson, 2013; Darby et al., 2014). Stimuli that affect the activation of fibroblasts include soluble factors, interactions with the extracellular matrix and mechanical microenvironments. Stiffer matrix materials have been shown to stimulate the activation and differentiation of fibroblasts into myofibroblasts, while low stiffness materials such as soft collagen gels showed little activation of fibroblasts (Yeung et al., 2005; Darby et al., 2014). The compressive moduli of the "non-porous"- and "porous"-scaffolds were relatively low and considered compatible with soft tissue engineering. This could potentially subdue the activation and differentiation of fibroblasts and the positive feedback loop. However, no difference in the grading of fibroblast infiltration or granulation tissue were noted between the "Jelonet"-, "non-porous"-, and "porous"-groups. Further investigation into the expression of α-smooth muscle actin (α-SMA) by fibroblasts will provide better insight into the differentiation of fibroblasts into myofibroblasts and its potential contribution to the near scarless healing observed for the "porous"-group.

Table 5.5 Semi-quantitative histological grading of the granulation tissue present in the wounds treated over 20 days

Day	Granulation Tissue Grading			
	"Jelonet"	**"Bactigras"**	**"Non-porous"**	**"Porous"**
5	3	3	3	3
10	3	3	3	3
15	3	3	2*	3
20	0	1	0	0

*Mode was not applicable due to high variability in group and grading reported as the median

Table 5.6 Semi-quantitative histological grading of the fibroblasts present in the wounds treated over 20 days

Day	Fibroblasts Grading			
	"Jelonet"	**"Bactigras"**	**"Non-porous"**	**"Porous"**
5	3	3	3	3
10	3	3	3	3
15	3	3	3	3
20	2	3	2	2

5.3.4.3 Assessment of epithelialisation and remodelling

Mild epithelialisation along the edges of the ulcerated defect was noted in all treatment groups at day 5. It was mostly associated with acanthosis of the epidermal layers. The epithelialisation increased over the 20 days to reach complete re-epithelialisation at day 20 for the "Jelonet"- and "Bactigras"-groups, and at day 15 for the "non-porous"- and "porous" groups (Table 5.7). At this stage, the lesions were contracted and small.

Collagen fibers and fibrosis were associated with the granulation tissue from day 5 in all treatment groups. This was mostly seen in the dermis but sometimes extending into the subcutis. During normal wound healing, collagen type III is synthesised by fibroblasts as part of a provisional matrix (Broughton, Janis and Attinger, 2006; Levinson, 2013; Sorg et al., 2017). As the wound healing progresses, collagen type III is replaced by collagen type I. This process is part of the remodelling phase where collagen finally forms an organised network representing the fibrotic scar tissue. A decrease in the collagen content was noted for the "Jelonet", "non-porous"- and "porous"-groups between day 15 and day 20 (Table 5.8). Nonetheless, severe dermal fibrosis was observed in all groups with the arrangement of the fibrosis varying from haphazard to horizontal.

Table 5.7 Semi-quantitative histological grading of the epithelialisation present in the wounds treated over 20 days

Day	Epithelialisation Grading			
	"Jelonet"	**"Bactigras"**	**"Non-porous"**	**"Porous"**
5	1	1	1	1
10	1	1	1	1
15	2	2	3	3
20	3	3	3	3

Table 5.8 Semi-quantitative histological grading of the collagen present in the wounds treated over 20 days

Day	Collagen Grading			
	"Jelonet"	**"Bactigras"**	**"Non-porous"**	**"Porous"**
5	1	2	2	2
10	2	2	2	2
15	2	2	2	2
20	1	2	1	1*

*Mode was not applicable due to high variability in group and grading reported as the median

5.4 CONCLUSION

The partial-thickness burn wounds that were excised to create the full-thickness wound model used in this study, proved reproducible for the macroscopic evaluation of wound contraction and scar formation, and the histological evaluation of the wound healing process. The experimental groups

lead to a faster wound contraction in the first 5 days of treatment, compared to the control and comparison groups. Inflammation in the experimental groups, indicated an exogenous foreign body response to the CS-P(KA)/4-PEG material. Nonetheless, the granulation tissue in the experimental groups reached maturity within the first 5 days, which favoured faster epithelialisation compared to the control and comparative groups. Minor differences in the histological assessment of the groups treated with the "porous" 3D printed scaffold and the "non-porous" 3D printed scaffold were observed. This included a prolonged inflammation reaction in the "porous" scaffold, compared to the "non-porous" scaffold. However, on the macroscopic scale, the "porous" 3D printed scaffolds afforded near scarless lesions after only 20 days, compared to the "non-porous"-group and the control groups. The higher porosity and higher surface area of the "porous" 3D printed scaffold was expected to favour higher cell infiltration, while the lower compressive modulus of the scaffold was expected to limit the contractility of fibroblasts. However, it was difficult to correlate this with the histological evaluations. While a low inflammatory response and low contraction rates have been associated with scarless wound healing, the "porous" 3D printed scaffolds investigated in this study produced near-scarless wounds regardless of the prolonged inflammatory response and high contraction rates. Further immunohistochemistry is recommended to provide further insight into the scar-reducing mechanism of the "porous" 3D printed scaffolds.

5.5 REFERENCES

ADZICK, N.S. and LORENZ, H.P. (1994) Cells, matrix, growth factors and the surgeon: The biology of scarless fetal wound repair. *Annals of Surgery*, 220(1), pp. 10–18.

AHMADI, F. et al. (2015) Chitosan based hydrogels : characteristics and pharmaceutical applications. *Research in Pharmaceutical Sciences*, 10(1), pp. 1–16.

BROUGHTON, G., JANIS, J.E. and ATTINGER, C.E. (2006) The basic science of wound healing. *Plastic and reconstructive surgery*, 117(7S), pp. 12S-34S.

CAI, E.Z. et al. (2014) Creation of Consistent Burn Wounds : A Rat Model. *Archives of Plastic Surgery*, 41(4), pp. 317–324.

CHEN, Z. J. et al. (2014) A Novel Three-Dimensional Wound Healing Model. *Journal of Developmental Biology*, 2, pp. 198–209.

COOLEN, N. A., et al. (2008) Development of an in vitro burn wound model. *Wound Repair and Regeneration*, 16, pp. 559–567.

CUBO, N. et al. (2016) 3D bioprinting of functional human skin: production and in vivo analysis. *Biofabrication*, 9(1), p. 15006.

DARBY, I.A. et al. (2014) Fibroblasts and myofibroblasts in wound healing. *Clinical, Cosmetic and Investigational Dermatoloty*, 7, pp. 301–311.

DERR, K. et al. (2019) Fully Three-Dimensional Bioprinted Skin Equivalent Constructs with Validated Morphology and Barrier Function. *Tissue Engineering - Part C: Methods*, 25(6), pp. 334–343.

DORSETT-MARTIN, W.A. (2004) Rat models of skin wound healing : A review. *Wound repair and regeneration*, 12, pp. 591–599.

GUO, H. et al. (2017) A new model for studying deep partial-thickness burns in rats. *International Journal of Burns and Trauma*, 7(6), pp. 107–114.

HADDAD, A.G. et al. (2018) Skin Substitutes and Bioscaffolds:Temporary and Permanent Coverage. *Clinics in Plastic Surgery*, 44(3), pp. 627–634.

HE, P. et al. (2018) Bioprinting of skin constructs for wound healing. *Burns & Trauma*, 6(5), pp. 1–10.

INTINI, C. et al. (2018) 3D-printed chitosan-based scaffolds: An in vitro study of human skin cell growth and an in-vivo wound healing evaluation in experimental diabetes in rats. *Carbohydrate Polymers*, 199(July), pp. 593–602.

KELLY, C.N. et al. (2018) Design and Structure–Function Characterization of 3D Printed Synthetic

Porous Biomaterials for Tissue Engineering. *Advanced Healthcare Materials*, 7, p. 1701095.

KILSDONK, J. W. J. Van et al. (2013) An in vitro wound healing model for evaluation of dermal substitutes. *Wound Repair and Regeneration*, 21, pp. 890–896.

KIM, B.S. et al. (2018) 3D cell printing of in vitro stabilized skin model and in vivo pre-vascularized skin patch using tissue-specific extracellular matrix bioink: A step towards advanced skin tissue engineering. *Biomaterials*, 168, pp. 38–53.

LAN, Y. et al. (2014) Therapeutic efficacy of antibiotic-loaded gelatin microsphere / silk fibroin scaffolds in infected full-thickness burns. *Acta Biomaterialia*, 10, pp. 3167–3176.

LEE, K.C. et al. (2016) A systematic review of objective burn scar measurements. *Burns & Trauma*, [Online] Available from: doi.org/10.1186/s41038-016-0036-x.

LEVINSON, H. (2013) A Paradigm of Fibroblast Activation and Dermal Wound Contraction to Guide the Development of Therapies for Chronic Wounds and Pathologic Scars. *Advances in Wound Care*, 2(4), pp. 149–159.

LIU, P. et al. (2019) 3D bioprinting and in vitro study of bilayered membranous construct with human cells-laden alginate/gelatin composite hydrogels. *Colloids and Surfaces B: Biointerfaces*, 181, pp. 1026–1034.

MARTIN, P. (1997) Wound Healing — Aiming for Perfect Skin Regeneration. *Science*, 279, pp. 75–82.

MAYET, N. (2016) *Inflammatory Dependent Bioresponsive Smart Transdermal Delivery System Incorporating Suspended Nanofibrous Mats as a Platform for Wound Healing*. University of the Witwatersrand.

MEKHAIL, M., JAHAN, K. and TABRIZIAN, M. (2014) Genipin-crosslinked chitosan/poly-l-lysine gels promote fibroblast adhesion and proliferation. *Carbohydrate Polymers*, 108, pp. 91–98.

MITTAL, A. and KUMAR, N. (2014) A new, bioactive, antibacterial-eluting, composite graft for infection-free wound healing. *Wound Repair and Regeneration*, 22(4), pp. 527–36.

MUHAMMAD, A.A. et al. (2016) Evaluation of wound healing properties of bioactive aqueous fraction from Moringa oleifera Lam on experimentally induced diabetic animal model. *Drug Design, Development and Therapy*, 10, pp. 1715–1730.

NUSSBAUM, E.L., MAZZULLI, T. and PRITZKER, K.P.H. (2009) Effects of Low Intensity Laser Light on Wound Healing in the Rat Effects of Low Intensity Laser Irradiation During Healing of Skin Lesions in the Rat. *Lasers in Surgery and Medicine*, 41, pp. 372–381.

QU, M. & NOURBAKHSH, M. (2017) Current Experimental Models of Burns. *Discovery Medicine*, 23, pp. 95–103.

SAMI, D.G., HEIBA, H.H. and ABDELLATIF, A. (2019) Wound healing models : A systematic review of animal and non-animal models. *Wound Medicine*, 24(1), pp. 8–17.

SCHINDELIN, J. et al. (2012) Fiji: an open-source platform for biological-image analysis, *Nature methods*, 9(7), pp. 676-682.

SHAHROKHI, S., ARNO, A. and JESCHKE, M.G. (2014) The use of dermal substitutes in burn surgery: Acute phase. *Wound Repair and regeneration*, 22, pp. 14–22.

SHARPE, J.R. and MARTIN, Y. (2013) Strategies Demonstrating Efficacy in Reducing Wound Contraction In Vivo. *Advances in Wound Care*, 2(4), pp. 167–175.

SHEIKHOLESLAM, M. et al. (2018) Biomaterials for Skin Substitutes. *Advanced Healthcare Materials*, 7, p. 1700897.

SMITH, B.J. et al. (2015) Digital imaging analysis to assess scar phenotype. 22(2), pp. 319–335.

SORG, H. et al. (2017) Skin Wound Healing : An Update on the Current Knowledge and Concepts. *European Surgical Research*, 58, pp. 81–94.

STONE, R.I. et al. (2018) Advancements in Regenerative Strategies Through the Continuum of Burn Care. *Frontiers in Pharmacology*, 9, p. 672.

UENO, H., MORI, T. and FUJINAGA, T. (2001) Topical formulations and wound healing applications of chitosan. *Advanced Drug Delivery Reviews*, 52, pp. 105–115.

VEEN, V.C. VAN DER et al. (2010) Biological background of dermal substitutes. *Burns*, 36(3), pp. 305–321.

VIJAYAVENKATARAMAN, S., LU, W.F. and FUH, J.Y.H. (2016) 3D bioprinting of skin: a state-of-the-art review on modelling, materials, and processes. *Biofabrication*, 8, pp. 1–31.

YEUNG, T. et al. (2005) Effects of Substrate Stiffness on Cell Morphology , Cytoskeletal Structure , and Adhesion. *Cell Motility and the Cytoskeleton*, 60, pp. 24–34.

CHAPTER 6: EPILOGUE

The work presented in this thesis focused on developing and evaluating 3D printed polypeptide-based hydrogel scaffolds as potential wound healing devices for burn wounds. The interest in poly(Lys_{60}-*ran*-Ala_{40})-based hydrogels was initiated by their biofunctional properties as reported by Song, Rane and Christman (2012). The versatility of these hydrogels in terms of their hydrogel composition and 3D printability was explored to contribute to the development and utilisation of new 3D biomaterial inks, which is currently underutilised especially in wound healing studies. 3D printed acellular scaffolds with tailored physical properties were further investigated to contribute to the knowledge on structure-function relationships of such scaffolds in terms of their *in vitro* and *in vivo* wound healing performance. The main discoveries resulting from this work are discussed in the following section, and the chapter is concluded with recommendations for future work.

6.1 GENERAL CONCLUSIONS

In Chapter 3, a new library of low concentration poly(Lys_{60}-*ran*-Ala_{40})-based hydrogels was investigated. Poly(Lys_{60}-*ran*-Ala_{40}) with controlled molecular weight, molecular weight distribution and L-lysine to L-alanine ratio (K:A) was synthesised using a facile method of controlled ROP. Control over the polymer structure of the polypeptide was important for control over subsequent crosslinking reactions with 4-arm PEG-SG. The stoichiometric reactant ratios and total polymer concentrations were varied to develop a library of poly(Lys_{60}-*ran*-Ala_{40})/4-arm PEG (P(KA)/4-PEG) hydrogels. It was seen that (P(KA)/4-PEG) solutions with total polymer concentrations higher than 4 wt% favoured gelation over the solution state. This was related to the increase in the probability of intermolecular crosslinking with higher polymer concentrations. Also, as the functional molar ratio of amines from P(KA) to NHS-esters from 4-PEG approached 1:1, a denser polymer network was achieved.

The P(KA)/4-PEG hydrogels demonstrated high tunability in terms of their mechanical properties, amine content, swelling behaviour, pore sizes and degradation time. It was further demonstrated that the functional molar ratio during gel formation played a significant role on the biofunctionality of the P(KA)/4-PEG hydrogels. As the functional molar ratio increased from 1:1 to 16:1, the cytotoxicity of the P(KA)/4-PEG hydrogels towards NIH 3T3 fibroblasts significantly increased. This was ascribed to the higher free amine concentration and therefore higher positive charge density in the hydrogels. P(KA)/4-PEG hydrogels with low cytotoxicity also displayed excellent cell-adhesive properties. This included the 4 wt% hydrogels prepared from a 1:1 functional molar ratio, with P(KA) concentrations as low as 0.65 wt%. However, none of the P(KA)/4-PEG hydrogels within the range of concentration and molar ratios investigated in this study, displayed antibacterial properties. Nonetheless, the development of the library of P(KA)/4-PEG hydrogels allowed the identification of hydrogel compositions that displayed suitable combinations of physicochemical and biofunctional properties

for potential wound healing applications. It also allowed identification of P(KA)/4-PEG hydrogel compositions for potential processing into 3D biomaterial inks.

In Chapter 4, the 3D printability of P(KA)/4-PEG hydrogels as new 3D biomaterial inks was investigated. From the library of P(KA)/4-PEG hydrogels developed in Chapter 3, soft/gel-like compositions at the sol-gel transition and stiff compositions in the gel phase were selected for two respective approaches. However, from the two approaches investigated to develop P(KA)/4-PEG into 3D biomaterial inks, only the "composite microgel" inks were 3D printable. In this approach stiff P(KA)/4-PEG hydrogels were processed into microparticles and incorporated into a polymer solution to produce a composite microgel paste. Three polymer solutions composed of 4-arm PEG-acrylate (4-PEG-Ac), chitosan (CS), or poly(vinyl alcohol) (PVA) were used as the matrix material for the composite paste. These polymers are commonly used in tissue engineering applications and wound treatments. Their incorporation into the "composite microgel" ink demonstrated great versatility in terms of the physicochemical and biofunctional properties of the polymer matrix components and their solidification mechanism. For the solidification of the "composite microgel" inks, 4-PEG-Ac was chemically crosslinked through photopolymerisation, CS was physically crosslinked through pH neutralisation, and PVA was physically crosslinked through the partial crystallisation of PVA using freeze-thaw cycles. The three respective "composite microgel" inks displayed good 3D printability, in terms of extrudability, layer-stacking ability, solidification mechanism, and 3D print fidelity. The physical properties of the 3D printed scaffolds of 4-PEG-Ac-P(KA)/4-PEG, CS-P(KA)/4-PEG and PVA-P(KA)/4-PEG further demonstrated high tunability based on the composition of the polymer matrix material. In addition, the biocompatibility of P(KA)/4-PEG hydrogels was retained in the 3D printed scaffolds and the biofunctionality of bioinert 4-PEG and PVA hydrogels was enhanced. Apart from the contribution to new 3D biomaterial inks, this work also presented a new and facile method of processing covalently cross-linked hydrogels into 3D printed scaffolds. This could potentially "unlock" the 3D printability of biofunctional hydrogels, which are generally excluded from 3D printing applications.

The physical properties of CS-P(KA)/4-PEG was further controlled using different 3D printing patterns. CS-P(KA)/4-PEG inks demonstrated excellent 3D printability and proved highly successful in printing scaffolds with narrow strand diameter (~200 μm) and narrow strand spacing (~500 μm) while the integrity of the vertical and horizontal pores was maintained. By using different needle IDs and strand spacing, certain physical properties of the hydrogels could be tuned while the porosity was kept constant. This included the surface area to volume ratio, the macro-pore sizes, and the mechanical properties. While the mechanical properties of the 3D printed scaffolds were relatively low, the scaffolds demonstrated adequate adhesion and spreading of NIH 3T3 fibroblasts seeded on the scaffold surfaces for 4 days. Consequently, the scaffolds were considered suitable for potential applications in wound healing.

Chapter 5 provided an evaluation on the *in vivo* wound healing performance of 3D printed scaffolds of CS-P(KA)/4-PEG. 3D printing facilitated the fabrication of the scaffolds with dimension matching the intended lesion dimensions, while the physical properties of the scaffolds were fine-tuned according to their 3D printed internal architecture. To investigate the *in vivo* structure-function relationship of the scaffolds, two CS-P(KA)/4-PEG scaffolds with porous and non-porous 3D printed architectures were used. The wound healing was evaluated in terms of wound contraction, scar formation, and histological assessment using a previously reported full-thickness burn wound model of Sprague Dawley rats.

A previously reported burn wound model (Mayet, 2016) was validated based on its reproducibility in terms of wound appearance and histological characterisation of the wound depth. It was found that the wound correlated with partial-thickness burn wounds and further excision of the epidermal and dermal layers provided the full-thickness wound. On the macroscopic scale, the experimental groups demonstrated a faster wound contraction in the first 5 days of the treatment, compared to the control and comparison groups. Furthermore, the porous 3D printed scaffold produced near scarless lesions after only 20 days. On the microscopic scale, the experimental groups demonstrated an exogenous foreign body response to the CS-P(KA)/4-PEG material. The porous 3D printed scaffolds further caused a prolonged inflammatory response. In terms of the granulation tissue formation, the experimental groups demonstrated a faster maturation within the first 5 days of treatment. This also favoured faster epithelialisation of the experimental groups compared to the control groups. Apart from the prolonged inflammatory response, no distinct differences in the histological evaluations could account for the improved scar appearance caused by the porous 3D printed scaffold. Nonetheless, in terms of the structure-function relationship of the 3D printed scaffolds, it was evident that the physical properties of the scaffolds could be tailored to enhance the wound healing and final appearance of the scar.

6.2 RECOMMENDATIONS FOR FUTURE WORK

The results presented in this study indicate the potential of 3D printed P(KA)/4-PEG as biofunctional scaffolds for wound healing applications. Further optimizations and developments of the investigated system could expand the biofunctional properties to further enhance its wound healing performance and extend its application to other tissue engineering fields.

First of all, the antibacterial activity of the P(KA)/4-PEG hydrogels need to be addressed. This feature is ideal for the treatment of burn wounds, due to their high susceptibility to infections. Since the P(KA)/4-PEG hydrogels investigated in this study did not display antibacterial activity within the range of parameters tested, the concentrations of P(KA) in the hydrogel can be further increased to investigate its effect on the antibacterial activity. Zhou et al. (2010) also reported other random co-polypeptides containing lysine as hydrophilic amino acid and alanine, phenylalanine or leucine as

hydrophobic amino acid, with high antibacterial activity and broad-spectrum antimicrobial properties. However, these high potency polypeptides have also demonstrated haemolytic activity. By substituting P(KA) in the P(KA)/4-PEG hydrogels with the polypeptides reported by Zhou et al. (2010), the biocompatibility of the polypeptides and the antibacterial activity of the hydrogels can potentially be improved. Furthermore, this can provide a better understanding of the parameters that influence the antibacterial activity of polypeptides when incorporated in hydrogels, which is currently poorly understood.

In terms of the newly developed biomaterial inks, the P(KA)/4-PEG hydrogel microparticles indicated great versatility in terms of their incorporation into different composite microgel pastes. In future work, these compositions can be further explored to expand the physical properties of the materials. Higher concentrations of the 4-PEG-Ac, CS or PVA polymer matrix solutions could potentially increase the mechanical properties of the materials to suit a wider range of tissue engineering applications. Other natural or synthetic hydrogel precursors already used in 3D printing can also be investigated as the polymer matrix materials. In such cases, the incorporation of P(KA)/4-PEG hydrogel microparticles will not only enhance the biofunctionality, but can also potentially improve the 3D printability and ameliorate the optimisation processes. For example, popular biomaterial inks such as gelatin require tedious optimisations of ink temperature vs platform temperature, while alginate requires optimisation of crosslinker concentrations, application of crosslinker (sprayed, crosslinking medium or coaxial extrusion) and crosslinking speed (Maher et al., 2009; Ahn et al., 2012; Lee et al., 2013; Rajaram, Schreyer and Chen, 2014). The biomaterial inks of P(KA)/4-PEG microparticles on the other hand, were self-supporting without the need of *in situ* crosslinking or controlled platform temperatures. Furthermore, the 3D printed systems reported in this study can be investigated for controlled drug delivery at the wound site. Due to differences in the network structures of P(KA)/4-PEG and the polymer matrix material, dual release profiles could potentially be achieved. The release could further be tailored using different 3D printing patterns.

Finally, the performance of the CS-P(KA)/4-PEG 3D printed scaffolds as wound healing devices should be further investigated using immunohistochemistry (IHC). IHC was beyond the scope of the current study. However, difficulty in correlating the near-scarless macroscopic wound appearance of groups treated with porous 3D printed scaffolds with the histological evaluations motivates the need for IHC. IHC staining of α-SMA, CD31, collagens Type I, and PNCA for qualitative and quantitative assessments (Gupta and Kumar, 2015) will provide better insight with regards to differences in the wound healing performance between the porous and non-porous 3D printed scaffolds.

6.3 REFERENCES

AHN, S. et al. (2012) Fabrication of cell-laden three-dimensional alginate-scaffolds with an aerosol - cross-linking process. *Journal of Materials Chemistry*, 22, pp. 18735–18740.

GUPTA, A. and KUMAR, P. (2015) Assessment of the histological state of the healing wound. *Plastic and Aesthetic Research*, 2, pp. 239–242.

LEE, H. et al. (2013) Cell(MC3T3-E1)-Printed Poly(ε-caprolactone)/Alginate Hybrid Scaffolds for Tissue Regeneration. *Macromolecular Rapid Communications*, 34, pp. 142–149.

MAHER, P.S. et al. (2009) Construction of 3D biological matrices using rapid prototyping technology. *Rapid Prototyping Journal*, 15, pp. 204–210.

MAYET, N. (2016) *Inflammatory Dependent Bioresponsive Smart Transdermal Delivery System Incorporating Suspended Nanofibrous Mats as a Platform for Wound Healing*. University of the Witwatersrand.

RAJARAM, A., SCHREYER, D. and CHEN, D. (2014) Bioplotting Alginate / Hyaluronic Acid Hydrogel Scaffolds with Structural Integrity and Preserved Schwann Cell Viability. *3D Printing*, 1, pp. 194–203.

SONG, A., RANE, A.A. and CHRISTMAN, K.L. (2012) Antibacterial and cell-adhesive polypeptide and poly (ethylene glycol) hydrogel as a potential scaffold for wound healing. *Acta Biomaterialia*, 8, pp. 41–50.

ZHOU, C. et al. (2010) High Potency and Broad-Spectrum Antimicrobial Peptides Synthesized via Ring-Opening Polymerization of alpha-Aminoacid-N-carboxyanhydrides. *Biomacromolecules*, 11, pp. 60–67.

APPENDIX A

Research Outputs

Oral & Poster Presentations:

- Towards a polypeptide-based hydrogel suitable for 3D printing (Poster), *9th Wits Cross Faculty Postgraduate Symposium, University of the Witwatersrand, October 2018*

- Towards a biofunctional polypeptide-based hydrogel suitable for bioprinting (Oral), *13th International Conference on Materials Chemistry, Liverpool, UK, July 2017*

APPENDIX B

STRICTLY CONFIDENTIAL

ANIMAL ETHICS SCREENING COMMITTEE (AESC)

CLEARANCE CERTIFICATE NO. 2018/10/51/C

APPLICANT: Ms J Gilomee

SCHOOL: Pharmacy
DEPARTMENT:
LOCATION:

PROJECT TITLE: In vivo study of a 3D printed wound healing device on a severe burn wound model of Sprague Dawley Rats

Number and Species

70X 250-300 Male Sprague-Dawley rats

Approval was given for the use of animals for the project described above at an AESC meeting held on 2018/10/30. This approval remains valid until 2021/02/12.
Unreported changes to the application may invalidate the clearance given by the AESC
An annual progress report must be provided

The use of these animals is subject to AESC guidelines for the use and care of animals, is limited to the procedures described in the application form and is subject to any additional conditions listed below:

Signed: _____ (Chairperson, AESC) Date: 18/2/2019

I am satisfied that the persons listed in this application are competent to perform the procedures therein, in terms of Section 23 (1) (c) of the Veterinary and Para-Veterinary Professions Act (19 of 1982)

Signed: _____ (Registered Veterinarian) Date: 14/02/2018

cc: Supervisor: Prof V Pillay, Prof Y Choonara and Prof B Klumperman
Director: CAS

Works 2000/Ain0016/AESCcert.wps

APPENDIX C

REPORT ON PILOT STUDY FOR:

IN VIVO STUDY OF A 3D PRINTED WOUND HEALING DEVICE ON A SEVERE BURN WOUND MODEL OF SPRAGUE DAWLEY RATS

By: Johnel Giliomee Clearance certificate no. 2018/10/51C

1. Introduction

Ten (10) Sprague Dawley rats were used in the pilot study to evaluate the degree and reproducibility of the burn wound (n=5); and to ensure the efficacy of the pain management, as selected according to a burn wound study previously performed on rats at CAS (n=5)[1].

2. Experimental Procedures

The 10 rats were divided into 2 study groups:

Group A: Evaluation of degree and reproducibility of the burn wound

Group B: Evaluation of pain management

2.1. Timeline

The pilot study was performed from 21 May 2019 to 4 June 2019.

Day 0: Group A & B: Burn wound created

Day 2: Group A: Euthanased and tissue samples taken for histology

Group B: Scab removed and wound treated with non-medicated gauze

Day 7: Bandages changed (5 days after treatment applied)

Day 14: Group B: Euthanased

2.2. Evaluation of burn wound reproducibility

The size, position, and colour of the burn wound were visually inspected to determine the reproducibility of the burn wound. While histological analysis of the burned skin tissue will be used to analyse the depth of skin tissue damage, this information was not essentially requested by the Ethics Committee for the pilot study.

2.3. Evaluation of pain management

The pain management was evaluated by using the rodent monitoring score sheet designated for category D studies and by monitoring the rats 2-3 times per day for 3 days following the procedures.

Appendix C (Continued)

3. Observations and Recommendations

3.1. Burn wound reproducibility

According to the protocol, the burn wound should be made 1.5 cm towards the right of the spine on the upper dorsal, while the rats are in the dorsal position. This position made it difficult to place the rod 1.5 cm from the spine, and the rats were instead placed in the lateral position. It was found that 1.5cm was too far from the spine and that the burn wound approaches the abdominal area, rather than the back of the rats. To ensure better position and reproducibility, it is recommended that the position be clearly marked with a marker 0.5-1 cm towards the right of the spine for future procedures.

The burn wound was created using a metal rod (d=15mm) heated in boiling water. It can be seen from Figure 1 that the colouration of the burn wounds varied from white to red, with white coloured wounds being associated with deep partial thickness wounds[2]. The variation in wound colour is most likely due to fluctuation of the surface temperature of the metal rod on the day of the burn procedure, as water was continually added to the water bath to maintain water levels. Measurements of the surface temperature of the metal rod with a thermocouple delivered maximum temperatures of 75 °C after placing it in boiling water for more than 30 min. It was found that this temperature can be reached after 5 min heating time. Therefore, it is recommended that at least 5 min in between burn procedures be allowed while the addition of cold water to the water bath is avoided.

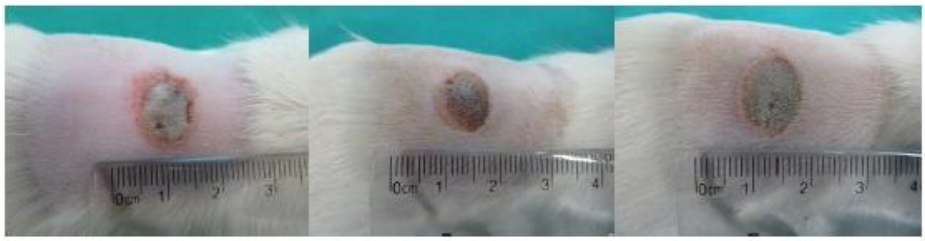


Figure 1. Burn wound colouration 2 days after burn procedure

3.2. Pain management

3.2.1. Burn procedure & Surgical removal of the scab

The medicated jelly cubes were well-received by the rats, being habituated to non-medicated jelly cubes for 3 days. The rats showed no severe signs of shock or pain to the burn treatment, suggesting that the pre-treatment with analgesics (tramadol 12 h before and morphine 1 h before) combined with the anaesthesia (isoflurane gas and lignocaine L-block local anaesthesia) was adequate. The rats also maintained their weight, gaining an average of 2.6 ±1.5 % per day for the two days following the burn procedure. The rats lost 1.0 ±1.3% weight the first day after the surgical removal of the scab, which can indicate to pain or distress. However, from the second day following the scab removal they started gaining weight again. Clinical signs of pain were rarely noticed.

Appendix C (Continued)

3.2.2. Bandage changes

The rats were monitored for a further 11 days following the surgical removal of the scab. A bandage change on Day 7 allowed inspection of the wound area. Anaesthesia with isoflurane gas was inadequate and the first rat showed severe signs of pain during the removal of the bandages. All the rats were then anaesthetized with injections of ketamine and xylazine (4:1; 0.1 ml/100mg) in addition to isoflurane gas. Following the bandage changes, clinical signs such as red eyes and inactivity was seen for the first two days. The rats also lost an average of 4.5 ±1.6% weight on the first day following the bandage change. Their diet was then supplemented with seeds and the administration of jelly cubes medicated with tramadol (4 mg/kg) was continued for the remainder of the study.

It is recommended that morphine (0.1ml/100g) be injected 1 hour prior to bandage changes to reduce their shock and pain to the procedure. It is further necessary that bandage changes be performed in the presence of the veterinary nurse and CAS staff. This will require doing bandage changes on days 5, 11, 15 and 20 after the respective treatments have been applied, instead of days 5, 10, 15 and 20 per the original protocol. This minor change in the timeline is not expected to affect the outcome of the study.

4. References

(1) Mayet, N. Inflammatory Dependent Bioresponsive Smart Transdermal Delivery System Incorporating Suspended Nanofibrous Mats as a Platform for Wound Healing, University of the Witwatersrand, 2016.

(2) Guo, H.; Ali, R. M.; Hamid, R. A.; Zaini, A. A.; Khaza, H. *Int. J. Burns Trauma* **2017**, *7*, 107.